The Mechanistic Study of C–H and H–H Bond Activation and C–C Coupling Reactions at the Interface of Homogeneous Catalysis and Heterogeneous Catalysis

Zhongwen Luo

Jiande-Hangzhou, Zhejiang Province, China

B.S. Applied Chemistry, Huazhong Agricultural University,
Wuhan, China, 2012

M.S. Chemistry, University of South Carolina,
Columbia, SC, 2015

A Dissertation presented to the Graduate Faculty of the University of Virginia in
Candidacy for the Degree of Doctor of Philosophy

Department of Chemistry

University of Virginia

December 2020

ABSTRACT

Luo, Zhongwen. The mechanistic study of C–H and H–H bond activation and C–C coupling reactions at the interface of homogeneous catalysis and heterogeneous catalysis. (Under the direction of Professors T. Brent Gunnoe and Robert J. Davis).

Commodity chemicals are produced annually on a large-scale via various catalyst-based technologies. Most of the industrially relevant catalytic processes operate based on molecular transition metal complexes, solid acid catalysts, or supported transition metal solid catalysts. The shale gas revolution has provided an abundance of methane and ethane, and has shifted the chemical industry's focus from the long-standing crude oil-based raw materials supply to a cost-effective natural gas components-based source. As a result, new catalytic processes to increase the efficiency of using natural gas-derived chemicals have become a high priority.

In the last few decades, extensive research has been focused on the catalytic oxidative coupling of methane (OCM) to generate C_2 products (*i.e.,* ethylene and ethane). Efforts have focused on mixed oxide catalysts such as Li/MgO and $Mn/Na_2WO_4/SiO_2$ to optimize the yield of C_2 products. One of the biggest challenges for OCM development is the radical-based C–H activation and methyl coupling, which hinders the selectivity and yield of the high-value C_2 products as often the products are more reactive than methane. Organometallic gold complexes are used in a range of catalytic reactions, and they often serve as catalyst precursors that mediate C–C bond formation. In Chapter 2, we investigate C–C coupling to form ethane from various phosphine ligated gem-digold(I) methyl complexes including $[Au_2(\mu\text{-}CH_3)(PMe_2Ar')_2][NTf_2]$ and $[Au_2(\mu\text{-}CH_3)(XPhos)_2][NTf_2]$ {Ar' = C_6H_3-2,6-(C_6H_3-2,6-Me)$_2$, C_6H_3-2,6-(C_6H_3-2,4,6-Me)$_2$, C_6H_3-2,6-(C_6H_3-2,6-iPr)$_2$, or

C_6H_3-2,6-(C_6H_3-2,4,6-iPr$)_2$; XPhos = 2-dicyclohexylphosphino-2′,4′,6′-triisopropylbiphenyl; NTf_2 = bis(trifluoromethyl sulfonyl)imide)}. The gem-digold methyl complexes are synthesized through reactions between Au(CH_3)L and Au(L)(NTf_2) (L = phosphines listed above). For [Au_2(μ-CH_3)(XPhos$)_2$][NTf_2] and [Au_2(μ-CH_3)(^{t}BuXPhos$)_2$][NTf_2], solid-state X-ray structures have been elucidated by single crystal X-ray diffraction. The rate of ethane formation from [Au_2(μ-CH_3)(PMe_2Ar’$)_2$][NTf_2] increases as the steric bulk of the phosphine substituent Ar’ decreases. Monitoring the rate of ethane elimination reactions by ^{1}H NMR spectroscopy provides evidence for a second-order dependence on the gem-digold methyl complexes. Using experimental and computational studies, it is proposed that the mechanism of C–C coupling likely involves: 1) cleavage of [Au_2(μ-CH_3)(PMe_2Ar’$)_2$][NTf_2] to form Au(PR_2Ar’)(NTf_2) and Au(CH_3)(PMe_2Ar’), 2) phosphine exchange from a second equivalent of [Au_2(μ-CH_3)(PMe_2Ar’$)_2$][NTf_2] aided by [Au_2(PMe_2Ar’)][NTf_2], formed in step 1, to produce [Au_2(μ-CH_3)(PMe_2Ar’)][NTf_2], and 3) recombination of [Au_2(μ-CH_3)(PMe_2Ar’)][NTf_2] and Au(CH_3)(PMe_2Ar’) to eliminate ethane.

Alkyl and alkenyl arenes such as ethylbenzene and styrene were produced on a scale of ~40 million tons and ~38 million tons annually in 2018. The synthesis of ethylbenzene and styrene relies on acid-based Friedel-Crafts alkylation or zeolite-based catalysis, which are multi-step and energy-intensive processes. Transition metal based arene alkylation or alkenylation could provide an alternative strategy towards high-value chemicals synthesis. Recently, molecular Rh(I) catalysts have been reported for the synthesis of alkenyl arenes from benzene and olefins using Cu(II) salts as the *in situ* oxidant (*e.g.*, *Acc. Chem. Res.* **2020**, *53*, 920-936). In Chapter 3, we focus on the synthesis of supported Rh materials and the study of their efficacy as pre-catalysts for the oxidative alkenylation of arenes. Rhodium nanoparticles supported on silica (Rh/SiO_2; ~3.6 wt% Rh) and nitrogen-doped carbon (Rh/NC; ~1 wt% Rh) are synthesized via liquid ion exchange and high-temperature pyrolysis, respectively. Heating mixtures of Rh/SiO_2 or Rh/NC with benzene and ethylene or α-olefins and CuX_2 {X = OPiv (trimethylacetate) or OHex (2-ethylhexanoate)} to 150 °C results in the production of alkenyl arenes. When using Rh/SiO_2 or Rh/NC as catalyst precursor, the conversion of benzene and propylene or toluene and 1-pentene yields a ratio of anti-Markovnikov to Markovnikov products that is nearly identical to the same ratios using the molecular precursor $[Rh(\mu\text{-}OAc)(\eta^2\text{-}C_2H_4)_2]_2$ as catalyst. These results and other observations are consistent with the formation of active catalysts by leaching of soluble Rh from the supported Rh materials.

In Chapter 4, we disclose efforts toward the development of nanoparticle-mediated tandem catalysis, in which a proof-of-concept study of nanoparticles catalyzed hydrogenolysis of (^{t}bpy)Pt(OPh)Cl complex is conducted. Three silica-supported nanoparticles (5.0 wt% Pd/SiO_2, 1.0 wt% Pt/SiO_2, and 3.6 wt% Rh/SiO_2) are synthesized and the study of their efficacy for hydrogenolysis of (^{t}bpy)Pt(OPh)Cl complex was performed. Using (^{t}bpy)Pt(OPh)Cl complex as a probe molecule, nanocatalysts effectively promote hydrogenolysis of Pt–OPh bonds to release HOPh at 50 °C. Monitoring the hydrogenolysis kinetics by ^{1}H NMR spectroscopy, a first-order dependence on Pd/SiO_2, and (^{t}bpy)Pt(OPh)Cl complex was observed. The rate for the noble metals mediated hydrogenolysis of (^{t}bpy)Pt(OPh)Cl complex and C=C bonds hydrogenation followed the same reactivity trend: Pd > Rh > Pt.

DEDICATION

For Bingchuan Luo, Yuanfa Luo, Juying Wang, Zhonglin Luo

My dad, grandparents and cousin.

ACKNOWLEDGEMENTS

Once upon a time, I believed chemistry was pronounced “Chem-is-a-try”, so I could probably try it too. Instead of pursuing an early career in business or geology, I ended up fulfilling my inner desire to be a scientist by becoming a chemical catalysis scientist. “Trying it” unexpectedly turned out to be a 12 year-long journey. My pursuit of chemistry knowledge, four years at Huazhong Agricultural University, three years at the University of South Carolina and now five years at the University of Virginia has been a wild ride. Although I have been mentally and physically prepared for a long race, a pure curiosity-driven scientific pursuit in chemistry feels like running a marathon. To be honest, finish a Ph.D. in Chemistry is challenging and sometimes it is filled with happiness, frustration, success, and failure. Now that 30 years of academic pursuit finally comes to an end at the University of Virginia, I am grateful for so many people who have helped me along the journey. I will feel guilty if they are not to be recognized.

I would like to give special thanks to my advisor, T. Brent Gunnoe, and co-advisor Robert J. Davis for the past five years. Thank you for taking a chance on me. I appreciate that you let me join your chemistry tree during my scientific knowledge pursuit. As leaders of the chemical catalysis community, your passion, enthusiasm, and dedication towards scientific innovation is inspiring. Your mentorship, guidance, and friendship are key to this dissertation. I was lucky to receive the cross-departmental training in Chemistry and Chemical Engineering at UVA. Receiving the training in both homogenous catalysis in the Gunnoe group and heterogeneous catalysis in the Davis group opened my eyes to chemical catalysis. I count it a blessing to have you as my advisors and I appreciate your kind support, patience, and mentorship. Thank you, Brent, for sharing with us the wisdom to make a real catalyst unhappy, and thank you, Professor Davis, for teaching me thoroughly evidence-based analytics and characterizations in catalysis. My thanks extend to Trecia and Leah; your hospitality ranging from hosting various bowling games, Christmas parties, and summer parties was greatly appreciated. Trecia, thank you for letting me join the Visa program. Through the language program I made great friends, connections, and constantly appreciated the program to help international students like myself with communication skills and cultural exchange. It was always fun to chat with you and Leah about ballroom dancing, too. Also, thanks to the mentorship from Dr. Hong Yuan and Dr. Richard D. Adams, I am grateful to have received scientific training from you prior to UVA. Without your guidance and support, I will not be here today talking about chemical catalysis.

To the Gunnoe Group members, past and present, it was my pleasure spending a good amount of quality time working, learning, and laughing with you: Dr. Jiajun Mei, John Dekarske, Bridgette Dale, Dr. Kathleen Taylor, Dr. Michael Webser-Gardiner, Dr. Benjamin Vaughan, Dr. Junqi Chen, Dr. Nichole Schwartz Liebov, Dr. Ana Geer, Dr. Ryan L. Holland, Dr. Brad McKeown, Dr. Shunyan Gu, Xiafan Jia, Weihao Zhu, Ke Zhang, Fanji Kong, Kaeleigh Olsen, Holly Tubbs, Zoë M. Gehman, Marc Bennett, Hannah Ketcham, Christopher Webber, and Lucas Frye.

To the Davis Group members, past and present, Dr. Kehua Yin, Dr. Jiahan Xie, Dr. Ben Huang, Dr. Derek Falcone, Dr. Zack Young, Dr. Nicholas Kaylor, Dr. James Kammert, Dr. Gordon Brezicki, Naomi Miyake, Yu Yang, Colby Whitcomb, and Konstantin Mamedov, it was great to overlap with you in the past five years, and your knowledge and advice have shaped me to become a better scientist. Also, thanks go to the Chris Paolucci and Bill Epling groups. I enjoyed a wonderful group discussion with you and the rest of catalysis community at UVA. Your constructive feedback and thoughts are appreciated.

I am thankful for the collaboration and learning opportunity through UVA-MAXNET Energy Initiative. Through state-of-the-art collaboration between UVA and Max Planck Society in Germany, I had the excellent educational experience to interact, learn, and discuss with the world’s leading catalytic experts in Germany, the United Kingdom, and the United States.

To our collaborators and technicians who have helped me in the completion of the projects and this dissertation, I appreciate your patience and technical support. For the gold project, thank you for being so wonderful to work with and learn from Juan Miranda-Pizarro, Dr. Juan J. Moreno Díaz, Dr. Jiahan Xie, Dr. Diane A. Dickie, and Dr. Jesús Campos. For the Rh project, thank you for your help and contribution: Colby Whitcomb, Dr. Nicholas Kaylor, Yulu Zhang, Dr. Sen Zhang, and Dr. Robert J. Davis. Our collaboration and discussion have helped me develop skills as a better chemist and a professional. Thank you to the NMR expert, Jeff Elena, XPS experts Catherine Dukes and Dmitry Pestov (VCU Nanomaterials Characterization center), TEM expert Helge Heinrich, XRD expert Diane A. Dickie, and Microwave/ICP-OES experts Chuck Kevin and Earl Ashcraft.

Thank you to my committees, Dr. Dean Harman, Dr. Ian Harrison, and Dr. Sen Zhang for your guidance and encouragement during the past five years. Thank you for taking the time to read this thesis and provide me with constructive feedback.

I would like to thank my family and friends for their encouragement and love. To my Chinese family, parents, Xiuzhen Wang and Bingchuan Luo, grandparents, Manfen Weng and Zhishan Wang, uncle, Guohong Wang, and aunt, Yanli Yao, and my American host family, Scott Derricks and Nichole Derricks. Thank you for all the unconditional love and enormous support. I am grateful that you let me worry about nothing, and make my own decisions in pursuing whatever that I decide to do. For the professional development outside of chemistry, I am thankful for tremendous mentorship and support from within UVA and beyond. Thanks go to the Ph.D. Plus program, Dr. Sonali Majumdar, Dr. Phil Trella, Dr. Yi Hao, Amy Garrou, Cav Angels team, Jim Cheng, Rich Diemer, Vincent Mascia, Jerry Peng, Batten Institute for Entrepreneurship and Innovation, David Touve, MJ Dougherty Toms, Jason Brewster, Rebecca Haydock, Zhongquan Wang, Nick Ford, Mike Fang, Richard Fu, Yuan Peng, Phil Bourne, Brendan Boler, John Stacey, UVA Licensing and Venture Group, Bob Creeden, Carleen Bowers, and Michael Straightiff.

Thank you to my peers and friends both near and far, Yuming Wu, Cheng Luo, Yu Fang, Jingyi Zhang, De Wang, Bowen Sun, Caitlin Dreisbach, Chad Vess, and Fang Yang. Salsa Club, Ballroom Club, Graduate Consulting Club, Data Science and Analytic Club, and Global Entrepreneurship and Venture Capital Club. Outside of UVA, I am thankful for the bonding and support from my soccer team, yoga teacher, Zoe, running friends, Steve, Monica, Vivian, and coach Mark, cooking teachers, Margaret and Zack, co-worker/dog person Kaeleigh, and church friend Avery. Latest friendship with the cute/knee/Michigan Emma C. Craig and the rest of the Miss house is greatly appreciated. Without your all encouragement and support, I would NOT have made it.

Last, I would like to give thanks to God for the wisdom, knowledge, and blessing. The spiritual growth in the past few years enlightens me to become a better person. I am thankful for that. But, encountering nineteen snakes, one fox, two land turtles, and one blue heron in the past month or two was wild. Now I slowly recognize that Charlottesville is not only for lovers/winery/hiking/hot balloon/retirement/golf, but also for WILDLIFE. Thank you for the uniquely fearful experience. I am thankful for your protection and appreciate your continuous love.

LIST of SCHEMES

LIST of FIGURES

LIST of TABLES

1. Introduction

1.1 Overview of natural gas and its derivatives

According to energy production and consumption analysis from the U.S. Energy Information Administration, petroleum and natural gas were estimated to account for 68.7% of U.S. energy consumption in 2019 (Figure 1.1). Since the mid-2000s, the paradigm of the energy and chemical industries have shifted from coal-based and heavy-crude oil-based raw material supplies to shale gas derived chemical resources.[1] This change is partly accelerated by technological advancement in the combination of horizontal drilling and hydraulic fracturing technologies,[2] which has unlocked access to a large amount of petroleum and natural gas trapped in fine-grained sedimentary rocks.[3] Shale (natural) gas is a mixture of light alkanes (*i.e.* methane, ethane, propane, and butane; (Scheme 1.1) with the primary component being methane, accounting for about 80%.[4] Due to low concentrations of sulfur and heavy metals such as As, Pb, and Hg, methane is a more environmentally friendly fuel compared to coal. Moreover, it is cost-effective to switch from coal-fired power plants to natural gas power generation systems. The supply and demand analysis shows an asymmetrical supply of natural gas, which in return demands more infrastructure implementation such as building small-scale and agile chemical processes to utilize natural gas on site.[5] However, building the infrastructure needed for natural gas is challenging. For example, one of the biggest challenges is a lack of pipeline structure, which is not in remote oil-drilling sites such as the Bakken areas in North Dakota. Compared with carbon dioxide, emitted methane is approximately 30 times more potent as a heat-trapping gas.[6] Therefore, excess natural gas is flared on-site. Similarly, controversial pipeline projects in the Southern and Appalachia regions of the United States (*i.e.* Atlantic Coast Pipeline) face a series of setbacks and delays due to safety, environmental and legal concerns.[7] In July 2020, Dominion Energy and Duke Energy announced the cancellation of the Atlantic Coast Pipeline project given the increasing legal uncertainty that overhangs large-scale energy and industrial infrastructure development in the United States.[7]

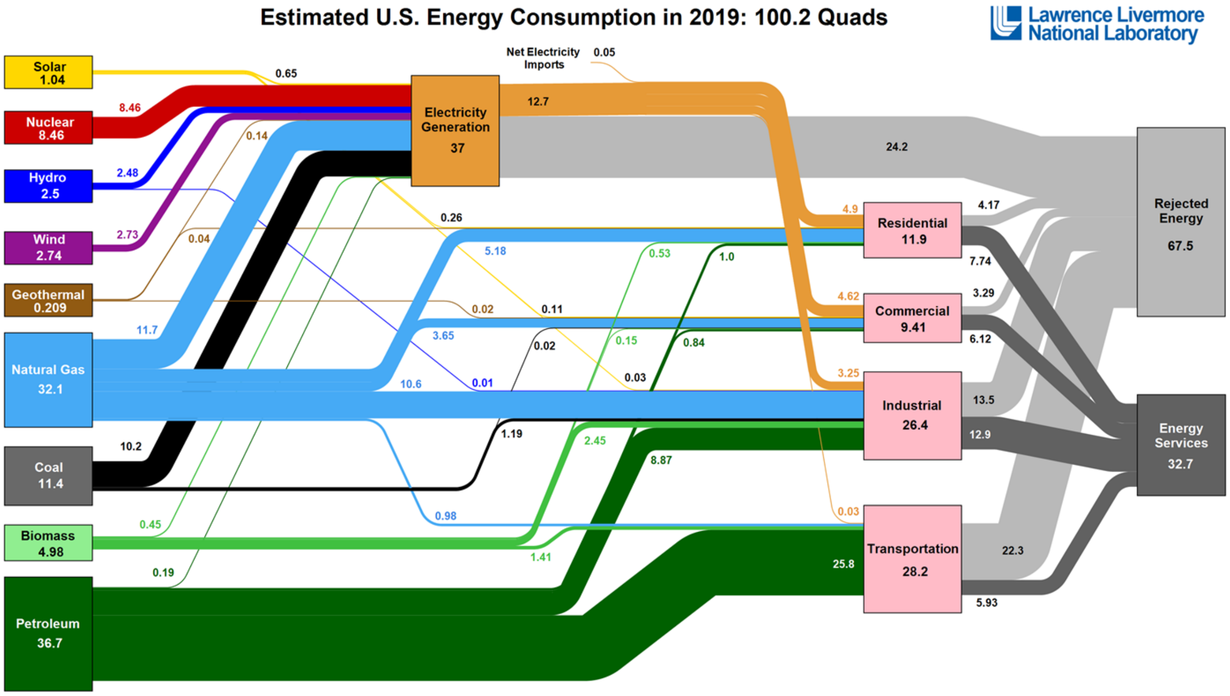
Estimated U.S. Energy Consumption in 2019: 100.2 Quads

Source: LLNL March, 2020. Data is based on DOE/EIA MER (2019). If this information or a reproduction of it is used, credit must be given to the Lawrence Livermore National Laboratory and the Department of Energy, under whose auspices the work was performed. Distributed electricity represents only retail electricity sales and does not include self-generation. EIA reports consumption of renewable resources (i.e., hydro, wind, geothermal and solar) for electricity in BTU-equivalent values by assuming a typical fossil fuel plant heat rate. The efficiency of electricity production is calculated as the total retail electricity delivered divided by the primary energy input into electricity generation. End use efficiency is estimated as 65% for the residential sector, 65% for the commercial sector, 21% for the transportation sector and 49% for the industrial sector, which was updated in 2017 to reflect DOE's analysis of manufacturing. Totals may not equal sum of components due to independent rounding. LLNL-MI-410527

Figure 1.1. Estimated U.S. Energy consumption in 2019, data is based on the Department of Energy/Energy Information Administration, Monthly Energy Review. (LLNL March 2020).

Applying catalytic technologies to oil and gas middle stream refinery plants has enabled the chemical industry to produce light alkanes, fuels, BTX (benzene, toluene, and xylene), and high-value chemical derivatives including light olefins (*e.g.*, ethylene, propene), alkyl arenes, and oxygenated products such as alcohols, ketones, acids, and esters (Scheme 1.2) on a large scale.[8] Catalysis plays a significant role in energy savings, pollution reduction, and emission control.[9]

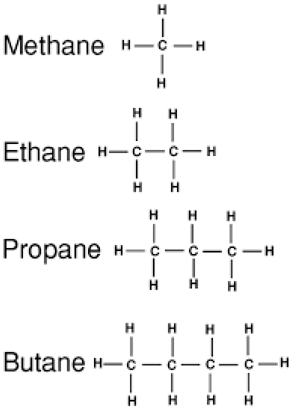

Scheme 1.1. Four major light alkane components of natural gas.

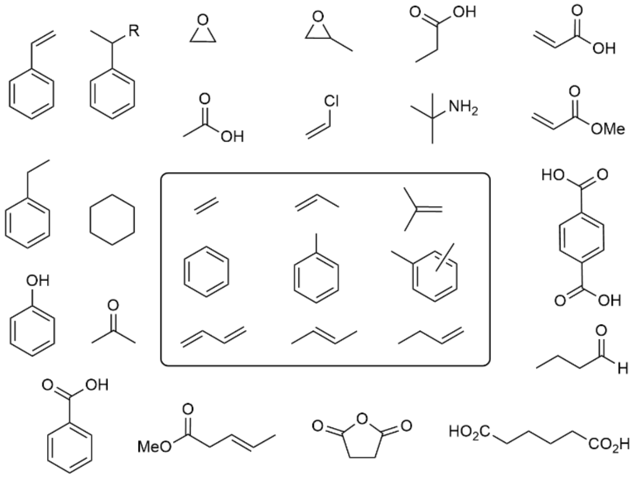

Scheme 1.2. Utilization of light olefins and BTX (benzene, toluene, and xylene) to produce corresponding oxygenated and high-value chemicals.

1.1.1 Overview of strategies for the conversion of methane to high-value chemicals

Natural gas, which is 70-90% methane by volume, serves as an abundant chemical building block for various high-value chemicals and fuels. For example, methane is the primary source of dihydrogen from steam reforming technology where methane and water are converted to syngas (a mixture of CO and H_2) (eq 1). The methane reforming reaction accounts for approximately 50% of the world's dihydrogen supply. The dihydrogen is then mainly used to synthesize ammonia, via the Haber-Bosch process, for fertilizer manufacturing.[10] Syngas can also be converted to synthetic gasoline and higher value hydrocarbons using Fe, Co or Ru catalysts in the Fischer-Tropsch synthesis,[11] as well as to methanol over $Cu/ZnO/Al_2O_3$ catalysts.[12] An alternative strategy to synthesize the syngas mixture is dry reforming using CO_2 and CH_4.[13]

$$H_2O + CH_4 \longrightarrow CO + 3H_2 \qquad (1)$$

The formation of syngas via methane steam reforming is endothermic, which results in an energy-intensive process.[1] Hene, the methane steam reforming process requires high temperature (~900 °C). Additionally, with steam reforming and syngas technologies, methane is indirectly converted to methanol, which is commercially synthesized and catalyzed by $Cu/ZnO/Al_2O_3$ based syngas process (Scheme 1.3).[12] In methanol synthesis, both CO and CO_2 can serve as a carbon source. The water-gas shift reaction(WGS) and the reverse water gas shift reaction (RWGS) play an important role in balancing the CO/H_2 ratio. From a commercial viability perspective, both the steam reforming process and the methanol synthesis plant must be large enough to achieve profitability. This limits the ability of current methods for methanol synthesis to be used for the conversion of methane to methanol.

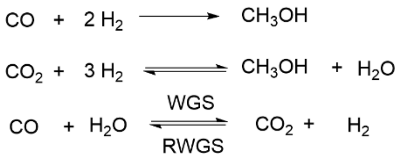

Scheme 1.3. Methanol synthesis via syngas steps.

Compared with energy-intensive steam reforming of methane, catalytic partial oxidation of methane (CPOM) to synthesize syngas in high yield and selectivity is less energy-intensive and exothermic (eq 2). The CPOM is an energy-efficient alternative for the production of syngas as it has fast kinetics, and thus avoiding the use of large-scale reactors and steam heating units.[14] However, controlling the reaction selectivity away from total combustion is the biggest challenge.[14] During the partial oxidation of methane reaction, typically it is energetically favorable to go all the way to the energy sink of CO_2.

$$CH_4 + 1/2O_2 \longrightarrow CO + 2H_2 \qquad (2)$$

Various approaches have been pursued to transform methane into higher-value chemicals or fuels. New methane functionalization routes include[13] 1) partial oxidation of methane to methanol, formaldehyde or acetic acid, 2) oxidative coupling to form ethane/ethylene, 3) non-oxidative conversion to aromatics, carbon, and dihydrogen (dehydraromatization), and 4) oxyhalogenation.[15] Despite intensive research efforts for the direct low-temperature (< 300 °C) partial oxidation of methane to methanol, a commercially viable process has not yet been developed. A primary challenge is the relatively weak C–H bonds of methanol (397 $kJmol^{-1}$) compared with methane (440 kJ mol^{-1}), which results in overoxidation for many catalytic processes.[16] Various strategies have been attempted to overcome the overoxidation challenge, including 1) use of an electrophilic catalyst to produce MeX product where X is an electron-withdrawing group (i.e. Periana-Catalytica system discussed in later Scheme 1.9); 2) use of periodate and chloride mediated methane functionalization to form MeTFA in trifluoroacetic acid media (*i.e.* oxy esterification developed by Gunnoe and coworkers). Below, some approaches to catalytic methane partial oxidation are summarized.

Cu-exchanged zeolites including Cu-ZSM-5 and Cu-MOR have been studied for direct methane to methanol synthesis at low conversions but relatively high selectivity (80%).[17] The active sites for Cu-zeolite-mediated methane to methanol synthesis at low temperature have been highly debated in the literature.[17-20] For example, in 2005, Schoonheydt and coworkers reported that Cu-ZSM-5 and Cu-MOR zeolite mediates methane oxidation to methanol conversion at 125 °C.[21] In this report, the bis(μ-oxo)dicopper core ($[Cu_2(\mu\text{-}O)_2]^{2+}$), observed at 22,700 cm^{-1} by UV-Vis spectroscopy, was proposed as the active site responsible for the methane partial oxidation. They rationalize that the formation of bis(μ-oxo) dicopper species is due to the activation of Cu-ZSM-5 zeolite by dioxygen at 300 °C. The core bis(μ-oxo) dicopper activates methane at 125 °C, in which the absorbed methoxy or methanol can be extracted in a water/acetonitrile mixture. Following that initial discovery of a bis(μ-oxo)dicopper core ($[Cu_2(\mu\text{-}O)_2]^{2+}$) active site, Solomon, Schoonheydt, and coworkers used $^{18}O_2$ labeling experiments, resonance-enhanced Raman vibrations, and DFT calculations to probe the active sites of dioxygen activated Cu-ZSM-5.[22] It was proposed that the dioxygen activated Cu core in the Cu-ZSM-5 zeolite is a bent mono-(μ-oxo) dicopper species, $[Cu_2O]^{2+}$. In this work, the $[Cu_2O]^{2+}$ core was proposed to be uniquely active for H atom abstraction from CH_4 with relatively low transition state energy, in which the polarized low-lying singly-occupied molecular orbital explains the low-temperature methane C–H activation. A study of copper-exchanged zeolite for methane hydroxylation to methanol was recently reported by Lercher and coworkers in 2015.[23] These new findings used the protonated form of mordenite instead of the typical sodium exchanged mordenite for the preparation of copper exchanged zeolites. Compared with other preparation methods, using H-MOR zeolite improved the methanol yield by an order of magnitude (160 versus 13 $\mu mol\ g^{-1}$) and achieved around 80% conversion of methane to methanol or dimethyl ether.[23, 24] Compared with previous studies, a tri-copper core, $[Cu_3(\mu\text{-}O)_3]^{2+}$, was proposed as the active site for the methane C–H bond activation. The calculated activation barrier for the $[Cu_3(\mu\text{-}O)_3]^{2+}$ cluster in H-MOR is 74 kJ mol^{-1}, which is similar to that of 78 kJ mol^{-1} for the dicopper site, ($[Cu_2O]^{2+}$), in ZSM-5. In a recent report, Davis, Gunnoe and coworkers investigated Cu-H-MOR.[25] They investigated how reaction time (4 to 20 h) and methane pressure (1 to 35 bar) affected the speciation of Cu sites for the cyclic oxidation of methane to methanol. The latest findings show that at lower pressures and shorter reaction times, methane activation and conversion are incomplete. The active sites for the Cu-H-MOR for the low-temperature methane hydroxylation to methanol are therefore likely dicopper active sites.[26] Currently, the catalytic conversion of methane to methanol was shown to be possible using direct dioxygen oxidation, but it is limited to ppm levels of dioxygen feed [27] or an alternative oxidant such as N_2O.[28-30] In the catalytic route, the steady-state production of methanol is observed in an extremely low quantity (ppm level).

Other strategies that are used to develop methane to methanol partial oxidation to methanol include 1) use of a sacrificial reductant coupled with dioxygen activation for an enzyme-catalyzed low-temperature methane to methanol synthesis (*i.e.* the particulate methane monooxygenase (pMMO) enzyme in methanotrophic bacteria with the enzyme-containing a multi-nuclear copper active site and oxidizing methane to methanol under ambient conditions using nicotinamide adenine dinucleotide (NAD) plus hydrogen (H) (NADH) as the sacrificial reductant)[31, 32] 2) *in situ* generations of sacrificial reductant hydrogen peroxide via Au-Pd nanoparticles.[33]

1.1.2 Oxyhalogenation of methane

Oxyhalogenation of methane or ethane, also called catalytic methane oxychlorination (MOC) or methane oxybromination (MOB), provides high-value halogenated chemicals such as haloalkanes (CH_3Cl and C_2H_5Br),[34, 35] laboratory and industry-based solvents (CH_2Cl_2, $CHCl_3$, $ClCH_2CH_2Cl$, and CCl_3CH_3), and additives for fire extinguisher systems

($CBrF_3$ or Halon-1301). In a typical oxyhalogenation of methane reaction, a mixture of oxygen, HX (X= Cl or Br), methane or light alkane is passed through a catalytic bed loaded with transition metal catalyst to generate valued-added alkyl halide under relatively mild conditions (T = 450 - 600 °C, p ≈ 1 bar). For example, a single-step methane oxychlorination generates various chloride/brominated products, oxygenates (*i.e.* CO or CO_2), and H_2O (Scheme 1.4). [35, 36]

$$CH_4 + HX + 1/2\ O_2 \xrightarrow[\text{solid catalyst}]{450 - 600\ ^\circ C} CH_3Cl + CH_2Cl_2 + CHCl_3 + CCl_4 + CO + CO_2 + H_2O$$

X = Cl or Br

Scheme 1.4. Catalytic oxyhalogenation of methane.

The methane oxychlorination reaction suffers from selectivity challenges because it likely involves a radical pathway via *in situ* generations of Cl_2 (eq 3). The incorporation of each successive chlorine equivalent makes the product more reactive, that is, the rate of chlorination increases in the order shown in Scheme 1.5.

$$2\ HCl + 1/2\ O_2 \longrightarrow Cl_2 + H_2O \qquad (3)$$

The rationale is that the C–H bond strength is weaker for chloride products compared with methane. For example, the bond strength of methyl chloride is 351 kJ mol^{-1}, while the methane C–H bond strength is 440 kJ mol^{-1}.

$$CH_4 < CH_3Cl < CH_2Cl_2 < CHCl_3$$

Scheme 1.5. Reactivity order of C_xCl_y products.

Recently, Gunnoe and coworkers reported a strategy of light alkane functionalization using iodate salts with a sub-stoichiometric halogen source in trifluoroacetic acid (HTFA), and it is often called oxy esterification of methane.[37] In initial studies, direct partial oxidation reactions of methane, ethane, and propane were achieved. Under optimized conditions, more than 20% methane conversion with a > 85% selectivity of MeTFA (TFA = trifluoroacetate) was obtained. Moreover, this transition metal-free system has been extended and improved to periodate salts (Scheme 1.6).[38] Up to 42% methane conversion to MeTFA has been. In a detailed mechanistic study, it was found that methane functionalization by iodate/chloride in HTFA likely occurs through H-atom abstraction by free radical species, including the chlorine radicals, that react to give alkyl radicals.[39] Iodine, which forms by the reduction of iodate, traps alkyl radicals as alkyl iodides, and then the alkyl iodides are subsequently converted to MeTFA in HTFA. The protection effect induced by trifluoroacetate further stabilizes the alkyl ester product in HTFA, which suppresses overoxidation of alky ester products. In a recent report, partial oxidation of light alkanes to corresponding alkyl esters under photochemical conditions has been demonstrated using mixtures of iodine oxides and chloride salts in trifluoracetic acid.[40] Under optimized conditions, yields of alkyl ester production of ~50% based on methane, ~60% based on ethane, and ~30% based on propane have been obtained. Similar to thermal functionalization of light alkanes via oxyesterification in trifluoroacetic acid, it was proposed that the photochemical process operates by a hydrogen atom abstraction by chlorine pathway, in which alkyl radicals are generated in situ, trapped by iodine forming alkyl iodate intermediates (R–I), and followed by the transformation in HTFA to form the alky trifluoroacetate products.

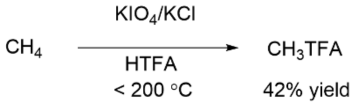

Scheme 1.6. Periodate and chloride mediated methane functionalization to form CH_3TFA in trifluoroacetic acid media.

1.2 Organometallic complex mediated C–H activation

Partial oxidation of methane by molecular inorganic complexes often involves a metal-mediated C**–**H bond breaking step with the formation of a metal-methyl bond. Four common mechanisms of transition-metal mediated C**–**H activation and functionalization have been proposed including,[41] a) electrophilic activation, b) oxidative addition, c) σ-bond metathesis, and d) ligand-assisted (*e.g.*, 1,2-CH-addition across M–X bonds (X = O, OR, NR, NHR) and carboxylate-assisted[42] C**–**H functionalization) (Scheme 1.7).

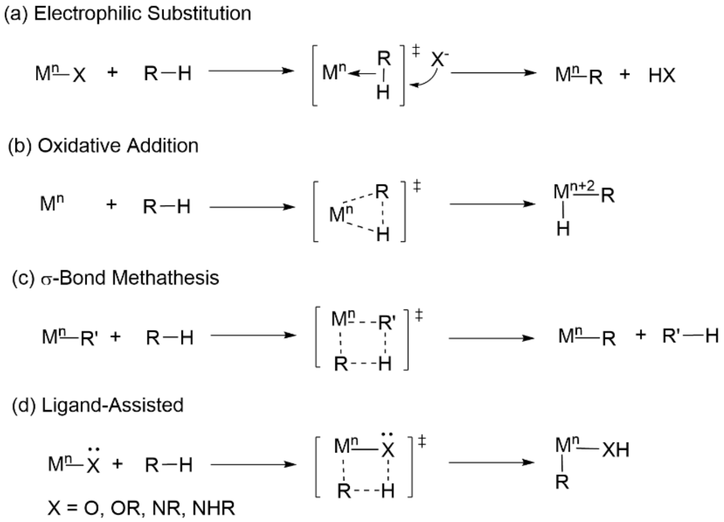

Scheme 1.7. Four general mechanisms for metal-mediated C**–**H activation.

Electrophilic substitution (Scheme 1.7a) takes place when a C–H bond coordinatives with the metal center rendering the C**–**H bond acidic. The acidic C**–**H bond can then be deprotonated by an external base X to form a new M–R bond and HX. This mechanism is typically observed in polar solvents like water or strong acidic media such as sulfuric acid. Examples of this approach for methane functionalization are Shilov[43] and the Catalytica Pt-based process.[44, 45]

Oxidative addition of a C–H bond (Scheme 1.7b) occurs when an unsaturated metal center coordinates a C**–**H bond followed by a two-electron donation from the metal center to a σ* anti-bonding orbital of the C–H bond. Insertion of the metal into the C–H bond results in formal two-electron oxidation of the metal center to form an M(H)(R) product. If C–H functionalization is desired, this intermediate must react to form a C–X bond (X = C, O or N, etc.). The reactive unsaturated metal species is often generated *in situ*. For example, irradiation of $(\eta^5\text{-}C_5Me_5)(PMe_3)Ir^{III}H_2$ releases dihydrogen, leaving the highly reactive and unsaturated complex $(\eta^5\text{-}C_5Me_5)\text{-}(PMe_3)Ir^{I}$.[46] When exposed to hydrocarbons, this intermediate undergoes oxidative addition forming $(\eta^5\text{-}C_5Me_5)(PMe_3)Ir^{III}(H)(R)$. Jones and coworkers discovered that the Tp'Rh(CΞN-neopentyl)(η^2-PhN=C=N-neopentyl) (Tp' = hydridotris(3,5-dimethylpyrazolyl)borate) fragment is active for various hydrocarbon C–H activations.[47] When the complex is thermally treated or photochemically irradiated, the oxidative addition of C–H bonds occurs at the Tp'Rh(CΞN-neopentyl) intermediate forming Tp'Rh(CΞN-neopentyl)(H)(R).

The C–H σ-bond metathesis is formally defined as the concerted exchange of M–H or M–R' σ-bond with a C–H σ-bond, resulting in forming a new M–C or M–H bond. Given that the metal center cannot donate electron density to the σ* anti-bonding orbital of the C–H bond, a 4-center, and 4-electron transition state is hypothesized, (Scheme 1.7c). The σ-bond metathesis reaction was first illustrated in the 1980s, by the exchange of lutetium(III) methyl complex with ahydrocarbons (R–H).[48] For example, heating $(Cp^*)_2Lu(CH_3)$ (Cp* = pentamethylcyclopentadiene) with $^{13}CH_4$ resulted in the formation of $(Cp^*)_2Lu(^{13}CH_3)$ and CH_4 (eq 3).

$$(Cp^*)_2Lu(CH_3) \quad + \quad {}^{13}CH_4 \quad \longrightarrow \quad (Cp^*)_2Lu({}^{13}CH_3) \quad + \quad CH_4 \qquad (3)$$

Ligand-assisted C–H activation includes a range of reactions in which the ligands on the metal center participate in the C–H activation step.[49] For example, 1,2-CH-addition (or internal electrophilic substitution, IES),[50] and concerted metalation-deprotonations[51] (or amphiphilic metal-ligand activation)[52, 53] are two common examples of ligand-assisted CH functionalization. A commonly observed is carboxylate-assisted C**–**H activation by group 8-10 transition metal complexes.[42, 54] In carboxylate-mediated C**–**H activation processes, a C**–**H bond coordinates with the metal-carboxylate center, in which the carboxylate group is protonated by the C**–**H bond forming a carboxylic acid ligand and a new M**–**C bond.

1.2.1 Methane functionalization based on Pt and Pd complexes

Despite the significant advancement for selective partial oxidation of methane to methanol or methyl halogen products discussed above, homogenous and organometallic complex-mediated methane C–H functionalization has drawn significant attention among the synthetic chemist community since the 1960s.[55] Molecular transition metal complexes such as $Pt^{II}Cl_2/[Pt^{IV}Cl_6]^{2-}$ were first discovered to enable methane C–H functionalization to form C–X bonds, (X = OH or Cl). An early example of transition metal-based methane functionalization is Shilov's $Pt^{II}Cl_2$ catalyst, in which electrophilic substitution of methane forming MeX was initially discovered.[56, 57] A general mechanistic pathway is shown in Scheme 1.8.[58] As shown, the $Pt(II)Cl_2$ salt activates methane through an electrophilic attack forming a $Pt^{II}(CH_3)X$ intermediate (X = Cl or OH). This step is proposed to be the rate-determining.[55] With the addition of stoichiometric $[Pt^{IV}Cl_6]^{2-}$ salt, the $Pt^{II}(CH_3)X$ intermediate is oxidized to a high energy $Pt^{IV}(CH_3)X_3$ intermediate. Reductive elimination from $Pt^{IV}(CH_3)X_3$ intermediate generates the $Pt^{II}Cl_2$ starting material, which also liberates the product CH_3X.

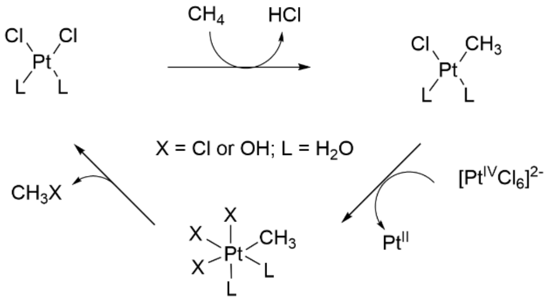

Scheme 1.8. Proposed catalytic cycle of the Shilov system for methane functionalization to make CH_3X, where X = Cl or OH, L = H_2O.

In the late 1980s, Sen and coworkers first developed the $Pd(OAc)_2$ catalyzed methane and other hydrocarbons partial oxidation in a peroxytrifluoroacetic acid solution at low-temperature (~100 °C or below).[59, 60] The Pd(II) mediated oxidation of arenes and alkanes including methane was proposed to operate by an electrophilic C–H bond activation mechanism.[59] Followed this work, Periana and coworkers discovered Hg(II) catalyzed low-temperature conversion of methane to methanol in liquid sulfuric acid.[61]

In 1998, Periana and coworkers developed the Catalytica process for selective methane functionalization, which uses molecular Pt complexes in oleum. It was found that the (bpym)$PtCl_2$ (bpym = 2, 2'-bipyrimidine) catalyzes methane oxidation to methyl bisulfate in fuming sulfuric acid with high selectivity (> 90%) and ~70% one pass yield based on methane (Scheme 1.9).[62] The methyl bisulfate can be hydrolyzed to produce methanol and sulfuric acid. Compared with the Shilov system, the Catalytica system uses sulfuric acid (SO_4^{2-} or SO_3) as the oxidant rather than Pt(IV) (Scheme 1.8), and reduced SO_2 can be oxidized directly with dioxygen to regenerate the SO_3 oxidant. Similar to Shilov's system, the mechanistic pathway of the Periana-Catalytica system is proposed to be:[44] 1) electrophilic C–H activation of methane forming a $Pt^{II}(CH_3)$ intermediate; 2) oxidation of $Pt^{II}(CH_3)$ by sulfuric acid to form a high oxidation state $Pt^{IV}(X)_2(CH_3)$ species; 3) $Pt^{IV}(X)_2(CH_3)$ reductive functionalization releasing CH_3X and $Pt^{II}(X)_2$ (Scheme 1.10). Possibly the most important feature of the Catalytica process is the protective effect induced by the withdrawing bisulfate group, which slows down a 2nd C–H activation step and thus, prevents methyl bisulfate from further oxidation. Under the catalytic conditions, the rate of methyl bisulfate oxidation is at least 100 times slower than methane.[62] The most significant limitation to the scale-up is the energy required to reconcentrate sulfuric acid after the conversion of methylbisulfate to methanol using water.[63] Following the initial success of the Pt system, the Catalytica catalytic cycle could be extended to other late transition metals including Au(I),[64] and Pd(II),[65] in which methane is oxidized to the corresponding methyl bisulfate or oxygenated products (methanol/acetic acid for Pd(II) case) in concentrated sulfuric acid.

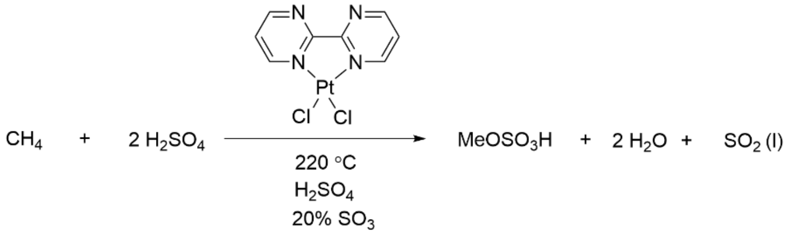

Scheme 1.9. Catalytica process for methane oxidation in oleum.

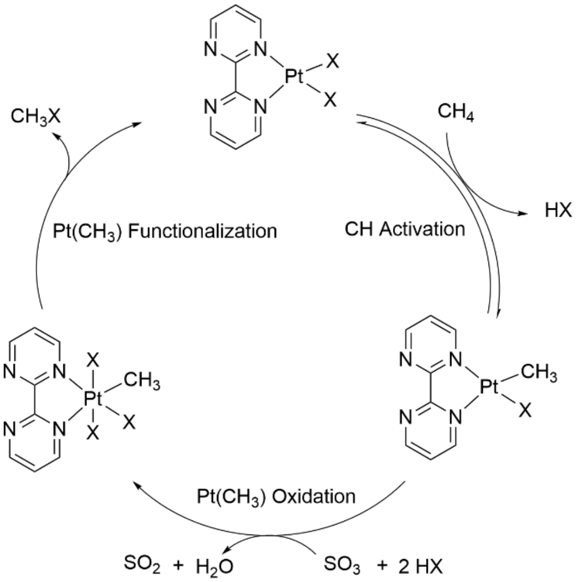

Scheme 1.10. Proposed catalytic cycle for the Catalytica process in concentrated sulfuric acid (X = Cl, HSO_4).

Due to the challenges and limitations of using concentrated sulfuric acid as reaction media as discussed above, the research community has studied the use of less acidic solvents. For example, HTFA is also a potential medium for methane to methanol partial oxidation (Scheme 1.11). The conjugate base, trifluoroacetate, can potentially protect from over oxidation in a manner similar to bisulfate (see above). Furthermore, there is a large difference in boiling point between MeTFA (43 °C) and solvent HTFA (72 °C), which makes the product MeTFA separation from the solution more attractive.[66] Also, HTFA is a monoprotic acid and the hydrogen bonding is dramatically reduced compared with a diprotic acid like sulfuric acid.

$$CH_4 + 1/2\ O_2 + CF_3C(O)OH \xrightarrow{\text{Cat.}} CF_3C(O)OCH_3 + H_2O$$

$$CF_3C(O)OCH_3 + H_2O \longrightarrow CF_3C(O)OH + CH_3OH$$

Scheme 1.11. General pathway for partial oxidation of methane to methanol in HTFA.

Recently, Strassner and coworkers found that Co(II/III) salt can catalyze the oxidation of methane to MeTFA in the presence of trifluoroacetic acid and dioxygen.[66] In their report, about 50% of product yield based on methane was obtained. However, deactivation of the cobalt catalyst by the formation of cobalt fluoride (*i.e.* CoF_2) precipitate occurred, which could be prevented by the addition of trifluoroacetic anhydride. Recently, the Strassner group reported N-heterocyclic carbene Pd(II) complex-mediated methane and propane functionalization in trifluoroacetic acid (Scheme 1.12). A key feature of the (NHC)Pd(II)Br_2 catalyst is the oxidation of Pd(II) by Br_2, which could be regenerated through HBr reoxidation by dioxygention.[67, 68]

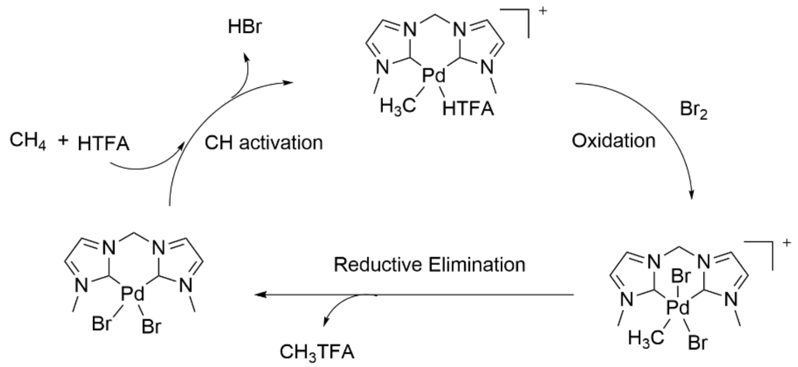

Scheme 1.12. $Pd^{II/IV}$ catalytic cycle for a (NHC)$PdBr_2$ (NHC = 1,10-dimethyl-3,3'-methylene-4-diimidazolin-2,2'-diylidene) mediated methane partial oxidation to MeTFA.

Periana and coworkers recently reported the use of main group compounds such as $Tl(TFA)_3$ and $Pb(TFA)_4$ in HTFA for light alkane (methane, ethane and propane) oxidation to corresponding alkyl ester products.[69] The main-group compounds $Tl(TFA)_3$ and $Pb(TFA)_4$ can stoichiometrically oxidize methane, ethane, and propane, separately or as a one-pot mixture at 180 °C with > 95% selectivity toward the corresponding alkyl esters. An electrophilic C–H bond activation is proposed for these d^{10} main-group cations.

1.2.2 Catalytic oxidative coupling of methane to ethane/ethylene

Oxidative coupling of methane (OCM) to synthesize ethane or ethylene has become an attractive process in the last several decades given the boom of shale gas and tight oil supply as discussed above.[70-73] The most desired products from the OCM reaction are ethane and ethylene. Most often, CO and CO_2 are the major byproducts (Scheme 1.13).[70, 72]

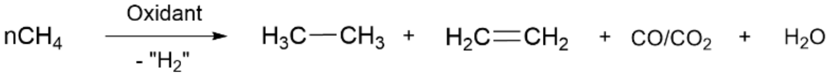

Scheme 1.13. Generic strategy for the oxidative coupling of methane to ethane/ethylene.

Catalytic OCM typically operates by a hydrogen atom extraction pathway in which a metal oxo surface breaks a methane C–H bond, forming M–OH intermediates and methyl radical species, respectively.[72] The remaining M–OH activates another equivalent of methane forming a second methyl radical species followed by the desorption of water molecules.[70] The methyl radical couples with another methyl radical in the gas phase forming ethane products, which completes the catalytic cycle. The ethylene product is formed through ethane oxidation over the catalyst bed, in which ethane C–H bond and β-hydride elimination occur. Metal oxides are typical catalysts, such as Li/MgO or $Mn/Na_2WO_4/SiO_2$, which give the highest C2 products (ethane and ethylene) yields between 20-30% at operating temperatures between 670 °C and 950 °C.[70] The techno-economic study for commercialization of OCM indicates that 30% of C2 product yield with a 90% selectivity is needed.[70] There is at least one example of the OCM process being taken to the pilot scale by Siluria technologies.[74] In the Siluria OCM process, OCM is targeted to react methane and oxygen over a catalyst exothermically to form ethylene, water, and heat. The catalyst is a mixed oxide base material compromising of lanthanide elements and various dopants.[75] However, continuously improving single-pass C2 product yield and selectivity remains a challenge. In addition to dioxygen as the oxidant, another oxidant such as S is also efficient for selective methane oxidation to ethylene using metal-sulfur catalysts.[76]

Organometallic complexes including Ni(II),[77]Au(III),[78] Pd(II),[79] Cu(I),[80]and Ru(III/II)[81] can react to release ethane in the liquid phase at a relatively low temperature (< 150°C). Although using organometallic complexes to study ethane formation is scientifically interesting, the reported yield of ethane formation is relatively low and the organometallic complexes are expensive. Therefore, organometallic complexes based ethane elimination does not apply to industrial applications.

1.3. Overview of light olefins and their utilization

Light olefins such as ethylene (ethene) and propylene (propene), are among the most important types of chemical building blocks in the chemical industry.[82] α-olefins such as ethylene and propene are produced primarily from the steam cracking of ethane and propane, respectively. Because of the boom of shale gas supply and technical advancement in steam cracking and fluid catalytic cracking processes, the chemical industry has shifted away from oil-based naphtha cracking to shale-based techniques.[83] In the United States, new ethane crackers have been constructed, and many naphtha crackers have either been dismantled or converted.[84] Light olefins are the feedstock for various chemical products including polymers (*e.g.*, polyethylene and polypropylene), oxygenates (*i.e.*, ethylene glycol, acetaldehyde, acetone, and propylene oxide), and important chemical intermediates (*e.g.*, ethylbenzene and propionaldehyde). Oligomerization of ethylene or propylene provides various high-value linear α-olefins

(LAO) or normal α -olefins (NAO). LAOs are a range of industrially important α-olefins, including, 1-butene, 1-hexene, 1-octene, 1-decene, 1-dodecene, and higher olefin blends or lubricants at the ranges of C_{20}-C_{24}, C_{24}-C_{30}, and C_{20}-C_{30}. Catalysts used for olefin oligomerization include Ta, Ti, Zr, Hf, Cr, and Ni.[85, 86] Some common ethylene oligomerization molecular catalysts are ligated Ni^{II} organometallic complexes. A notable development is the Shell Higher Olefin Polymerization Process,[87, 88] which uses a nickel-based catalyst for oligomerization of ethylene to produce α-olefins (Scheme 1.14).[89] However, the state-of-the-art catalysts are nickel (Ni^{I}/Ni^{II})-acid sites anchored on porous silicon aluminum mixed oxides or zeolite supports.[86]

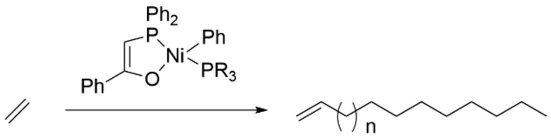

Scheme 1.14. The nickel-based catalyst for the Shell Higher Olefin Process.

Hydroformylation, also known as the “oxo-process,” is an industrially-relevant process to produce aldehydes from alkenes via the addition of CO and H_2.[90] A common example reaction is the hydroformylation of propylene to produce butanal (butyraldehyde) on the scale of a million tons per year (Scheme 1.15). More than 75% of the existing industrial hydroformylation units in the world are used for propylene hydroformylation to synthesize iso-butyraldehyde or *n*-butyraldehyde.[91] Besides the desired linear *n*-aldehydes, undesired branched isoaldehydes are often formed in a parallel reaction.[90, 92] The most common catalysts have a general formula of $(H)M(CO)_xL_y$ (M = Rh, Co, Ir, L = phosphine).[90] One of the best catalysts, $(H)Rh(CO)(PPh_3)_3$, showed a linear to branched (L:B) ratio of ~3:1 for propylene hydroformylation and approximately 20:1 for 1-pentene hydroformylation.[93]

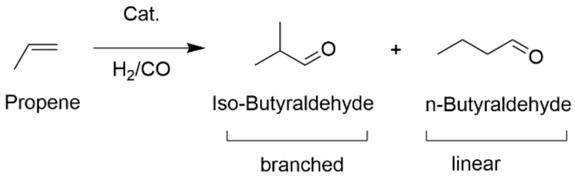

Scheme. 1.15. Hydroformylation of propylene.

Although the Rh-based catalytic process (*i.e.* $Rh(H)(PPh_3)_3(CO)$[94]) for light alkene hydroformylation was developed in the 1970s, cobalt-based catalysts such as $Co(H)(CO)_4$,[95] have become widely used in industrial processes to produce aldehydes (C10-C16) from heavy and long-chain alkenes (Scheme 1.16). Compared with Rh-based processes, Co-catalyzed processes are more cost-effective.

Scheme. 1.16. Hydroformylation catalysts: $Co(H)(CO)_4$ and $Rh(H)(PPh_3)_3(CO)$.

For a general cobalt-based hydroformylation catalytic cycle (Figure 1.2),[96] $(H)Co(CO)_4$ is generally in equilibrium with $Co_2(CO)_8$ when hydrogen is charged. Under catalytic conditions, the $16e^-$ active species $(H)Co(CO)_3$ is generated by the loss of a CO ligand from the $[(H)Co(CO)_4]$ intermediate. The catalytic cycle involves successive coordination of the alkene, hydride transfer to provide the linear alkyl species (or branched isomer in a parallel way), CO coordination and migratory insertion, oxidative addition of H_2 followed by the reductive elimination of the aldehyde which regenerates the active $16e^-$ species $(H)Co(CO)_3$ (Figure 1.2).

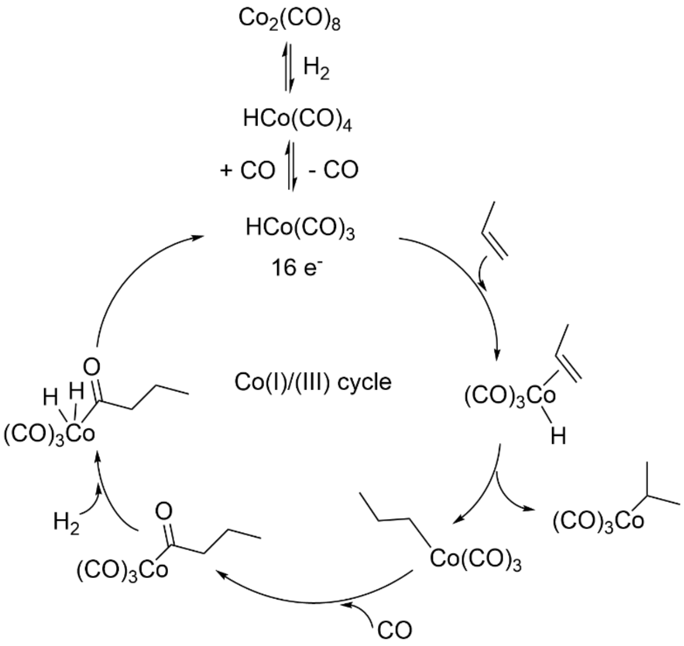

Figure 1.2. Mechanism of the cobalt catalyzed hydroformylation of alkenes.

Acetaldehyde, produced over 10^6 tons/year, is an important chemical intermediate for the production of various commodity chemicals such as acetic acid, acetic anhydride, ethyl acetate, crotonaldehyde, 1-butanal, and more.[97, 98] The Wacker-Hoechst process or the Wacker Process, developed by Wacker Chemie in 1956, was one of the major routes for acetaldehyde production in the chemical industry.[99, 100] The Wacker process refers to a catalytic process that uses palladium chloride and copper chloride catalysts for ethylene oxidation to acetaldehyde (Scheme 1.17). This chemical reaction is one of the earliest industrial-scale processes that used a homogenous organometallic Pd catalyst. In a typical reaction, the ethylene is oxidized with Pd(II) and Cu(II) catalysts in the presence of water and HCl. In the proposed catalytic cycle, Pd catalyzes ethylene C–H bond activation and oxidation, while copper plays a key role in air recycling and Pd(0) to Pd(II) oxidation.[101] It is rationalized that under industrial conditions, the syn-hydroxypalladation is the active site that is responsible for the ethylene oxidation. One notable feature of the

Wacker process is using air-recyclable $CuCl_2$ as a co-catalyst, which also serves as two-electron sources for palladium re-oxidation.[102] Depending on the location and cost of pure oxygen, either *in situ* regeneration of Cu(II) or two-stage recycling of Cu(I)/(II) are comparable. On the other hand, the Wacker process suffers the challenges of equipment corrosion and product selectivity due to excessive use of aqueous chloride solvent (*i.e.,* HCl) and the formation of chlorinated byproducts. To overcome these challenges, attempts to heterogenize chloride-free Wacker processes including zeolite supported Pd and Cu catalysts have been pursued.[103, 104] In a recent report by Nachtegaal and coworkers, redox chemistry among Pd-Cu/zeolite Y interface has been quantified by *in situ* X-ray absorption spectroscopic (XAS) investigation and chemometric analysis. In the heterogeneous Wacker oxidation over Pd-Cu/zeolite catalysts, two one-electron transfers from Cu(II) ions to Pd(0) oxidation in a supported system was first rationalized and suggested.[104] However, the Pd-Cu/Y zeolite mediated heterogenous Wacker oxidation suffers low conversions (< 10%), over oxidation of ethylene to CO and CO_2 (5-10%), carbon depositions, and irreversible Pd deactivation or sintering.[105]

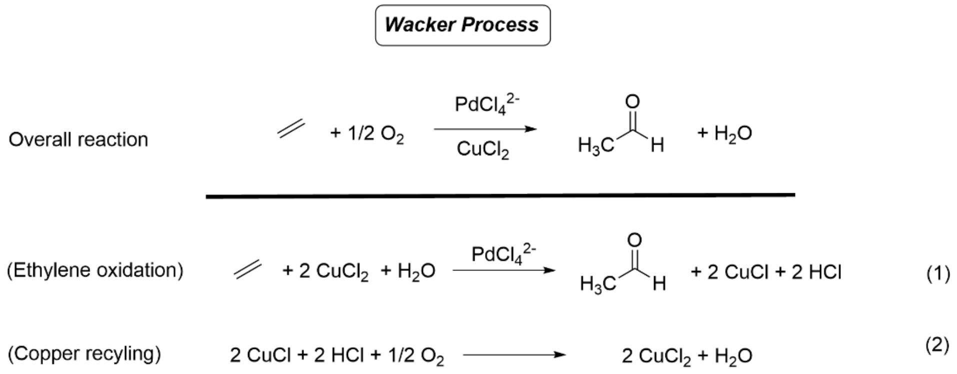

Scheme 1.17. Wacker process for ethylene oxidation to produce acetaldehyde where $PdCl_4^{2-}$ and $CuCl_2$ serve as the catalysts.

1.4 Overview of arene alkylation and alkenylations

Alkyl and alkenyl arenes are one of the most important commodity chemicals.[106, 107] They are widely used as precursors or intermediates for the production of high-value chemicals such as plastics, elastomers, detergents/surfactants, agrochemicals, pharmaceutical ingredients, synthetic lubricants, and fuels (Figure 1.3).[106, 108-113] Some common examples of alkyl and alkenyl arenes include ethylbenzene/styrene, stilbene, and its derivatives, C10-C14 alkylbenzene sulfonate surfactants, and oxindole,[114, 115] to name a few. Traditionally, the alkylation of benzene and other aromatics often called Friedel-Crafts alkylation,[116] is carried out by hydrogen fluoride (Brønsted acid), aluminum chloride (Lewis acid), or solid-acid zeolite catalysts. These alkylation processes operate via an acid-based mechanistic route, in which an electrophilic aromatic substitution occurs through a stable carbocation intermediate addition to arenes generating an arenium intermediate, followed by proton loss to produce the alkyl arene products (Scheme 1.18). One of the earliest applications of utilizing a Friedel-Crafts catalyst for alkylation reactions (*i.e.,* $AlCl_3$-HCl/HF) is related to ethylbenzene and linear alkylarene synthesis (Scheme 1.19).[116, 117] The advantages of using a Friedel-Crafts catalyst for alkylation reactions (*i.e.,* benzene and ethylene reactions) are 1) it is often a single-step unit for both alkylation and transalkylation; 2) it operates at a low benzene/ethylene ratio; 3) it requires a relatively mild operating condition (160 °C and 0.7 Mpa). However, it also suffers significant challenges including the use of corrosive reagents (*i.e.*, HF) and generating acidic waste, and halogenated impurities.[117]

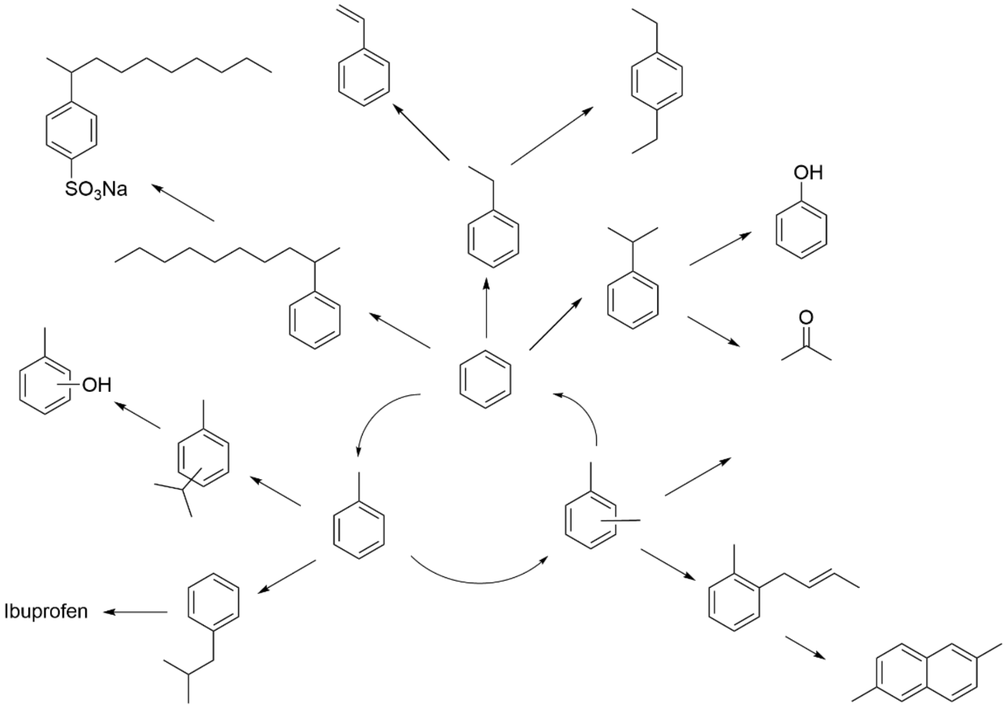

Figure. 1.3. The industrial alkylation of BTX (benzene, toluene, and xylene).[117]

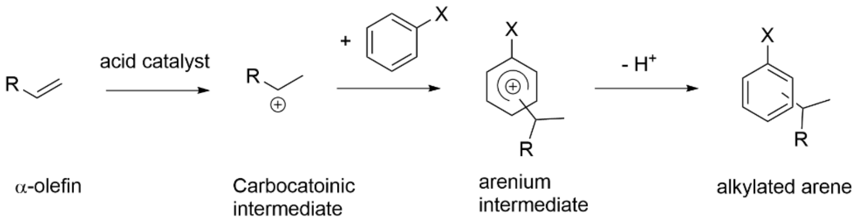

Scheme 1.18. General reaction pathways for acid-catalyzed arene alkylation using an olefin and arenes with an electron-donating group (X = H, alkyl, or electron-donating groups).

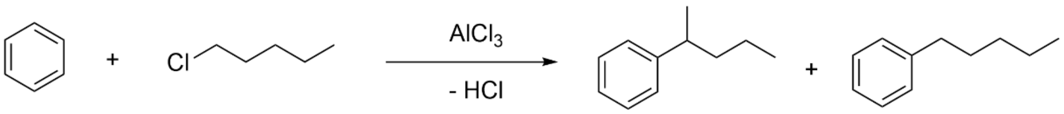

Scheme 1.19. $AlCl_3$-based alkylation reaction between n-pentyl chloride and benzene is discovered by Friedel and Crafts in 1887.[118]

As an alternative to the traditional Friedel-Crafts based alkylation process, zeolite-based catalysis, which utilizes solid-state acid sites on aluminosilicates, was commercialized in fluid catalytic alkylation reactions in 1976. Zeolite catalysts offer enhanced catalyst stability, recyclability, and products/catalyst separation.[107, 117, 119-121]

Despite the significant advancement of zeolite-based catalytic technology development, the solid acid zeolite catalysts still operate by the same fundamental mechanism as the Friedel-Crafts process. A notable example is the use of zeolite catalysts for the manufacturing of ethylbenzene (EB).[121] However, the zeolite-based technology for ethylbenzene synthesis suffers from selectivity challenges in a one-pass reaction because ethylbenzene is more reactive than benzene and thus, polyalkylation occurs at higher benzene conversions. To improve the yield of ethylbenzene and overcome polyalkylation, a separate transalkylation process is required, which also occurs over zeolite catalysts. Some common catalysts for transalkylation units are Beta zeolite, Zeolite Socony Mobil-5 (ZSM-5), Faujasite (*e.g.*, zeolite Y), and Mordenite.[121]

In addition to acid-mediated alkylation reactions, transition metal-based methods including Heck,[122] Stille,[123] Suzuki,[124] Negishi,[125] and other related C–C coupling reactions[126, 127] are widely used to synthesize alkyl or alkenyl arenes. However, the coupling substrates used for Pd-mediated reactions are often limited to activated arenes and aryl halides, which leads to the generation of halogenated byproducts. Also, a stoichiometric organometallic reagent is usually required.

Transition metal-catalyzed arene alkenylation (*i.e.*, oxidative olefin hydroarylation) often functions by a pathway involving arene C–H activation and olefin insertion. Transition metal-based arene alkylation or alkenylation offers a few advantages over traditional acid-based arene alkylation.[54, 106, 128-131] Potential advantages of using transition metal-mediated catalysis include: a) direct arene alkenylation via β-hydride elimination after the olefin insertion step, b) selective production of 1-aryl alkane/alkene by circumventing carbocationic intermediates, c) conversion of electron-deficient arenes,

d) new regioselectivity for alkenylation and alkylation of substituted arenes, and e) inhibition of polyalkylation. For example, organometallic catalysts involving Co, Ni, Ir, Ru, Pt, Pd, and Rh have been studied for catalytic C–H alkylation of arenes (*e.g.*, benzene, toluene or functionalized arenes) with α-olefins.[126, 132-144] Among these reports, a few examples developed by Gunnoe and coworkers, which mainly uses organometallic complexes including Ru, Pd, and Rh for styrene and linear alkenyl arene syntheses, are highlighted. Rh-catalyzed styrene and linear arene alkenylation syntheses will be discussed in detail as it is directly relevant to Chapter 3.

Under 2 atm O_2, 6.1 atm CO and 180 °C, the use of $RuCl_3$ as catalyst precursor has been reported by Milstein and coworkers for direct styrene synthesis from benzene and ethylene with 19 turnovers numbers (TONs) (Table 1.1).[145] Under 40 psig of ethylene and 150 °C, our group reported that the cationic Ru(II) complex $[(MeOTTM)Ru(P(OCH_2)_3CEt)(NCMe)Ph][BAr'_4]$ (MeOTMM=4,4',4''-(methoxymethanetriyl)-tris(1-benzyl-1H-1,2,3-triazole)] catalyzes styrene synthesis with 53 TONs and 92% selectivity. In this reaction, ethylene is the *in situ* oxidant (Table 1.1).[139] $Pd(OAc)_2$ is a catalyst precursor for styrene synthesis using oxidants such as oxygen or CuX_2/oxygen {X = OAc or = OPiv (pivalate)}.[126, 146-148] For example, in the presence of acetylacetone and oxygen, Periana and coworkers reported styrene synthesis using $Pd(OAc)_2$ and $Cu(OAc)_2/O_2$ as the oxidant, which achieved 39 TONs of styrene at 180 °C.[141] However, a major byproduct under conditions studied was vinyl acetate (44 TONs). Using a more soluble copper oxidant such as $Cu(OPiv)_2$ and purified oxygen, Gunnoe and coworkers reported 2410 TONs of styrene with 87% selectivity after 24h at 150 °C and 60 psig ethylene.[146]

Catalyst	$RuCl_3 \cdot 3H_2O$	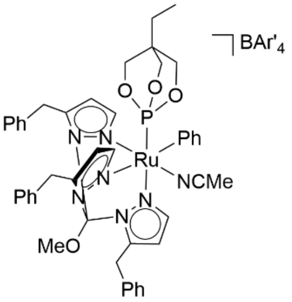	$Pd(OAc)_2$	$Pd(OAc)_2$
Oxidant	O_2	C_2H_4	$Cu(OAc)_2/O_2$	$Cu(OPiv)_2/O_2$
TONs	19	53	19	2410
	Milstein	Gunnoe	Periana	Gunnoe

Table 1.1. Reported catalytic styrene production using Ru and Pd catalyst precursors.[106]

Although significant progress has been made towards transition metal-mediated styrene synthesis, the catalysts discussed above suffered low TOs of products along with limited catalyst stability. Similar to Pd(II) catalyst precursors, Rh complexes have been reported as catalysts for arene alkenylation reactions.[141] It has been shown that Rh complexes are active for C–H functionalization,[149-151] olefin insertion,[152-154] and β-hydride elimination reactions.[155] The common C–H activation modes for rhodium-based catalyst are 1) concerted metalation-deprotonation (CMD); 2) oxidative addition (OA); 3) Fridel-Crafts-type electrophilic aromatic substitution; and 4) σ-complex assisted metathesis (σ-CAM).[151]

Hong and coworkers first discovered $Rh_4(CO)_{12}$ cluster mediated direct styrene synthesis from a mixture of benzene, ethylene and carbon monoxide at 200-250 °C, in which the ethylene and carbon monoxide serve as the oxidants. Under optimized conditions, 53 moles styrene per rhodium atom could be achieved with 60 moles of pent-

3-one as the main byproduct.[156] Following this discovery, Periana and coworkers developed an oxidative coupling of olefins and benzene using various Rh(I)/Rh(III) complexes and Cu(II) oxidant as the co-catalysts (eq 4).[141] Under some optimized conditions, a turnover frequency (TOF) of 0.01-0.03 s^{-1} with 77% selectivity towards styrene was obtained at 180 °C.[141] Examples of active Rh complexes include $Rh(ppy)_2(OAc)$, (ppy = 2-phenylpyridine), $Rh(ppy)_2(acac–O,O')$ (acac = acetylacetonato), and $Rh(acac)(CO)_2$. The precursor $Rh(acac)(CO)_2$ catalyzed styrene synthesis in the presence of acacH and O_2.

Recently, our group reported various Rh(I) catalyst precursors mediated styrene and linear alkenyl arenes synthesis with relatively high yield (~90% based on limiting agent Cu(II) salt) and selectivity at 150 °C.[106, 150, 157] Based on mechanistic studies, our initial proposed catalytic cycle involves: a) Rh-carboxylate group assisted arene C–H activation (Scheme 1.20), b) ethylene insertion into an Rh-aryl bond, c) β-hydride elimination from the resulting $Rh–CH_2CH_2Ar$ intermediate, and d) alkenyl arene dissociation and oxidation of the Rh–H intermediate with CuX_2 (X = carboxylate) to regenerate the starting catalyst.

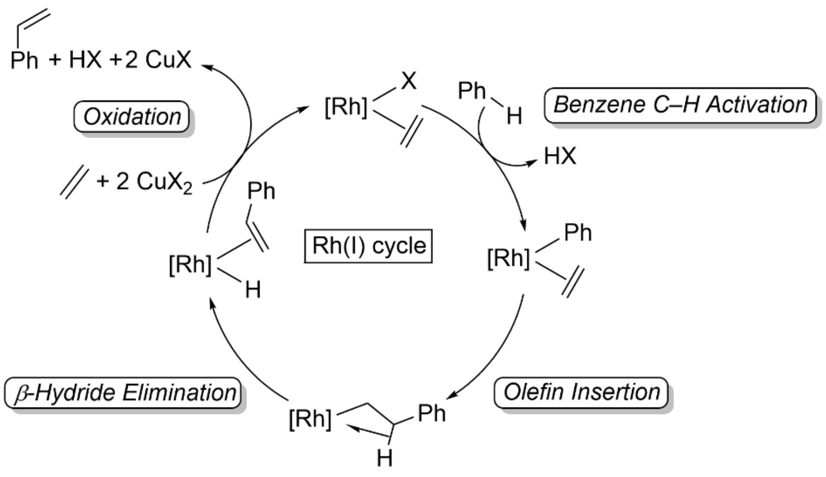

X = OAc, OPiv or OHex

Scheme 1.20. General catalytic cycle for transition metal-catalyzed arene alkenylation using benzene and ethylene.[106]

Under some conditions, we observed an induction period.[157-159] For example, we reported that an induction period of approximately 4 h was observed when heating a mixture of the Rh(I) complex ($^{\text{Fl}}$DAB)Rh(TFA)(η^2-C_2H_4) ($^{\text{Fl}}$DAB = *N*,*N*'-bis(pentafluorophenyl)-2,3-dimethyl-1,4-diaza-1,3-butadiene) or (Rh(μ-OAc)(η^2-C_2H_4)$_2$)$_2$, $Cu(OAc)_2$, benzene and ethylene at 150 °C (Figure 1.4). For examples of Rh catalyzed hydrogenations using soluble molecular precursors, it has been found that induction periods often originate from the decomposition of soluble Rh precursors to form active Rh nanoparticles.[160-164] In contrast, the apparent induction period of Rh(I) catalyzed styrene synthesis was initially proposed to be the transformation of the Rh-TFA precursor to an Rh-OAc complex, which catalyzed the styrene synthesis at a faster rate.[158] However, as discussed in Chapter 3, the induction period for our Rh catalyzed arene alkenylation is likely due to rapid decomposition of the soluble Rh catalyst precursor to form insoluble Rh(s) (pathway 1, Scheme 1.21) followed by active catalyst formation through the dissolution of inactive Rh(0) species. The induction period is minimized when soluble

Cu(II) such as $Cu(OHex)_2$ is used (pathway 2, Scheme 1.21). Similarly, an induction period of dissolution of supported Pd(0) to soluble Pd(II) species is well-documented in the literature. In these reports, a molecular Pd(II)/Pd(0) catalytic cycle occurs during a typical Pd-catalyzed C–C coupling reactions.[165-172]

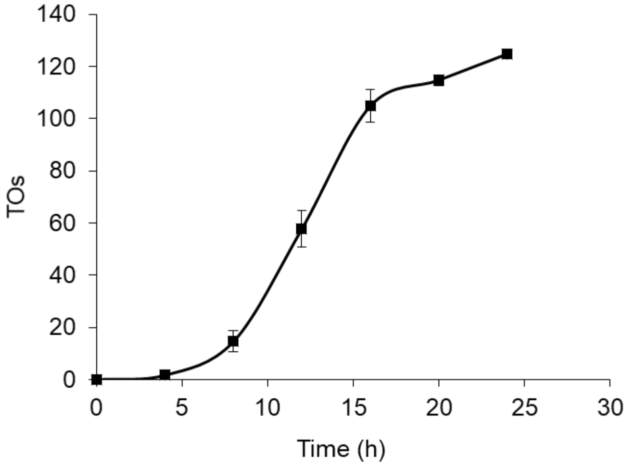

Figure 1.4. The plot of TO versus time for styrene production catalyzed by $[Rh(\mu\text{-}OAc)(\eta^2\text{-}C_2H_4)_2]_2$. Reaction conditions: 0.001 mol % of Rh (relative to benzene), 240 equiv. of $Cu(OAc)_2$ (relative to Rh),10 mL C_6H_6, 40 psig C_2H_4, 150 °C. Each data point is the average of three separate experiments. Error bars represent the standard deviations based on three independent experiments.[159]

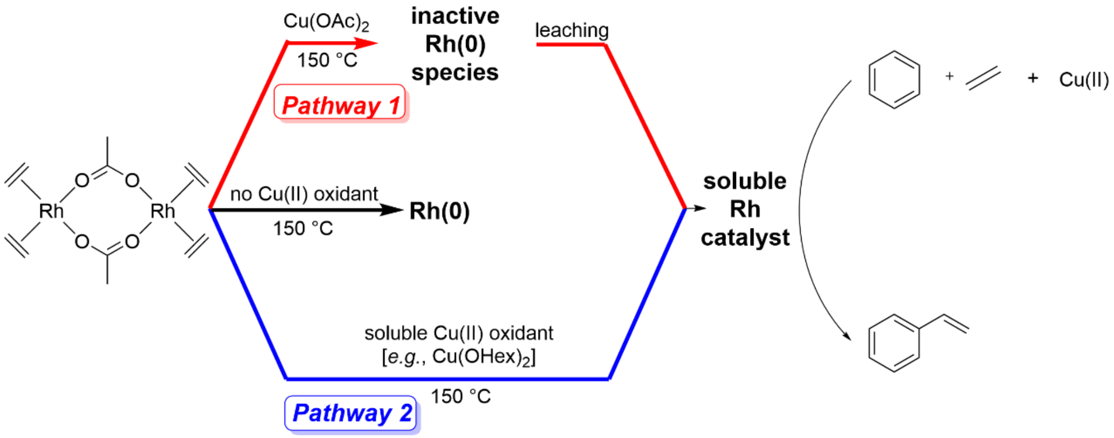

Scheme 1.21. Proposed pathways for styrene formation using diimine Rh(I) complexes as catalyst precursors under different conditions.[106, 159]

Compared with traditional acid-mediated arene alkylation, Rh catalyzed arene alkenylation using long-chain mono-substituent terminal olefins (*e.g.*, propylene, 1-pentene, 1-hexene, etc.) provide several novel features including 1) high selectivity towards anti-Markovnikov products (linear) relative to Markovnikov (branched) products; 2) the formation of unsaturated alkenyl arene products, which can be hydrogenated to form alkyl arenes; 3) unique regioselectivity for alkenylation of substituted arenes. For example, Rh catalyzed alkenylation of benzene with propylene provides a high L:B product ratio ranging from 7:1 to 11:1 when CuX_2 oxidant is used (Scheme 1.22). In one case when (5-FP)Rh(TFA)(η^2-C_2H_4) (5-FP = 1,2-bis(*N*-7-azaindolyl)benzene; TFA = trifluoroacetate) is used as catalyst precursor for the conversion of benzene and propylene at 150 °C, >13,000 TONs of alkenyl arene products is achieved with catalyst longevity of about two weeks.[173] Multiple Cu(II) regeneration steps using air were demonstrated, in which Cu(I)X and HX reacts with oxygen to recycle CuX_2 oxidants.

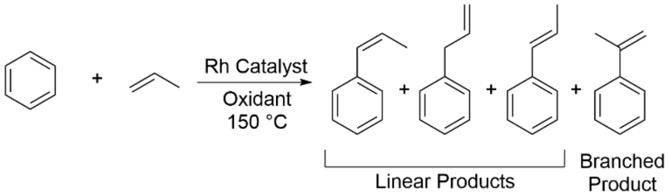

Catalyst Precursor	**Oxidant**	**Time/h**	**Linear:Branched**	**Total TOs**
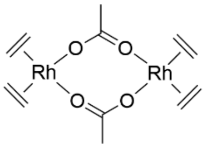	$Cu(OAc)_2$ (3600 equiv)	96	8:1	> 1,400
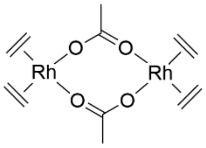	$Cu(OPiv)_2$ (240 equiv) (regenerated *in situ* by air) HOPiv (480 equiv)	69	8:1	~ 300
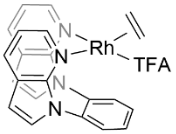	$Cu(OPiv)_2$ (2400 equiv)	10	11:1	953(48)
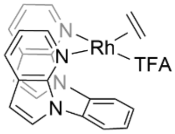	$Cu(OPiv)_2$ (240 equiv) (regenerated *in situ* by air) HOPiv (480 equiv)	60	11:1	> 1,000
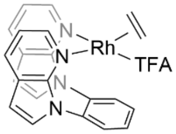	$Cu(OPiv)_2$ (2400 equiv) HOPiv (48,000 equiv) 1 atm Air	336	~7:1	> 13,000
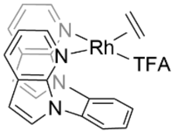	1 atm Air	240	~5:1	> 500

Scheme 1.22. Comparison of catalysis results under different conditions.[106]

For coupling reactions between toluene and 1-pentene (Scheme 1.23), various 1-aryl alkanes or alkenes (*i.e.*, anti-Markovnikov addition products) with unique *meta/para* selectivity (usually ~2:1 *meta/para* ratio between m-toyl-1-pentane and p-toyl-1-pentane products) are obtained.[174] Under optimized conditions, molecular Rh catalyst precursor $[Rh(\mu\text{-}OAc)(\eta^2\text{-}C_2H_4)_2]_2$ catalyzed toluene and 1-pentene coupling reactions yield the desired L:B products ratio from 7.2(7):1 up to 15(1):1 without the observation of 3-toly-2-pentenes (Scheme 1.22). This Rh-based unique selectivity towards metal products is complimentary to acid-catalyzed reactions, which offers the product selectivity on *para* positions.[174]

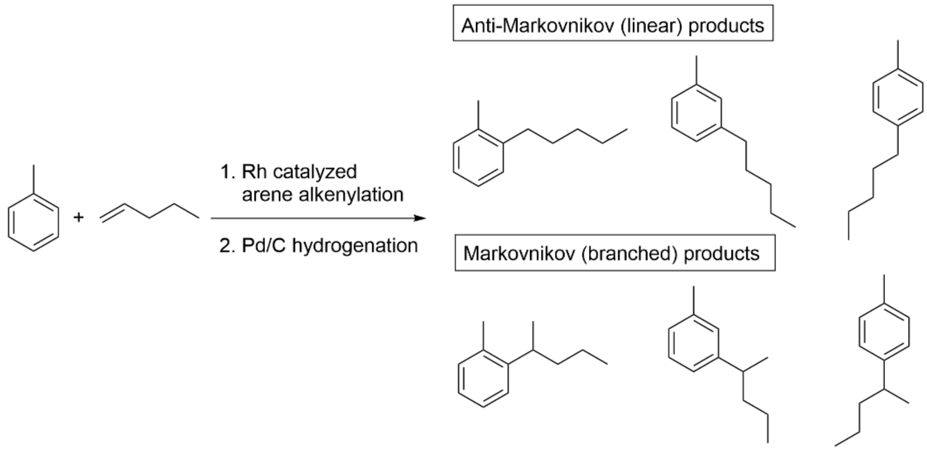

Scheme 1.23. Rh catalyst mediated linear/branched product selectivity for coupling reactions between toluene and 1-pentene with different *ortho*, *meta*, and *para* selectivity, Rh catalyst = Rh(μ-OAc)(η^2-C_2H_4)$_2$]$_2$.[174]

In a recent report, our group reported an extension of the Rh catalyzed arene alkenylation for the synthesis and isolation of a variety of stilbenes (Scheme 1.24).[112] In the study, it was demonstrated that (Rh(μ-OAc)(η^2-C_2H_4)$_2$) catalyzes the synthesis of resveratrol with a 68% isolated yield from a single coupling reaction/two-step conversion between vinyl anisole and poly-methoxybenzenes at 135 °C (Scheme 1.24). Similarly, a 71% isolated yield of DMU-212 could be achieved from a direct coupling reaction.

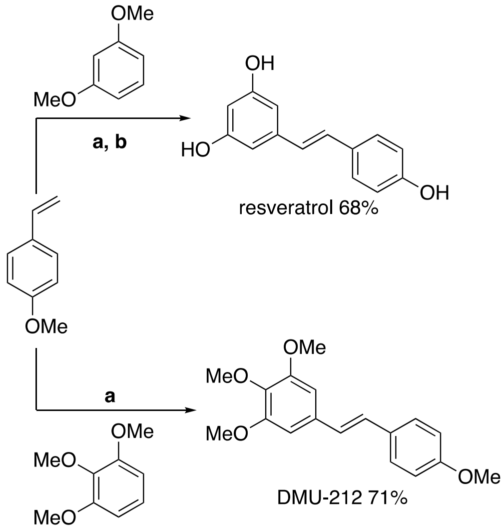

Scheme 1.24. Rh catalyzed synthesis of resveratrol and DMU-212. Conditions: (a): 0.25 mol% [Rh(μ-OAc)(η^2-C_2H_4)$_2$]$_2$ (0.5 mol% based on rhodium), 160 equiv. copper(II) pivalate, 800 equiv. pivalic acid, 60 psig N_2, 15 psig air, 5 mL arene as the solvent, 500 µmol of 4-vinylanisole, 135 °C, 96 hours, reactors were opened to air every 24 hours; (b) BBr_3, 0-30 °C, overnight.[112]

1.5 Summary and Thesis Aims

The top 10 most energy-intensive chemical processes include the synthesis of ammonia, methanol, ethylene, propylene, terephthalic acid, para-xylene, polyethylene, polypropylene and styrene.[1] Catalyst (reactive, selective, and stable) innovation and process optimization play significant roles in developing energy-efficient solutions for the synthesis of these large-scale commodity chemicals. Among the strategies applied for hydrocarbon utilization, C–X (X=C, O, N), C–H, or H–H bond breaking and formation are important steps. Presented here are a few projects that we developed during my Ph.D. study related to the C–C coupling of gold-methyl complexes to make ethane, the single-step synthesis of alkyl and alkenyl arenes by supported Rh catalysts as well as H–H bond activation.

Although various strategies, including the oxidative coupling of methane and super-acid mediated methane C–H activation have been developed, direct methane conversion to ethane/ethylene or methanol has not proven to be commercially viable. Therefore, it is of great importance to understand the fundamentals of C–C coupling from a metal-methyl species, which can shine a light on the further development of oxidative coupling of methane to C2 products. In Chapter 2, we synthesize a series of phosphine ligated gold methyl compounds and study reductive C–C coupling to form ethane. For this project, our collaborators from Spain (Juan Miranda-Pizarro, Juan J. Moreno Díaz, and Jesús Campos) focus on the kinetic study of terphenyl phosphine ligated complexes and DFT calculations. My contribution to the project has been the synthesis and characterization of various Buchwald phosphines ligated gold complexes, kinetic study of biaryl phosphines gold(I) complexes, mechanistic probe testing, and TEM characterization.

Multi-step processes for styrene monomer and linear alkyl arene synthesis have been commercialized via Friedel-Crafts chemistry or zeolite-based technologies. From a chemical innovation perspective, a single-step and energy-efficient process for styrene and linear alkenyl arenes synthesis are of great interest. In the past decade, the Gunnoe group and others have developed Rh-mediated styrene and superlinear alkenyl arene synthesis at relatively low temperatures (*i.e.*, 135 °C - 175 °C). Under some conditions, an induction period is observed for Rh-catalyzed styrene and linear alkenyl arenes synthesis. In Chapter 3, I contribute to a reexamination of the Rh-Cu catalytic system using X-ray photoelectron spectroscopy (XPS) and transmission electron microscopy (TEM). Direct catalytic performance comparison between $(Rh(\mu\text{-}OAc)(\eta^2\text{-}C_2H_4)_2)_2$ and various supported-Rh catalysts (*i.e.*, Rh/SiO_2 and Rh/NC (nitrogen-doped carbon)) is conducted to elucidate possible mechanistic details. For Rh-mediated styrene and linear alkenyl arenes synthesis, it has been shown that the induction period is likely due to Rh deactivation when $Cu(OAc)_2$ is used and redissolution under that catalytic conditions when supported Rh catalyst are used. The active catalyst is likely a soluble molecular Rh species.

The innovation of heterogeneous and homogeneous catalytic technologies for hydrogenation reactions has grown steadily over the past 20 years. In Chapter 4, one new strategy we proposed is to develop nanoparticle-mediated tandem catalysis. We aim to study a model reaction of nanoparticle-mediated hydrogenolysis of organometallic M–OPh complexes. Using various silica-supported noble metal catalysts (*i.e.,* Pd/SiO_2, Rh/SiO_2, and Pt/SiO_2), we investigated hydrogenation and hydrogenolysis reactions at the interface of homogeneous catalysis and heterogeneous catalysis reactions.

Finally, in Chapter 5, a new direction using a single-atom catalyst such as Rh-Na-Y zeolite for alkenyl arene synthesis is briefly presented. Applications of Rh-based catalysis towards the synthesis of high-value fine chemicals/pharmaceuticals are also attractive for commercialization consideration.

1.6 References

1. Schiffer, Z. J.; Manthiram, K. Electrification and Decarbonization of the Chemical Industry. *Joule* **2017,** *1*, 10-14.

2. Li, Q.; Xing, H.; Liu, J.; Liu, X. A review on hydraulic fracturing of unconventional reservoir. *Petroleum* **2015,** *1*, 8-15.

3. Striolo, A.; Cole, D. R. Understanding Shale Gas: Recent Progress and Remaining Challenges. *Energy & Fuels* **2017,** *31*, 10300-10310.

4. Wang, Q.; Li, R. Research status of shale gas: A review. *Renewable and Sustainable Energy Reviews* **2017,** *74*, 715-720.

5. Marcinkowski, M. D.; Darby, M. T.; Liu, J.; Wimble, J. M.; Lucci, F. R.; Lee, S.; Michaelides, A.; Flytzani-Stephanopoulos, M.; Stamatakis, M.; Sykes, E. C. H. Pt/Cu single-atom alloys as coke-resistant catalysts for efficient C–H activation. *Nat. Chem.* **2018,** *10*, 325-332.

6. Shindell, D. T.; Faluvegi, G.; Koch, D. M.; Schmidt, G. A.; Unger, N.; Bauer, S. E. Improved Attribution of Climate Forcing to Emissions. *Science* **2009,** *326*, 716.

7. Pipeline, A. C. Domonion Energy and Duke Energy Cancel the Atlantic Coast Pipeline. https://atlanticcoastpipeline.com/default.aspx.

8. Vogt, E. T. C.; Weckhuysen, B. M. Fluid catalytic cracking: recent developments on the grand old lady of zeolite catalysis. *Chem. Soc. Rev.* **2015,** *44*, 7342-7370.

9. Liu, L.; Corma, A. Metal Catalysts for Heterogeneous Catalysis: From Single Atoms to Nanoclusters and Nanoparticles. *Chem. Rev.* **2018,** *118*, 4981-5079.

10. Kandemir, T.; Schuster, M. E.; Senyshyn, A.; Behrens, M.; Schlögl, R. The Haber–Bosch Process Revisited: On the Real Structure and Stability of “Ammonia Iron” under Working Conditions. *Angew. Chem. Int. Ed.* **2013,** *52*, 12723-12726.

11. Jahangiri, H.; Bennett, J.; Mahjoubi, P.; Wilson, K.; Gu, S. A review of advanced catalyst development for Fischer–Tropsch synthesis of hydrocarbons from biomass derived syn-gas. *Catal. Sci. Technol.* **2014,** *4*, 2210-2229.

12. Behrens, M.; Studt, F.; Kasatkin, I.; Kühl, S.; Hävecker, M.; Abild-Pedersen, F.; Zander, S.; Girgsdies, F.; Kurr, P.; Kniep, B.-L.; Tovar, M.; Fischer, R. W.; Nørskov, J. K.; Schlögl, R. The Active Site of Methanol Synthesis over Cu/ZnO/Al2O3 Industrial Catalysts. *Science* **2012,** *336*, 893.

13. Lunsford, J. H. Catalytic conversion of methane to more useful chemicals and fuels: a challenge for the 21st century. *Catal. Today* **2000,** *63*, 165-174.

14. Alvarez-Galvan, C.; Melian, M.; Ruiz-Matas, L.; Eslava, J. L.; Navarro, R. M.; Ahmadi, M.; Roldan Cuenya, B.; Fierro, J. L. G. Partial Oxidation of Methane to Syngas Over Nickel-Based Catalysts: Influence of Support Type, Addition of Rhodium, and Preparation Method. *Frontiers in Chemistry* **2019,** *7*, 104.

15. Zichittella, G.; Paunović, V.; Amrute, A. P.; Pérez-Ramírez, J. Catalytic Oxychlorination versus Oxybromination for Methane Functionalization. *ACS Catal.* **2017,** *7*, 1805-1817.

16. Horn, R.; Schlögl, R. Methane Activation by Heterogeneous Catalysis. *Catal. Lett.* **2015,** *145*, 23-39.

17. Newton, M. A.; Knorpp, A. J.; Sushkevich, V. L.; Palagin, D.; van Bokhoven, J. A. Active sites and mechanisms in the direct conversion of methane to methanol using Cu in zeolitic hosts: a critical examination. *Chem. Soc. Rev.* **2020,** *49*, 1449-1486.

18. Newton, M. A.; Knorpp, A. J.; Pinar, A. B.; Sushkevich, V. L.; Palagin, D.; van Bokhoven, J. A. On the Mechanism Underlying the Direct Conversion of Methane to Methanol by Copper Hosted in Zeolites; Braiding Cu K-Edge XANES and Reactivity Studies. *J. Am. Chem. Soc.* **2018,** *140*, 10090-10093.

19. Wu, J.-F.; Gao, X.-D.; Wu, L.-M.; Wang, W. D.; Yu, S.-M.; Bai, S. Mechanistic Insights on the Direct Conversion of Methane into Methanol over Cu/Na–ZSM-5 Zeolite: Evidence from EPR and Solid-State NMR. *ACS Catal.* **2019,** *9*, 8677-8681.

20. Park, M. B.; Park, E. D.; Ahn, W.-S. Recent Progress in Direct Conversion of Methane to Methanol Over Copper-Exchanged Zeolites. *Frontiers in Chemistry* **2019,** *7*, 514.

21. Groothaert, M. H.; Smeets, P. J.; Sels, B. F.; Jacobs, P. A.; Schoonheydt, R. A. Selective Oxidation of Methane by the Bis(μ-oxo)dicopper Core Stabilized on ZSM-5 and Mordenite Zeolites. *J. Am. Chem. Soc.* **2005,** *127*, 1394-1395.

22. Woertink, J. S.; Smeets, P. J.; Groothaert, M. H.; Vance, M. A.; Sels, B. F.; Schoonheydt, R. A.; Solomon, E. I. A [Cu<sub>2</sub>O]<sup>2+</sup> core in Cu-ZSM-5, the active site in the oxidation of methane to methanol. *Proceedings of the National Academy of Sciences* **2009,** *106*, 18908.

23. Grundner, S.; Markovits, M. A. C.; Li, G.; Tromp, M.; Pidko, E. A.; Hensen, E. J. M.; Jentys, A.; Sanchez-Sanchez, M.; Lercher, J. A. Single-site trinuclear copper oxygen clusters in mordenite for selective conversion of methane to methanol. *Nat. Commun.* **2015,** *6*, 7546.

24. Alayon, E. M. C.; Nachtegaal, M.; Kleymenov, E.; van Bokhoven, J. A. Determination of the electronic and geometric structure of Cu sites during methane conversion over Cu-MOR with X-ray absorption spectroscopy. *Microporous Mesoporous Mater.* **2013,** *166*, 131-136.

25. Brezicki, G.; Kammert, J. D.; Gunnoe, T. B.; Paolucci, C.; Davis, R. J. Insights into the Speciation of Cu in the Cu-H-Mordenite Catalyst for the Oxidation of Methane to Methanol. *ACS Catal.* **2019,** *9*, 5308-5319.

26. Vanelderen, P.; Snyder, B. E. R.; Tsai, M.-L.; Hadt, R. G.; Vancauwenbergh, J.; Coussens, O.; Schoonheydt, R. A.; Sels, B. F.; Solomon, E. I. Spectroscopic Definition of the Copper Active Sites in Mordenite: Selective Methane Oxidation. *J. Am. Chem. Soc.* **2015,** *137*, 6383-6392.

27. Narsimhan, K.; Iyoki, K.; Dinh, K.; Román-Leshkov, Y. Catalytic Oxidation of Methane into Methanol over Copper-Exchanged Zeolites with Oxygen at Low Temperature. *ACS Cent. Sci.* **2016,** *2*, 424-429.

28. Ipek, B.; Lobo, R. F. Catalytic conversion of methane to methanol on Cu-SSZ-13 using N2O as oxidant. *Chem. Commun.* **2016,** *52*, 13401-13404.

29. Kim, Y.; Kim, T. Y.; Lee, H.; Yi, J. Distinct activation of Cu-MOR for direct oxidation of methane to methanol. *Chem. Commun.* **2017,** *53*, 4116-4119.

30. Starokon, E. V.; Parfenov, M. V.; Arzumanov, S. S.; Pirutko, L. V.; Stepanov, A. G.; Panov, G. I. Oxidation of methane to methanol on the surface of FeZSM-5 zeolite. *J. Catal.* **2013,** *300*, 47-54.

31. Ross, M. O.; Rosenzweig, A. C. A tale of two methane monooxygenases. *JBIC Journal of Biological Inorganic Chemistry* **2017,** *22*, 307-319.

32. Wei, P.-p.; Skulan, A. J.; Mitić, N.; Yang, Y.-S.; Saleh, L.; Bollinger, J. M.; Solomon, E. I. Electronic and Spectroscopic Studies of the Non-Heme Reduced Binuclear Iron Sites of Two Ribonucleotide Reductase Variants: Comparison to Reduced Methane

Monooxygenase and Contributions to O2 Reactivity. *J. Am. Chem. Soc.* **2004,** *126*, 3777-3788.

33. Ab Rahim, M. H.; Forde, M. M.; Jenkins, R. L.; Hammond, C.; He, Q.; Dimitratos, N.; Lopez-Sanchez, J. A.; Carley, A. F.; Taylor, S. H.; Willock, D. J.; Murphy, D. M.; Kiely, C. J.; Hutchings, G. J. Oxidation of Methane to Methanol with Hydrogen Peroxide Using Supported Gold–Palladium Alloy Nanoparticles. *Angew. Chem. Int. Ed.* **2013,** *52*, 1280-1284.

34. Paunović, V.; Zichittella, G.; Verel, R.; Amrute, A. P.; Pérez-Ramírez, J. Selective Production of Carbon Monoxide via Methane Oxychlorination over Vanadyl Pyrophosphate. *Angew. Chem. Int. Ed.* **2016,** *55*, 15619-15623.

35. Paunović, V.; Zichittella, G.; Hemberger, P.; Bodi, A.; Pérez-Ramírez, J. Selective Methane Functionalization via Oxyhalogenation over Supported Noble Metal Nanoparticles. *ACS Catal.* **2019,** *9*, 1710-1725.

36. Paunović, V.; Pérez-Ramírez, J. Catalytic halogenation of methane: a dream reaction with practical scope? *Catal. Sci. Technol.* **2019,** *9*, 4515-4530.

37. Fortman, G. C.; Boaz, N. C.; Munz, D.; Konnick, M. M.; Periana, R. A.; Groves, J. T.; Gunnoe, T. B. Selective Monooxidation of Light Alkanes Using Chloride and Iodate. *J. Am. Chem. Soc.* **2014,** *136*, 8393-8401.

38. Kalman, S. E.; Munz, D.; Fortman, G. C.; Boaz, N. C.; Groves, J. T.; Gunnoe, T. B. Partial oxidation of light alkanes by periodate and chloride salts. *Dalton Transactions* **2015,** *44*, 5294-5298.

39. Schwartz, N. A.; Boaz, N. C.; Kalman, S. E.; Zhuang, T.; Goldberg, J. M.; Fu, R.; Nielsen, R. J.; Goddard, W. A.; Groves, J. T.; Gunnoe, T. B. Mechanism of

Hydrocarbon Functionalization by an Iodate/Chloride System: The Role of Ester Protection. *ACS Catal.* **2018,** *8*, 3138-3149.

40. Liebov, N. S.; Goldberg, J. M.; Boaz, N. C.; Coutard, N.; Kalman, S. E.; Zhuang, T.; Groves, J. T.; Gunnoe, T. B. Selective Photo-Oxygenation of Light Alkanes Using Iodine Oxides and Chloride. *ChemCatChem* **2019,** *11*, 5045-5054.

41. Labinger, J. A.; Bercaw, J. E. Understanding and exploiting C–H bond activation. *Nature* **2002,** *417*, 507-514.

42. Davies, D. L.; Macgregor, S. A.; McMullin, C. L. Computational Studies of Carboxylate-Assisted C–H Activation and Functionalization at Group 8–10 Transition Metal Centers. *Chem. Rev.* **2017,** *117*, 8649-8709.

43. Shteinman, A. A. Shilov alkane platinum chemistry: 45 years. *J. Organomet. Chem.* **2015,** *793*, 34-40.

44. Mironov, O. A.; Bischof, S. M.; Konnick, M. M.; Hashiguchi, B. G.; Ziatdinov, V. R.; Goddard, W. A.; Ahlquist, M.; Periana, R. A. Using Reduced Catalysts for Oxidation Reactions: Mechanistic Studies of the “Periana-Catalytica” System for CH4 Oxidation. *J. Am. Chem. Soc.* **2013,** *135*, 14644-14658.

45. Zimmermann, T.; Soorholtz, M.; Bilke, M.; Schüth, F. Selective Methane Oxidation Catalyzed by Platinum Salts in Oleum at Turnover Frequencies of Large-Scale Industrial Processes. *J. Am. Chem. Soc.* **2016,** *138*, 12395-12400.

46. Janowicz, A. H.; Bergman, R. G. Carbon-hydrogen activation in completely saturated hydrocarbons: direct observation of M + R-H .fwdarw. M(R)(H). *J. Am. Chem. Soc.* **1982,** *104*, 352-354.

47. Jones, W. D.; Hessell, E. T. Photolysis of Tp'Rh(CN-neopentyl)(.eta.2-PhN:C:N-neopentyl) in alkanes and arenes: kinetic and thermodynamic selectivity of [Tp'Rh(CN-neopentyl)] for various types of carbon-hydrogen bonds. *J. Am. Chem. Soc.* **1993,** *115*, 554-562.

48. Watson, P. L. Methane exchange reactions of lanthanide and early-transition-metal methyl complexes. *J. Am. Chem. Soc.* **1983,** *105*, 6491-6493.

49. Webb, J. R.; Burgess, S. A.; Cundari, T. R.; Gunnoe, T. B. Activation of carbon–hydrogen bonds and dihydrogen by 1,2-CH-addition across metal–heteroatom bonds. *Dalton Transactions* **2013,** *42*, 16646-16665.

50. Oxgaard, J.; Tenn, W. J.; Nielsen, R. J.; Periana, R. A.; Goddard, W. A. Mechanistic Analysis of Iridium Heteroatom C−H Activation: Evidence for an Internal Electrophilic Substitution Mechanism. *Organometallics* **2007,** *26*, 1565-1567.

51. Lapointe, D.; Fagnou, K. Overview of the Mechanistic Work on the Concerted Metallation–Deprotonation Pathway. *Chem. Lett.* **2010,** *39*, 1118-1126.

52. Hashiguchi, B. G.; Young, K. J. H.; Yousufuddin, M.; Goddard, W. A.; Periana, R. A. Acceleration of Nucleophilic CH Activation by Strongly Basic Solvents. *J. Am. Chem. Soc.* **2010,** *132*, 12542-12545.

53. Boutadla, Y.; Davies, D. L.; Macgregor, S. A.; Poblador-Bahamonde, A. I. Mechanisms of C–H bond activation: rich synergy between computation and experiment. *Dalton Transactions* **2009**, 5820-5831.

54. Ackermann, L. Carboxylate-Assisted Transition-Metal-Catalyzed C−H Bond Functionalizations: Mechanism and Scope. *Chem. Rev.* **2011,** *111*, 1315-1345.

55. Shilov, A. E.; Shul'pin, G. B. Activation of C−H Bonds by Metal Complexes. *Chem. Rev.* **1997,** *97*, 2879-2932.

56. Shilov, A. E.; Shteinman, A. A. Activation of saturated hydrocarbons by metal complexes in solution. *Coord. Chem. Rev.* **1977,** *24*, 97-143.

57. Shilov, A. E.; Shul'pin, G. B. Activation and Catalytic Reactions of Alkanes in Solutions of Metal Complexes. *Russian Chemical Reviews* **1987,** *56*, 442-464.

58. Labinger, J. A.; Bercaw, J. E. Mechanistic studies on the Shilov system: A retrospective. *J. Organomet. Chem.* **2015,** *793*, 47-53.

59. Gretz, E.; Oliver, T. F.; Sen, A. Carbon-hydrogen bond activation by electrophilic transition-metal compounds. Palladium(II)-mediated oxidation of arenes and alkanes including methane. *J. Am. Chem. Soc.* **1987,** *109*, 8109-8111.

60. Kao, L. C.; Hutson, A. C.; Sen, A. Low-temperature, palladium(II)-catalyzed, solution-phase oxidation of methane to methanol derivative. *J. Am. Chem. Soc.* **1991,** *113*, 700-701.

61. Periana, R. A.; Taube, D. J.; Evitt, E. R.; Löffler, D. G.; Wentrcek, P. R.; Voss, G.; Masuda, T. A Mercury-Catalyzed, High-Yield System for the Oxidation of Methane to Methanol. *Science* **1993,** *259*, 340.

62. Periana, R. A.; Taube, D. J.; Gamble, S.; Taube, H.; Satoh, T.; Fujii, H. Platinum Catalysts for the High-Yield Oxidation of Methane to a Methanol Derivative. *Science* **1998,** *280*, 560.

63. Ahlquist, M.; Nielsen, R. J.; Periana, R. A.; Goddard Iii, W. A. Product Protection, the Key to Developing High Performance Methane Selective Oxidation Catalysts. *J. Am. Chem. Soc.* **2009,** *131*, 17110-17115.

64. Jones, C. J.; Taube, D.; Ziatdinov, V. R.; Periana, R. A.; Nielsen, R. J.; Oxgaard, J.; Goddard Iii, W. A. Selective Oxidation of Methane to Methanol Catalyzed, with C□H Activation, by Homogeneous, Cationic Gold. *Angew. Chem. Int. Ed.* **2004,** *43*, 4626-4629.

65. Periana, R. A.; Mironov, O.; Taube, D.; Bhalla, G.; Jones, C. J. Catalytic, Oxidative Condensation of CH4 to CH3COOH in One Step via CH Activation. *Science* **2003,** *301*, 814.

66. Strassner, T.; Ahrens, S.; Muehlhofer, M.; Munz, D.; Zeller, A. Cobalt-Catalyzed Oxidation of Methane to Methyl Trifluoroacetate by Dioxygen. *Eur. J. Inorg. Chem.* **2013,** *2013*, 3659-3663.

67. Munz, D.; Strassner, T. Propane Activation by Palladium Complexes with Chelating Bis(NHC) Ligands and Aerobic Cooxidation. *Angew. Chem. Int. Ed.* **2014,** *53*, 2485-2488.

68. Munz, D.; Strassner, T. Alkane C–H Functionalization and Oxidation with Molecular Oxygen. *Inorg. Chem.* **2015,** *54*, 5043-5052.

69. Hashiguchi, B. G.; Konnick, M. M.; Bischof, S. M.; Gustafson, S. J.; Devarajan, D.; Gunsalus, N.; Ess, D. H.; Periana, R. A. Main-Group Compounds Selectively Oxidize Mixtures of Methane, Ethane, and Propane to Alcohol Esters. *Science* **2014,** *343*, 1232.

70. Farrell, B. L.; Igenegbai, V. O.; Linic, S. A Viewpoint on Direct Methane Conversion to Ethane and Ethylene Using Oxidative Coupling on Solid Catalysts. *ACS Catal.* **2016,** *6*, 4340-4346.

71. Lunsford, J. H. The Catalytic Oxidative Coupling of Methane. *Angewandte Chemie International Edition in English* **1995,** *34*, 970-980.

72. Zavyalova, U.; Holena, M.; Schlögl, R.; Baerns, M. Statistical Analysis of Past Catalytic Data on Oxidative Methane Coupling for New Insights into the Composition of High-Performance Catalysts. *ChemCatChem* **2011,** *3*, 1935-1947.

73. Mleczko, L.; Baerns, M. Catalytic oxidative coupling of methane—reaction engineering aspects and process schemes. *Fuel Processing Technology* **1995,** *42*, 217-248.

74. Siluria Oxidative Coupling of Methane. https://siluria.com/Technology/Demonstration_Plant.

75. Gamoras, W. P. S. R. R. Z. C. S. M. C. Heterogeneous catalysts. May 1 , 2018 2015.

76. Zhu, Q.; Wegener, S. L.; Xie, C.; Uche, O.; Neurock, M.; Marks, T. J. Sulfur as a selective ‘soft’ oxidant for catalytic methane conversion probed by experiment and theory. *Nat. Chem.* **2013,** *5*, 104-109.

77. Xu, H.; Diccianni, J. B.; Katigbak, J.; Hu, C.; Zhang, Y.; Diao, T. Bimetallic C–C Bond-Forming Reductive Elimination from Nickel. *J. Am. Chem. Soc.* **2016,** *138*, 4779-4786.

78. Komiya, S.; Kochi, J. K. Electrophilic cleavage of organogold complexes with acids. The mechanism of the reductive elimination of dialkyl(aniono)gold(III) species. *J. Am. Chem. Soc.* **1976,** *98*, 7599-7607.

79. Lotz, M. D.; Remy, M. S.; Lao, D. B.; Ariafard, A.; Yates, B. F.; Canty, A. J.; Mayer, J. M.; Sanford, M. S. Formation of Ethane from Mono-Methyl Palladium(II) Complexes. *J. Am. Chem. Soc.* **2014,** *136*, 8237-8242.

80. Díez-González, S.; Scott, N. M.; Nolan, S. P. Cationic Copper(I) Complexes as Efficient Precatalysts for the Hydrosilylation of Carbonyl Compounds. *Organometallics* **2006,** *25*, 2355-2358.

81. Lail, M.; Gunnoe, T. B.; Barakat, K. A.; Cundari, T. R. Conversions of Ruthenium(III) Alkyl Complexes to Ruthenium(II) through Ru−Calkyl Bond Homolysis. *Organometallics* **2005,** *24*, 1301-1305.

82. Sattler, J. J. H. B.; Ruiz-Martinez, J.; Santillan-Jimenez, E.; Weckhuysen, B. M. Catalytic Dehydrogenation of Light Alkanes on Metals and Metal Oxides. *Chem. Rev.* **2014,** *114*, 10613-10653.

83. Akah, A.; Williams, J.; Ghrami, M. An Overview of Light Olefins Production via Steam Enhanced Catalytic Cracking. *Catal. Surv. Asia* **2019,** *23*, 265-276.

84. Amghizar, I.; Vandewalle, L. A.; Van Geem, K. M.; Marin, G. B. New Trends in Olefin Production. *Engineering* **2017,** *3*, 171-178.

85. Fujita, T.; Kawai, K. FI Catalysts for Olefin Oligomerization and Polymerization: Production of Useful Olefin-Based Materials by Unique Catalysis. *Top. Catal.* **2014,** *57*, 852-877.

86. Finiels, A.; Fajula, F.; Hulea, V. Nickel-based solid catalysts for ethylene oligomerization – a review. *Catal. Sci. Technol.* **2014,** *4*, 2412-2426.

87. Lutz, E. F. Shell higher olefins process. *Journal of Chemical Education* **1986,** *63*, 202.

88. Keim, W. Oligomerization of Ethylene to α-Olefins: Discovery and Development of the Shell Higher Olefin Process (SHOP). *Angew. Chem. Int. Ed.* **2013,** *52*, 12492-12496.

89. Keim, W. Nickel: An Element with Wide Application in Industrial Homogeneous Catalysis. *Angewandte Chemie International Edition in English* **1990,** *29*, 235-244.

90. Bohnen, H.-W.; Cornils, B., Hydroformylation of alkenes: An industrial view of the status and importance. In *Advances in Catalysis*, Academic Press: 2002; Vol. 47, pp 1-64.

91. Liu, D.; Chaudhari, R. V.; Subramaniam, B. Homogeneous catalytic hydroformylation of propylene in propane-expanded solvent media. *Chem. Eng. Sci.* **2018,** *187*, 148-156.

92. Bernas, A.; Mäki-Arvela, P.; Lehtonen, J.; Salmi, T.; Murzin, D. Y. Kinetic Modeling of Propene Hydroformylation with Rh/TPP and Rh/CHDPP Catalysts. *Ind. Eng. Chem. Res.* **2008,** *47*, 4317-4324.

93. Evans, D.; Osborn, J. A.; Wilkinson, G. Hydroformylation of alkenes by use of rhodium complex catalysts. *Journal of the Chemical Society A: Inorganic, Physical, Theoretical* **1968**, 3133-3142.

94. Deshpande, R. M.; Chaudhari, R. V. Kinetics of hydroformylation of 1-hexene using homogeneous HRh(CO)(PPh3)3 complex catalyst. *Ind. Eng. Chem. Res.* **1988,** *27*, 1996-2002.

95. Wender, I.; Sternberg, H. W.; Orchin, M. EVIDENCE FOR COBALT HYDROCARBONYL AS THE HYDROFORMYLATION CATALYST. *J. Am. Chem. Soc.* **1953,** *75*, 3041-3042.

96. Hebrard, F.; Kalck, P. Cobalt-Catalyzed Hydroformylation of Alkenes: Generation and Recycling of the Carbonyl Species, and Catalytic Cycle. *Chem. Rev.* **2009,** *109*, 4272-4282.

97. Angelici, C.; Weckhuysen, B. M.; Bruijnincx, P. C. A. Chemocatalytic Conversion of Ethanol into Butadiene and Other Bulk Chemicals. *ChemSusChem* **2013,** *6*, 1595-1614.

98. Liu, P.; Hensen, E. J. M. Highly Efficient and Robust Au/MgCuCr2O4 Catalyst for Gas-Phase Oxidation of Ethanol to Acetaldehyde. *J. Am. Chem. Soc.* **2013,** *135*, 14032-14035.

99. House, J. E., Chapter 22 - Coordination Compounds in Catalysis. In *Inorganic Chemistry (Second Edition)*, House, J. E., Ed. Academic Press: 2013; pp 747-772.

100. Hoechst Reveals Wacker Process Details. *Chemical & Engineering News Archive* **1961,** *39*, 52-55.

101. Keith, J. A.; Henry, P. M. The Mechanism of the Wacker Reaction: A Tale of Two Hydroxypalladations. *Angew. Chem. Int. Ed.* **2009,** *48*, 9038-9049.

102. Henry, P. M. Kinetics of the Oxidation of Ethylene by Aqueous Palladium(II) Chloride. *J. Am. Chem. Soc.* **1964,** *86*, 3246-3250.

103. Espeel, P. H.; Tielen, M. C.; Jacobs, P. A. Palladium–copper-exchanged Y type zeolites: a true heterogeneous Wacker catalyst. *Journal of the Chemical Society, Chemical Communications* **1991**, 669-671.

104. Imbao, J.; van Bokhoven, J. A.; Clark, A.; Nachtegaal, M. Elucidating the mechanism of heterogeneous Wacker oxidation over Pd-Cu/zeolite Y by transient XAS. *Nat. Commun.* **2020,** *11*, 1118.

105. Imbao, J.; van Bokhoven, J. A.; Nachtegaal, M. Optimization of a heterogeneous Pd–Cu/zeolite Y Wacker catalyst for ethylene oxidation. *Chem. Commun.* **2020,** *56*, 1377-1380.

106. Zhu, W.; Gunnoe, T. B. Advances in Rhodium-Catalyzed Oxidative Arene Alkenylation. *Acc. Chem. Res.* **2020,** *53*, 920-936.

107. Perego, C.; Ingallina, P. Recent advances in the industrial alkylation of aromatics: new catalysts and new processes. *Catal. Today* **2002,** *73*, 3-22.

108. de Almeida, J. L. G.; Dufaux, M.; Taarit, Y. B.; Naccache, C. Linear alkylbenzene. *J. Am. Oil Chem. Soc.* **1994,** *71*, 675-694.

109. Kocal, J. A.; Vora, B. V.; Imai, T. Production of linear alkylbenzenes. *Appl. Catal., A* **2001,** *221*, 295-301.

110. Evano, G.; Theunissen, C. Beyond Friedel and Crafts: Directed Alkylation of C−H Bonds in Arenes. *Angew. Chem. Int. Ed.* **2019,** *58*, 7202-7236.

111. Hourani, M. J.; Hessell, T.; Abramshe, R. A.; Liang, J. Alkylated Naphthalenes as High-Performance Synthetic Lubricating Fluids. *Tribology Transactions* **2007,** *50*, 82-87.

112. Jia, X.; Frye, L. I.; Zhu, W.; Gu, S.; Gunnoe, T. B. Synthesis of Stilbenes by Rhodium-Catalyzed Aerobic Alkenylation of Arenes via C–H Activation. *J. Am. Chem. Soc.* **2020**.

113. Gatto, V. J.; Elnagar, H. Y.; Moehle, W. E.; Schneller, E. R. Redesigning alkylated diphenylamine antioxidants for modern lubricants. *Lubrication Science* **2007,** *19*, 25-40.

114. Kaur, M.; Singh, M.; Chadha, N.; Silakari, O. Oxindole: A chemical prism carrying plethora of therapeutic benefits. *Eur. J. Med. Chem.* **2016,** *123*, 858-894.

115. Rokade, B. V.; Guiry, P. J. Synthesis of α-Aryl Oxindoles by Friedel–Crafts Alkylation of Arenes. *The Journal of Organic Chemistry* **2020,** *85*, 6172-6180.

116. Crafts, C. F. J. M. Organic chemistry. *Journal of the Chemical Society* **1877,** *32*, 725-791.

117. Perego, C.; Ingallina, P. Combining alkylation and transalkylation for alkylaromatic production. *Green Chem.* **2004,** *6*, 274-279.

118. Rueping, M.; Nachtsheim, B. J. A review of new developments in the Friedel–Crafts alkylation – From green chemistry to asymmetric catalysis. *Beilstein Journal of Organic Chemistry* **2010,** *6*, 6.

119. Čejka, J.; Wichterlová, B. ACID-CATALYZED SYNTHESIS OF MONO- AND DIALKYL BENZENES OVER ZEOLITES: ACTIVE SITES, ZEOLITE TOPOLOGY, AND REACTION MECHANISMS. *Catal. Rev.* **2002,** *44*, 375-421.

120. Perego, C.; Pollesel, P., Chapter 2 - Advances in Aromatics Processing Using Zeolite Catalysts. In *Advances in Nanoporous Materials*, Ernst, S., Ed. Elsevier: 2010; Vol. 1, pp 97-149.

121. Gerzeliev, I. M.; Khadzhiev, S. N.; Sakharova, I. E. Ethylbenzene synthesis and benzene transalkylation with diethylbenzenes on zeolite catalysts. *Pet. Chem.* **2011,** *51*, 39-48.

122. Dieck, H. A.; Heck, R. F. Organophosphinepalladium complexes as catalysts for vinylic hydrogen substitution reactions. *J. Am. Chem. Soc.* **1974,** *96*, 1133-1136.

123. Stille, J. K. The Palladium-Catalyzed Cross-Coupling Reactions of Organotin Reagents with Organic Electrophiles [New Synthetic Methods (58)]. *Angewandte Chemie International Edition in English* **1986,** *25*, 508-524.

124. Miyaura, N.; Suzuki, A. Stereoselective synthesis of arylated (E)-alkenes by the reaction of alk-1-enylboranes with aryl halides in the presence of palladium catalyst. *Journal of the Chemical Society, Chemical Communications* **1979**, 866-867.

125. Negishi, E.; King, A. O.; Okukado, N. Selective carbon-carbon bond formation via transition metal catalysis. 3. A highly selective synthesis of unsymmetrical biaryls and diarylmethanes by the nickel- or palladium-catalyzed reaction of aryl- and benzylzinc derivatives with aryl halides. *The Journal of Organic Chemistry* **1977,** *42*, 1821-1823.

126. Fujiwara, Y.; Moritani, I.; Danno, S.; Asano, R.; Teranishi, S. Aromatic substitution of olefins. VI. Arylation of olefins with palladium(II) acetate. *J. Am. Chem. Soc.* **1969,** *91*, 7166-7169.

127. Mizoroki, T.; Mori, K.; Ozaki, A. Arylation of Olefin with Aryl Iodide Catalyzed by Palladium. *Bull. Chem. Soc. Jpn.* **1971,** *44*, 581-581.

128. Foley, N. A.; Lee, J. P.; Ke, Z.; Gunnoe, T. B.; Cundari, T. R. Ru(II) Catalysts Supported by Hydridotris(pyrazolyl)borate for the Hydroarylation of Olefins: Reaction Scope, Mechanistic Studies, and Guides for the Development of Improved Catalysts. *Acc. Chem. Res.* **2009,** *42*, 585-597.

129. Andreatta, J. R.; McKeown, B. A.; Gunnoe, T. B. Transition metal catalyzed hydroarylation of olefins using unactivated substrates: Recent developments and challenges. *J. Organomet. Chem.* **2011,** *696*, 305-315.

130. Ritleng, V.; Sirlin, C.; Pfeffer, M. Ru-, Rh-, and Pd-Catalyzed C−C Bond Formation Involving C−H Activation and Addition on Unsaturated Substrates: Reactions and Mechanistic Aspects. *Chem. Rev.* **2002,** *102*, 1731-1770.

131. Gandeepan, P.; Müller, T.; Zell, D.; Cera, G.; Warratz, S.; Ackermann, L. 3d Transition Metals for C–H Activation. *Chem. Rev.* **2019,** *119*, 2192-2452.

132. Luedtke, A. T.; Goldberg, K. I. Intermolecular Hydroarylation of Unactivated Olefins Catalyzed by Homogeneous Platinum Complexes. *Angew. Chem. Int. Ed.* **2008,** *47*, 7694-7696.

133. Suslick, B. A.; Liberman-Martin, A. L.; Wambach, T. C.; Tilley, T. D. Olefin Hydroarylation Catalyzed by (pyridyl-indolate)Pt(II) Complexes: Catalytic Efficiencies and Mechanistic Aspects. *ACS Catal.* **2017,** *7*, 4313-4322.

134. McKeown, B. A.; Gonzalez, H. E.; Gunnoe, T. B.; Cundari, T. R.; Sabat, M. PtII-Catalyzed Ethylene Hydrophenylation: Influence of Dipyridyl Chelate Ring Size on Catalyst Activity and Longevity. *ACS Catal.* **2013,** *3*, 1165-1171.

135. McKeown, B. A.; Prince, B. M.; Ramiro, Z.; Gunnoe, T. B.; Cundari, T. R. PtII-Catalyzed Hydrophenylation of α-Olefins: Variation of Linear/Branched Products as a Function of Ligand Donor Ability. *ACS Catal.* **2014,** *4*, 1607-1615.

136. Clement, M. L.; Grice, K. A.; Luedtke, A. T.; Kaminsky, W.; Goldberg, K. I. Platinum(II) Olefin Hydroarylation Catalysts: Tuning Selectivity for the anti-Markovnikov Product. *Chem. - Eur. J.* **2014,** *20*, 17287-17291.

137. Rej, S.; Chatani, N. Rhodium(I)-Catalyzed C8-Alkylation of 1-Naphthylamide Derivatives with Alkenes through a Bidentate Picolinamide Chelation System. *ACS Catal.* **2018,** *8*, 6699-6706.

138. Zell, D.; Bursch, M.; Müller, V.; Grimme, S.; Ackermann, L. Full Selectivity Control in Cobalt(III)-Catalyzed C−H Alkylations by Switching of the C−H Activation Mechanism. *Angew. Chem. Int. Ed.* **2017,** *56*, 10378-10382.

139. Jia, X.; Gary, J. B.; Gu, S.; Cundari, T. R.; Gunnoe, T. B. Oxidative Hydrophenylation of Ethylene Using a Cationic Ru(II) Catalyst: Styrene Production with Ethylene as the Oxidant. *Isr. J. Chem.* **2017,** *57*, 1037-1046.

140. Matsumoto, T.; Taube, D. J.; Periana, R. A.; Taube, H.; Yoshida, H. Anti-Markovnikov Olefin Arylation Catalyzed by an Iridium Complex. *J. Am. Chem. Soc.* **2000,** *122*, 7414-7415.

141. Matsumoto, T.; Periana, R. A.; Taube, D. J.; Yoshida, H. Direct Synthesis of Styrene by Rhodium-Catalyzed Oxidative Arylation of Ethylene with Benzene. *J. Catal.* **2002,** *206*, 272-280.

142. Bhalla, G.; Bischof, S. M.; Ganesh, S. K.; Liu, X. Y.; Jones, C. J.; Borzenko, A.; Tenn, I. I. I. W. J.; Ess, D. H.; Hashiguchi, B. G.; Lokare, K. S.; Leung, C. H.; Oxgaard, J.; Goddard, I. I. I. W. A.; Periana, R. A. Mechanism of efficient anti-Markovnikov olefin hydroarylation catalyzed by homogeneous Ir(iii) complexes. *Green Chem.* **2011,** *13*, 69-81.

143. Oxgaard, J.; Muller, R. P.; Goddard, W. A.; Periana, R. A. Mechanism of Homogeneous Ir(III) Catalyzed Regioselective Arylation of Olefins. *J. Am. Chem. Soc.* **2004,** *126*, 352-363.

144. Saper, N. I.; Ohgi, A.; Small, D. W.; Semba, K.; Nakao, Y.; Hartwig, J. F. Nickel-catalysed anti-Markovnikov hydroarylation of unactivated alkenes with unactivated arenes facilitated by non-covalent interactions. *Nat. Chem.* **2020,** *12*, 276-283.

145. Weissman, H.; Song, X.; Milstein, D. Ru-Catalyzed Oxidative Coupling of Arenes with Olefins Using O2. *J. Am. Chem. Soc.* **2001,** *123*, 337-338.

146. Jia, X.; Foley, A. M.; Liu, C.; Vaughan, B. A.; McKeown, B. A.; Zhang, S.; Gunnoe, T. B. Styrene Production from Benzene and Ethylene Catalyzed by Palladium(II): Enhancement of Selectivity toward Styrene via Temperature-dependent Vinyl Ester Consumption. *Organometallics* **2019,** *38*, 3532-3541.

147. Yamada, T.; Sakakura, A.; Sakaguchi, S.; Obora, Y.; Ishii, Y. Oxidative arylation of ethylene with benzene catalyzed by Pd(OAc)2/heteropoly acid/O2 system. *New Journal of Chemistry* **2008,** *32*, 738-742.

148. Kubota, A.; Emmert, M. H.; Sanford, M. S. Pyridine Ligands as Promoters in PdII/0-Catalyzed C–H Olefination Reactions. *Organic Letters* **2012,** *14*, 1760-1763.

149. Webster-Gardiner, M. S.; Fu, R.; Fortman, G. C.; Nielsen, R. J.; Gunnoe, T. B.; Goddard Iii, W. A. Arene C–H activation using Rh(i) catalysts supported by bidentate nitrogen chelates. *Catal. Sci. Technol.* **2015,** *5*, 96-100.

150. Webster-Gardiner, M. S.; Chen, J.; Vaughan, B. A.; McKeown, B. A.; Schinski, W.; Gunnoe, T. B. Catalytic Synthesis of “Super” Linear Alkenyl Arenes Using an Easily Prepared Rh(I) Catalyst. *J. Am. Chem. Soc.* **2017,** *139*, 5474-5480.

151. Qi, X.; Li, Y.; Bai, R.; Lan, Y. Mechanism of Rhodium-Catalyzed C–H Functionalization: Advances in Theoretical Investigation. *Acc. Chem. Res.* **2017,** *50*, 2799-2808.

152. Halpern, J.; Okamoto, T.; Zakhariev, A. Mechanism of the chlorotris(triphenylphosphine) rhodium(I)-catalyzed hydrogenation of alkenes. The reaction of chlorodihydridotris(triphenyl-phosphine)rhodium(III) with cyclohexene. *J. Mol. Catal.* **1977,** *2*, 65-68.

153. Roe, D. C. Mechanistic investigation of olefin insertion into the rhodium-hydrogen bond. *J. Am. Chem. Soc.* **1983,** *105*, 7770-7771.

154. Alagona, G.; Ghio, C.; Lazzaroni, R.; Settambolo, R. Olefin Insertion into the Rhodium−Hydrogen Bond as the Step Determining the Regioselectivity of Rhodium-Catalyzed Hydroformylation of Vinyl Substrates: Comparison between Theoretical and Experimental Results. *Organometallics* **2001,** *20*, 5394-5404.

155. Azpeitia, S.; Prieto, U.; San Sebastián, E.; Rodríguez-Diéguez, A.; Garralda, M. A.; Huertos, M. A. Alkene-alkyl interconversion: an experimental and computational study of the olefin insertion and β-hydride elimination processes. *Dalton Transactions* **2018,** *47*, 6808-6818.

156. Hong, P.; Yamazaki, H. Rhodium carbonyl-catalyzed activation of carbon-hydrogen bonds for application in organic synthesis.: V11For Part IV see ref. 1.. phenylation of olefins with benzenes. *J. Mol. Catal.* **1984,** *26*, 297-311.

157. Vaughan, B. A.; Webster-Gardiner, M. S.; Cundari, T. R.; Gunnoe, T. B. A rhodium catalyst for single-step styrene production from benzene and ethylene. *Science* **2015,** *348*, 421.

158. Vaughan, B. A.; Khani, S. K.; Gary, J. B.; Kammert, J. D.; Webster-Gardiner, M. S.; McKeown, B. A.; Davis, R. J.; Cundari, T. R.; Gunnoe, T. B. Mechanistic Studies of Single-Step Styrene Production Using a Rhodium(I) Catalyst. *J. Am. Chem. Soc.* **2017,** *139*, 1485-1498.

159. Zhu, W.; Luo, Z.; Chen, J.; Liu, C.; Yang, L.; Dickie, D. A.; Liu, N.; Zhang, S.; Davis, R. J.; Gunnoe, T. B. Mechanistic Studies of Single-Step Styrene Production

Catalyzed by Rh Complexes with Diimine Ligands: An Evaluation of the Role of Ligands and Induction Period. *ACS Catal.* **2019,** *9*, 7457-7475.

160. Tran, B. L.; Fulton, J. L.; Linehan, J. C.; Lercher, J. A.; Bullock, R. M. Rh(CAAC)-Catalyzed Arene Hydrogenation: Evidence for Nanocatalysis and Sterically Controlled Site-Selective Hydrogenation. *ACS Catal.* **2018,** *8*, 8441-8449.

161. Moock, D.; Wiesenfeldt, M. P.; Freitag, M.; Muratsugu, S.; Ikemoto, S.; Knitsch, R.; Schneidewind, J.; Baumann, W.; Schäfer, A. H.; Timmer, A.; Tada, M.; Hansen, M. R.; Glorius, F. Mechanistic Understanding of the Heterogeneous, Rhodium-Cyclic (Alkyl)(Amino)Carbene-Catalyzed (Fluoro-)Arene Hydrogenation. *ACS Catal.* **2020,** *10*, 6309-6317.

162. Tran, B. L.; Fulton, J. L.; Linehan, J. C.; Balasubramanian, M.; Lercher, J. A.; Bullock, R. M. Operando XAFS Studies on Rh(CAAC)-Catalyzed Arene Hydrogenation. *ACS Catal.* **2019,** *9*, 4106-4114.

163. Bayram, E.; Linehan, J. C.; Fulton, J. L.; Roberts, J. A. S.; Szymczak, N. K.; Smurthwaite, T. D.; Özkar, S.; Balasubramanian, M.; Finke, R. G. Is It Homogeneous or Heterogeneous Catalysis Derived from [RhCp*Cl2]2? In Operando XAFS, Kinetic, and Crucial Kinetic Poisoning Evidence for Subnanometer Rh4 Cluster-Based Benzene Hydrogenation Catalysis. *J. Am. Chem. Soc.* **2011,** *133*, 18889-18902.

164. Bayram, E.; Linehan, J. C.; Fulton, J. L.; Szymczak, N. K.; Finke, R. G. Determination of the Dominant Catalyst Derived from the Classic [RhCp*Cl2]2 Precatalyst System: Is it Single-Metal Rh1Cp*-Based, Subnanometer Rh4 Cluster-Based, or Rh(0)n Nanoparticle-Based Cyclohexene Hydrogenation Catalysis at Room Temperature and Mild Pressures? *ACS Catal.* **2015,** *5*, 3876-3886.

165. Ji, Y.; Jain, S.; Davis, R. J. Investigation of Pd Leaching from Supported Pd Catalysts during the Heck Reaction. *J. Phys. Chem. B* **2005,** *109*, 17232-17238.

166. Davies, I. W.; Matty, L.; Hughes, D. L.; Reider, P. J. Are Heterogeneous Catalysts Precursors to Homogeneous Catalysts? *J. Am. Chem. Soc.* **2001,** *123*, 10139-10140.

167. Zalesskiy, S. S.; Ananikov, V. P. Pd2(dba)3 as a Precursor of Soluble Metal Complexes and Nanoparticles: Determination of Palladium Active Species for Catalysis and Synthesis. *Organometallics* **2012,** *31*, 2302-2309.

168. Reay, A. J.; Fairlamb, I. J. S. Catalytic C–H bond functionalisation chemistry: the case for quasi-heterogeneous catalysis. *Chem. Commun.* **2015,** *51*, 16289-16307.

169. Pröckl, S. S.; Kleist, W.; Gruber, M. A.; Köhler, K. In Situ Generation of Highly Active Dissolved Palladium Species from Solid Catalysts—A Concept for the Activation of Aryl Chlorides in the Heck Reaction. *Angew. Chem. Int. Ed.* **2004,** *43*, 1881-1882.

170. Röhlich, C.; Köhler, K. Macrocyclic Palladium(II) Complexes in C□C Coupling Reactions: Efficient Catalysis by Controlled Temporary Release of Active Species. *Adv. Synth. Catal.* **2010,** *352*, 2263-2274.

171. Gnad, C.; Abram, A.; Urstöger, A.; Weigl, F.; Schuster, M.; Köhler, K. Leaching Mechanism of Different Palladium Surface Species in Heck Reactions of Aryl Bromides and Chlorides. *ACS Catal.* **2020**, 6030-6041.

172. Phan, N. T. S.; Van Der Sluys, M.; Jones, C. W. On the Nature of the Active Species in Palladium Catalyzed Mizoroki–Heck and Suzuki–Miyaura Couplings – Homogeneous or Heterogeneous Catalysis, A Critical Review. *Adv. Synth. Catal.* **2006,** *348*, 609-679.

173. Chen, J.; Nielsen, R. J.; Goddard, W. A.; McKeown, B. A.; Dickie, D. A.; Gunnoe, T. B. Catalytic Synthesis of Superlinear Alkenyl Arenes Using a Rh(I) Catalyst Supported by a “Capping Arene” Ligand: Access to Aerobic Catalysis. *J. Am. Chem. Soc.* **2018,** *140*, 17007-17018.

174. Liebov, N. S.; Zhu, W.; Chen, J.; Webster-Gardiner, M. S.; Schinski, W. L.; Gunnoe, T. B. Rhodium-Catalyzed Alkenylation of Toluene Using 1-Pentene: Regioselectivity To Generate Precursors for Bicyclic Compounds. *Organometallics* **2019,** *38*, 3860-3870.

2 Reductive C–C coupling from Molecular Au(I) Hydrocarbyl Complexes: A Mechanistic Study

2.1 Introduction

Organometallic gold pre-catalysts have been applied to a range of catalytic organic syntheses.[1-7] Among the Au-catalyzed processes, many involve C–C bond forming reactions as a key step. Thus, the mechanisms of Au-mediated C–C bond formation have been of substantial interest.[8-14] Also, Au-catalyzed partial oxidation of methane in oleum to form methylbisulfate has been reported.[15, 16] The demonstration, separately, of Au-mediated methane C–H activation[17, 18] and the ability of molecular Au complexes to mediate C–C bond forming reactions[8-16] sparked our interest in ethane elimination since combined methane C–H activation and ethane reductive elimination provides a strategy for the oxidative conversion of methane to ethane.[19, 20] In this chapter, we conduct a mechanistic study of ethane elimination from phosphine ligated gem-digold methyl complexes with the general formula $[Au_2(\mu\text{-}CH_3)(PMe_2Ar')_2][NTf_2]$ and $[Au_2(\mu\text{-}CH_3)(XPhos)_2][NTf_2]$ {Ar = C_6H_3-2,6-(C_6H_3-2,6-Me)$_2$, C_6H_3-2,6-(C_6H_3-2,4,6-Me)$_2$, C_6H_3-2,6-(C_6H_3-2,6-iPr)$_2$, or C_6H_3-2,6-(C_6H_3-2,4,6-iPr)$_2$; XPhos = **2-dicyclohexylphosphino-2′,4′,6′-triisopropylbiphenyl; NTf_2 = bis(trifluoromethyl sulfonyl)imide**)}.

Proposed mechanisms for Au-mediated C–C bond formation include reductive elimination from Au^{III} intermediates (Scheme 2.1).[21] For example, reductive elimination from $(R)_2Au(X)(L)$ (L = phosphine; R = Me, Et or *n*-Pr; X = anionic ligand such as Cl, OTf, NO_3, O_2CCF_3 or another alkyl ligand) was investigated by Kochi and coworkers.[12, 22, 23] The proposed mechanism involves initial phosphine dissociation followed by C–C reductive elimination from the three-coordinate $R_2Au^{III}X$ intermediate (Scheme 1a). When R = Me, isotopic labeling studies with $(Me)_2AuX(L)$ and $(CD_3)_2Au(X)(L)$ (L = phosphine) indicate kinetically competitive intermolecular transfer of Me between two Au centers, but these alkyl transfers appear to occur only in non-polar solvents.[17] Further, the putative binuclear Au intermediates responsible for alkyl transfer were not directly implicated in the C–C coupling reactions. From the starting complexes $(Me)_2Au(X)(L)$ (L = phosphine), it was proposed that larger phosphines facilitate ethane reductive elimination.[23] Alternatively, Kochi has proposed that ethane formation could result from digold alkyl intermediates, but to our knowledge such reactions were not directly observed.[24, 25] Other examples of ethane formation through bimolecular reductive elimination from $M–CH_3$ species include Ni^{II},[26] Cu^{I},[27] and Ru^{II}.[28]

The formation of C–C bonds from $(NHC)Au^{I}–R$ (NHC = *N*-heterocyclic carbene; R = Ph, Me or *p*-tolyl) occurs upon addition of electrophiles (R'X), such as PhI, MeI and MeOTf, to form R–R' as well as homo-coupled products R–R and R'–R' (Scheme 1b).[29] The proposed mechanism involves formal *trans* oxidative addition of the electrophile (R'X) to form an $(NHC)Au^{III}(R')(X)(R)$ intermediate followed by competitive a) C–C reductive elimination to form R'–R and b) intermolecular transfer of RX from a Au(III) intermediate to $(NHC)Au^{I}–R$ to form $(NHC)Au^{III}(R)_2(X)$ followed by C–C reductive elimination to give the homo-coupled product R–R.

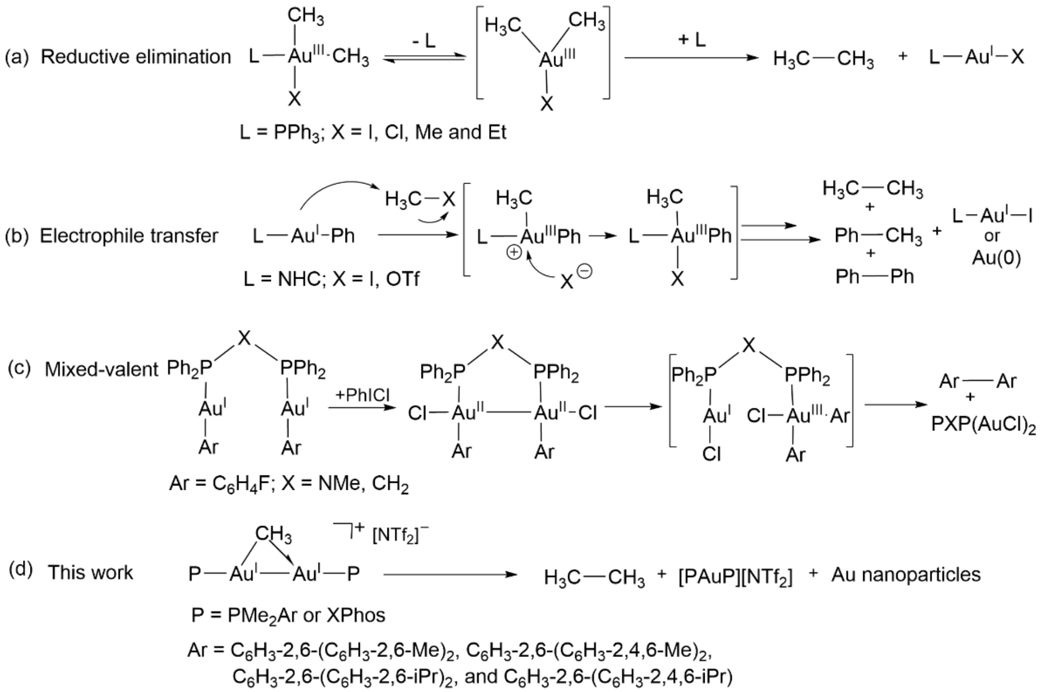

Scheme 2.1. Proposed pathways of C–C bond coupling reactions mediated by molecular gold complexes.[11, 12, 24, 29]

Mixed-valent gold hydrocarbyl complexes have also been proposed as intermediates responsible for the C–C bond formation.[11] For example, Toste and coworkers reported a fast biaryl C–C bond reductive elimination from a mixed-valent bimetallic Au^I/Au^{III} complex $[ClAu]PNP[AuCl(4\text{-}F\text{-}C_6H_4)_2]$ (PNP = $Ph_2P–N(CH_3)–PPh_2$) (Scheme 1c).[11, 30] In this study, the Au(I) complex $[Au(4\text{-}F\text{-}C_6H_4)]PNP[Au(4\text{-}F\text{-}C_6H_4)]$ is oxidized with $PhICl_2$ to generate a symmetric bimetallic Au(II) species, $[ClAu(4\text{-}F\text{-}C_6H_4)]PNP[Au(4\text{-}F\text{-}C_6H_4)Cl]$. The latter isomerizes to a mixed-valent Au^I/Au^{III} complex, $[ClAu]PNP[AuCl(4\text{-}F\text{-}C_6H_4)_2]$, which undergoes reductive elimination to form a biaryl product. Similarly, O'Hair and co-workers reported a concerted redox couple mechanism from a reaction between allylic halides ($CH_2 = CHCH_2X$, X = Cl, Br, and I) and a gem-digold(I) compound, $[(dppm)_2Au_2Ph]^+$ (dppm = bis(diphenylphosphino)methane, $(Ph_2P)_2CH_2$).[31] It is hypothesized that the reductive coupling occurs from a Au^I/Au^{III} complex, $[ClAu^I](dppm)[Au^{III}(CH_2{=}CHCH_2)(Ph)]$.

Germane to these proposed binuclear Au precursors to C–C elimination, several gem-digold intermediates have been reported, including $[Au_2(\sigma,\pi\text{-}CH{=}CHC_3H_5)(PPh_3)_2][NTf_2]$,[32] $[Au_2(\mu\text{-}Ph)L_2][NTf_2]$,[33] (L = PPh_3 or NHC) and $[Au_2(\mu\text{-}R)(PMe_2Ar^{Dipp2})_2][NTf_2]$ (R = CH_3, $CH{=}CH_2$, $C{\equiv}CH$, Ar^{Dipp2} = $C_6H_3\text{-}2,6\text{-}(C_6H_3\text{-}2,6\text{-}iPr)_2$).[34] The thermal stabilities of phosphine ligated gem-digold hydrocarbyl complexes have been reported to depend on the steric properties of the ancillary ligands.[34] Other related examples, including $([Au_2(\mu\text{-}vinyl^{cypr})(PPh_3)_2][NTf_2]$[8, 9, 32] and $([Au_2(\mu\text{-}vinyl^{cypr})(PPh_3)_2][NTf_2]$ readily decompose to the corresponding diene, $[Au(PPh_3)_2][NTf_2]$ and colloidal gold byproducts. Nonetheless, a mechanistic understanding of these C–C coupling processes and, in general, of C–C formation from Au^I complexes, is lacking.

In this work, we explore the formation of ethane from one of the simplest possible gold-based system, namely $Au(CH_3)(PPh_3)$. To enable reliable mechanistic investigations, we extended our preliminary observations on triphenylphosphine ligated systems to bulkier terphenyl and biaryl phosphines that provide kinetic stabilization of key digold intermediates. In particular, we have focused on C–C coupling reactions from gem-digold methyl complexes with a general formula $[Au_2(\mu\text{-}CH_3)(PMe_2Ar')_2][NTf_2]$ and $[Au_2(\mu\text{-}CH_3)(XPhos)_2][NTf_2]$ (Figure 2.1). We studied the impact of the phosphine ligand on the stability of digold complexes, especially the influence on ethane elimination.

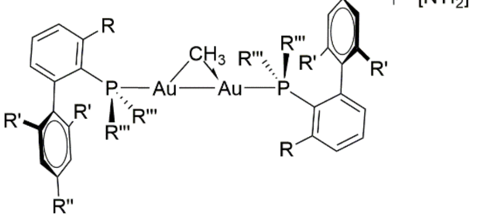

4a, R = Xyl; R' = Me; R'' = H; R''' = Me, **4d**, R = Trip; R' = iPr; R'' = iPr; R''' = Me
4b, R = Mes; R' = Me; R'' = Me; R''' = Me, **4e**, R = H; R' = iPr; R'' = iPr; R''' = Cy
4c, R = Dipp; R' = iPr; R'' = H; R''' = Me, **4f**, R = H; R' = iPr; R'' = iPr; R''' = tBu

Figure 2.1. Phosphine ligated gem-digold methyl complexes with the general formula $[Au_2(\mu\text{-}CH_3)(PR_2Ar')_2][NTf_2]$ investigated in this work (Xyl = 2,6-C_6H_3-Me_2; Mes = 2,4,6-C_6H_2-Me_3; Dipp = 2,6-C_6H_3-^{i}Pr_2; Tripp = 2,4,6-C_6H_2-^{i}Pr_3).

2.2 Results and Discussion

2.2.1 Synthesis of Neutral Gold Complexes based on Terphenyl and Biaryl Phosphines. Gold complexes with terphenyl phosphine (complexes **1a**-**d** in Scheme 2.2) and with biaryl "Buchwald phosphine" ligands (**1e** and **1f**) were synthesized by methylation of Au(I) chloride precursors with MeMgX (X = Cl or Br) with 60-80% isolated yields. Formation of the new Au–C bonds is evidenced by the appearance of ^1H NMR resonances in the range from 0.08 to 0.45 ppm with associated $^{13}C\{^1H\}$ signals at 3.4 to 8.3 ppm ($^2J_{CP} \approx 100$ Hz). Single crystals of **1a**, **1e** and **1f** were obtained by slow evaporation from a mixture of pentane and diethyl ether or pentane and dichloromethane solution from 5 to -25 ºC (Figure 2.2). The solid-state structures of complexes **1e** and **1f** show a weak κ^1 type interaction (localized Au···π(arene) contact)[35,36,37] between the Au(I) center and the *ipso* carbon of the arenes (C20, **1e**; C16, **1f**) with bond distances of 3.1748(2) and 3.180(4) Å, respectively. The distances between Au centers and arene ring centroids are 3.2659(1) Å (**1e**) and 3.449(2) Å (**1f**), also indicative of intramolecular Au···π(arene) interactions.[37, 38] Structure **1a** does not exhibit this type of contact, in agreement with the preferred geometry adopted by the smaller phosphines of the terphenyl series.[39] The Au–CH_3 bond distances are 2.123(2) Å (**1a**), 2.115(1) Å (**1e**) and 2.096(4) Å (**1f**).

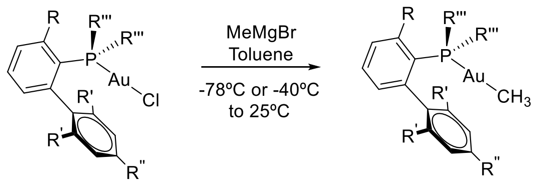

1a-f

1a, R = Xyl; R' = Me; R'' = H; R''' = Me, **1d**, R = Trip; R' = iPr; R'' = iPr; R''' = Me
1b, R = Mes; R' = Me; R'' = Me; R''' = Me, **1e**, R = H; R' = iPr; R'' = iPr; R''' = Cy
1c, R = Dipp; R' = iPr; R'' = H; R''' = Me, **1f**, R = H; R' = iPr; R'' = iPr; R''' = tBu

Scheme 2.2. Synthesis of phosphine ligated gold methyl compounds with terphenyl phosphines (**1a−d**) and Buchwald phosphines (**1e−f**).

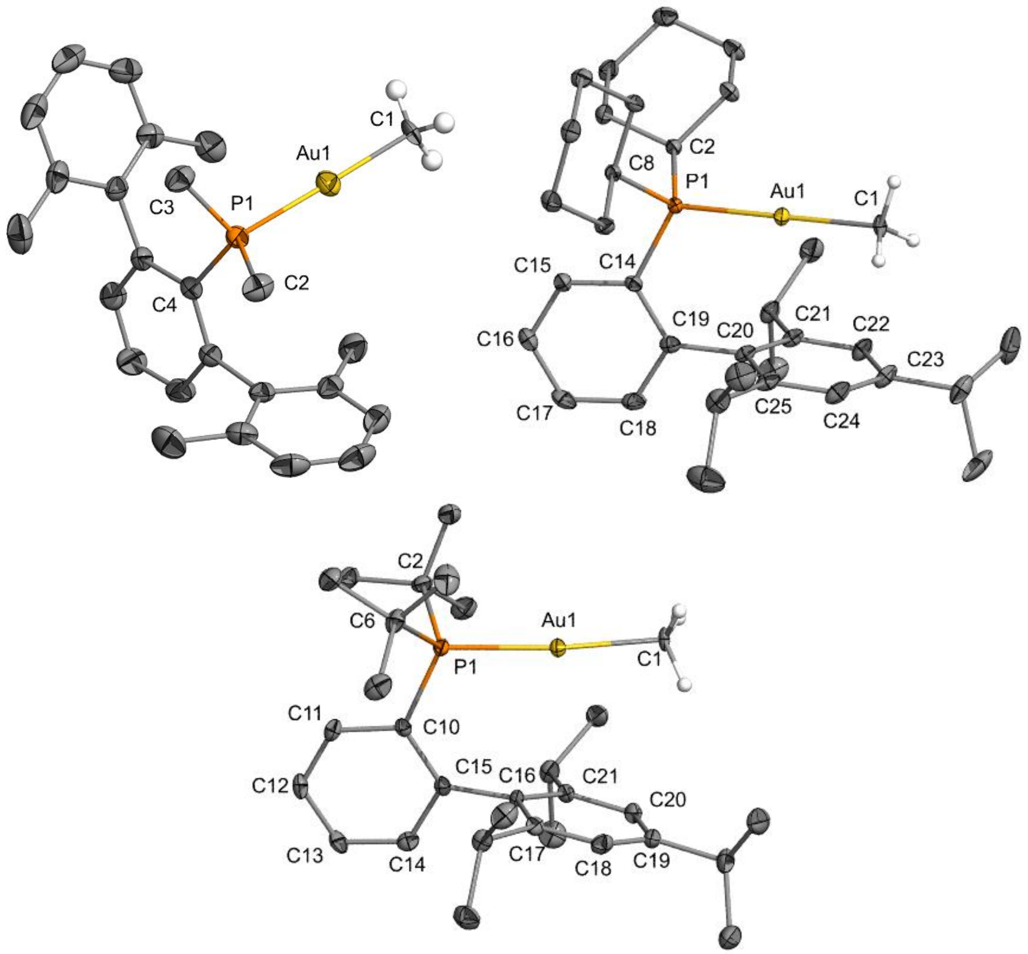

Figure 2.2. ORTEP of compounds Au(CH_3)(PMe_2Ar^{Xyl2}) (**1a**), Au(CH_3)(XPhos) (**1e**) and Au(CH_3)(^{t}BuXPhos) (**1f**) represented at 50% probability (for **1f** one of the two chemically equivalent, but crystallographically distinct structures, is shown. For second structure, see Supporting Information). Hydrogen atoms on the phosphine ligands are omitted for clarity. Selected bond lengths (Å): **1a**: Au1–C1 = 2.123(2); P1–C2 = 1.825(3); P1–C3 = 1.823(3); P1–C4 = 1.852(2); Au1–P1 = 2.2900(7); **1e**: Au1–C1 = 2.115(1); Au1–C20 = 3.1748(2); Au1–C25 = 3.2510(2); Au1–C21 = 3.5023(2); Au–arene (arene ring centroid) = 3.2659(1); Au1–P1 = 2.292(4); **1f**: Au1–C1 = 2.096(4); Au1–C16 = 3.180(4); Au1–C17 = 3.551(4); Au1–C21 = 3.409(4); Au–arene (benzene ring centroid) = 3.449(2); Au1–P1 = 2.301(1). Selected bond angles (°): **1a**: P1–Au1–C1 = 178.97(8); C2–P1–Au1 = 112.8(1); C3–P1–Au1 = 111.95(10); C4–P1–Au1 = 113.14(8); **1e**: P1–Au1–C1 = 179.57(4); C14–P1–Au1 = 117.53(5); **1f**: C1–Au1–P1 = 172.8(1); C10–P1–Au1 = 115.2(1).

Terminal ethyl and phenyl complexes Au(C_2H_5)(PMe_2Ar^{Xyl2}) (**2a**) and Au(C_6H_5)(PMe_2Ar^{Xyl2}) (**3a**) were synthesized to explore the possibility of C–C bond heterocoupling with different hydrocarbyl substituents bound to gold (*vide infra*). These compounds were prepared by a similar procedure to their methyl analogs and characterized by spectroscopic techniques and single-crystal X-ray diffraction (Figures 2.3 and 2.4). The σ Au–C bond distances are 2.085(5) Å (**2a**) and 2.087(7) (**3a**) Å, respectively, similar to neutral Au–CH_3 bond distances discussed above. Complex **2a** co-crystalizes in a 1:1 ratio with a molecule of Au(C_2H_5)(PMe_2Ar^{Mes2}) (**2b**, see Figure S1), whose geometric parameters are comparable to those of **2a**. This is because these crystals were obtained from a phosphine exchange experiment between **2a** and free PMe_2Ar^{Mes2} that was conducted as part of our mechanistic investigations (*vide infra*) (Figure 2.3). The bond distance between C1 and C2 in the Au-ethyl fragment of **2a** is 1.41(2) Å, lying between the carbon-carbon lengths of ethylene (1.34 Å) and ethane (1.54 Å). The electrophilic nature of gold may enhance the C–C bond strength and thus shorten bond length compared to a typical C–C single bond. The structure of complex **3a** is similar to those of compounds **1** and **2a** and does not require further discussion.

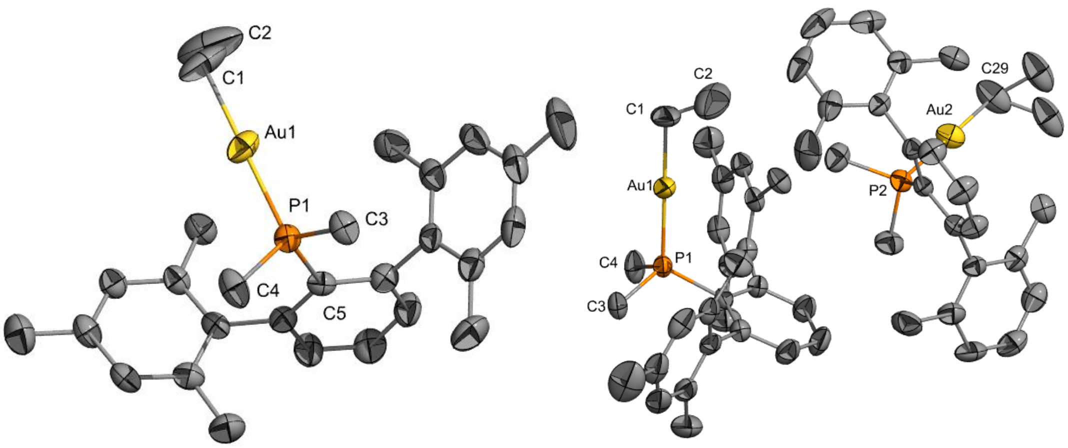

Figure 2.3. ORTEP of Au(C_2H_5)(PMe$_2$Ar^{Mes2}) (**2a**) at 50% probability (one of the two crystallographically distinct structures (Left), the other one being Au(C_2H_5)(PMe$_2$Ar^{Xyl2}). ORTEP structure of co-crystallized [Au(C_2H_5)(PMe$_2$Ar^{Xyl2})] (**2a**), and [Au(C_2H_5)(PMe$_2$Ar^{Mes2})] (**2b**) at 50% probability (Right). Hydrogen atoms on the phosphine ligands are omitted for clarity. Selected bond lengths (Å): Au1–C1 = 2.085(5); C1–C2 = 1.41(2); Selected bond angles (°): C1–Au1–P1 = 178.6(4); Au1–C1–C2 = 113.7(9); C3–P1–Au1 = 112.5(4); C5–P1–Au1 = 115.6(2); C4–P1–Au1 = 111.4(3).

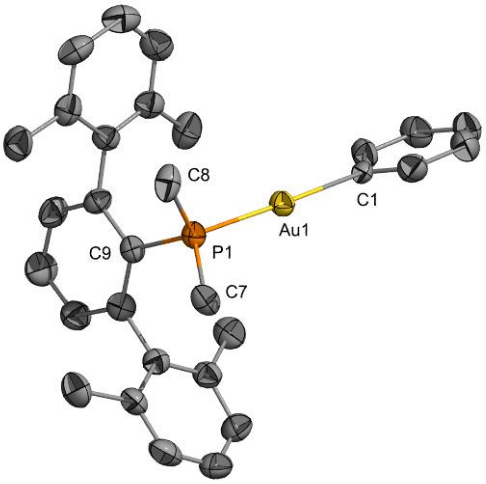

Figure 2.4. ORTEP of Au(C_6H_5)(PMe$_2$Ar^{Xyl2}) (**3a**) at 50% probability. Hydrogen atoms on the phosphine ligands are omitted for clarity. Selected bond lengths(Å): Au1–C1 = 2.087(7); Au1–P1 = 2.302(2); Selected bond angles (°): C1–Au1–P1 = 177.7(2); C8–P1–Au1 = 108.1(4); C7–P1–Au1 = 109.7(4); C9–P1–Au1 = 117.5(2).

2.2.2 Ethane Elimination from [Au(CH_3)(PPh_3)]. For the sake of simplicity and considering the widespread utilization of PPh_3-based gold complexes, we commenced our studies by exploring ethane elimination from Au(CH_3)(PPh_3). This compound is stable at moderate temperatures as heating at 40 °C caused no apparent alteration when monitoring by ^{1}H and ^{31}P{^{1}H} NMR spectroscopy and no ethane formation was detected. However, in the presence of one equivalent of Au(PPh_3)(NTf_2), Au(CH_3)(PPh_3) readily decomposes and ethane immediately evolves at room temperature with complete consumption of Au(CH_3)(PPh_3) by the time of placing the sample in the NMR probe (< 5 min; Scheme 2.3). The release of ethane is accompanied by the clean formation of the homoleptic diphosphine complex [Au(PPh_3)$_2$][NTf_2], along with Au(0), as evinced by the formation of black insoluble material. The nature of this solid was interrogated by transmission electron microscopy (TEM) analysis (Figure 2.5). When a 1:1 molar mixture of Au(PPh_3)(NTf_2) and Au(CH_3)(PPh_3) was dissolved in dichloromethane at -70 °C, ethane formation was detected immediately by ^{1}H NMR spectroscopy (Figure 2.6). Variable temperature ^{1}H and ^{31}P{^{1}H} NMR analysis from -70 °C to 25 ºC revealed the formation of an intermediate species characterized by a broad ^{1}H NMR resonance at 1.6 ppm associated with a ^{31}P{^{1}H} NMR resonance at 37.5 ppm, which we attribute to the corresponding gem-digold methyl species [Au_2(μ-CH_3)(PPh_3)$_2$][NTf_2] (Figure 2.7).[34] However, this compound is only detectable at temperatures below -40 ºC, and it rapidly evolves to the final products above this temperature.

$$\mathrm{Ph_3P{-}Au{-}Me} + \mathrm{Ph_3P{-}Au{-}NTf_2} \xrightarrow[\text{-40ºC}]{\mathrm{CD_2Cl_2}} 1/2\ \mathrm{CH_3CH_3} + [\mathrm{Ph_3P{-}Au{-}PPh_3}][\mathrm{NTf_2}] + \mathrm{Au^0}$$

Scheme 2.3. Ethane elimination from Au(CH_3)(PPh_3) in the presence of 1 equivalent of Au(PPh_3)(NTf_2).

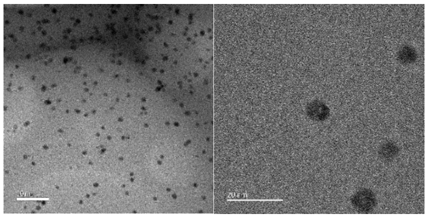

Figure 2.5. Transmission electron microscopy (TEM) analysis of the insoluble Au^0 particles produced during ethane evolution in Scheme 2.3.

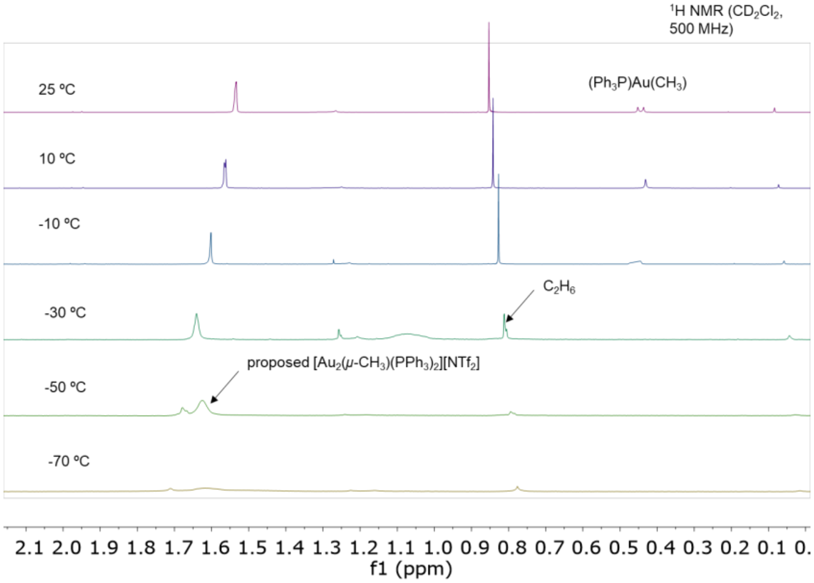

Figure 2.6. Variable temperature ^{1}H NMR monitoring of the reaction between an equimolar mixture of Au(CH_3)(PPh_3) and Au(PPh_3)(NTf_2) to yield [Au(PPh_3)$_2$][NTf_2], Au(0), and C_2H_6.

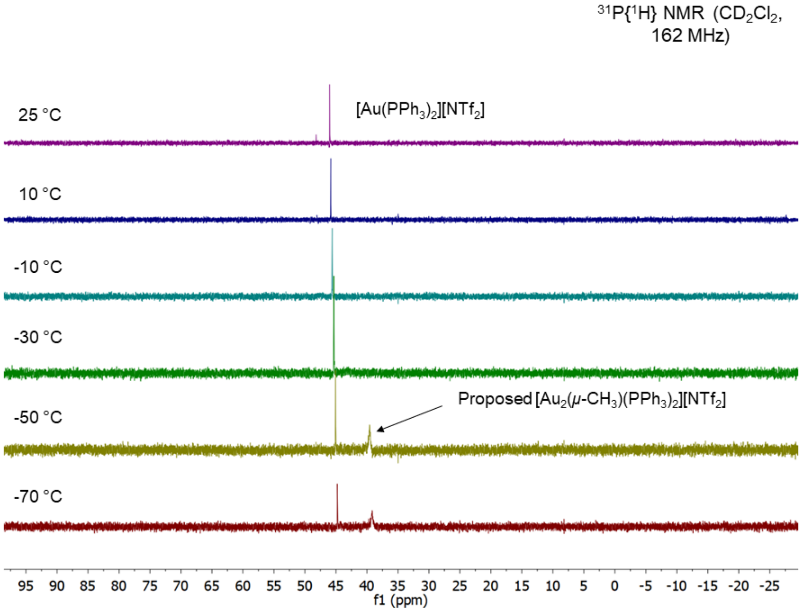

Figure 2.7. Variable temperature ^{31}P NMR monitoring of the reaction between an equimolar mixture of Au(CH_3)(PPh_3) and Au(PPh_3)(NTf_2) to yield [Au(PPh_3)$_2$][NTf_2], Au(0), and C_2H_6.

Though the transient nature of [Au_2(μ-CH_3)(PPh_3)$_2$][NTf_2] prevented us from exploring its role in further detail, our initial kinetic investigations using one equivalent of the related Au(PPh_3)(NO_3) revealed a second-order dependence on neutral Au(CH_3)(PPh_3) for ethane elimination (Figure 2.8). Nonetheless, we could carry out these studies with related methyl complexes based on biaryl and terphenyl phosphines, as discussed in the following sections. Since we observed the formation of gold nanoparticles during ethane elimination, we decided to probe for a possible catalytic role for Au nanoparticles in the C–C coupling reaction, particularly considering their catalytic role in related processes.[40-42] However, using independently prepared gold nanoparticles (*i.e.* Au/TiO_2 and Au/Fe_2O_3) as catalysts did not promote methyl C–C coupling at a comparable rate ($t_{1/2} \approx 1$ day at 25 ºC), ruling out their direct involvement. Besides, we tested for the possibility of a radical-mediated pathway. To do so, we combined equimolar amounts of $Au(CH_3)(PPh_3)$ and $[Au(PPh_3)][NTf_2]$ in the presence of excess toluene (10 equiv.) as a radical probe. Under these conditions, the formation of CH_3• radicals should be quenched by toluene through hydrogen atom abstraction from the benzylic position.[43] This process would have released methane, which was not observed during our experiments, thus favoring the likelihood of a non-radical route.

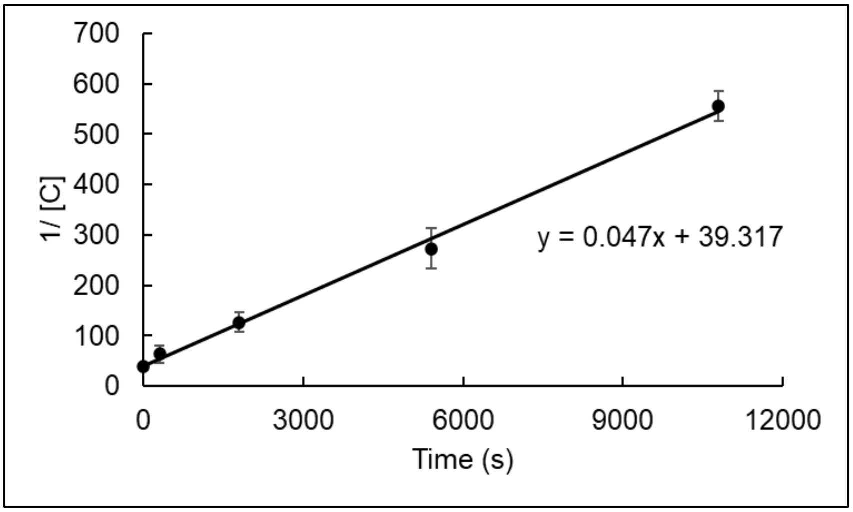

Figure 2.8. Selected second-order kinetic plot for ethane evolution from the equimolar reaction between $Au(CH_3)(PPh_3)$ and $Au(PPh_3)(NO_3)$ in CD_2Cl_2 at 25 ºC.

2.2.3 Synthesis of Cationic gem-Digold Methyl Complexes. To probe if gem-digold methyl complexes are relevant intermediates during C–C coupling reactions, bulky terphenyl, and Buchwald phosphines were used. Campos group and coworkers have recently demonstrated that gem-digold methyl species are kinetically stabilized by large phosphine substituents,[34] which should facilitate kinetic investigations. Indeed, using the bulky terphenyl phosphines enabled the isolation and characterization of various uncommon gem-digold methyl complexes of the type $[Au_2(\mu\text{-}CH_3)(PMe_2Ar')_2][NTf_2]$ (**4a-d**). These were synthesized in high yields by mixing a 1:1 molar ratio of an Au(I) methyl complex $Au(CH_3)(PR_2Ar')$ and the corresponding Au(I) **bis(trifluoromethyl sulfonyl)imide** (Scheme 2.4). Alternatively, the addition of 0.5 equivalents of $[Ph_3C][B(C_6F_5)_4]$ to neutral Au(I) methyl complexes $Au(CH_3)(PR_2Ar')$ lead to the same gem-digold species in comparable yields.

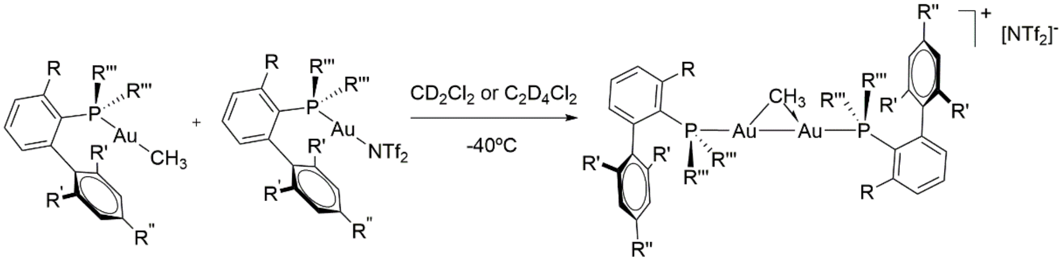

1a - f

4a - f

1,4a, R = Xyl; R' = Me; R" = H; R''' = Me, **1,4d**, R = Trip; R' = iPr; R" = iPr; R''' = Me
1,4b, R = Mes; R' = Me; R" = Me; R''' = Me, **1,4e**, R = H; R' = iPr; R" = iPr; R''' = Cy
1,4c, R = Dipp; R' = iPr; R" = H; R''' = Me, **1,4f**, R = H; R' = iPr; R" = iPr; R''' = tBu

Scheme 2.4. General synthesis of the gem-digold methyl complexes with terphenyl phosphines (**4a−d**) and Buchwald phosphines ligated gem-digold methyl complexes (**4e−f**).

Compounds **4a-d** were characterized by multinuclear NMR spectroscopy and their purity confirmed by microanalysis. Distinctive ^1H NMR signals due to the methyl group that is slightly shifted to higher frequencies (*ca.* 0.5-1.2 ppm) compared to their corresponding neutral precursor (**1a-f**) are consistent with the formation of the gem-digold complexes. The presence of the bridging methyl ligand is further confirmed by $^{13}C\{^1H\}$

NMR resonances shifted to lower frequencies by approximately 5 ppm compared to the parent compounds **1a-f** and characterized by a drastically reduced scalar-coupling to ^{31}P (*ca.* 50 Hz; c.f. ~100 Hz for **1a-f**). The compounds [Au$_2$(μ-CH$_3$)(XPhos)$_2$][NTf$_2$] (**4e**) and [(Au)$_2$(μ-CH$_3$)(^{t}BuXPhos)$_2$][NTf$_2$] (**4f**) were additionally authenticated by single-crystal X-ray diffraction (Figures 2.9; Table 2.1). The gold methyl bond distances in **4e** and **4f** are ~0.1 Å longer than in their corresponding neutral methyl complexes **1e** and **1f**. A characteristic Au-arene interaction is discernible for the two structures. While the structure of **4f** exhibits a slightly shortened Au-arene distance (3.390(3) Å on average) than its neutral complex **1f** (3.449(2) Å), compound **4e** (3.432(2) Å on average) presents a weaker Au-arene interaction than its neutral gold compound **1e** (3.2659(1) Å). The presence of intense aurophilic interactions[44, 45] is evinced by Au···Au distances in complexes **4e** and **4f** of 2.7330 (4) and 2.7765(5) Å, respectively, slightly longer than those reported for the related **4c** (2.7120 (8) Å), and 0.1 Å shorter than the Au–Au distance in metallic gold (2.878 Å).

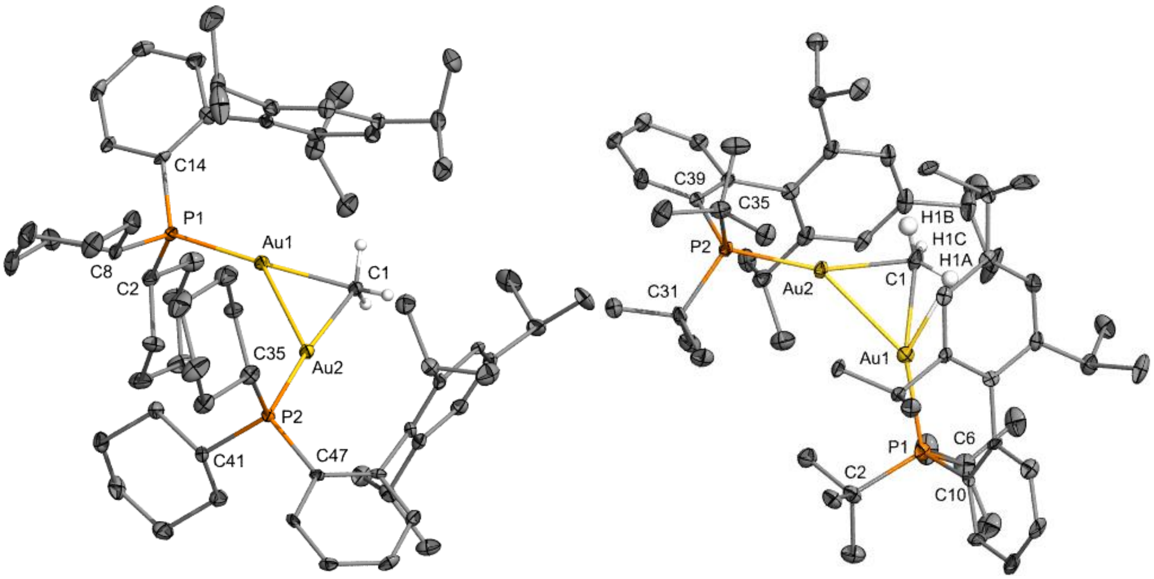

Figure 2.9. ORTEP of [Au$_2$(μ-CH$_3$)(XPhos)$_2$][NTf$_2$] (**4e**) and [(Au)$_2$(μ-CH$_3$)(^{t}BuXPhos)$_2$][NTf$_2$] (**4f**) at 50% probability (for **4e** only one of the three chemically equivalent, but crystallographically distinct structures, is

represented). Hydrogen atoms on the phosphine ligands are omitted for clarity. Selected bond lengths (Å): **4e**: Au1–C1 = 2.221(5); Au2–C1 = 2.235(5); Au1–Au2 = 2.7466 (4); Au1–P1 = 2.2637(1); Au1–P2 = 2.2662(1); **4f**: Au1–C1 = 2.204 (9); Au2–C1 = 2.207 (8); Au1–Au2 = 2.7765 (5); Au1–P1 = 2.285(2); Au1–P2 = 2.279(2). Selected bond angles (°): **4e**: C1–Au1–P1 = 168.41(1); C1–Au2–P2 = 172.39(1); Au1–C1–Au2 = 76.11(2); C1–Au1–Au2 = 52.17(1); C1–Au2–Au1 = 51.72(1); **4f**: C1–Au1–P1 = 162.9(2); C1–Au2–P2 = 160.9(2); Au1–C1–Au2 = 78.0(3); C1–Au1–Au2 = 51.0 (2); C1–Au2–Au1 = 50.9 (2).

Table 2.1. Summary of selected bond distances of the gem-digold methyl complexes.

Gem-digold methyl Complexes	Au–arene (Å)[a]	Au–Au (Å)	Au–*ipso* carbon of arene (Å)	Au–CH_3 (Å)
$[Au_2(\mu\text{-}CH_3)(PMe_2Ar^{Dipp2})_2][BAr_F]$[34] (**4c**)	3.259(3) 3.321(3)	2.7120(8)	3.027(3) 3.102(3)	2.210(5) 2.227(4)
$[Au_2(\mu\text{-}CH_3)(XPhos)_2][NTf_2]$ (**4e**)[b]	3.400(2) 3.465(2)	2.7330(4)	3.093(5) 3.185(5)	2.215(5) 2.238(5)
$[(Au)_2(\mu\text{-}CH_3)(^tBuXPhos)_2][NTf_2]$ (**4f**)	3.366(3) 3.413(3)	2.7765 (5)	3.082(8) 3.406(8)	2.207(8) 2.204(9)

[a] Distance from Au to the centroid of the arene rings; [b]Average over three independent molecules present in the asymmetric unit.

2.2.4 Ethane Elimination from Gem-Digold Methyl Complexes. As anticipated, the stability of gem-digold methyl complexes largely depends on the steric shielding provided by the phosphine ligand. Thus, compound $[Au_2(\mu\text{-}CH_3)(PMe_2Ar^{Xyl2})_2][NTf_2]$ (**4a**) is only stable in dichloromethane solution at -30 °C or below. Above -20 ºC **4a** cleanly converts into $[Au(PMe_2Ar^{Xyl})_2][NTf_2]$ (**5a**), metallic gold(0) and ethane (Scheme 2.5). Complex $[Au_2(\mu\text{-}CH_3)(PMe_2Ar^{Mes2})_2][NTf_2]$ (**4b**) reacted similarly, whereas bulkier phosphines provide enhance stability. As such, compounds $[Au_2(\mu\text{-}CH_3)(PMe_2Ar^{Dipp2})_2][NTf_2]$ (**4c**) and $[Au_2(\mu\text{-}CH_3)(PMe_2Ar^{Trip2})_2][NTf_2]$ (**4d**), in which the methyl substituents in the lateral aryl rings of the terphenyl moiety have been substituted by *iso*propyl groups are fairly stable at room temperature, while complexes **4e** and **4f** remain unaltered for hours even at temperatures up to 80 °C. Thus, the investigated Buchwald phosphines confer enhanced stability to gem-digold methyl species compared to terphenyl-based ligands, most likely as a result of the increased steric shielding provided by the cyclohexyl and *tert*-butyl groups directly bound to the phosphorus center close to the gold nuclei.

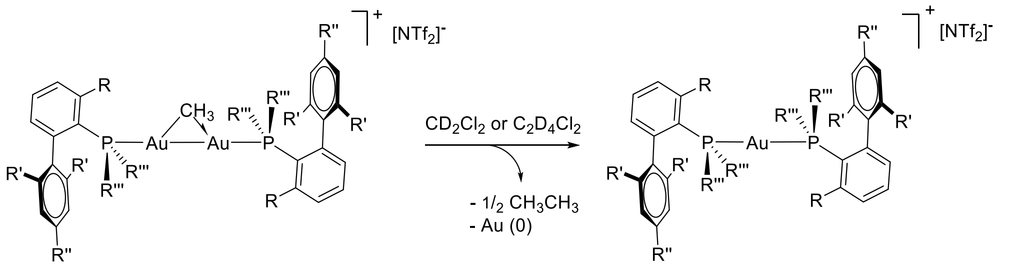

4a - e **5a - e**

4,5a, R = Xyl; R' = Me; R'' = H; R''' = Me, **4,5d**, R = Trip; R' = iPr; R'' = iPr; R''' = Me
4,5b, R = Mes; R' = Me; R'' = Me; R''' = Me, **4,5e**, R = H; R' = iPr; R'' = iPr; R''' = Cy
4,5c, R = Dipp; R' = iPr; R'' = H; R''' = Me, **4,5f**, R = H; R' = iPr; R'' = iPr; R''' = tBu

Scheme 2.5. Thermal decomposition of terphenyl and biaryl phosphine methyl-bridged digold complexes (**4a−e**) to gold bisphosphine (**5a−e**).

Overall, these observations indicate that kinetic analysis by ^{1}H and ^{31}P{^{1}H} NMR spectroscopy monitoring is facilitated by larger phosphine ligands compared to PPh$_3$. For instance, heating complex **4e** in dichloroethane at 90 °C enabled us to monitor by NMR spectroscopy its evolution to [Au(XPhos)$_2$][NTf$_2$] (**5e**) with concomitant release of ethane and formation of Au(0) (Figure 2.10). The thermolysis of **4e** follows a second-order dependence on the digold complex with k_{obs} = 5.2(1) x 10^{-4} M^{-1}s^{-1} at 90 °C (Table 2.2), as previously observed for the PPh$_3$-based system. In the case of the more hindered compound **4f** this reaction does not take place at 100 °C, and intractable digold decomposition occurs at temperatures above 100 °C where the formation of methane, instead of ethane, was observed (Figure 2.11). This finding indicates that the C–C coupling is likely not viable in the most sterically constrained digold system studied herein. This seems to be consistent with a second-order dependence on digold complex concentration during ethane formation, which might imply the need for more than two gold nuclei in close proximity along the reaction coordinate (see below for additional discussion).

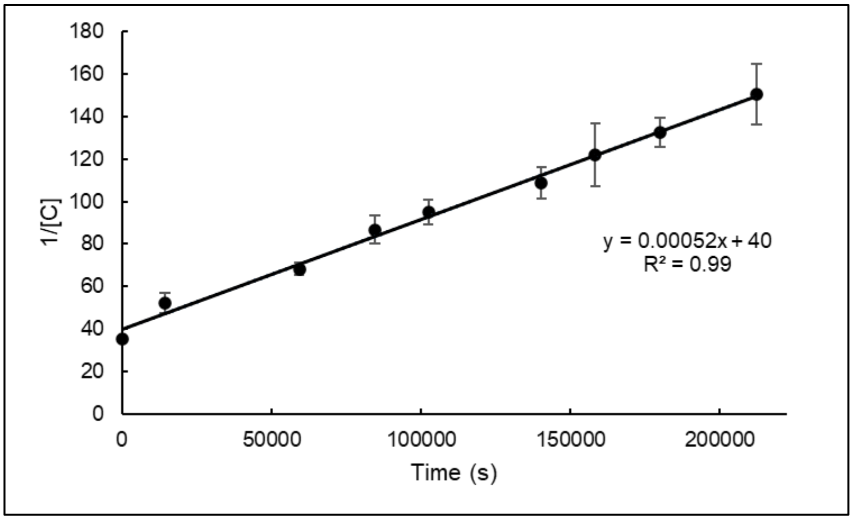

Figure 2.10. Selected representative second-order kinetic plot for ethane evolution from [Au_2(μ-CH_3)(XPhos)$_2$][NTf_2] (**4e**) in CD_2ClCD_2Cl at 90ºC.

Table 2.2. Summary of kinetic data for ethane elimination from gem-digold complexes **4a-e**.

Compound	**T (ºC)**	***k* ($M^{-1}\cdot s^{-1}$)**	**Δ*G*‡ (kcal/mol)**
[Au_2(μ-CH_3)(PMe_2Ar^{Xyl2})$_2$][NTf_2] **(4a)**	0	9.8(3) x 10^{-2}	17.2(1)
[Au_2(μ-CH_3)(PMe_2Ar^{Mes2})$_2$][NTf_2] **(4b)**	0	4.9(1) x 10^{-2}	17.6(1)
[Au_2(μ-CH_3)(PMe_2Ar^{Dipp2})$_2$][NTf_2] **(4c)**	50	4.8(3) x 10^{-3}	22.4(5)
[Au_2(μ-CH_3)(PMe_2Ar^{Tipp2})$_2$][NTf_2] **(4d)**	50	2.0(1) x 10^{-3}	22.9(4)
[Au_2(μ-CH_3)(XPhos)$_2$][NTf_2] **(4e)**	90	5.2(1) x 10^{-4}	26.4(3)
[Au_2(μ-CH_3)(^{t}BuXPhos)$_2$][NTf_2] **(4f)**	100*	N.A.	N.A.
*methane formation is observed instead; N.A. (not available)			

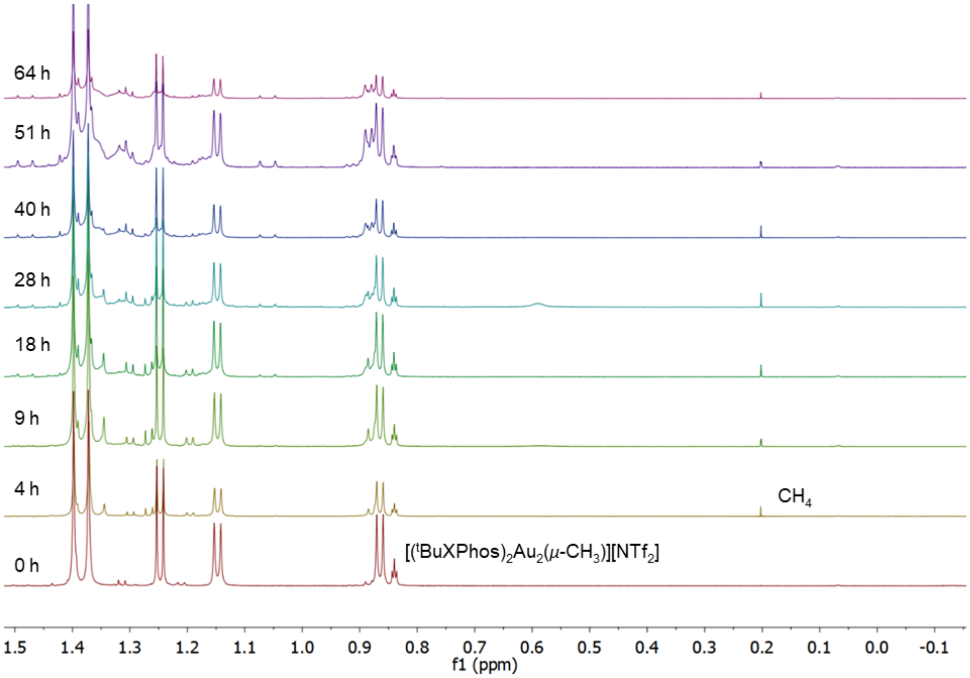

Figure 2.11. ^{1}H NMR monitoring of the thermolysis of compound **4f** at 90 ºC in $C_2D_4Cl_2$.

Similar to complex **4e**, ethane elimination from terphenyl ligated gem-digold methyl complexes follow a second-order dependence on **4a-d** (Figure 2.12a), which implicates that the rate-limiting step for the overall processes requires the participation of two gem-digold fragments. As introduced above, in bimetallic Au complexes bearing the less bulky PMe_2Ar^{Xyl2} and PMe_2Ar^{Mes2} phosphines, the evolution of ethane occurs rapidly in dichlormethane solutions at 25 ºC, while those constructed around the more congested PMe_2Ar^{Dipp2} and PMe_2Ar^{Tripp2} counterparts remain stable under the same conditions for several days. Kinetic studies provide rates for ethane elimination from the sterically hindered **4c** and **4d** of k_{obs} = 4.8(3) x 10^{-3} and 2.0(1) x 10^{-2} $M^{-1}s^{-1}$ at 50 °C, respectively. In contrast, the rates of ethane elimination from **4a** and **4b** had to be analyzed at lower temperatures (0 ºC), resulting in rates of k_{obs} = 9.8(3) x 10^{-2} and 4.9(1) x 10^{-1} $M^{-1}s^{-1}$ at 0 °C, respectively. The corresponding half-life ($t_{1/2}$) values associated with these kinetic parameters at the working temperatures are approximately 260 (**4a**, 0 ºC), 800 (**4b**, 0 ºC) 5,600 (**4c**, 50 ºC) and 13,000 (**4d**, 50 ºC) seconds.

Table 2.2 collects the corresponding activation barriers for C–C coupling from the methyl-bridged complexes **4a-e**, which range from 17.2 kcal/mol at 0 ºC for **4a** to 26.4 kcal/mol at 90 ºC for **4e**. To complete these studies, we monitored the evolution of ethane from the gem-digold complex **4a** in the temperature interval from -20 to 10 ºC (Table 2.3). An Eyring analysis provided activation parameters of $\Delta H^{\ddagger} = 20.5 \pm 1.3$ kcal/mol and $\Delta S^{\ddagger} = 11.9 \pm 4.8$ e.u. (Figure 2.12b), which correspond to $\Delta G_{298}^{\ddagger} = 16.9 \pm 2.7$ kcal/mol. We ascribe the relatively high and positive value of the entropic parameter to the formation of ethane gas in the rate-limiting step, as further discussed below.

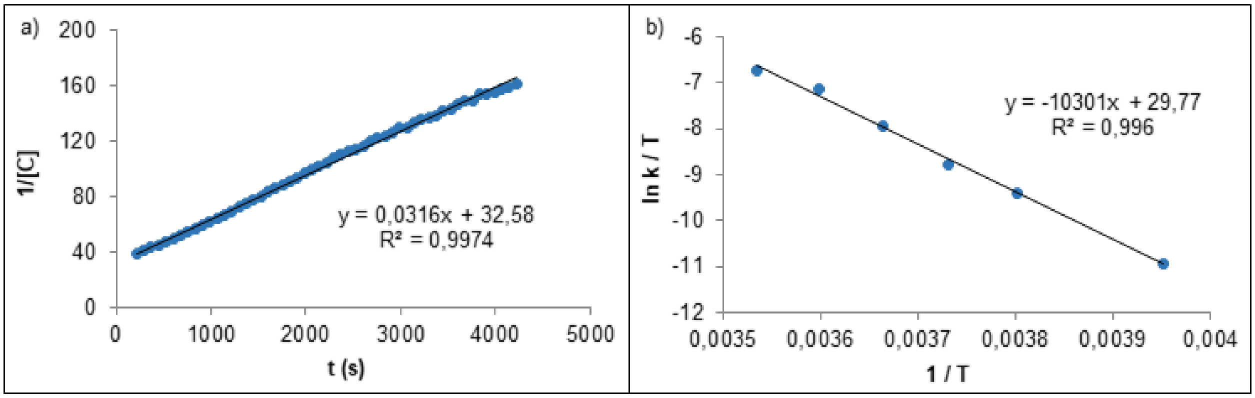

Figure 2.12. (a) Second-order kinetic representation for the consumption of **4a** at -5 ºC in CD_2Cl_2; (b) Eyring plot for ethane formation from gem-digold methyl $[Au_2(\mu\text{-}CH_3)(PMe_2Ar^{Xyl2})_2][NTf_2]$ (**4a**).

Table 2.3. Summary of kinetic data for C-C bond formation from compounds **4a** at various temperatures.

Compound	T (ºC)	k ($M^{-1}\cdot s^{1}$)	ΔG‡ (kcal mol^{-1})
$[Au_2(\mu\text{-}CH_3)(PMe_2Ar^{Xyl2})_2][NTf_2]$ (**4a**)	10	2.9(4) x 10^{-1}	17.2(8)
$[Au_2(\mu\text{-}CH_3)(PMe_2Ar^{Xyl2})_2][NTf_2]$ (**4a**)	5	2.2(9) x 10^{-1}	17.1(1)
$[Au_2(\mu\text{-}CH_3)(PMe_2Ar^{Xyl2})_2][NTf_2]$ (**4a**)	0	9.8(4) x 10^{-2}	17.2(1)
$[Au_2(\mu\text{-}CH_3)(PMe_2Ar^{Xyl2})_2][NTf_2]$ (**4a**)	-5	4.2(1) x 10^{-2}	17.3(2)
$[Au_2(\mu\text{-}CH_3)(PMe_2Ar^{Xyl2})_2][NTf_2]$ (**4a**)	-10	2.2(5) x 10^{-2}	17.3(2)
$[Au_2(\mu\text{-}CH_3)(PMe_2Ar^{Xyl2})_2][NTf_2]$ (**4a**)	-20	4.8(1) x 10^{-4}	17.4(1)

To have a deeper insight on the nature of the Au species involved in C–C coupling processes, we first considered whether dissociation of complexes **4** into their monometallic components,[46] namely neutral methyl compounds **1** and triflimide species of type $Au(PR_2Ar')(NTf_2)$, might be relevant. To check the viability of such equilibrium, we decided to explore the exchange processes of the methyl bridge in compound **4a**. In a first experiment, we examined the exchange between **1a** and **4a** at variable temperature. For experimental convenience, we accessed an equimolar mixture of both species by adding 0.33 equiv. of $[Ph_3C][B(C_6F_5)_4]$ to **1a** at -40 ºC. Under these conditions, one-third of the neutral methyl compound is transformed by methyl abstraction into a cationic gold species that is immediately trapped by unreacted **1a** to provide gem-digold **4a**. Variable temperature ^1H and $^{31}P\{^1H\}$ NMR spectroscopy analysis revealed dynamic behavior in solution (Figure 2.13) that we attribute to the exchange equilibrium depicted in Scheme 6a. It was possible to identify **4a** by a $^{31}P\{^1H\}$ NMR resonance at 0.1 ppm recorded at -85 ºC, whereas a broad signal at 21.1 ppm was assigned to **1a**. These signals coalesce at approximately -50 ºC, while the major component when reaching 25 ºC is the homoleptic bisphosphine compound **5a** that accompanies ethane formation. We further investigated this dynamic behavior by DFT methods (see computational sections for details). Calculations indicate that dissociation of the dinuclear species $[Au_2(\mu\text{-}CH_3)(PMe_2Ar^{Xyl2})_2][NTf_2]$ (**4a**) into the corresponding fragments, $Au(CH_3)(PMe_2Ar^{Xyl2})$ (**1a**) and $Au(PMe_2Ar^{Xyl2})(NTf_2)$, is only slightly endergonic ($\Delta G = +0.5$ kcal/mol), in agreement with our experimental results. The kinetic profile of ethane evolution in these equimolar mixtures is identical, within the experimental error, to that of pure **4a**. This suggests that, even if carbon-carbon coupling takes place from a trimetallic species involving the participation of compounds **1**, the required dissociation of gem-digold methyl compounds **4** into compounds **1** and $[Au(PR_2Ar')]^+$ is not likely kinetically relevant.

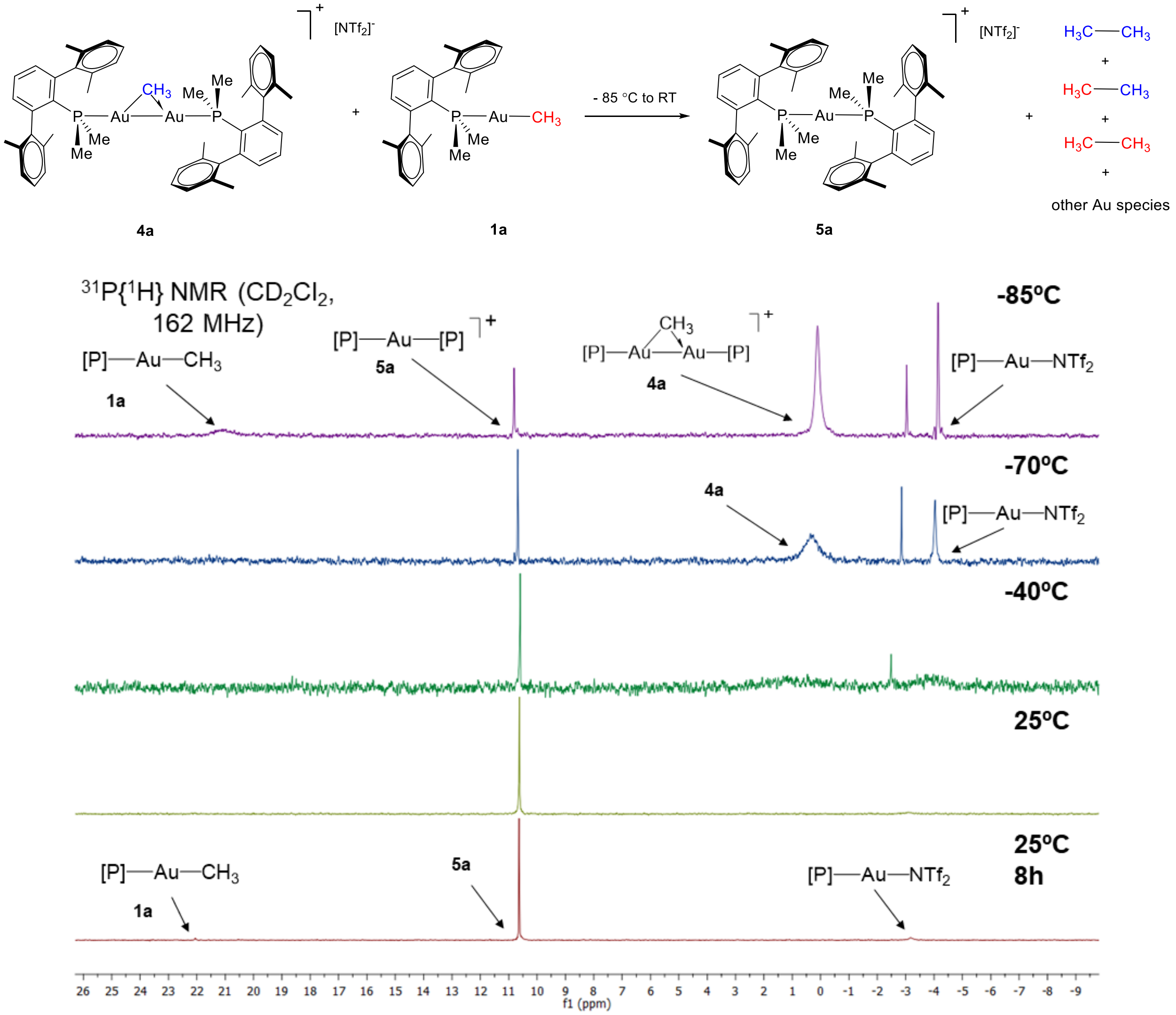

Figure 2.13. Variable temperature $^{31}P\{^1H\}$ NMR monitoring of the reaction between $Au(CH_3)(PMe_2Ar^{Xyl2})$ (**1a**) (0.012 mmol) and $[Au_2(\mu\text{-}CH_3)(PMe_2Ar^{Xyl2})_2][NTf_2]$ (**4a**) (0.012 mmol) in CD_2Cl_2 evidencing rapid dynamic exchange (coalescence at around -40 ºC).

Substituting methyl compound **1a** by its related ethyl (**2a**) and phenyl (**3a**) derivatives evinced the formation of cross-coupling products (Schemes 2.6b and 2.6c). In the case of **2a** the formation of propane and butane was apparent by ^1H NMR spectroscopy, while in the reaction between **4a** and **3a** the formation of ethane, biphenyl and toluene was detected in comparable amounts. GC-MS analysis of solution and gas headspace provided further evidence for cross-coupling, since variable amounts of ethane, propane, and butane were measured from the reaction between **2a** and **4a** (Figure 2.14). In both cases, the main homogeneous gold-containing species when reaching room temperature is **5a**.

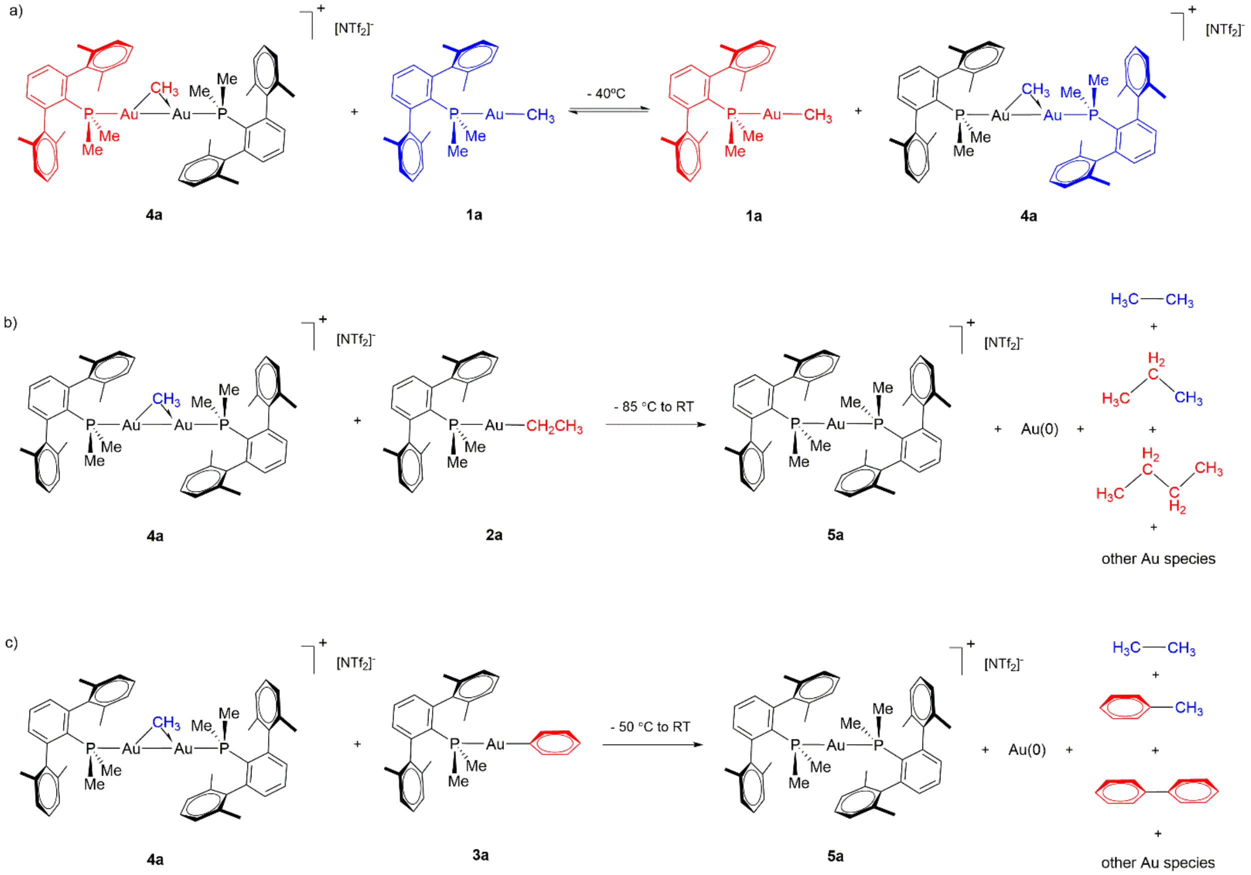

Scheme 2.6. (a) Dynamic Me/Me exchange equilibrium between $[Au_2(\mu\text{-}CH_3)(PMe_2Ar^{Xyl2})_2][NTf_2]$ (**4a**) and $Au(CH_3)(PMe_2Ar^{Xyl2})$ (**1a**) species at -40ºC; (b) C-C coupling and product distribution in the reaction between $Au(C_2H_5)(PMe_2Ar^{Xyl2})$ (**2a**) and $[Au_2(\mu\text{-}CH_3)(PMe_2Ar^{Xyl2})_2][NTf_2]$ (**4a**); (c) C-C coupling and product distribution in the reaction between $Au(C_6H_5)(PMe_2Ar^{Xyl2})$ (**3a**) and $[Au_2(\mu\text{-}CH_3)(PMe_2Ar^{Xyl2})_2][NTf_2]$ (**4a**).

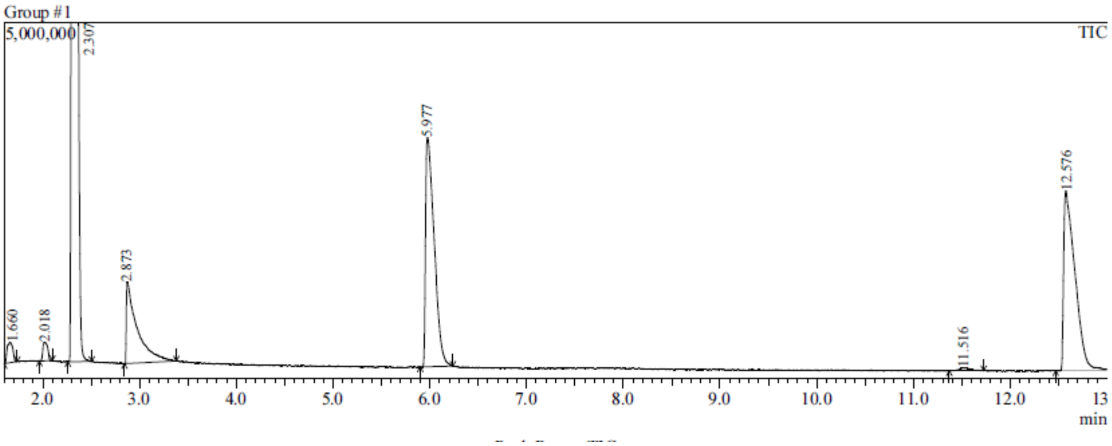

Peak Report TIC

Peak#	R.Time	Area	Area%	Mark	Name
1	1.660	1134110	0.96	MI	Carbon dioxide (CAS) Dry ice
2	2.018	904971	0.76	MI	Ethene (CAS) Ethylene
3	2.307	66970637	56.50	MI	Ethane (CAS) Bimethyl
4	2.873	8837406	7.46	MI	Water (CAS) Ice
5	5.977	19856765	16.75	MI	Propane (CAS) R 290
6	11.516	348395	0.29	MI	Propane, 2-methyl- (CAS) Isobutane
7	12.576	20474715	17.27	MI	Butane (CAS) n-Butane
		118526999	100.00		

Figure 2.14. GC-MS spectra and analysis of the reaction described in Scheme 6b and Figure 8 between [Au_2(μ-CH_3)(PMe_2Ar^{Xyl2})$_2$] (**4a**) (0.012 mmol) and [Au(C_2H_5)(PMe_2Ar^{Xyl2})] (**2a**) (0.012 mmol) after 3 hours at 25 ^oC.

To gather more information on the exchange between bridging and terminal hydrocarbyl substituents present in gem-digold and neutral compounds, respectively, we examined spectroscopically the reaction depicted in Scheme 2.6b at variable temperature (Figure 2.15). A solid mixture of **2a** and **4a** in equimolar amounts was dissolved in CD_2Cl_2 at -40 ^oC to allow the exchange to take place and then cooled down to -85 ^oC. At the latter temperature, the exchange process is halted, and a variety of gold-containing products are identified by $^{31}P\{^1H\}$ NMR. These include the neutral hydrocarbyl compounds **1a** and **2a** and their corresponding gem-digold species **4a** and [Au_2(μ-CH_2CH_3)(PMe_2Ar^{Xyl2})$_2$] (**6a**), whose broad resonances were recorded at 21.2, 21.9, 0.1, and 1.4 ppm, respectively. Besides, sharp signals due to Au(PMe_2Ar^{Xyl2})(NTf_2) and [Au(PMe_2Ar^{Xyl2})$_2$][NTf_2] (**5a**) at -

4.2 and 10.8 ppm, respectively, were identified. The latter likely results from local solution warm-up during sample handling. Increasing the temperature to -40 ºC results in the coalescence of all prior resonances except for that of **5a**, which is not involved in the exchange process. Further raising the temperature to 25 ºC leads to full consumption of gold precursors and quantitative formation of bisphosphine compound **5a** along with the appearance of solid Au(0). Similarly, a rapid exchange between **4a** and **3a** is evinced by the immediate conversion of an equimolar mixture of those compounds into **1a** and [$Au_2(\mu\text{-}C_6H_5)(PMe_2Ar^{Xyl2})_2$] **7a** (Figure 2.16).

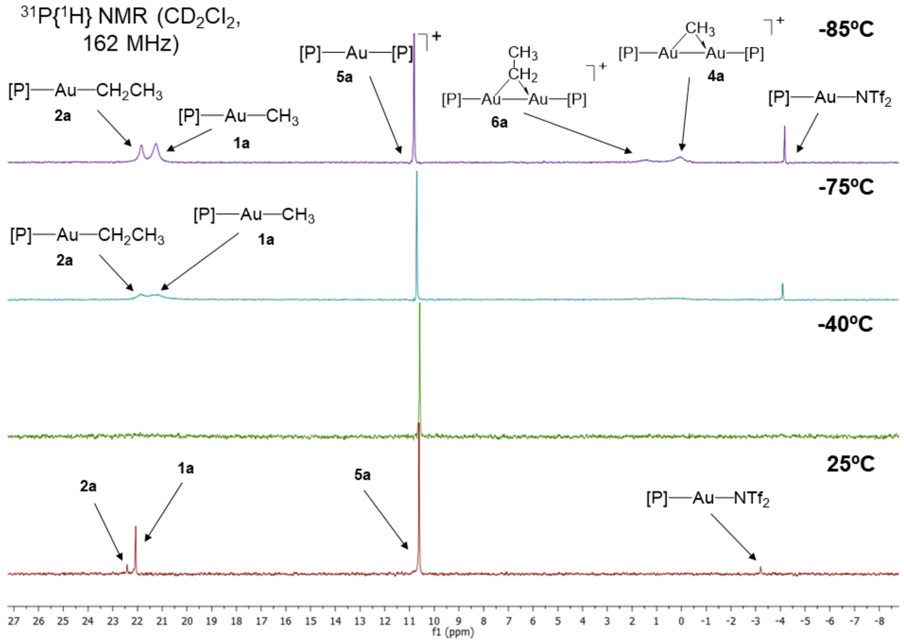

Figure 2.15. Variable temperature of exchange processes between $Au(C_2H_5)(PMe_2Ar^{Xyl2})$ (**2a**) and [$Au_2(\mu\text{-}CH_3)(PMe_2Ar^{Xyl2})_2$][$NTf_2$] (**4a**) monitored by $^{31}P\{^1H\}$ NMR spectroscopy.

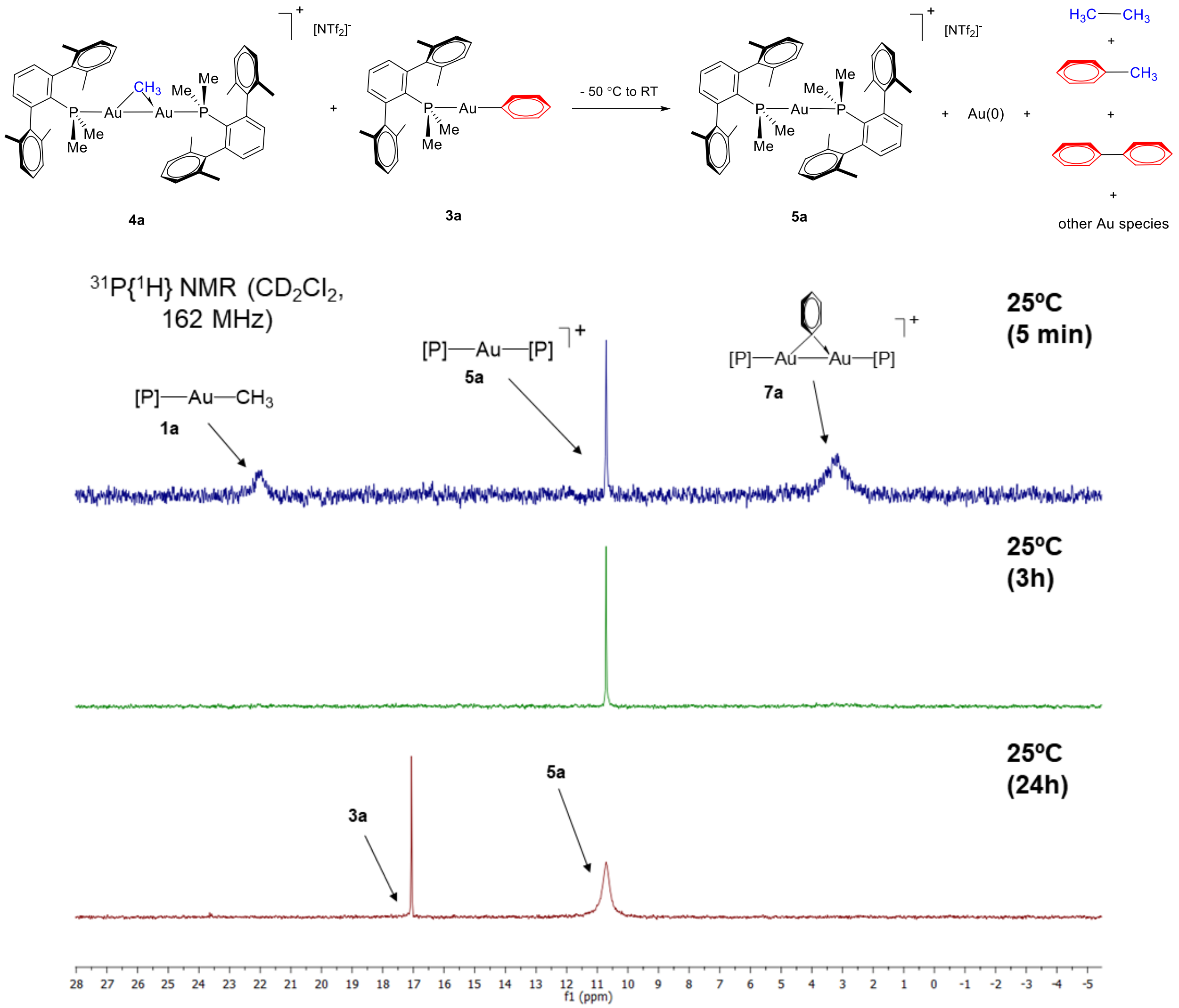

Figure 2.16. $^{31}P\{^1H\}$ NMR monitoring of the reaction between $[Au_2(\mu\text{-}CH_3)(PMe_2Ar^{Xyl2})_2][NTf_2]$ (**4a**) (0.012 mmol) and $Au(C_6H_5)(PMe_2Ar^{Xyl2})$ (**3a**) (0.012 mmol) in CD_2Cl_2 at 25 ºC.

Having in mind that the above dynamic behavior reveals the presence in solution of compounds **1**, **4,** and $Au(PR_2Ar')(NTf_2)$, and also because ethane evolution follows a second-order dependence on bridging methyl complexes **4**, we considered three possible routes (Scheme 2.7). In the first, reductive coupling from two neutral gold methyl compounds of type **1** may take place, similar to prior work by Kochi and coworkers (Scheme 2.7a).[24, 25] However, it is important to highlight two distinctive features of our studies that contrast with those prior reports. First, reductive coupling from Au(CH_3)(PPh_3) only occurred at high temperatures (~100 ºC), while C—C bond formation from bridging digold complexes **4** is more facile. The C–C coupling reaction readily proceeds at temperatures as low as -60 ºC in the case of the PPh_3-based system (Figures 2.6 and 2.7). Secondly, whereas the first-order dependence on gold was demonstrated for reductive coupling from Au(CH_3)(PPh_3),[24, 25] with phosphine dissociation towards 'AuMe' as the rate-determining step, we have determined a second-order dependence on digold compounds **4** during ethane evolution. These observations suggest different operating mechanisms in the two cases, a notion that is further supported by DFT methods based on the PMe_2Ar^{Xyl2} system. In agreement with Kochi's findings, the computed reaction free energy for phosphine dissociation at **1a** is +32.1 kcal/mol, much higher than experimentally determined for the overall process ($\Delta G^‡ = 16.9 \pm 2.7$ kcal/mol). Phosphine dissociation from **4a** to yield [Au_2(μ-CH_3)(PMe_2Ar^{Xyl2})][NTf_2], where the metal-metal and metal-arene interactions could stabilize the unsaturated gold center, presented nonetheless a similarly high value (+31.1 kcal/mol; Figure 2.17). As anticipated, these data confirm a dissimilar C-C coupling mechanism for compounds **4** compared to that exhibited by monometallic gold-alkyl species.

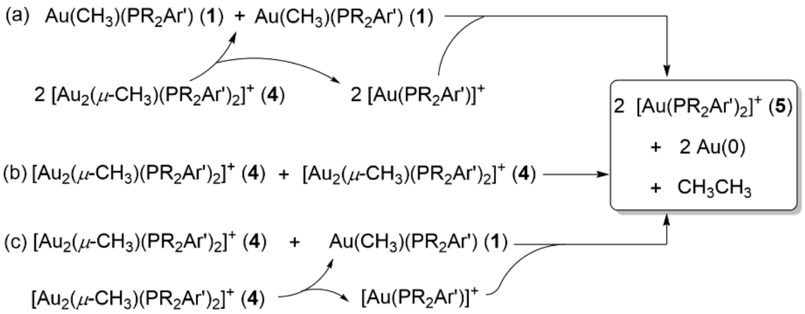

Scheme 2.7. Potential routes for ethane evolution with regards to the gold coupling partners.

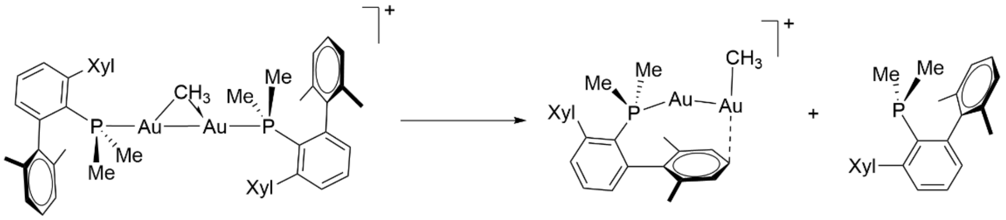

Figure 2.17. Phosphine dissociation from [$Au_2(\mu\text{-}CH_3)(PMe_2Ar^{Xyl2})_2$][$NTf_2$] (**4a**) is calculated to occur with ΔG = +31.1 kcal/mol.

An alternative route consists of two gem-digold methyl fragments **4** approaching to facilitate the C–C coupling event (Scheme 2.7b). Instead, a third pathway to consider given the Coulombic repulsion derived from approximating two cationic species in route (b) is the reaction between **4** and its corresponding neutral methyl species **1** formed by dissociation of the second molecule of **4** into their monometallic fragments (Scheme 2.7c). First, we explored computationally the direct coupling of methyl groups between two molecules of **4a** {route (a)} as well as between **4a** and **1a** {route (b)} by relaxed potential energy scans. These studies indicate that those pathways are unfeasible, both in the singlet and triplet state (see Supporting Information for details). We also evaluated the possibility of accessing the hypothetical Au(III) species [$Au(CH_3)_2(PMe_2Ar^{Xyl2})$][$NTf_2$] from the above routes, since the reductive coupling of ethane with such a complex should be accessible.[12, 22, 23] In fact, we found a feasible barrier (+16.1 kcal/mol) for ethane formation from the latter Au(III) complex [$Au(CH_3)_2(PMe_2Ar^{Xyl2})$][$NTf_2$]. However, [$Au(CH_3)_2(PMe_2Ar^{Xyl2})$][$NTf_2$] would be formed alongside the digold(0) species [$Au_2(PMe_2Ar^{Xyl2})_2$], which was calculated to be 42.1 kcal/mol higher in energy than its precursors, rendering this pathway inaccessible under the reaction conditions (Figure 2.18). Similarly, CH_3^+ transfer[29] from **4a** to **1a** presents a computed transition state of +47.0 kcal/mol (**TS1** in Figure 2.19). Besides, we examined reductive coupling from the hypothetical trinuclear species derived from the above CH_3^+ transfer, though a transition state at +33.6 kcal/mol was estimated (**TS2** in Figure 2.19), further suggesting such a pathway to be unaffordable.

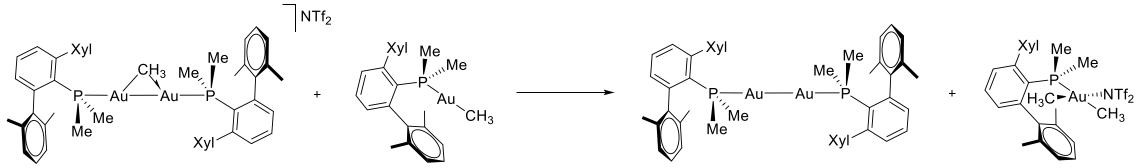

Figure 2.18. Computationally estimated formation of $[Au_2(PMe_2Ar^{Xyl2})_2]$ and $Au(CH_3)_2(PMe_2Ar^{Xyl2})(NTf_2)$ from complexes **4a** and **1a**; ΔG = +42.1 kcal/mol.

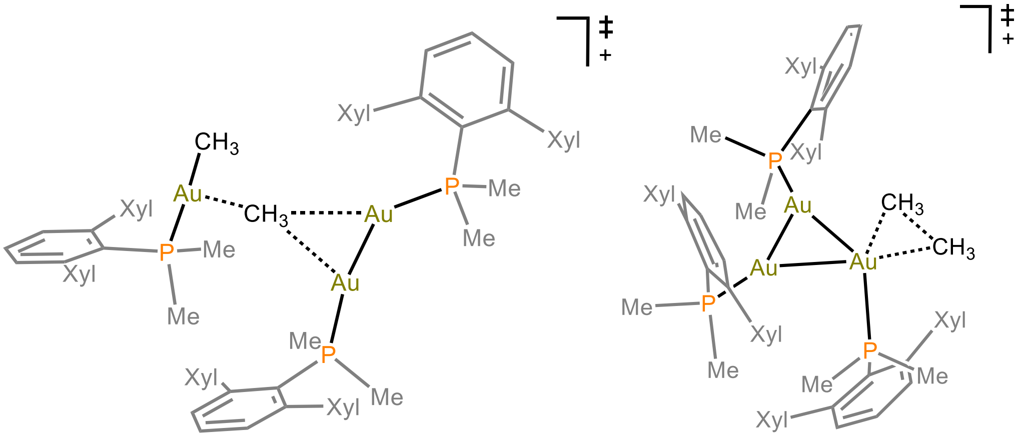

Figure 2.19. High energy CH_3^+ transfer (left, **TS1**; ΔG‡ = 47.0 kcal/mol) and C-C coupling (right, **TS2;** ΔG‡ = 33.6 kcal/mol) transition states.

Having ruled out the most direct mechanisms involving **1a** and **4a**, we decided to interrogate the participation of compounds $Au(PR_2Ar')(NTf_2)$, especially in consideration of the experimental results indicating that such complexes are accessible under reaction conditions (see above). These compounds serve as a source of highly electrophilic $[Au(PR_2Ar')]^+$ fragments[47, 48] and, as such, they might facilitate phosphine dissociation from other Au complexes. Phosphine dissociation is also confirmed from straightforward ligand exchange experiments (Figure 2.20) and since it was proposed as the rate-limiting step in earlier Kochi's system,[24, 25] it is conceivable that it could also play a role for C–C coupling from compounds **4**. To examine this, we monitored ethane evolution from **4a** in the presence of 3 equiv. of Au(PMe$_2$Ar^{Xyl2})(NTf$_2$), though this excess of gold-triflimide did not have notable effects on the rate of ethane formation. Nonetheless, even if Au(PMe$_2$Ar^{Xyl2})(NTf$_2$) is required to facilitate phosphine dissociation, its presence may also affect the observed rate of ethane evolution contrarily by reducing the concentration of Au(CH$_3$)(PMe$_2$Ar^{Xyl2}) (**1a**) in solution, the latter species also required for C–C coupling. This is because [Au$_2$(μ-CH$_3$)(PMe$_2$Ar^{Xyl2})$_2$][NTf$_2$] (**4a**) is in dynamic equilibrium in solution with **1a** and Au(PMe$_2$Ar^{Xyl2})(NTf$_2$), as discussed above. To circumvent the influence of added Au(PMe$_2$Ar^{Xyl2})(NTf$_2$) on that equilibrium, we investigated the effect of adding five equivalents of BPh$_3$ as an alternative and less disruptive Lewis acid that could facilitate phosphine dissociation. While ethane evolution proceeded at a rate ($t_{1/2}$ = 340 s) comparable to that of pure **4a** ($t_{1/2}$ = 260 s), we did observe a distinctive change in the kinetic profile. More precisely, this experiment revealed a first-order kinetic dependence on **4a** (Figure 2.21), in stark contrast to the second-order profile observed when the consumption of the latter was monitored in pure form.

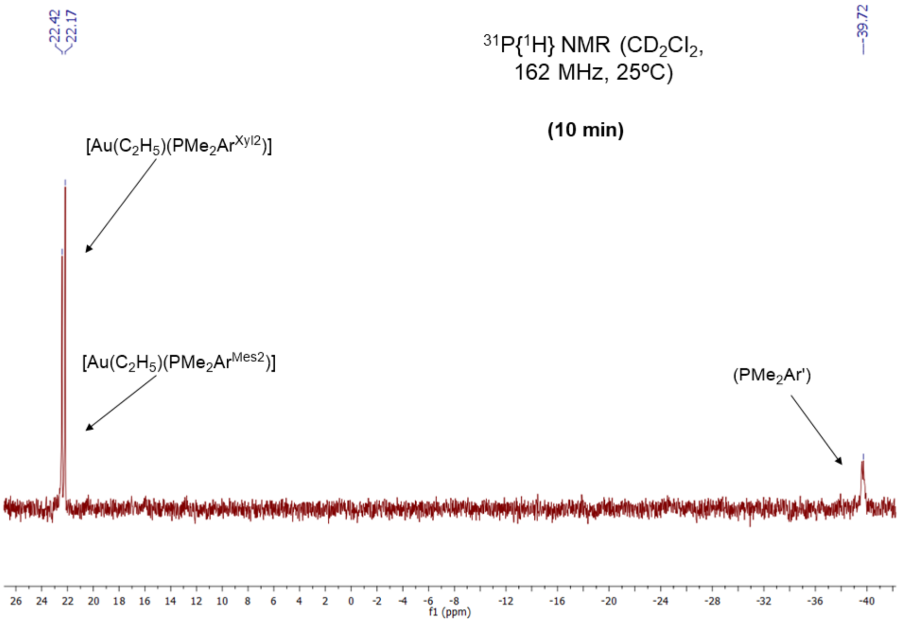

Figure 2.20. $^{31}P\{^1H\}$ NMR spectrum resulting from the exchange reaction between $Au(C_2H_5)(PMe_2Ar^{Xyl2})$ (**2a**) (0.0175 mmol) and PMe_2Ar^{Mes2} (0.0175 mmol) in CD_2Cl_2 at 25 ºC after 10 minutes.

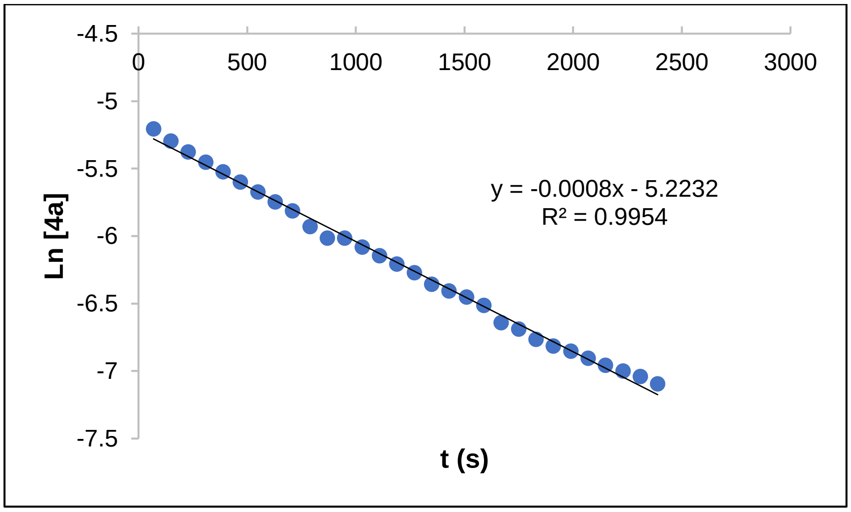

Figure 2.21. One of the representative pseudo-first-order kinetic experiments performed with $[Au_2(\mu\text{-}CH_3)(PMe_2Ar^{Xyl2})_2][NTf_2]$ (**4a**) at -10 ºC with 5 equivalents of BPh_3.

Next, we directed our efforts to examine, by computational means, the role of $Au(PMe_2Ar^{Xyl2})(NTf_2)$ on the pathways and energetics for the formation of ethane (Figure 22). For convenience and since we attribute a Lewis acidic role to this fragment, as supported by our experiments with BPh_3, we first studied BH_3 as a model Lewis acid.

Thus, we examined the reaction between BH_3 and complex $Au(CH_3)(PMe_2Ar^{Xyl2})$ (**1a**). The formation of an Au–BH_3 adduct is slightly exergonic (ΔG = −0.9 kcal/mol), from which the transition state for the formation of a P–B bond (**TS3**) lies at +16.2 kcal/mol above the independently computed **1a** and BH_3, giving the product at −7.4 kcal/mol (Figure 2.22). Encouraged by this result, we studied the analogous process with cation $[Au(PMe_2Ar^{Xyl2})]^+$ instead of BH_3 as the Lewis acid.[49] A transition state for that process (**TS4**) was found at +29.3 kcal/mol, leading to the formation of a species of formula $[(PMe_2Ar^{Xyl2})AuAu(CH_3)]^+$, **A** in Figure 11, that lies at +18.5 kcal/mol and represents a form of masked 'AuMe' stabilized by a $[Au(PMe_2Ar^{Xyl2})_2]^+$ fragment. Nonetheless, the large barrier renders this process inaccessible from **4a**, in agreement with the experimentally determined second-order dependence on its concentration.

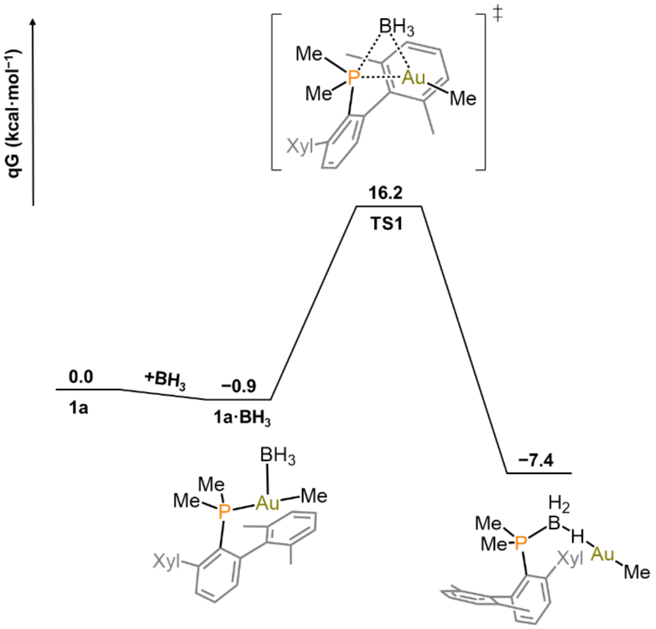

Figure 2.22. DFT-computed reaction coordinated for the BH_3-mediated P-Au bond cleavage from $Au(CH_3)(PMe_2Ar^{Xyl2})$ (**1a**).

To account for the second-order dependence on **4a**, we considered its initial dissociation into **1a** and Au(PMe_2Ar^{Xyl2})(NTf_2), the latter providing one equivalent of cation [Au(PMe_2Ar^{Xyl2})]$^+$ amenable to bind a second molecule of **4a**. The corresponding trigonal dicationic adduct [Au_3(μ-CH_3)(PMe_2Ar^{Xyl2})$_3$]$^{2+}$ (**B**) plus **1a** are only 1.2 kcal/mol above two molecules of **4a** (Figure 2.23). From trimetallic adduct **B**, the transition state for the formal transfer of a phosphine ligand between gold atoms was found at +21.3 kcal/mol (**TS5**), close enough to the experimentally determined value for the overall process of ethane evolution. This transition state gives trinuclear species **C** at +10.7 kcal/mol, from which dissociation of **5a** is assumed to be facile. This would render the bimetallic intermediate [Au_2(μ-CH_3)(PMe_2Ar^{Xyl2})]$^+$, which is reminiscent of the proposed highly reactive 'AuMe' fragment proposed by Kochi.[24, 25] From such a reactive fragment, masked as [Au_2(μ-CH_3)(PMe_2Ar^{Xyl2})]$^+$, it is expected that the approach of **1a** would result in ethane elimination and formation of colloidal gold, not necessarily in that order.

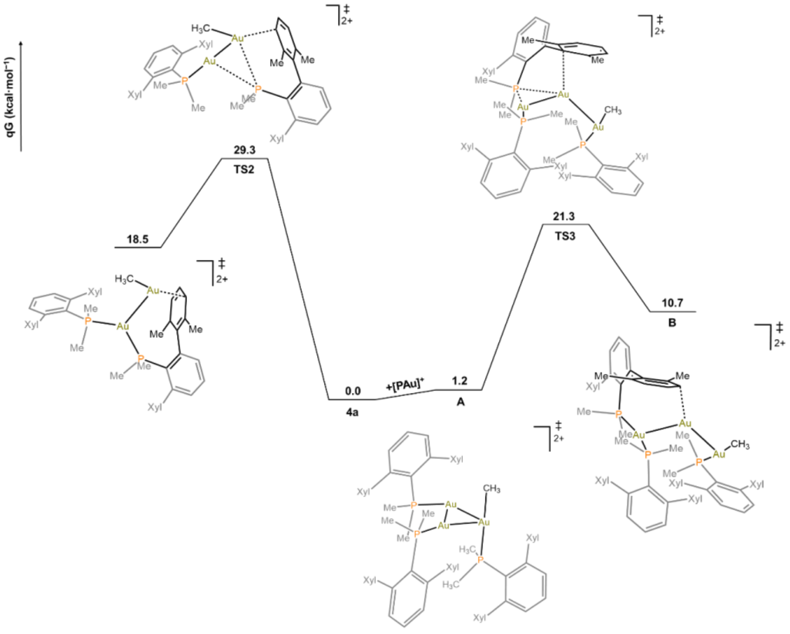

Figure 2.23. Calculated free energy profile for [Au(PMe_2Ar^{Xyl2})]$^+$-promoted phosphine dissociation and formation of masked 'AuMe' from Au(CH_3)(PMe_2Ar^{Xyl2}) (**1a**, left) or [Au_2(μ-CH_3)(PMe_2Ar^{Xyl2})$_2$]$^+$ (**4a**, right) complexes.

Our combined experimental/computational approach led us to propose the mechanistic picture for C–C coupling at gem-digold compounds **4** depicted in Scheme 2.8. Compounds **4** readily dissociate in solution to form **1** and Au(PR_2Ar')(NTf_2), the latter functioning as a Lewis acid to favor phosphine dissociation from a second molecule of **4** by forming a trimetallic intermediate of type **B**. Following the release of diphosphine compounds **5**, the resulting masked 'AuMe' fragment reacts with **1a** to liberate ethane with concomitant formation of elemental Au, eventually leading to the formation of Au nanoparticles. In this picture, phosphine dissociation from **4a** constitutes the rate-limiting step of the overall process, in analogy to the previously proposed mechanism for reductive coupling from Au(CH_3)(PPh_3).[24, 25] In contrast, the remarkable acceleration observed for C–C coupling in compounds **4** compared to **1** seems to be the result of kinetic stabilization of key intermediates by the presence of aurophilic interactions combined with the Lewis acidic character of $[Au(PR_2Ar')]^+$, thus representing an example of rate acceleration by bimetallic entities compared to monometallic counterparts.[50-52]

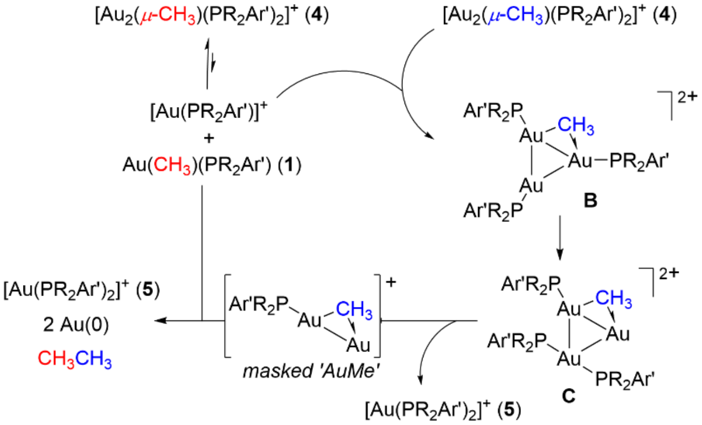

Scheme 2.8. Proposed mechanism for the reductive coupling of ethane from gem-digold compounds **4**.

2.3 Conclusions

Au-mediated C-C coupling processes have rapidly emerged as versatile and powerful strategies for organic synthesis. Despite numerous reports on the synthetic applicability of gold catalysts, mechanistic understanding has evolved at a considerably slower pace. Previous studies have placed the Au(I)/Au(III) redox couple at the heart of all these transformations, while mechanistic investigations on C–C coupling processes without the apparent advent of Au(III) species is lacking. Herein, we have demonstrated that gem-digold methyl complexes $[Au_2(\mu\text{-}CH_3)(PR_2Ar')_2][NTf_2]$ (**4**) promote the homocoupling of the bridging methyl fragments to produce ethane at a remarkably higher rate than from its parent neutral species $Au(CH_3)(PR_2Ar')$ (**1**). We have also evinced that this approach permits the heterocoupling of the bridging methyl group with ethyl and phenyl fragments. The stability of compounds **4** towards reductive homocoupling is highly dependent on the steric bulk of the phosphine ligand. Whereas the system based on PPh_3 readily liberates ethane at -40 ºC, those bearing terphenyl phosphines (PMe_2Ar') exhibit considerably enhanced stability, which is further increased by the use of the more hindered XPhos and tBuXPhos, the latter being unable to mediate C–C coupling even at 90 ºC. Our kinetic studies revealed second-order dependence on gem-digold methyl complexes **4** during ethane evolution, whereas a distinctive change towards a first-order dependence on the latter was ascertained in the presence of excess BPh_3 as an external Lewis acid. Based on our experimental studies combined with DFT computational methods we have proposed a mechanism that involves rapid dissociation of a molecule of $[Au_2(\mu\text{-}CH_3)(PMe_2Ar')_2][NTf_2]$ (**4**) towards $Au(PMe_2Ar')(NTf_2)$ and $Au(CH_3)(PMe_2Ar')$ (**1**). While $Au(PMe_2Ar')(NTf_2)$ mediates phosphine dissociation from a second molecule of **4** by a trimetallic intermediate, compound **1** reacts with the resulting highly reactive and masked

'AuMe' fragment to effect the C–C coupling event, most likely by a multinuclear gold species. These studies highlight the relevance of multimetallic mechanisms in mediating uncommon transformations, herein also boosting up the rate at which the C–C coupling transformation occurs.

2.4 Experimental section

2.4.1 General Methods. Unless otherwise noted, all reactions and manipulations were performed under a nitrogen atmosphere in a glovebox or using standard Schlenk techniques with dried and degassed solvents. All solvents were purified via Solvent Purification System or by common distillation techniques: Dichloromethane (CH_2Cl_2) was distilled under nitrogen over CaH_2. Toluene (C_7H_8), benzene (C_6H_6), n-hexane (C_6H_{14}), and n-pentane (C_5H_{12}) were distilled under nitrogen over sodium. Tetrahydrofuran (THF) and diethyl ether were distilled under nitrogen over sodium/benzophenone. Benzene (C_6D_6) was dried over sodium, while $CDCl_3$ and CD_2Cl_2 over molecular sieves (4 Å) and distilled under nitrogen. Compounds PMe_2Ar',[53] AuCl(THT) (THT = tetrahydrothiophene),[54] $Au(PPh_3)(NTf_2)$,[55, 56] $Au(PPh_3)(NO_3)$,[57, 58] AuCl(XPhos),[59] AuCl(tBuXPhos),[59] $Au(XPhos)(NTf_2)$,[34, 60-62] $Au(^tBuXPhos)(NTf_2)$,[63] $AuCl(PMe_2\mathit{Ar}^{Xyl2})$[48], $AuCl(PMe_2\mathit{Ar}^{Dipp2})$,[34] $AuCl(PMe_2Ar^{Tripp2})$,[34, 64] $Au(PMe_2\mathit{Ar}^{Xyl2})(NTf_2)$,[48] $Au(PMe_2\mathit{Ar}^{Dipp2})(NTf_2)$,[34] $Au(PMe_2Ar^{Tripp2})(NTf_2)$[64] $Au(CH_3)(PMe_2\mathit{Ar}^{Dipp2})$,[34] (**1c**) and $[Au_2(\mu\text{-}CH_3)(PMe_2Ar^{Dipp2})_2][NTf_2]$[34] (**4c**) where prepared according to previously reported procedures. Compounds **1e** and **1f** were prepared according to the general method described below in yields of around 75%, exhibiting identical spectroscopic data to those previously reported. $Au(CH_3)(XPhos)$[62] and $Au(CH_3)(^tBuXPhos)$[65] were prepared by an alternative method of the published procedures and fully characterized.

Methyl(triphenylphosphine)gold(I), chloro(dimethylsulfide)gold(I), silver bis(trifluoromethanesulfonyl)imide acetonitrile adduct, chlorotriphenylphosphinegold(I), 2-dicyclohexylphosphino-2′,4′,6′-triisopropylbiphenyl (XPhos) and 2-di-*tert*-butylphosphino-2′,4′,6′-triisopropylbiphenyl (*t*BuXPhos) were purchased from STREM Chemicals and were used as received. Other chemicals were purchased from Sigma-Aldrich and used as received. All new compounds have been characterized by ^{1}H NMR spectroscopy, ^{31}P NMR spectroscopy, ^{13}C NMR spectroscopy, and elemental analysis. Solution NMR spectra were recorded on Varian Inova 600 MHz or 500 MHz, or on Bruker AMX-300, DRX-400, DRX-500, and Avance III 800MHz spectrometers. Spectra were referenced to external $SiMe_4$ or using the residual proton solvent peaks as internal standards (^{1}H NMR experiments), or the characteristic resonances of the solvent nuclei (^{13}C NMR experiments), while ^{31}P was referenced to H_3PO_4. Spectral assignments were made by routine one- and two-dimensional NMR experiments where appropriate. For elemental analyses, the LECO TruSpec CHN elementary analyser and Perkin-Elmer 2400 Series II analyzer were utilized. GC analysis was performed using a Shimadzu GCMSQP2010-Plus equipped with a PoraBOND-Q capillary column (25 m, 0.25 mm i.d., 3.0 um film thickness, Agilent Technologies). Helium carrier gas was supplied at a head pressure of 10 psi to provide an initial flow rate of 1.4 mL/min. A 1 mL injection with a split ratio of 1:10 was employed. GC temperature was initially held at 40 °C for 1 min, and gradually increased to 120 °C at 5 °C/ min. Full-scan mass spectra were collected from 5 to 70 m/z at a data acquisition rate of 3.5 spectra/s. The MS transfer line was held at 250 °C and the ion source temperature was 200 °C. Samples analyzed by transmission electron microscopy (TEM) were prepared by dispersing the powders in cyclohexane or hexanes (99.5%, anhydrous, Sigma-Aldrich) and sonicating for 1 minute before mounting on Cu-supported holey carbon grids. The Au samples were imaged using an FEI Titan 80–300 operating at 300 kV. The structures of compounds **1a**, **1e**, **1f**, **2a**, **3a**, **4e**, **4f**, Au(tBuPhos)(NTf$_2$) have been authenticated by X-ray diffraction studies and their corresponding CIF files deposited in the Cambridge Crystallographic Data Centre with no. 2024182-2024189.

2.4.2 General synthesis of compounds 1. A suspension of the corresponding gold chloride precursor AuCl(PR$_2$Ar') (0.20 mmol) in toluene (10 mL) was cooled to -78 ºC and a solution of MeMgX (X = Cl or Br; 2.5 equiv) in toluene was added dropwise. The mixture was allowed to warm up slowly for 16 hours. The volatiles were removed in vacuo and the residue extracted with benzene for **1a-d** or pentane for **1e-f**. Evaporation of the organic solvent led to compounds **1a-f** as white powders in around 60 - 80 % yields. Suitable crystals of these compounds can be obtained by slow solvent evaporation from pentane/Et$_2$O or pentane/dichloromethane solutions. Spectroscopic and analytical data for selected compounds (others can be found in the later section). **Compound 1a.** Yield: 84 mg, 75%. Anal. Calcd. for $C_{25}H_{30}AuP$: C, 53.8; H, 5.4. Found: C, 53.4; H, 5.5. ^{1}H NMR (400 MHz, CD$_2$Cl$_2$, 25 ºC) δ: 7.53 (td, 1 H, $^5J_{HP}$ = 1.7 Hz, H$_b$), 7.23 (t, 2 H, H$_d$), 7.14 (d, 4 H, H$_c$), 7.07 (dd, 2 H, $^4J_{HP}$ = 2.9 Hz, H$_a$), 2.13 (s, 12 H, *C*H$_3$(Xyl)), 1.02 (d, 6 H, $^2J_{HP}$ = 7.7 Hz, PMe$_2$), -0.08 (d, 3 H, $^3J_{HP}$ = 8.2 Hz, AuCH$_3$). All aromatic couplings are of *ca*. 7.5 Hz. ^{13}C{^{1}H} NMR (100 MHz, CD$_2$Cl$_2$, 25 ºC) δ: 147.0 (d, $^2J_{CP}$ = 10 Hz, C$_2$), 142.3 (d, $^4J_{CP}$ = 4 Hz, C$_3$), 137.2 (C$_4$), 131.8 (d, $^1J_{CP}$ = 35 Hz, C$_1$), 131.6 (d, $^4J_{CP}$ = 3 Hz, CH$_b$), 131.5 (d, $^3J_{CP}$ = 7 Hz, CH$_a$), 128.6 (CH$_d$), 128.4 (CH$_c$), 22.4 (*C*H$_3$(Xyl)), 16.8 (d, $^1J_{CP}$ = 30 Hz, PMe$_2$), 4.7 (d, $^2J_{CP}$ = 100 Hz, AuCH$_3$). ^{31}P{^{1}H} NMR (162 MHz, CD$_2$Cl$_2$, 25 ºC) δ: 22.1. MS (ESI) m/*z* Calcd. for M(Na)$^+$: 581.2. Expt.: 581.4. **Compound 1d.** Yield: 106 mg, 70%. Anal. Calcd. for $C_{39}H_{58}AuP$: C, 62.1; H, 7.7. Found: C, 62.0; H, 7.5. ^{1}H NMR (300 MHz, CD_2Cl_2, 25 ºC) δ: 7.42 (td, 1 H, $^5J_{HP}$ = 1.8 Hz, H_b), 7.15 (dd, 2 H, $^4J_{HP}$ = 3.0 Hz, H_a), 7.08 (s, 4 H, H_c), 2.94 (hept, 2 H, $^3J_{HH}$ = 6.9 Hz, *p*-^{i}Pr(CH)), 2.58 (hept, 4 H, $^3J_{HH}$ = 6.9 Hz, *o*-^{i}Pr(CH)), 1.31 (d, 12 H, $^3J_{HH}$ = 6.9 Hz; d, 12 H, $^3J_{HH}$ = 6.9 Hz, *o*-^{i}Pr(CH_3), *p*-^{i}Pr(CH_3)), 1.07 (d, 6 H, $^2J_{HP}$ = 7.4 Hz, PMe_2), 1.02 (d, 12 H, $^3J_{HH}$ = 6.9 Hz, *o*-^{i}Pr(CH_3)), -0.36 (d, 3 H, $^3J_{HP}$ = 8.2 Hz, $AuCH_3$). All aromatic couplings are of *ca*. 7.5 Hz. $^{13}C\{^1H\}$ NMR (125 MHz, CD_2Cl_2, 25 ºC) δ: 149.9 (C_5), 146.9 (C_4), 146.6 (d, $^2J_{CP}$ = 11 Hz, C_2), 137.9 (d, $^4J_{CP}$ = 5 Hz, C_3), 133.7 (C_1), 133.4 (d, $^3J_{CP}$ = 7 Hz, CH_a), 129.3 (CH_b), 121.8 (CH_c), 35.1 (*p*-^{i}Pr(CH)), 31.9 (*o*-^{i}Pr(CH)), 26.1 (*o*-^{i}Pr(CH_3)), 24.9 (*p*-^{i}Pr(CH_3)), 23.4 (*o*-^{i}Pr(CH_3)), 17.3 (d, $^1J_{CP}$ = 30 Hz, PMe_2), 5.7 (d, $^2J_{CP}$ = 102 Hz, $AuCH_3$). $^{31}P\{^1H\}$ NMR (121 MHz, CD_2Cl_2, 25 ºC) δ: 19.8. MS (ESI) m/*z* Calcd. for M(Na)$^+$: 777.4. Expt.: 777.5.

2.4.3 General synthesis of compounds 4. A solid mixture of the corresponding methyl gold precursor **1a-f** (0.0175 mmol) with 1 equivalent of its parent compound $[Au(PR_2Ar')][NTf_2]$ (0.0175 mmol) were dissolved in CD_2Cl_2 (0.6 mL) under nitrogen at -50ºC to rapidly yield the desired methyl-bridged complex **4a-f** in a quantitative NMR spectroscopic yield. Characterization of the less stable compounds **4a** and **4b** was carried out by multinuclear NMR spectroscopy at low temperature without further purification. Compounds **4c-f** were obtained as colourless microcrystalline substances by precipitation with pentane at -20 ºC (**4c**, **4d**) or 25 ºC (**4e**, **4f**) in around 90% yields. Alternatively **4a-f** can be prepared in comparable by treating compounds **1a-f** with half equivalent of $[Ph_3C][B(C_6F_5)_4]$ in dichloromethane by an otherwise identical procedure. Spectroscopic and analytical data for selected compounds (others can be found in later section). **Compound 4a**. ^{1}H NMR (400 MHz, CD_2Cl_2, -30 ºC) δ: 7.61 (t, 2 H, H_b), 7.25 (t, 4 H, H_d), 7.08 (m, 12 H, H_a, H_c), 1.98 (s, 24 H, *C*H_3(Xyl)), 1.16 (d, 12 H, $^2J_{HP}$ = 7.7 Hz, PMe_2), 0.45 (br. s, 3 H, $AuCH_3\cdots Au$). All aromatic couplings are of *ca*. 7.5 Hz. $^{13}C\{^1H\}$ NMR (100 MHz, CD_2Cl_2, -30 ºC) δ: 147.1 (d, $^2J_{CP}$ = 11 Hz, C_2), 141.1 (d, $^4J_{CP}$ = 5 Hz, C_3), 136.7 (C_4), 133.3 (CH_b), 131.8 (d, $^3J_{CP}$ = 8 Hz, CH_a), 129.0 (CH_d), 128.2 (CH_c), 127.8 (d, $^1J_{CP}$ = 38 Hz, C_1), 21.9 (*C*H_3(Xyl)), 16.9 (d, $^1J_{CP}$ = 37 Hz, PMe_2), 0.6 ($AuCH_3\cdots Au$). $^{31}P\{^1H\}$ NMR (162 MHz, CD_2Cl_2, -20 ºC) δ: 1.1. **Compound 4d.** Anal. Calcd. for $C_{101}H_{113}Au_2BF_{20}P_2$: C, 55.8; H, 5.2. Found: C, 56.1; H, 4.9. ^{1}H NMR (400 MHz, CD_2Cl_2, 25 ºC) δ: 7.51 (t, 2 H, H_b), 7.17 (dd, 4 H, $^4J_{HP}$ = 3.3 Hz, H_a), 7.05 (s, 8 H, H_c), 2.94 (hept, 4 H, $^3J_{HH}$ = 7.0 Hz, *p*-^{i}Pr(CH)), 2.41 (hept, 8 H, $^3J_{HH}$ = 6.7 Hz, *o*-^{i}Pr(CH)), 1.31 (d, 24 H, $^3J_{HH}$ = 7.0 Hz, *p*-^{i}Pr(CH_3)), 1.22 (m, 36 H, *o*-^{i}Pr(CH_3), PMe_2), 1.00 (d, 24 H, $^3J_{HH}$ = 6.6 Hz, *o*-^{i}Pr(CH_3)), 0.25 (s, 3 H, $AuCH_3\cdots Au$). All aromatic couplings are of *ca*. 7.5 Hz. $^{13}C\{^1H\}$ NMR (100 MHz, CD_2Cl_2, 25 ºC) δ: 151.1 (C_5), 147.3 (C_4), 146.8 (d, $^2J_{CP}$ = 12 Hz, C_2), 137.0 (d, $^4J_{CP}$ = 6 Hz, C_3), 134.0 (d, $^3J_{CP}$ = 8 Hz, CH_a), 131.2 (CH_b), 129.4 (d, $^1J_{CP}$ = 56 Hz, C_1), 122.2 (CH_c), 35.0 (*p*-^{i}Pr(CH)), 32.0 (*o*-^{i}Pr(CH)), 25.8 (*o*-^{i}Pr(CH_3)), 24.8 (*p*-^{i}Pr(CH_3)), 23.5 (*o*-^{i}Pr(CH_3)), 17.7 (d, $^1J_{CP}$ = 37 Hz, PMe_2), 0.5 (t, $^2J_{CP}$ = 53 Hz, $^1J_{CH}$ = 130 Hz, $AuCH_3\cdots Au$). $^{31}P\{^1H\}$ NMR (162 MHz, CD_2Cl_2, 25 ºC) δ: 0.5. MS (ESI) m/*z* Calcd. for M^+: 1493.8. Expt.: 1493.8. **Compound 4e.** Anal. Calcd. for $C_{69}H_{101}Au_2F_6NO_4P_2S_2$: C, 50.5; H, 6.2; N, 0.9 Found: C, 50.3; H, 6.2; N, 0.9. ^{1}H NMR (500 MHz, CD_2Cl_2, 25 ºC)[66] δ: 7.76 (m, 2 H, H_a), 7.64 (m, 4 H, H_b), 7.22 (m, 2 H, H_c), 7.09 (s, 4 H, H_d), 3.06 (hept, 2 H, $^3J_{HH}$ = 7.1 Hz, *o*-^{i}Pr(CH), 2.37 (hept, 4 H, $^3J_{HH}$ = 7.0 Hz, *p*-^{i}Pr(CH)), 2.15 (m, 2 H, Cy(CH_2)), 1.92 (m, 8 H, Cy(CH_2)), 1.85 (m, 2 H, Cy(CH)), 1.46 (m, 8 H, Cy(CH)), 1.44 (d, 12 H, $^3J_{HH}$ = 6.0 Hz, *p*-^{i}Pr(CH_3)), 1.37 (m, 8 H, Cy(CH)), 1.24 (m, 8 H, Cy(CH)), 1.26 (d, 12 H, $^3J_{HH}$ = 6.0 Hz, o-^{i}Pr(CH$_3$)), 1.03 (d, 6 H, $^3J_{HH}$ = 6.0 Hz, o-^{i}Pr(CH$_3$), c), 0.67 (t, 3 H, $^3J_{HP}$ = 2.2 Hz, AuCH$_3$⋯Au). ^{13}C{^{1}H} NMR (201 MHz, CD$_2$Cl$_2$, 25 ºC) δ: 150.3, 147.1, 146.7 (d, *J* = 14 Hz), 137.2 (d, *J* = 6 Hz), 134.2 (d, *J* = 10 Hz), 133.2, 131.1, 127.8 (d, *J* = 6 Hz), 127.5 (d, $^2J_{C\text{-}P}$ = 48 Hz), 121.3, 37.5 (d, *J* = 32 Hz), 34.2, 30.8 (d, *J* = 4 Hz), 30.8, 30.0 (d, *J* = 4 Hz), 26.8 (d, *J* = 12 Hz), 26.7 (d, *J* = 14 Hz), 25.7, 24.9, 24.2, 23.0, 3.1 (t, $^2J_{CP}$ = 48 Hz). ^{31}P{^{1}H} NMR (243 MHz, CD$_2$Cl$_2$, 25 ºC) δ: 39.5.

2.4.4 General procedure to measure kinetic constants. Kinetic studies were carried using an identical procedure to that described for the general synthesis of compounds **4**, in J-Young NMR tubes under nitrogen atmosphere, and monitoring the disappearance of the *in situ* formed gem-digold methyl compounds **4** by ^{1}H and ^{31}P{^{1}H} NMR. Each kinetic experiment was run in triplicates and average data are given.

2.4.5 General synthesis compounds AuCl(PMe$_2$Ar') The corresponding terphenyl phosphine (PMe$_2$Ar^{Xyl2}, PMe$_2$Ar^{Mes2}, PMe$_2$Ar^{Dipp2}, PMe$_2$Ar^{Trip2}: 0.94 mmol) and [Au(tht)Cl] (tht = tetrahydrothiophene) (300 mg, 0.94 mmol) were dissolved in toluene (10 mL) in a Schlenk flask under nitrogen. The initial white suspension became a solution after several hours and was stirred for an overall period of 12 hours. The solvent was removed under vacuum and the resulting white solid washed with pentane and dried to give the corresponding terphenyl phosphine gold chloride complexes as fine white powders in around 90% yields. These complexes can be recrystallized from a 1:3 mixture of CH$_2$Cl$_2$/pentane.

2.4.6 AuCl(PMe$_2$Ar^{Mes2}), Ar^{Mes2} =C$_6$H$_3$-2,6-(C$_6$H$_2$-2,4,6-Me$_3$)$_2$

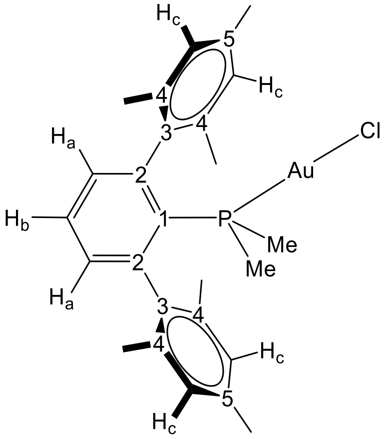

Anal. Calcd. for $C_{26}H_{31}AuClP$: C, 51.5; H, 5.2. **Found:** C, 51.0; H, 5.3.

^{1}H NMR (400 MHz, CD_2Cl_2, 25 ºC) δ: 7.58 (td, 1 H, $^5J_{HP}$ = 1.9 Hz, H$_b$), 7.08 (dd, 2 H, $^4J_{HP}$ = 3.5 Hz, H$_a$), 6.98 (s, 4 H, H$_c$), 2.35 (s, 6 H, *p*-*C*H$_3$(Mes)), 2.08 (s, 12 H, *o*-*C*H$_3$(Mes)), 1.20 (d, 6 H, $^2J_{HP}$ = 10.5 Hz, PMe$_2$). All aromatic couplings are of *ca*. 7.5 Hz.

^{13}C{^{1}H} NMR (100 MHz, CD_2Cl_2, 25 ºC) δ: 147.1 (d, $^2J_{CP}$ = 10 Hz, C$_2$), 139.1 (C$_5$), 138.5 (d, $^4J_{CP}$ = 5 Hz, C$_3$), 136.8 (C$_4$), 132.5 (d, $^4J_{CP}$ = 3 Hz, CH$_b$), 132.2 (d, $^3J_{CP}$ = 8 Hz, CH$_a$), 129.5 (CH$_c$), 127.9 (d, $^1J_{CP}$ = 58 Hz, C$_1$), 22.2 (*p*-*C*H$_3$(Mes)), 21.7 (*o*-*C*H$_3$(Mes)), 18.0 (d, $^1J_{CP}$ = 40 Hz, PMe$_2$).

^{31}P{^{1}H} NMR (162 MHz, CD_2Cl_2, 25 ºC) δ: -3.5.

MS (ESI) m/*z* Calcd. for M(Na)$^+$: 629.1. **Expt.:** 629.3.

2.4.7 Compounds Au(CH$_3$)(PMe$_2$Ar’) (1a-f)

Au(CH$_3$)(PMe$_2$Ar^{Mes2}), Ar^{Mes2} =C$_6$H$_3$-2,6-(C$_6$H$_2$-2,4,6-Me$_3$)$_2$, (1b)

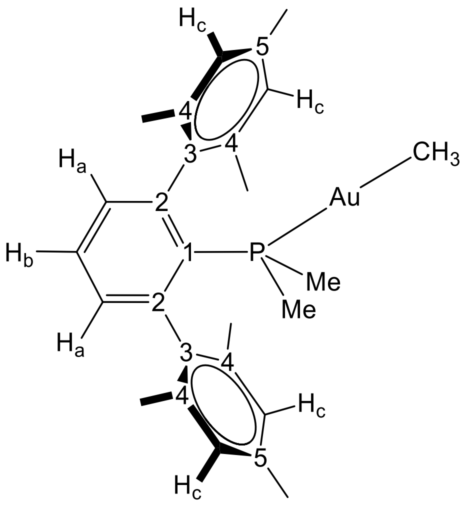

Yield: 70 mg, 60 %

Anal. Calcd. for $C_{27}H_{34}AuP$: C, 55.3; H, 5.8. **Found**: C, 54.9; H, 5.5.

^{1}H NMR (300 MHz, CD_2Cl_2, 25 ºC) δ: 7.49 (td, 1 H, $^{5}J_{HP}$ = 1.7 Hz, H_b), 7.03 (dd, 2 H, $^{4}J_{HP}$ = 2.9 Hz, H_a), 6.95 (s, 4 H, H_c), 2.34 (s, 6 H, *p*-*C*H_3(Mes)), 2.08 (s, 12 H, *o*-*C*H_3(Mes)), 1.03 (d, 6 H, $^{2}J_{HP}$ = 7.7 Hz, PMe_2), -0.08 (d, 3 H, $^{3}J_{HP}$ = 8.2 Hz, $AuCH_3$). All aromatic couplings are of *ca*. 7.5 Hz.

^{13}C{^{1}H} NMR (100 MHz, CD_2Cl_2, 25 ºC) δ: 147.1 (d, $^{2}J_{CP}$ = 10 Hz, C_2), 139.5 (d, $^{4}J_{CP}$ = 4 Hz, C_3), 138.3 (C_5), 136.1 (C_4), 132.4 (d, $^{1}J_{CP}$ = 36 Hz, C_1), 131.7 (d, $^{4}J_{CP}$ = 7 Hz, CH_a), 131.4 (d, $^{3}J_{CP}$ = 2 Hz, CH_b), 128.2 (CH_c), 22.3 (*o*-*C*H_3(Mes)), 21.7 (*p*-*C*H_3(Mes)), 17.0 (d, $^{1}J_{CP}$ = 30 Hz, PMe_2), 3.4 (d, $^{2}J_{CP}$ = 100 Hz, $AuCH_3$).

^{31}P{^{1}H} NMR (160 MHz, CD_2Cl_2, 25 ºC) δ: 21.1.

MS (ESI) m/*z* Calcd. for $M(Na)^+$: 609.2. **Expt.**: 609.3.

[Au(CH_3)(XPhos)] (1e)

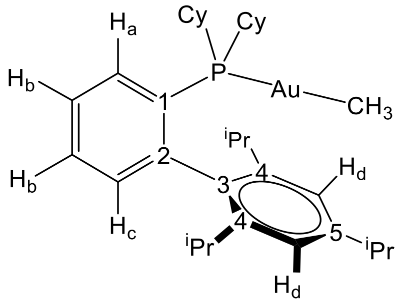

Yield: 103 mg, 75%.

Anal. Calcd. for $C_{34}H_{52}AuP$: C, 59.3; H, 7.6. **Found**: C, 59.1; H, 7.8.

^{1}H NMR (500 MHz, CD_2Cl_2, 25 ºC) δ: 7.63 (td, 1 H, $^3J_{HH}$ = 7.5 Hz, H_a), 7.46 (q, 2 H, $^3J_{HH}$ = 7.7 Hz, H_b), 7.18 (m, 1 H, H_c), 7.05 (s, 2 H, H_d), 2.95 (hept, 1 H, $^3J_{HH}$ = 6.9 Hz, *o*-^{i}Pr(CH)), 2.34 (hept, 2 H, $^3J_{HH}$ = 7.0, *p*-^{i}Pr(CH)), 2.18 (m, 2 H, Cy(CH)), 2.1 (m, 2 H, Cy(CH)), 1.84 (m, 4 H, Cy(CH)), 1.76 (m, 2 H, Cy(CH)), 1.69 (m, 2 H, Cy(CH)), 1.38 (m, 2 H, Cy(CH)), 1.24 (m, 6 H, Cy(CH)), 1.34 (d, 6 H, $^3J_{HH}$ = 6.9 Hz, *p*-^{i}Pr(CH_3)), 1.31 (d, 6 H, $^3J_{HH}$ = 7.0 Hz, *o*-^{i}Pr(CH_3)), 0.96 (d, 6 H, $^3J_{HH}$ = 6.8 Hz, *o*-^{i}Pr(CH_3), (c)), -0.41 (d, 3 H, $^3J_{HP}$ = 7.6 Hz, $AuCH_3$).

^{13}C{^{1}H} NMR (201 MHz CD_2Cl_2, 25 ºC)[1] δ: 148.6, 147.4 (d, *J* = 18.1 Hz), 145.9, 137.4 (d, *J* = 4.0 Hz), 133.4 (d, *J* = 8.0 Hz), 131.5 (d, *J* = 34.2 Hz), 129.5 (d, *J* = 2.0 Hz), 126.7 (d, $^2J_{CP}$ = 6.0 Hz), 121.0, 37.5 (d, *J* = 26.1 Hz), 34.2, 30.8, 30.5 (d, *J* = 4.0 Hz), 30.0 (d, *J* = 4.0 Hz), 27.2 (d, *J* = 12.1 Hz), 26.9 (d, *J* = 12.1 Hz), 26.0, 25.3, 24.2, 22.62, 8.3 (d, $^2J_{CP}$ = 94.5 Hz).

^{31}P{^{1}H} NMR (243 MHz, CD_2Cl_2, 25 ºC) δ: 47.5.

[Au(CH_3)(^{t}BuXPhos)] (1f)

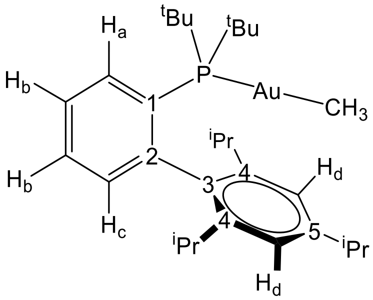

Yield: 93 mg, 73%.

Anal. Calcd. for $C_{30}H_{48}AuP$: C, 56.6; H, 7.6. **Found**: C, 56.5; H, 7.2.

^{1}H NMR (500 MHz, CD_2Cl_2, 25 ºC) δ: 7.92 (td, 1 H, $^3J_{HH}$ = 7.7 Hz, H_a), 7.46 (q, 2 H, $^3J_{HH}$ = 7.5 Hz, H_b), 7.22 (m, 1 H, H_c), 7.04 (s, 2 H, H_d), 2.95 (hept, 1 H, $^3J_{HH}$ = 6.7 Hz, *p*-^{i}Pr(CH)), 2.44 (hept, 2 H, $^3J_{HH}$ = 6.6 Hz, *o*-^{i}Pr(CH)), 1.42 (d, 18 H, $^3J_{HP}$ = 14.2 Hz, ^{t}Bu), 1.34 (d, 6 H, $^3J_{HH}$ = 6.9 Hz, *p*-^{i}Pr(CH_3)), 1.30 (d, 6 H, $^3J_{HH}$ = 7.0 Hz, *o*-^{i}Pr(CH_3)), 0.92 (d, 6 H, $^3J_{HH}$ = 6.9 Hz, *o*-^{i}Pr(CH_3)), -0.45 (d, 3 H, $^3J_{HP}$ = 7.4 Hz, $AuCH_3$).

^{13}C{^{1}H} NMR (201 MHz, CD_2Cl_2, 25 ºC)[1] δ: 148.6, 148.2, 146.1, 137.8, 136.4, 134.62, 132.19 (d, $^1J_{C\text{-}P}$ = 28.1 Hz), 129.36, 126.0, 121.1, 37.75 (d, $^1J_{C\text{-}P}$ = 18 Hz), 34.1, 31.15 (d, $^2J_{C\text{-}P}$ = 6.0 Hz), 30.71, 25.79, 24.13, 22.55, 6.2 (d, $^2J_{C\text{-}P}$ = 90.5 Hz).

^{31}P{^{1}H} NMR (243 MHz, CD_2Cl_2, 25 ºC) δ: 70.6.

2.4.8 Compound Au(CH_2CH_3)(PMe_2Ar^{Xyl2}) (2a)

A suspension of AuCl(PMe_2Ar^{Xyl2}) (116 mg, 0.20 mmol) in toluene (10 mL) was cooled to -78 ºC and a commercial solution of EtMgBr in Et_2O (3 M, 130 µL, 0.4 mmol) was added dropwise. The mixture was allowed to warm up slowly for 16 hours. The volatiles was removed in a vacuum and the residue was extracted with benzene. Evaporation of the organic solvent led to compound **2a** as an analytically pure white powder (69 mg, 60%).

Suitable crystals of **2a** can be obtained by slow solvent evaporation from pentane/Et_2O solutions.

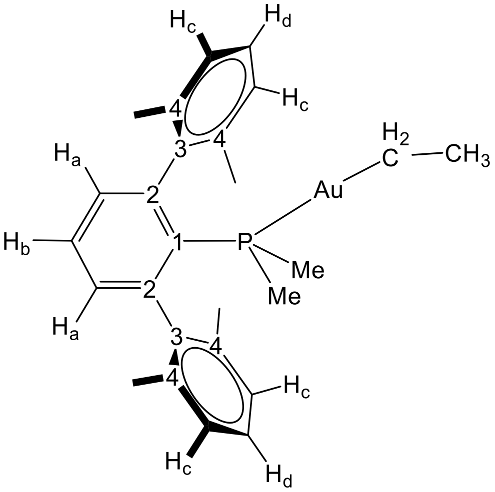

Anal. Calcd. for $C_{26}H_{32}AuP$: C, 54.6; H, 5.6. **Found**: C, 54.7; H, 5.2.

^{1}H NMR (300 MHz, CD_2Cl_2, 25 ºC) δ: 7.52 (td, 1 H, $^5J_{HP}$ = 1.6 Hz, H_b), 7.23 (m, 2 H, H_d), 7.13 (d, 4 H, H_c), 7.05 (dd, 2 H, $^4J_{HP}$ = 2.7 Hz, H_a), 2.15 (s, 12 H, CH_3(Xyl)), 1.16 (q, 3 H, $^3J_{HH}$ = 7.7 Hz, $AuCH_2CH_3$), 0.94 (d, 6 H, $^2J_{HP}$ = 7.4 Hz, PMe_2), 0.81(quint, 2 H, $^3J_{HH}$ = 7.7 Hz, $AuCH_2CH_3$). All aromatic couplings are of *ca*. 7.5 Hz.

^{13}C{^{1}H} NMR (100 MHz, CD_2Cl_2, 25 ºC) δ: 146.7 (d, $^2J_{CP}$ = 9 Hz, C_2), 142.2 (d, $^3J_{CP}$ = 3 Hz, C_3), 137.2 (C_4), 131.4 (d, $^3J_{CP}$ = 7 Hz, CH_a), 131.4 (s, CH_b), 123.2 (d, $^1J_{CP}$ = 40 Hz, C_1), 128.7 (s, CH_d), 128.4 (CH_c), 22.4 (CH_3(Xyl)), 19.8 (d, $^2J_{CP}$ = 102 Hz, $AuCH_2CH_3$), 17.3 (d, $^3J_{CP}$ = 4 Hz, $AuCH_2CH_3$), 16.7 (d, $^1J_{CP}$ = 30 Hz, PMe_2).

^{31}P{^{1}H} NMR (160 MHz, C_6D_6, 25 ºC) δ: 23.1.

2.4.9 Compound Au(C_6H_5)(PMe_2Ar^{Xyl2}) (3a)

A suspension of AuCl(PMe_2Ar^{Xyl2}) (116 mg, 0.20 mmol) in toluene (10 mL) was cooled to -78 ºC and a commercial solution of PhLi in dibutyl ether (1.8 M, 220 µL, 0.4 mmol) was added dropwise. The mixture was allowed to warm up slowly for 16 hours. The volatiles was removed in a vacuum and the residue was extracted with benzene. Evaporation of the organic solvent led to compound **3a** as an analytically pure white powder (77 mg, 62%). Suitable crystals of **3a** can be obtained by slow solvent evaporation from pentane/Et_2O solutions.

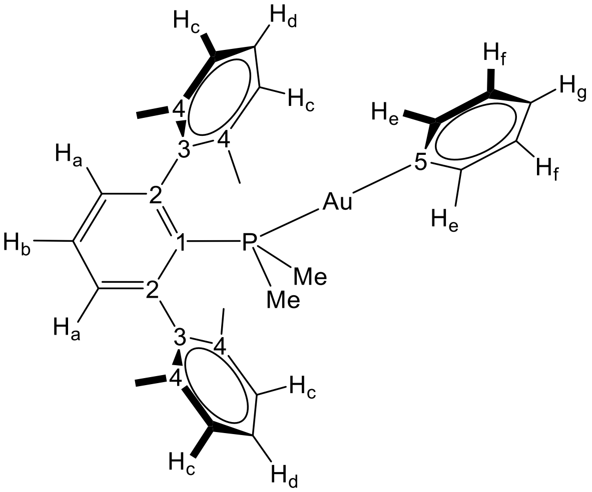

Anal. Calcd. for $C_{30}H_{32}AuP$: C, 58.1; H, 5.2. **Found**: C, 58.1; H, 5.4.

^{1}H NMR (400 MHz, CD_2Cl_2, 25 °C) δ: 7.59 (td, 1 H, $^5J_{HP}$ = 1.5 Hz, H_b), 7.32-7.24 (m, 4 H, H_d, H_f), 7.22-7.14 (m, 6 H, H_c, H_e), 7.12(dd, 2 H, $^4J_{HP}$ = 2.9Hz, H_a), 6.98 (t, 1 H, H_g), 2.25 (s, 12 H, CH_3(Xyl)), 1.08 (d, 6 H, $^2J_{HP}$ = 8.0 Hz, PMe_2). All aromatic couplings are of *ca*. 7.5 Hz.

^{13}C{^{1}H} NMR (100 MHz, CD_2Cl_2, 25 °C) δ: 171.7 (d, $^2J_{CP}$ = 122 Hz, C_5), 146.6 (d, $^2J_{CP}$ = 9 Hz, C_2), 142.0 (d, $^3J_{CP}$ = 3 Hz, C_3), 140.4 (CH_f), 137.3 (C_4), 131.6 (CH_b), 131.6 (d, $^3J_{CP}$ = 7 Hz, CH_a), 131.2 (d, $^1J_{CP}$ = 37 Hz, C_1), 128.9 (CH_d), 128.6 (CH_c), 127.8 (d, $^3J_{CP}$ = 7 Hz, CH_e), 125.7 (CH_g), 22.5 (CH_3(Xyl)), 17.0 (d, $^1J_{CP}$ = 31 Hz, PMe_2).

^{31}P{^{1}H} NMR (162 MHz, CD_2Cl_2, 25 °C) δ: 17.1.

2.4.10 Cationic gem-Digold Methyl Complexes (4b, 4e, 4f)

$[Au_2(\mu\text{-}CH_3)(PMe_2Ar^{Mes2})_2][B(C_6F_5)_4]$ (4b)

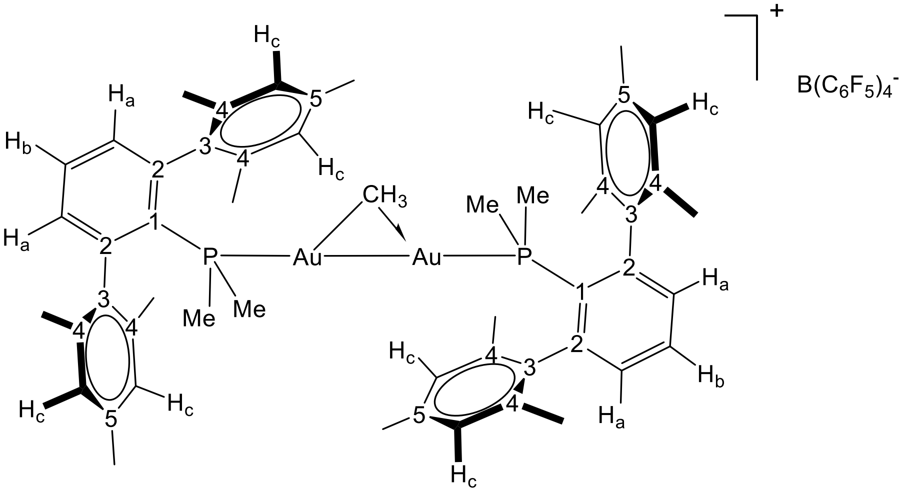

^{1}H NMR (400 MHz, CD_2Cl_2, -30 ºC) δ: 7.59 (td, 2 H, $^5J_{HP}$ = 1.4 Hz, H_b), 7.08 (dd, 4 H, $^4J_{HP}$ = 3.3 Hz, H_a), 6.91 (s, 8 H, H_c), 2.31 (s, 12 H, *p*-CH_3(Mes)), 1.91 (s, 24 H, *o*-CH_3(Mes)), 1.24 (d, 12 H, $^2J_{HP}$ = 9.8 Hz, PMe_2), 0.63 (s, 3 H, $AuCH_3\cdots Au$). All aromatic couplings are of *ca*. 7.5 Hz.

$^{13}C\{^1H\}$ NMR (100 MHz, CD_2Cl_2, -30 ºC) δ: 147.4 (d, $^2J_{CP}$ = 12 Hz, C_2), 138.6 (C_5), 138.2 (d, $^4J_{CP}$ = 6 Hz, C_3), 136.5 (C_4), 133.2 (CH_b), 132.0 (d, $^4J_{CP}$ = 8 Hz, CH_a), 129.0 (CH_c), 126.7 (d, $^1J_{CP}$ = 54 Hz, C_1), 21.8 (*o*-CH_3(Mes)), 21.4 (*p*-CH_3(Mes)), 16.9 (d, $^1J_{CP}$ = 37 Hz, PMe_2), 1.2 (t, $^2J_{CP}$ = 54 Hz, $AuCH_3\cdots Au$).

$^{31}P\{^1H\}$ NMR (162 MHz, CD_2Cl_2, 0 ºC) δ: 2.0.

[Au$_2$(μ-CH$_3$)(XPhos)$_2$][NTf$_2$] (4e)

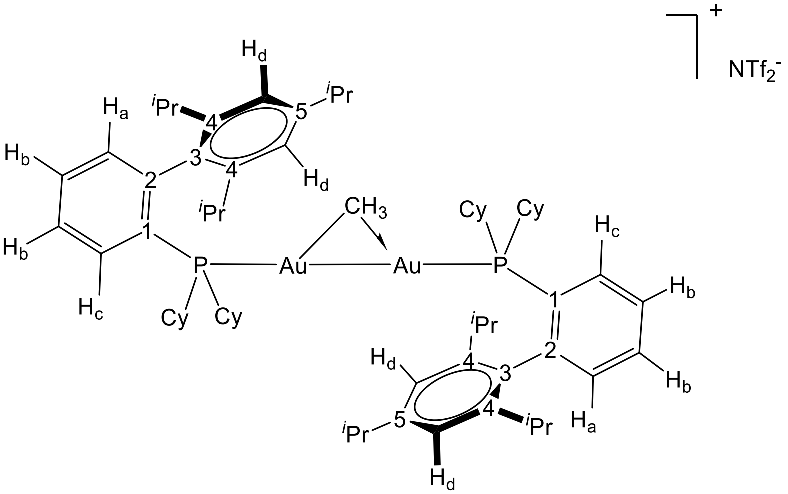

Anal. Calcd. for $C_{69}H_{101}Au_2F_6NO_4P_2S_2$: C, 50.5; H, 6.2; N, 0.9 **Found**: C, 50.3; H, 6.2; N, 0.9.

^{1}H NMR (500 MHz, CD_2Cl_2, 25 ºC) δ: 7.76 (m, 2 H, H$_a$), 7.64 (m, 4 H, H$_b$), 7.22 (m, 2 H, H$_c$), 7.09 (s, 4 H, H$_d$), 3.06 (hept, 2 H, $^3J_{HH}$ = 7.1 Hz, *o*-^{i}Pr(CH), 2.37 (hept, 4 H, $^3J_{HH}$ = 7.0 Hz, *p*-^{i}Pr(CH)), 2.15 (m, 2 H, Cy(CH$_2$)), 1.92 (m, 8 H, Cy(CH$_2$)), 1.85 (m, 2 H, Cy(CH)), 1.46 (m, 8 H, Cy(CH)), 1.44 (d, 12 H, $^3J_{HH}$ = 6.0 Hz, *p*-^{i}Pr(CH$_3$)), 1.37 (m, 8 H, Cy(CH)), 1.24 (m, 8 H, Cy(CH)), 1.26 (d, 12 H, $^3J_{HH}$ = 6.0 Hz, *o*-^{i}Pr(CH$_3$)), 1.03 (d, 6 H, $^3J_{HH}$ = 6.0 Hz, *o*-^{i}Pr(CH$_3$), c), 0.67 (t, 3 H, $^3J_{HP}$ = 2.2 Hz, AuCH$_3$···Au).

^{13}C{^{1}H} NMR (201 MHz, CD_2Cl_2, 25 ºC) δ: 150.3, 147.1, 146.7 (d, *J* = 14 Hz), 137.2 (d, *J* = 6 Hz), 134.2 (d, *J* = 10 Hz), 133.2, 131.1, 127.8 (d, *J* = 6 Hz), 127.5 (d, $^2J_{C\text{-}P}$ = 48 Hz), 121.3, 37.5 (d, *J* = 32 Hz), 34.2, 30.8 (d, *J* = 4 Hz), 30.8, 30.0 (d, *J* = 4 Hz), 26.8 (d, *J* = 12 Hz), 26.7 (d, *J* = 14 Hz), 25.7, 24.9, 24.2, 23.0, 3.1 (t, $^2J_{CP}$ = 48 Hz).

^{31}P{^{1}H} NMR (243 MHz, CD_2Cl_2, 25 ºC) δ: 39.5.

^{19}F{^{1}H} NMR (565 MHz, CD_2Cl_2, 25 ºC) δ: -79.7.

[Au_2(μ-CH_3)(^{t}BuXPhos)$_2$][NTf_2] (4f)

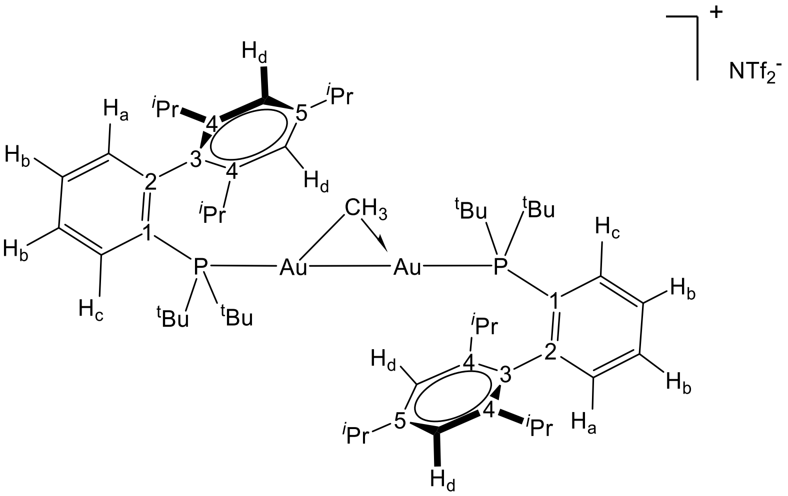

Anal. Calcd. for $C_{61}H_{93}Au_2F_6NO_4P_2S_2$: C, 47.6; H, 6.1; N, 0.9. **Found**: C, 47.9; H, 5.9; N, 0.9.

^{1}H NMR (500 MHz, CD_2Cl_2, 25 ºC) δ: 7.90 (m, 2H, H$_a$), 7.54 (m, 4 H , H$_b$), 7.15 (m, 2 H, H$_c$), 6.98 (s, 4 H, H$_d$), 2.91 (hept, 2 H, $^{3}J_{HH}$ = 6.8 Hz, *p*-^{i}Pr(CH)), 2.44 (hept, 4H, $^{3}J_{HH}$ = 6.4 Hz, *p*-^{i}Pr(CH)), 1.42 (d, 36 H, $^{3}J_{HP}$ = 18.0 Hz, ^{t}Bu), 1.26 (d, 6 H, $^{3}J_{HH}$ = 6.0 Hz, *o*-^{i}Pr(CH_3)), 1.16 (d, 6 H, $^{3}J_{HH}$ = 6.0 Hz, *p*-^{i}Pr(CH_3)), 0.88 (d, 6 H, $^{3}J_{HH}$ = 6.0 Hz, *o*-^{i}Pr(CH_3)), 0.87 (d, 3 H, $^{3}J_{HP}$ = 2.3 Hz, AuCH_3···Au).

^{13}C{^{1}H} NMR (201 MHz, CD_2Cl_2, 25 ºC) δ: 150.2, 147.5, 147.0 (d, $^{1}J_{C\text{-}P}$ = 14 Hz), 137.4(d, $^{2}J_{C\text{-}P}$ = 4 Hz), 135.2 (d, $^{2}J_{C\text{-}P}$ = 4 Hz), 135.1, 130.9, 128.7 (d, $^{2}J_{C\text{-}P}$ = 40 Hz), 127.1 (d, $^{2}J_{C\text{-}P}$ = 6.0 Hz), 121.7, 38.9 (d, $^{1}J_{C\text{-}P}$ = 24 Hz), 34.2, 31.3 (d, $^{2}J_{C\text{-}P}$ = 6 Hz), 30.7, 25.4, 24.0, 23.2, 2.7 (d, $^{2}J_{C\text{-}P}$ = 46 Hz, CH_3).

^{31}P{^{1}H} NMR (243 MHz, CD_2Cl_2, 25 ºC) δ: 66.8.

^{19}F{^{1}H} NMR (565 MHz, CD_2Cl_2, 25 ºC) δ: -79.6.

2.4.11 Compounds [Au(PMe$_2$Ar')$_2$]$^+$ (5)

For convenience, compounds **5** can be independently prepared by dissolving in dichloromethane (5 mL) an equimolar solid mixture of a halide gold precursor AuCl(PMe$_2$Ar') (116 mg, 0.20 mmol) with the same PMe$_2$Ar' phosphine (69 mg, 0.20 mmol) in the presence of one equivalent of AgNTf$_2$ (78 mg, 0.20 mmol) or NaBAr^F (117 mg, 0.20 mmol). The solution was stirred for 30 minutes and then filtrated through a celite bed. The volatiles was reduced under vacuum, and the residue washed with pentane to provide compounds **5** as white solids in *ca*. 90% yields.

[Au(PMe$_2$Ar^{Xyl2})$_2$][BAr$^F{}_4$] (5a)

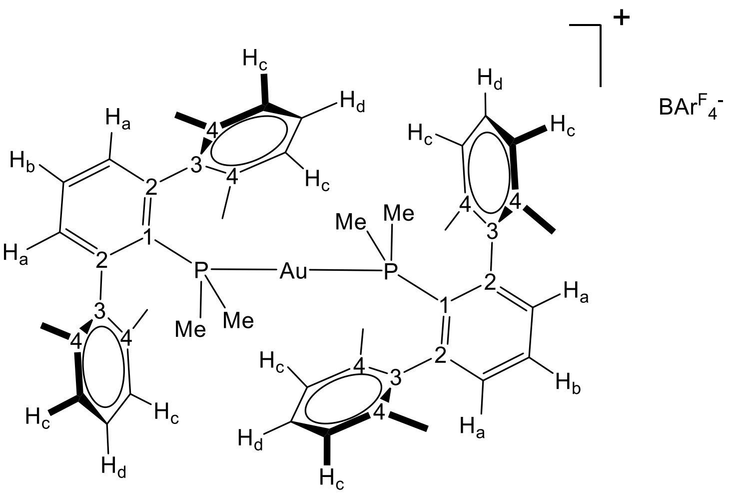

Anal. Calcd. for $C_{80}H_{66}AuBF_{24}P_2$: C, 54.8; H, 3.8. **Found**: C, 54.4; H, 3.9.

^{1}H NMR (400 MHz, CD$_2$Cl$_2$, 25 ºC) δ: 7.63 (t, 2 H, H$_b$), 7.23 (t, 4 H, H$_d$), 7.11 (d, 12 H, H$_a$, H$_c$), 2.03 (s, 24 H, *C*H$_3$(Xyl)), 1.05 (vt, 12 H, $^2J_{HP}$ = 3.7 Hz, PMe$_2$). All aromatic couplings are of *ca*. 7.5 Hz.

^{13}C{^{1}H} NMR (100 MHz, CD$_2$Cl$_2$, 25 ºC) δ: 146.8 (vt, $^2J_{CP}$ = 6 Hz, C$_2$), 140.9 (vt, $^4J_{CP}$ = 2 Hz, C$_3$), 136.9 (C$_4$), 133.5 (CH$_b$), 132.3 (vt, $^3J_{CP}$ = 4 Hz, CH$_a$), 129.6 (CH$_d$), 128.8 (CH$_c$), 126.7 (vt, $^1J_{CP}$ = 28 Hz, C$_1$), 22.3 (*C*H$_3$(Xyl)), 16.8 (vt, $^1J_{CP}$ = 18 Hz, PMe$_2$).

^{31}P{^{1}H} NMR (162 MHz, CD_2Cl_2, 25 ºC) δ: 10.6.

EM (ES) m/*z* Calcd. for M^+: 889.34. **Expt.**: 889.5.

[Au(PMe$_2$Ar^{Mes2})$_2$][BAr^F$_4$] (5b)

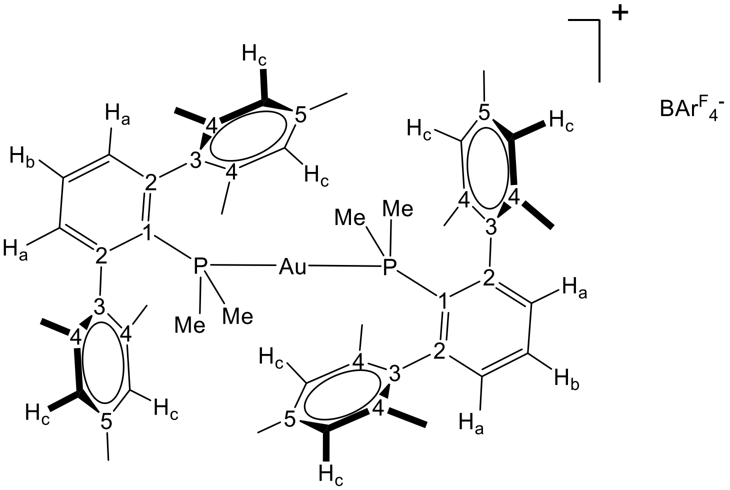

Anal. Calcd. for $C_{84}H_{74}AuBF_{24}P_2$: C, 55.8; H, 4.1. **Found**: C, 55.9; H, 4.1.

^{1}H NMR (500 MHz, CD_2Cl_2, 25 ºC) δ: 7.61 (t, 1 H, H$_b$), 7.08 (dd, 2 H, $^{4}J_{HP}$ = 3.5 Hz, H$_a$), 6.93 (s, 4 H, H$_c$), 2.30 (s, 12 H, *p*-CH$_3$(Mes)), 2.00 (s, 24 H, *o*-CH$_3$(Mes)), 1.06 (vt, 6 H, $^{2}J_{HP}$ = 3.7 Hz, PMe$_2$). All aromatic couplings are of *ca*. 7.5 Hz.

^{13}C{^{1}H} NMR (125 MHz, CD_2Cl_2, 25 ºC) δ: 146.9 (vt, $^{2}J_{CP}$ = 6 Hz, C$_2$), 139.2 (C$_5$), 138.2 (C$_3$), 136.8 (C$_4$), 133.3 (CH$_b$), 132.4 (vt, $^{3}J_{CP}$ = 4 Hz, CH$_a$), 129.5 (CH$_c$), 127.3 (vt, $^{1}J_{CP}$ = 29 Hz, C$_1$), 22.2 (*p*-CH$_3$(Mes)), 21.6 (*o*-CH$_3$(Mes)), 16.9 (vt, $^{1}J_{CP}$ = 18 Hz, PMe$_2$).

^{31}P{^{1}H} NMR (162 MHz, CD_2Cl_2, 25 ºC) δ: 11.5.

EM (ES) m/*z* Calcd. for M^+: 945.40. **Expt.**: 945.4.

[Au(PMe$_2$Ar^{Dipp2})$_2$][BAr$^F{}_4$] (5c)

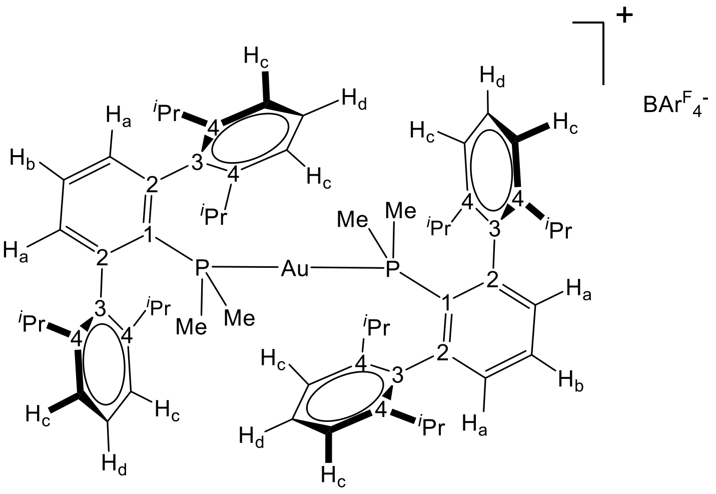

Anal. Calcd. for $C_{96}H_{98}AuBF_{24}P_2$: C, 58.3; H, 5.0. **Found**: C, 58.0; H, 4.7.

^{1}H NMR (500 MHz, CD_2Cl_2, 25 ºC) δ: 7.50 (t, 2 H, H$_b$), 7.38 (t, 4 H, H$_d$), 7.23 (d, 8 H, H$_c$), 7.07 (dd, 4 H, $^4J_{HP}$ = 4.0 Hz, H$_a$), 2.42 (hept, 8 H, $^3J_{HH}$ = 6.8 Hz, ^{i}Pr(CH)), 1.23 (d, 24 H, $^3J_{HH}$ = 6.9 Hz ^{i}Pr(CH$_3$)), 1.13 (vt, 12 H, $^2J_{HP}$ = 3.6 Hz, PMe$_2$), 0.99 (d, 24 H, $^3J_{HH}$ = 6.6 Hz, ^{i}Pr(CH$_3$)). All aromatic couplings are of *ca*. 7.5 Hz.

^{13}C{^{1}H} NMR (125 MHz, CD_2Cl_2, 25 ºC) δ: 147.6 (C$_4$), 146.1 (vt, $^2J_{CP}$ = 6 Hz, C$_2$), 139.3 (C$_3$), 134.2 (vt, $^3J_{CP}$ = 5 Hz, CH$_a$), 131.3 (CH$_b$), 130.5 (CH$_d$), 1228.1 (d, $^1J_{CP}$ = 40 Hz, C$_1$), 124.5 (CH$_c$), 32.1 (^{i}Pr(CH)), 25.6 (^{i}Pr(CH$_3$)), 23.4 (^{i}Pr(CH$_3$)), 16.7 (vt, $^1J_{CP}$ = 17 Hz, PMe$_2$).

^{31}P{^{1}H} NMR (200 MHz, CD_2Cl_2, 25 ºC) δ: 6.3.

EM (ES) m/*z* Calcd. for M$^+$: 1113.59. **Expt.**: 1113.7.

$[Au(PMe_2Ar^{Trip2})_2][B(C_6F_5)_4]$ (5d)

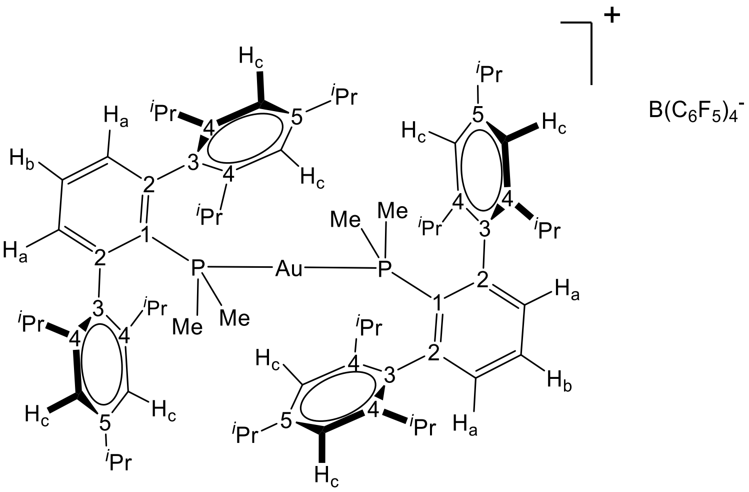

Anal. Calcd. for $C_{108}H_{122}AuBF_{24}P_2$: C, 60.5; H, 5.7. **Found**: C, 60.1; H, 5.3.

^{1}H NMR (400 MHz, CD_2Cl_2, 25 ºC) δ: 7.45 (t, 2 H, H_b), 7.05 (s, 8 H, H_c), 7.03 (vdt, 4 H, $^4J_{HP}$ = 2.0 Hz, H_a), 2.84 (hept, 4 H, $^3J_{HH}$ = 7.0 Hz, *p*-^{i}Pr(CH)), 2.39 (hept, 8 H, $^3J_{HH}$ = 6.8 Hz, *o*-^{i}Pr(CH)), 1.22 (d, 48 H, $^3J_{HH}$ = 6.9 Hz, *o,p*-^{i}Pr(CH_3)), 1.03 (m, 12 H, $^2J_{HP}$ = 3.7 Hz, PMe_2), 0.97 (d, 24 H, $^3J_{HH}$ = 6.9 Hz, *o*-^{i}Pr(CH_3)). All aromatic couplings are of *ca*. 7.5 Hz.

^{13}C{^{1}H} NMR (100 MHz, CD_2Cl_2, 25 ºC) δ: 150.4 (C_5), 147.5 (C_4), 146.5 (vt, $^2J_{CP}$ = 7 Hz, C_2), 137.0 ($^3J_{CP}$ = 3 Hz, C_3), 134.3 (m, $^3J_{CP}$ = 4 Hz, CH_a), 131.2 (CH_b), 128.1 (m, $^1J_{CP}$ = 31 Hz, C_1), 122.4 (CH_c), 35.0 (*p*-^{i}Pr(CH)), 32.1 (*o*-^{i}Pr(CH)), 25.6 (*o*-^{i}Pr(CH_3)), 24.4 (*o/p*-^{i}Pr(CH_3)), 23.3 (*o/p*-^{i}Pr(CH_3)), 16.8 (m, $^1J_{CP}$ = 17 Hz, PMe_2).

^{31}P{^{1}H} NMR (162 MHz, CD_2Cl_2, 25 ºC) δ: 7.1.

EM (ES) m/*z* Calcd. for M^+: 1281.77. **Expt.**: 1282.0.

2.4.12 Compound $[Au_2(\mu\text{-}C_2H_5)(PMe_2Ar')_2][NTf_2]$ (6a)

A solid mixture of ethyl gold precursor **2a** (10 mg, 0.0175 mmol) with 1 equivalent of its parent compound $[Au(PMe_2Ar^{Xyl2})][NTf_2]$ (14 mg, 0.0175 mmol) were dissolved in CD_2Cl_2 (0.6 mL) under nitrogen at -50ºC to rapidly yield the desired ethyl-bridged complex **6a** in quantitative NMR spectroscopic yield. Characterization of compound **6a** was carried out by multinuclear NMR spectroscopy at low temperature without further purification. Alternatively, **6a** can be prepared in comparable yield by treating compounds **2a** (20 mg, 0.035 mmol) with half equivalent of $[Ph_3C][B(C_6F_5)_4]$ (16 mg, 0.0175 mmol) in dichloromethane under otherwise identical conditions.

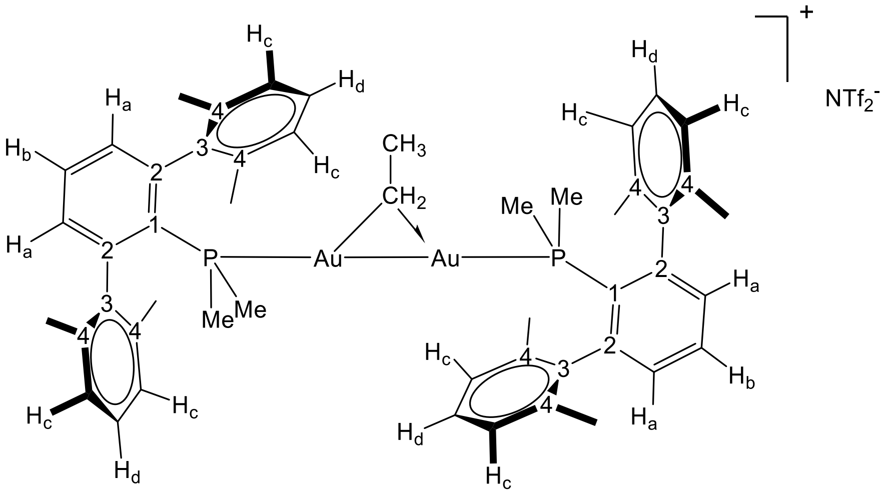

^{1}H NMR (400 MHz, CD_2Cl_2, -65 ºC) δ: 7.62 (br t, 2 H, H_b), 7.26 (t, 4 H, H_d), 7.16 -6.96 (m, 12 H, H_a, H_c), 1.94 (s, 24 H, CH_3(Xyl)), 1.38 (broad, 3 H, $AuCH_2CH_3$...Au), 1.18 (broad, 12 H, $^2J_{HP}$ = 7.8 Hz, PMe_2), 0.96 (m, 3 H, $AuCH_2CH_3$...Au). All aromatic couplings are of *ca*. 7.5 Hz.

$^{13}C\{^1H\}$ NMR (100 MHz, CD_2Cl_2, -65 ºC) δ: 146.5 (d, $^2J_{CP}$ = 13 Hz, C_2) , 140.5 (C_3), 136.3 (C_4), 133.0 (CH_b), 131.1 (CH_a), 128.2 (CH_d), 127.5 (CH_c), 125.7 (d, $^1J_{CP}$ = 52 Hz, C_1), 21.8 (CH_3(Xyl)), 16.2 (d, $^1J_{CP}$ = 37 Hz, PMe_2), 20.8 (d, $^1J_{CP}$ = 131 Hz, AuCH_2CH_3···Au), 15.7 (AuCH_2CH_3···Au).

^{31}P{^{1}H} NMR (162 MHz, CD_2Cl_2, -65 ºC) δ: 2.08.

2.4.13 Compound $[Au_2(\mu\text{-}C_6H_5)(PMe_2Ar')_2][NTf_2]$ (7a)

A solid mixture of ethyl gold precursor **3a** (11 mg, 0.0175 mmol) with 1 equivalent of its parent compound $[Au(PMe_2Ar^{Xyl2})][NTf_2]$ (14 mg, 0.0175 mmol) were dissolved in CD_2Cl_2 (0.6 mL) under nitrogen at -50ºC to rapidly yield the desired phenyl-bridged complex **7a** in quantitative NMR spectroscopic yield. Characterization of compound **7a** was carried out by multinuclear NMR spectroscopy at low temperature without further purification. Alternatively, **7a** can be prepared in comparable yield by treating compounds **3a** (22 mg, 0.035 mmol) with half equivalent of $[Ph_3C][B(C_6F_5)_4]$ (16 mg, 0.0175 mmol) in dichloromethane under otherwise identical conditions.

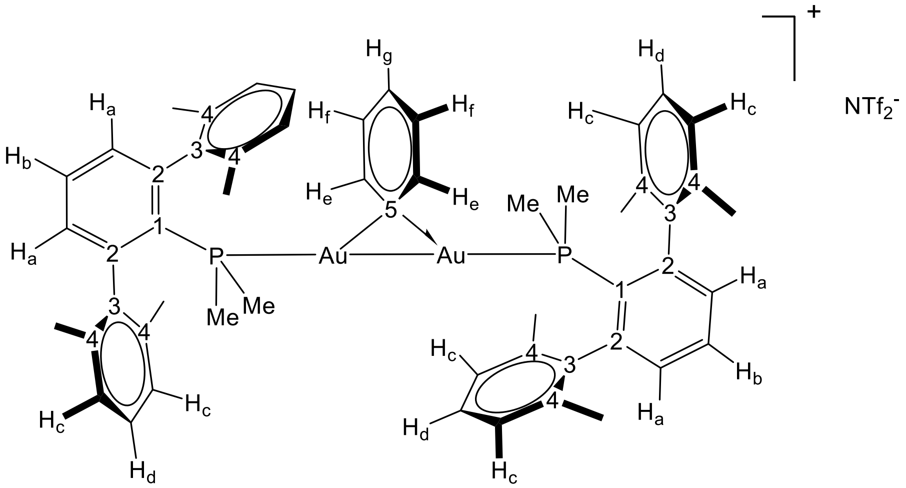

^{1}H NMR (400 MHz, CD_2Cl_2, -20 ºC) δ: 7.58 (t, 3 H, $^5J_{HP}$ = 1.6 Hz (H_b), H_b, H_g), 7.50 (t, 2 H, H_f), 7.42 (d, 2 H, H_e), 7.09 (t, 4 H, H_d), 7.04 (dd, 4 H, $^4J_{HP}$ = 3.3 Hz, H_a), 6.96 (d, 8 H, H_c), 1.92 (s, 24 H, CH_3(Xyl)), 1.01 (d, 12 H, $^2J_{HP}$ = 9.7 Hz, PMe_2). All aromatic couplings are of *ca*. 7.5 Hz.

^{13}C{^{1}H} NMR (100 MHz, CD_2Cl_2, -35 ºC) δ: 150.2 (CH_e), 146.0 (d, $^{2}J_{CP}$ = 10 Hz, C_2), 140.5 (C_{arom}), 136.7 (d, $^{2}J_{CP}$ = 27 Hz,), 136.4 (C_{arom}), 132.6 (CH_b), 131.3 (d, $^{3}J_{CP}$ = 8 Hz, CH_a), 128.8 (CH_d), 128.8 (d, $^{3}J_{CP}$ = 34 Hz,), 128.2 (CH_f), 128.0 (CH_c), 126.3 (d, $^{1}J_{CP}$ = 52 Hz, C_1), 22.0 (CH_3(Xyl)), 16.8 (d, $^{1}J_{CP}$ = 37 Hz, PMe_2).

^{31}P{^{1}H} NMR (162 MHz, CD_2Cl_2, -20 ºC) δ: 3.1.

2.4.14 X-Ray Structural Characterization of new compounds.

A suitable single crystal of **1a, 1e, 4e, 1f, 4f, 2a, 3a,** or [Au^{t}BuXPhos][NTf_2] was coated with Paratone oil and mounted on a MiTeGen MicroLoop. The X-ray intensity data were measured on a Bruker Kappa APEXII Duo system (**1e**, **4e**, **1f**, **4f**, [Au^{t}BuXPhos][NTf_2]), a Bruker D8 Quest APEX-III single crystal diffractometer with a Photon III detector, and a IμS 3.0 microfocus X-ray source (**1a**, **2a,** and **3a**). The frames were integrated with the Bruker SAINT software package using a narrow-frame algorithm. Data were corrected for absorption effects using the Multi-Scan method (SADABS). The structure was solved and refined using the Bruker SHELXTL Software Package[67] within APEX3[68] and OLEX2.[69] Non-hydrogen atoms were refined anisotropically. Hydrogen atoms were placed in geometrically calculated positions with $U_{iso} = 1.2U_{equiv}$ of the parent atom ($U_{iso} = 1.5U_{equiv}$ for methyl), except for the hydrogen atoms of the bridging methyls in 4a and 5a. Those were located in the diffraction map and refined isotropically with restraints on their bonds.

In **4e**, the relative occupancies of the disordered gold atoms were freely refined, with constraints on the anisotropic displacement parameters of the disordered atoms. In **1f**, one isopropyl substituent was found to be disordered over two positions. The relative occupancies were allowed to refine freely, with constraints on the anisotropic displacement parameters of the disordered atoms. In **2a**, one ethyl group was disordered over two positions. The relative occupancies were allowed to refine freely, with constraints on the anisotropic displacement parameters of the disordered atoms and restraints on the disordered bonds.

A summary of all crystallographic data and refinement parameters for each compound is provided in Tables 2.4 and 2.5. Atomic coordinates, anisotropic displacement parameters, and bond lengths and angles can be found in the cif files which have been deposited in the Cambridge Crystallographic Data Centre with no. 2024182-2024189. These data can be obtained free of charge from The Cambridge Crystallographic Data Centre via www.ccdc.cam.ac.uk/data_request/cif.

Table 2.4. Crystal data table for **1a**, **1e**, **4e,** and **1f**.

	1a	**1e**	**4e**	**1f**
CCDC	2024182	2024183	2024187	2024184
Chemical formula	$C_{25}H_{30}AuP$	$C_{34}H_{52}AuP$	$C_{69}H_{101}Au_2F_6NO_4P_2S_2$	$C_{30}H_{48}AuP$
FW (g/mol)	558.42	688.69	1642.49	636.62
T (K)	193.0	100(2)	100(2)	100(2)
λ (Å)	0.71073	0.71073	0.71073	0.71073
Crystal size (mm)	0.20 x 0.18 x 0.12	0.152 x 0.240 x 0.325	0.238 x 0.379 x 0.478	0.224 x 0.248 x 0.275
Crystal habit	colorless block	colorless block	colorless block	colorless block
Crystal system	orthorhombic	monoclinic	triclinic	monoclinic
Space group	Pbca	C 2/c	P 1	P c
a (Å)	13.8037(8)	40.915(2)	15.0694(16)	18.9574(17)
b (Å)	18.0029(11)	8.9350(5)	16.8288(18)	8.4438(8)
c (Å)	18.0091(10)	17.4189(9)	22.109(3)	19.3004(17)
α (°)	90	90	104.309(3)	90
β (°)	90	97.5600(10)	98.936(3)	111.859(2)
γ (°)	90	90	95.867(3)	90
V (Å^3)	4475.4(5)	6312.6(6)	5308.7(10)	2867.3(5)
Z	8	8	3	4

ρ_{calc} (g/cm$^{3)}$	1.658	1.449	1.541	1.475
μ (mm^{-1})	6.653	4.731	4.306	5.201
F(000)	2192.0	2800	2484	1288
θ range (°)	2.18 to 28.30	2.01 to 30.54	1.38 to 30.61	2.13 to 30.55
Index ranges	-18 ≤ h ≤ 18 -23 ≤ k ≤ 23 -21 ≤ h ≤ 24	-42 ≤ h ≤ 58 -12 ≤ k ≤ 12 -24 ≤ h ≤ 24	-21 ≤ h ≤ 21 -24 ≤ k ≤ 24 -31 ≤ h ≤ 31	-27 ≤ h ≤ 27 -12 ≤ k ≤ 12 -27 ≤ h ≤ 27
Reflns coll.	95964	40992	129263	64529
Ind. reflns	5544 [R_{int} = 0.0366	9646 [R_{int} = 0.0241]	63746 [R_{int} = 0.0333]	17476 [R_{int} = 0.0345]
Data / restraints / parameters	5544/0/251	9646 / 0 / 332	63746 / 25 / 2370	17476 / 2 / 616
Goodness-of-fit on F^2	1.093	1.051	0.864	1.030
R_1 [I>2σ(I)]	0.0203	0.0166	0.0312	0.0222
wR_2 [all data]	0.0529	0.0375	0.0644	0.0434

Table 2.5. Crystal data table for **4f**, **2a**, **3a** and [Au^{t}BuXPhos][NTf_2].

	4f	**2a**	**3a**	**[Au^{t}BuXPhos][NTf_2]**
CCDC	2024188	2024185	2024186	2024189
Chemical formula	$C_{62}H_{95}Au_2Cl_2F_6NO_4P_2S_2$	$C_{54}H_{68}Au_2P_2$	$C_{30}H_{32}AuP$	$C_{31}H_{45}AuF_6NO_4PS_2$
FW (g/mol)	1623.28	1172.95	620.49	901.73
T (K)	100(2)	193(2)	193(2)	100(2)
λ (Å)	0.71073	0.71073	0.71073	0.71073
Crystal size (mm)	0.110 x 0.220 x 0.302	0.18 x 0.16 x 0.11	0.13 x 0.10 x 0.10	0.135 x 0.137 x 0.201
Crystal habit	colorless plate	colorless block	colorless block	colorless block
Crystal system	orthorhombic	monoclinic	monoclinic	triclinic
Space group	P na2_1	P2_1/c	P2_1/c	P -1
a (Å)	20.9449(16)	14.2800(9)	13.316(2)	9.2643(10)
b (Å)	24.264(2)	18.6671(12)	11.617(2)	11.2170(12)
c (Å)	13.1754(10)	18.2973(11)	17.075(3)	18.946(2)
α (°)	90	90	90	104.572(3)
β (°)	90	91.008(3)	102.132(11)	96.137(3)
γ (°)	90	90	90	105.686(3)
V (Å^3)	6695.8(9)	4876.7(5)	2582.4(8)	1801.9(3)
Z	4	4	4	2
ρ_{calc} (g/cm$^{3)}$	1.610	1.598	1.596	1.662
μ (mm^{-1})	4.628	6.109	5.774	4.308
F(000)	3256	2320	1224	900
θ range (°)	1.28 to 26.46	2.10 to 27.54	2.14 to 27.49	1.97 to 30.57
Index ranges	-25 ≤ h ≤ 26 -30 ≤ k ≤ 30 -16 ≤ h ≤ 16	-18 ≤ h ≤ 18 -24 ≤ k ≤ 24 -23 ≤ h ≤ 20	-16 ≤ h ≤ 17 -15 ≤ k ≤ 15 -22 ≤ h ≤ 22	-13 ≤ h ≤ 13 -16 ≤ k ≤ 16 -27 ≤ h ≤ 27

Reflns coll.	60632	60230	39055	44948
Ind. reflns	13651 [R_{int} = 0.0470]	11214 [R_{int} = 0.0408	5914 [R_{int} = 0.0752	11031 [R_{int} = 0.0356]
Data / restraints / parameters	13651 / 7 / 766	11214 / 1 / 545	5914 / 0 / 295	11031 / 0 / 427
Goodness-of-fit on F^2	1.071	1.027	1.097	1.023
R_1 [I>2σ(I)]	0.0323	0.0456	0.0448	0.0210
wR_2 [all data]	0.0697	0.1242	0.1292	0.0454

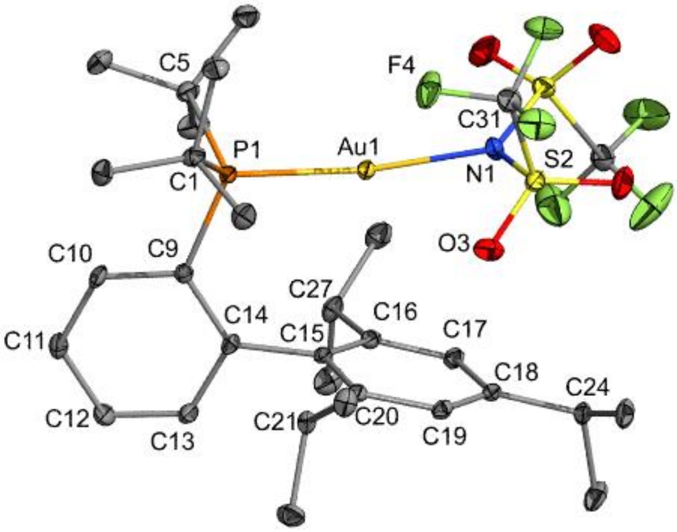

Figure 2.24. ORTEP structure of [Au^{t}BuXPhos][NTf_2] represented at 50% probability and where hydrogen atoms have been omitted for clarity. Selected bond lengths (Å): Au1–C15 = 3.1904(2); Au1–C16 = 3.3652(2); Au1–C20 = 3.6406(2); Au···arene centroid = 3.4804(9); Au1–N1 = 2.132(2); Au1–P1 = 2.250(3); Selected bond angles (°): P1–Au1–N1 = 170.05(5); C9–P1–Au1 = 114.70(6).

2.4.15 Kinetic studies. Kinetic studies were performed to determine the order on bridging digold methyl compounds (**4**) during C-C coupling processes. Ethane evolution and the disappearance of compounds **4** have been monitored at several temperatures by ^1H and $^{31}P\{^1H\}$ NMR spectroscopy as reported in the Experimental Section of the main text. Table 2.2 collects the average data obtained for triplicates run for each experiment. Figures 2.12 represent selected examples of the second-order kinetic plots from which data were acquired. Figure 2.8 depicts the corresponding kinetic plot for our preliminary experiments run under the same conditions but between an equimolar mixture of $Au(CH_3)(PPh_3)$ and $Au(PPh_3)(NO_3)$.

2.4.16 Effect of BPh_3. To examine the effect of BPh_3 on the rate of ethane evolution under pseudo-first-order conditions a similar procedure to that employed for other kinetic experiments was followed. An equimolar solid mixture of **1a** (2 mg, 0.0038 mmol) and $Au(PMe_2Ar^{Xyl2})(NTf_2)$ (3 mg, 0.0038 mmol) was placed in a J-Young NMR tube. Excess BPh_3 (5 mg, 0.019 mmol) was added under nitrogen and the mixture dissolved in CD_2Cl_2 at -40ºC. The reaction was monitored at -10 ºC by ^1H and $^{31}P\{^1H\}$ NMR spectroscopy, resulting in a measured pseudo-first-order kinetic constant of $-8.1(2) \times 10^{-4}$ s^{-1}.

2.4.17 DFT calculations. Calculations were performed with Gaussian 09, Revision E.01 software package[70] employing the range-separated hybrid functional ωB97X-D[71] without geometry constraints. The 6-31G(d,p)[72] basis set was used to represent the C, H, P, N, O, S, F, and B atoms and the Stuttgart/Dresden Effective Core Potential and its associated basis set (SDD)[73] to describe the Au atoms. Solvent effects (dichloromethane) were included during optimization with the SMD continuum model.[74] Vibrational analysis was carried out on the stationary points to characterize them as minima or transition states as well as to calculate the thermal corrections to enthalpy and free energy. Free energies were corrected (ΔG_{qh}) to account for errors associated with the harmonic oscillator approximation. Thus, according to Truhlar's quasi-harmonic approximation, all vibrational frequencies below 100 cm^{-1} were set to this value so that the entropy contribution was not overestimated.[75] These anharmonic corrections were calculated with the Goodvibes code.[76]

2.4.18 GC-MS spectra.

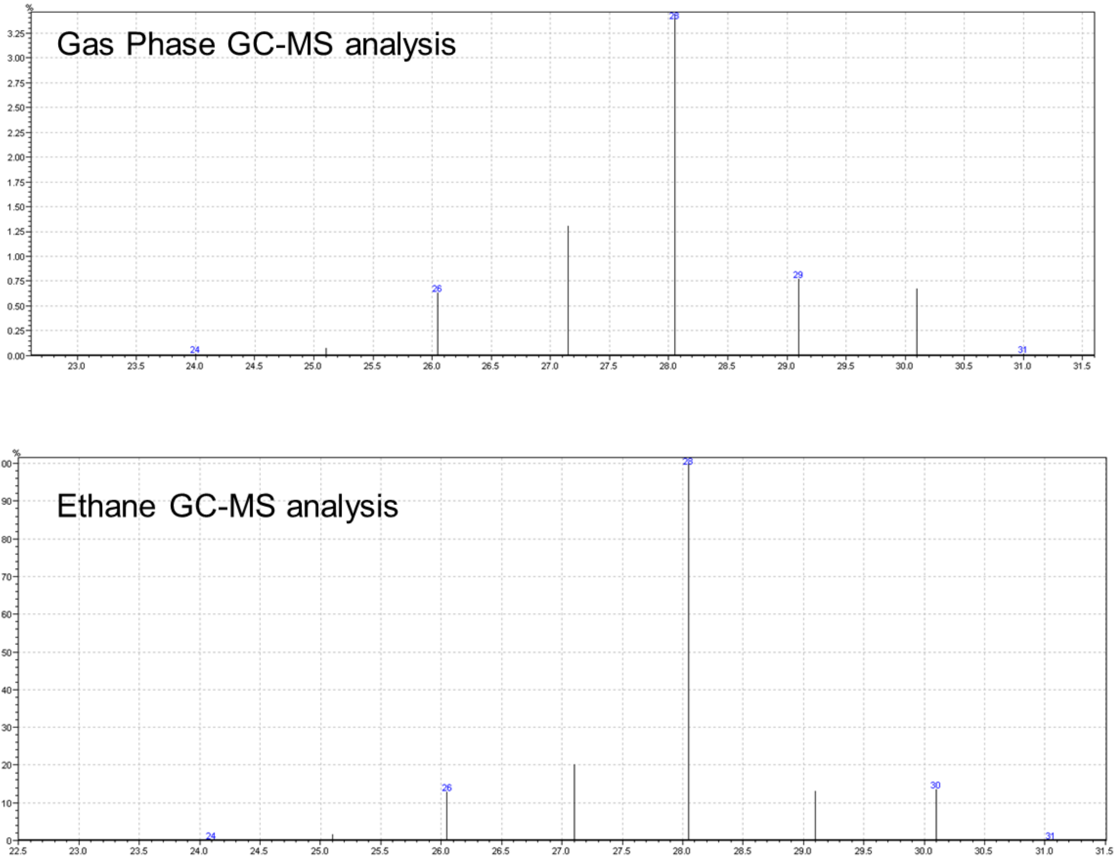

Figure 2.25. MS spectra from GC-MS analysis of the headspace from the C-C coupling reaction from [$Au_2(\mu\text{-}CH_3)(XPhos)_2$][$NTf_2$] (**4f**) (above) and pure ethane (below).

2.4.19 NMR spectra of gold (I) compounds.

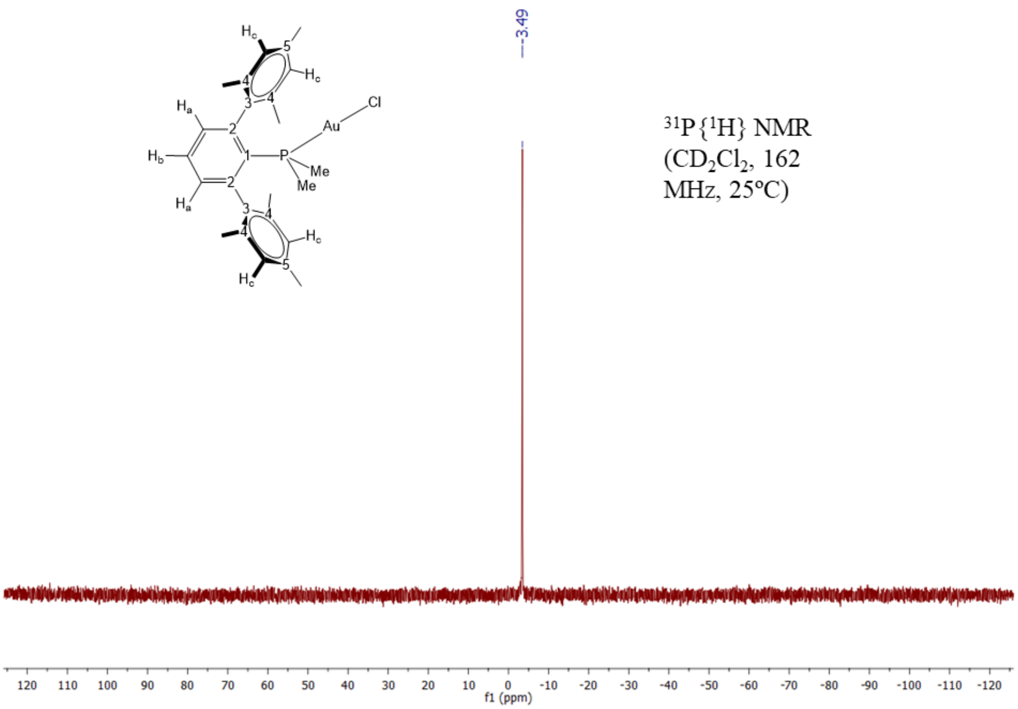

^{31}P{^{1}H} NMR (CD_2Cl_2, 162 MHz, 25ºC)

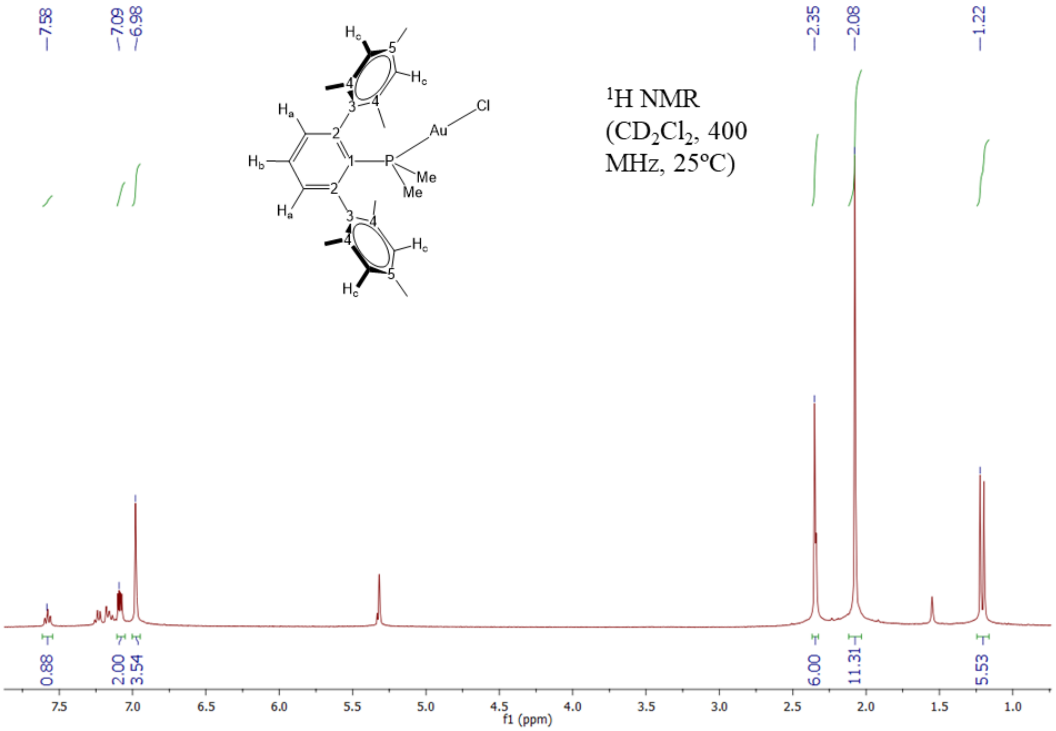
7.58
7.09
6.98
2.35
2.08
1.22
^{1}H NMR (CD$_2$Cl$_2$, 400 MHz, 25ºC)
H$_c$
H$_a$
H$_b$
P
Me
Au
Cl
0.88
2.00
3.54
6.00
11.31
5.53
7.5
7.0
6.5
6.0
5.5
5.0
4.5
4.0
3.5
3.0
2.5
2.0
1.5
1.0
f1 (ppm)

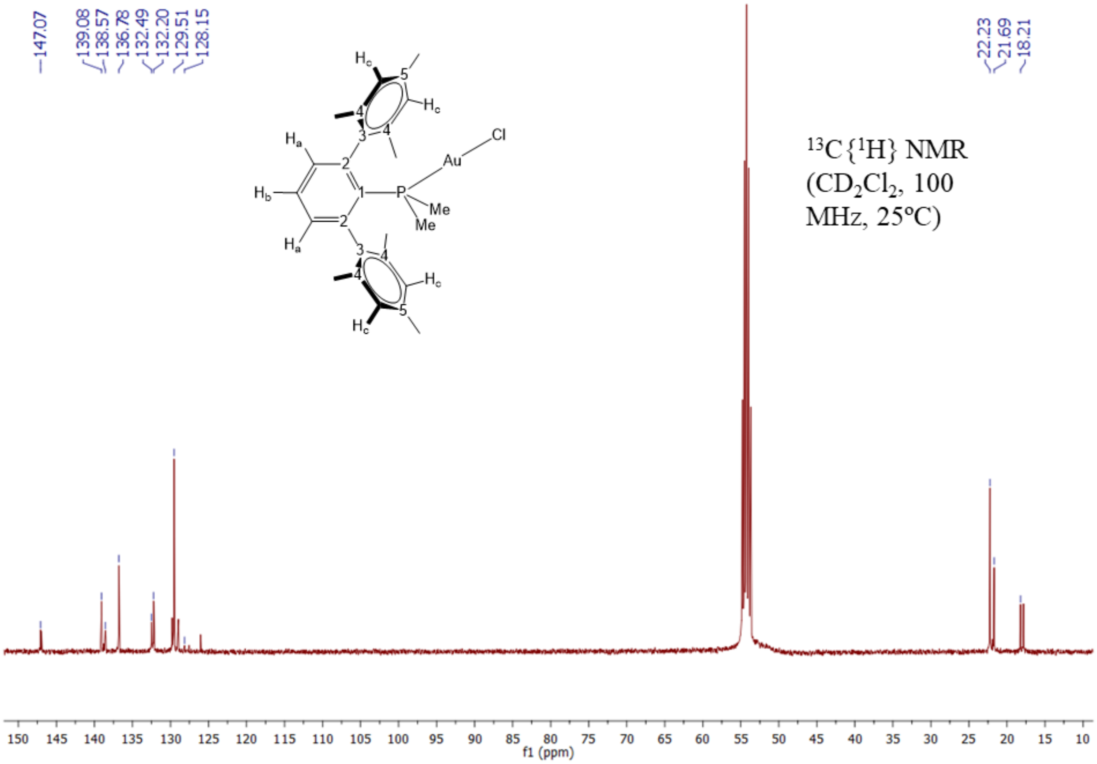
147.07
139.08
138.57
136.78
132.49
132.20
129.51
128.15
22.23
21.69
18.21
^{13}C{^{1}H} NMR (CD$_2$Cl$_2$, 100 MHz, 25ºC)
H$_c$
H$_a$
H$_b$
P
Me
Au
Cl
150
145
140
135
130
125
120
115
110
105
100
95
90
85
80
75
70
65
60
55
50
45
40
35
30
25
20
15
10
f1 (ppm)

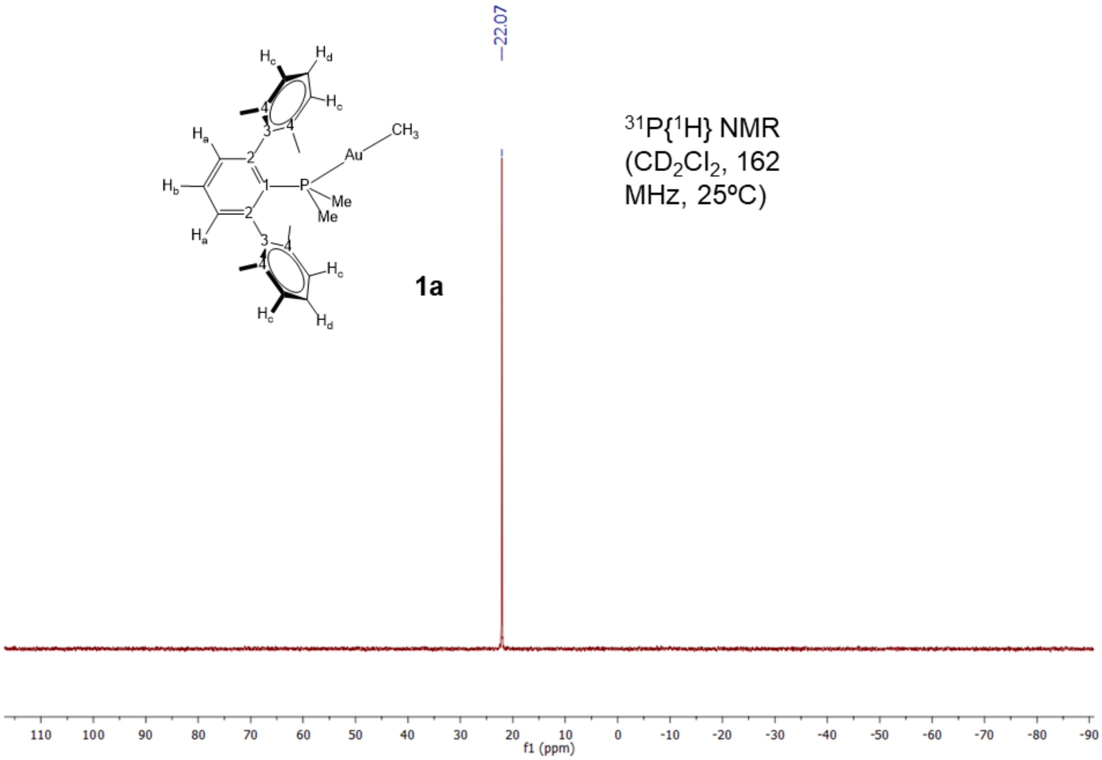

1a

$^{31}P\{^{1}H\}$ NMR (CD_2Cl_2, 162 MHz, 25ºC)

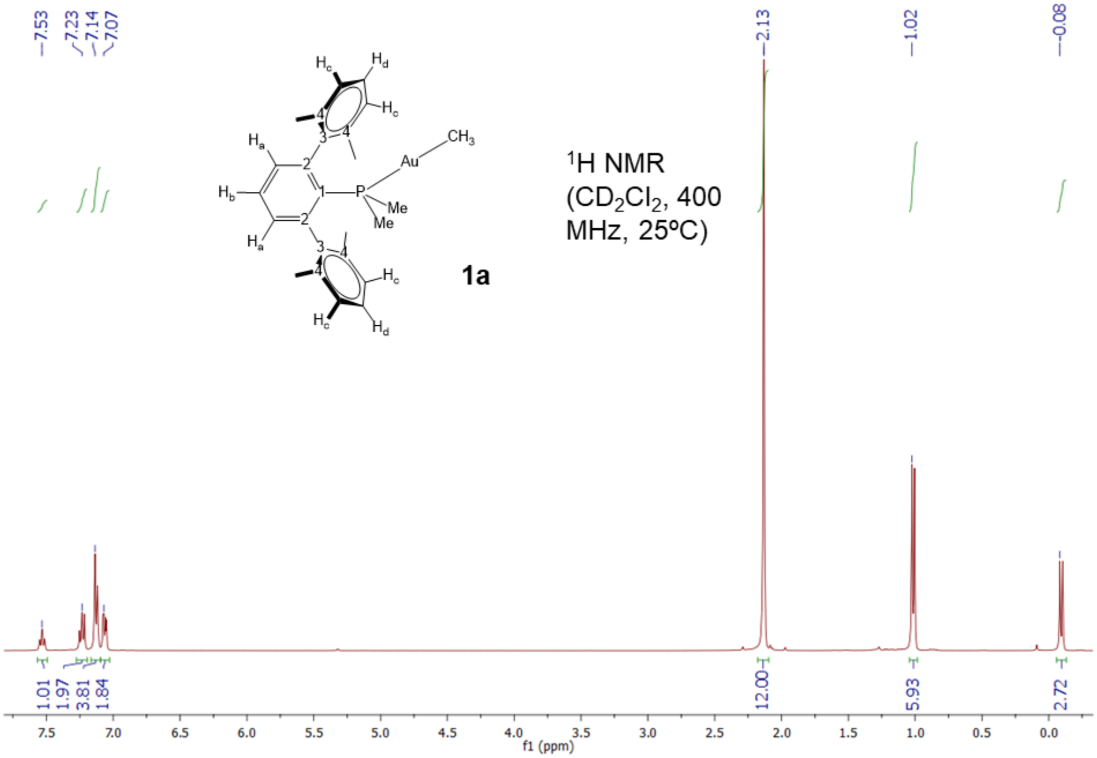

1a

^{1}H NMR (CD_2Cl_2, 400 MHz, 25ºC)

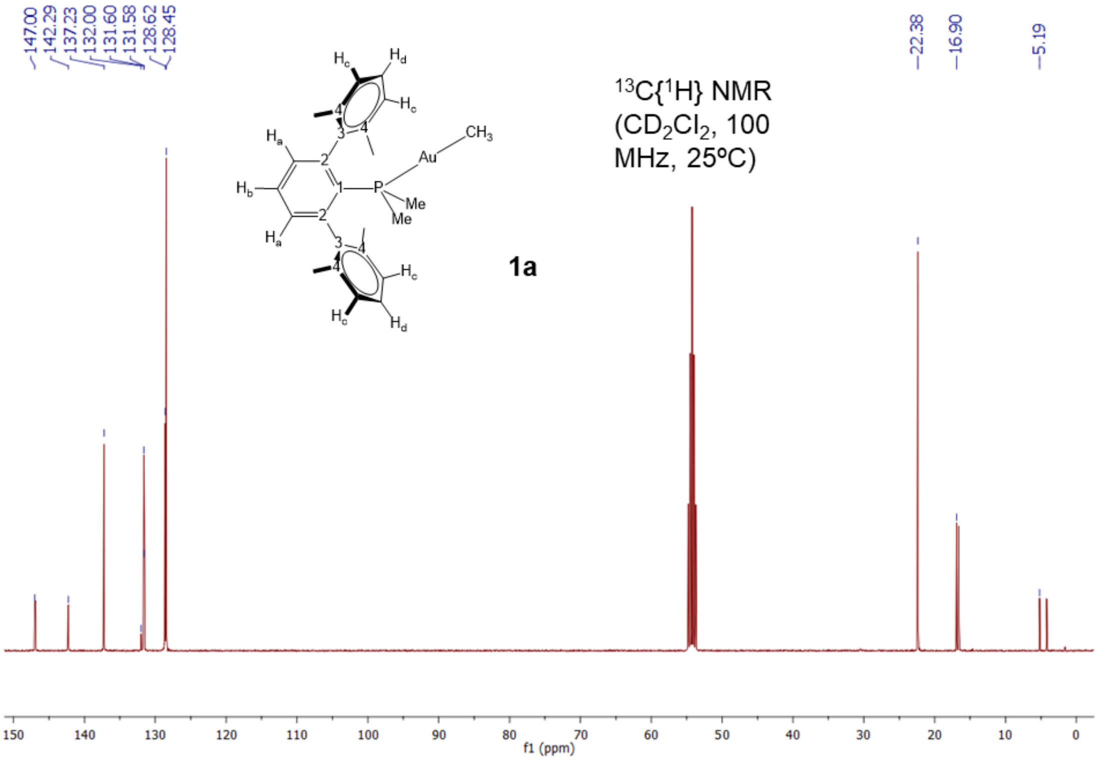

$^{13}C\{^{1}H\}$ NMR (CD_2Cl_2, 100 MHz, 25ºC)

1a

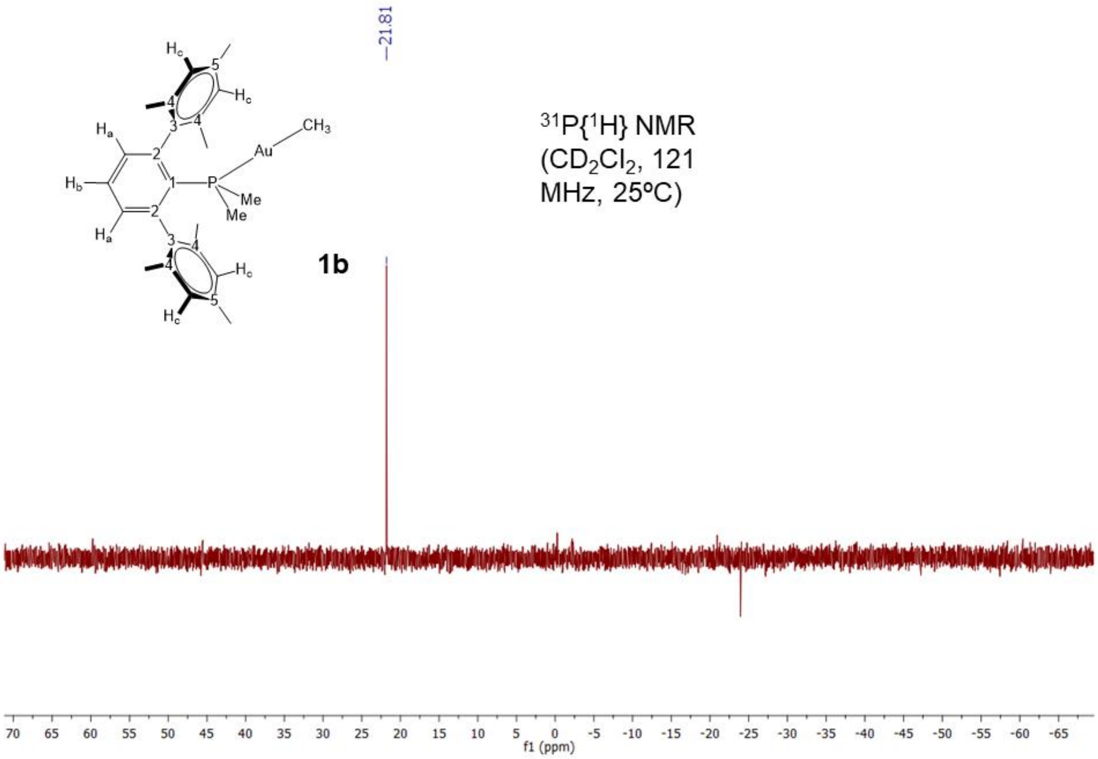

$^{31}P\{^{1}H\}$ NMR (CD_2Cl_2, 121 MHz, 25ºC)

1b

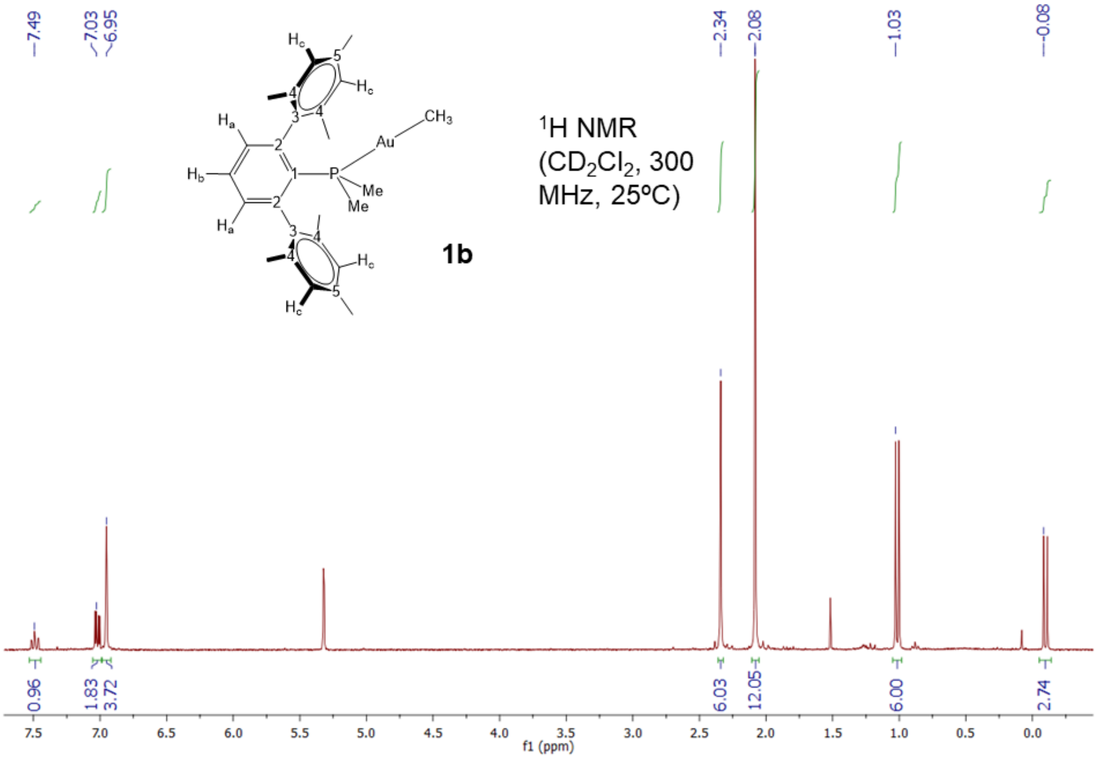

1b

^{1}H NMR (CD_2Cl_2, 300 MHz, 25ºC)

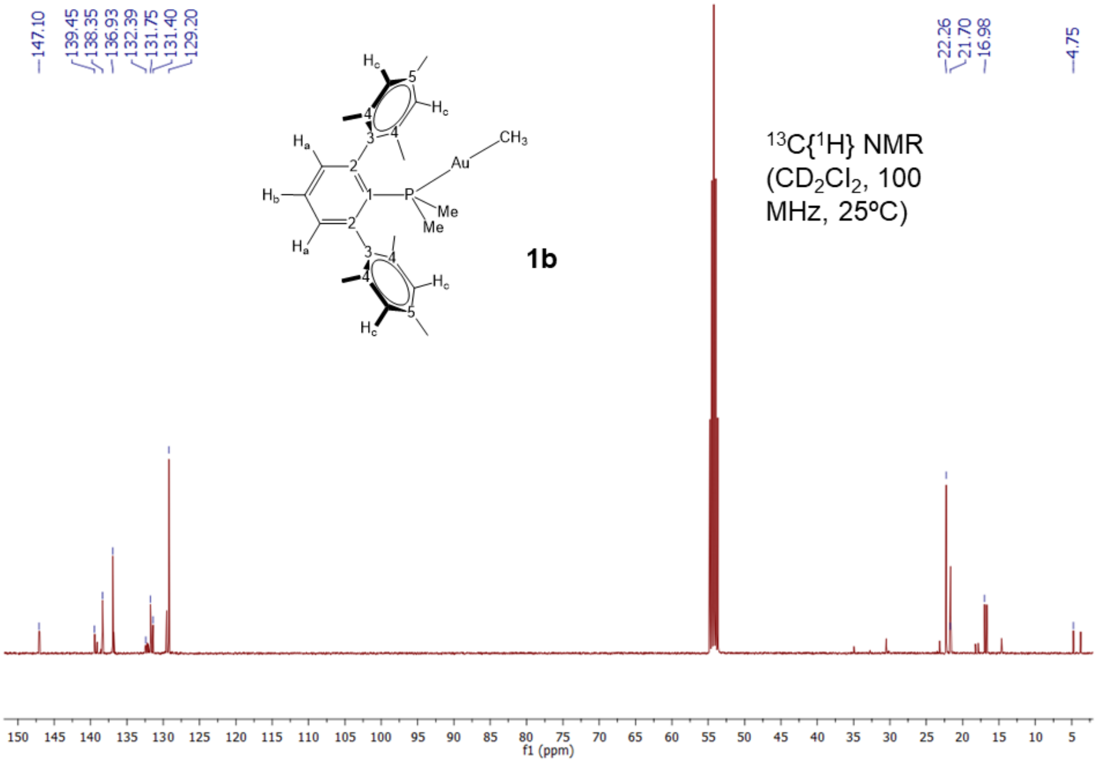
147.10
139.45
138.35
136.93
132.39
131.75
131.40
129.20
22.26
21.70
16.98
4.75
$^{13}C\{^{1}H\}$ NMR
(CD_2Cl_2, 100 MHz, 25ºC)
1b
H_c
H_a
H_b
Au
CH_3
P
Me
150 145 140 135 130 125 120 115 110 105 100 95 90 85 80 75 70 65 60 55 50 45 40 35 30 25 20 15 10 5
f1 (ppm)

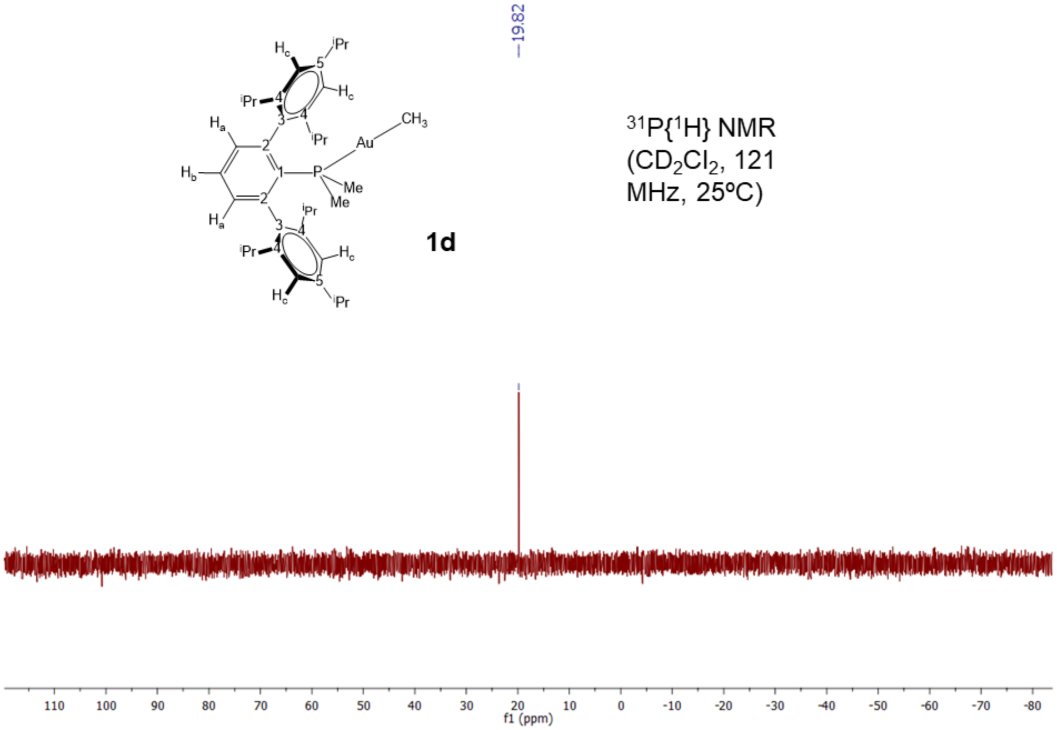
19.82
$^{31}P\{^{1}H\}$ NMR
(CD_2Cl_2, 121 MHz, 25ºC)
1d
H_c
H_a
H_b
^{i}Pr
Au
CH_3
P
Me
110 100 90 80 70 60 50 40 30 20 10 0 -10 -20 -30 -40 -50 -60 -70 -80
f1 (ppm)

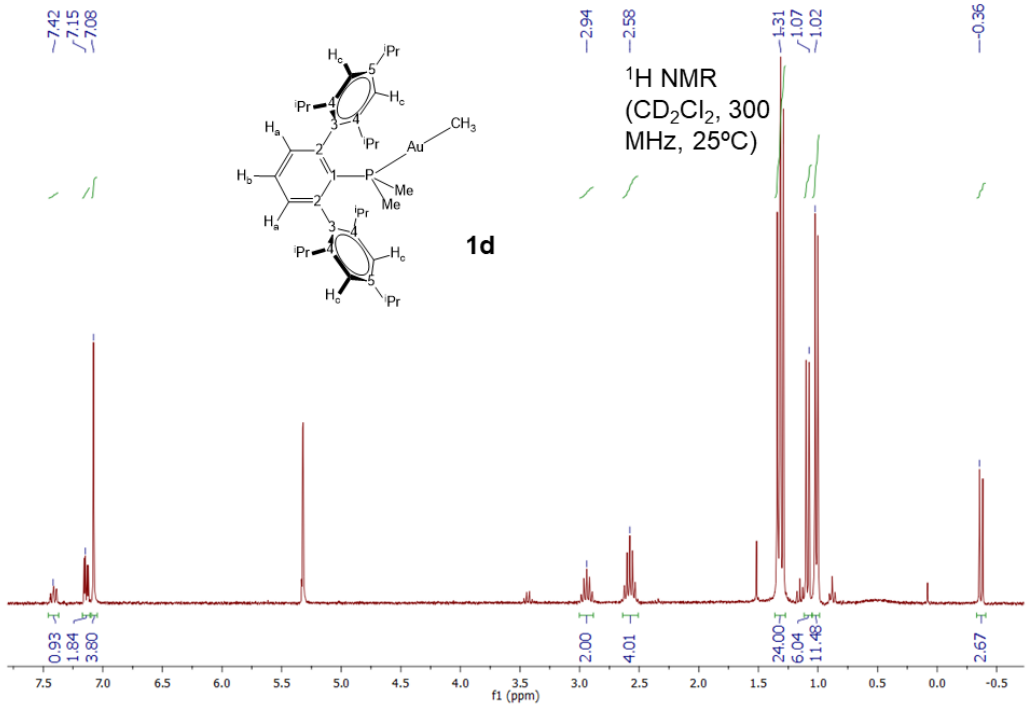
7.42
7.15
7.08
2.94
2.58
1.31
1.07
1.02
-0.36
^{1}H NMR (CD_2Cl_2, 300 MHz, 25ºC)
1d
Hc
iPr
Ha
Hb
P
Au
CH3
Me
Me
0.93
1.84
3.80
2.00
4.01
24.00
6.04
11.48
2.67
7.5
7.0
6.5
6.0
5.5
5.0
4.5
4.0
3.5
3.0
2.5
2.0
1.5
1.0
0.5
0.0
-0.5
f1 (ppm)

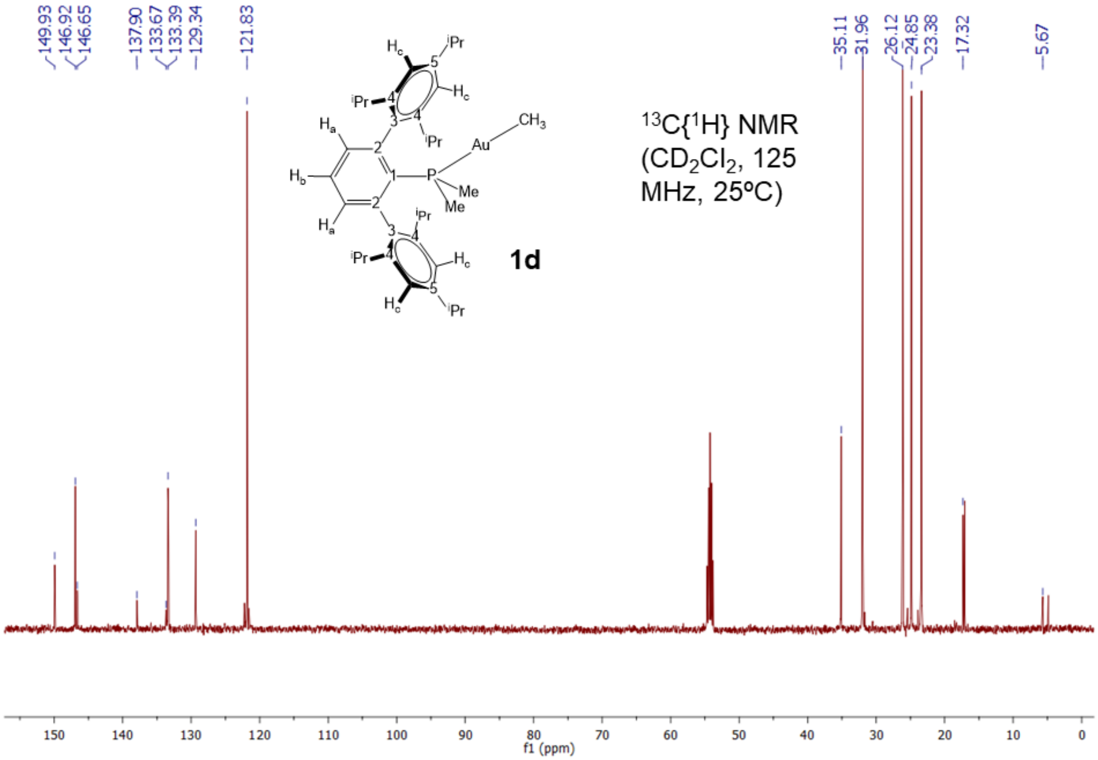
149.93
146.92
146.65
137.90
133.67
133.39
129.34
121.83
35.11
31.96
26.12
24.85
23.38
17.32
5.67
$^{13}C\{^1H\}$ NMR (CD_2Cl_2, 125 MHz, 25ºC)
1d
Hc
iPr
Ha
Hb
P
Au
CH3
Me
Me
150
140
130
120
110
100
90
80
70
60
50
40
30
20
10
0
f1 (ppm)

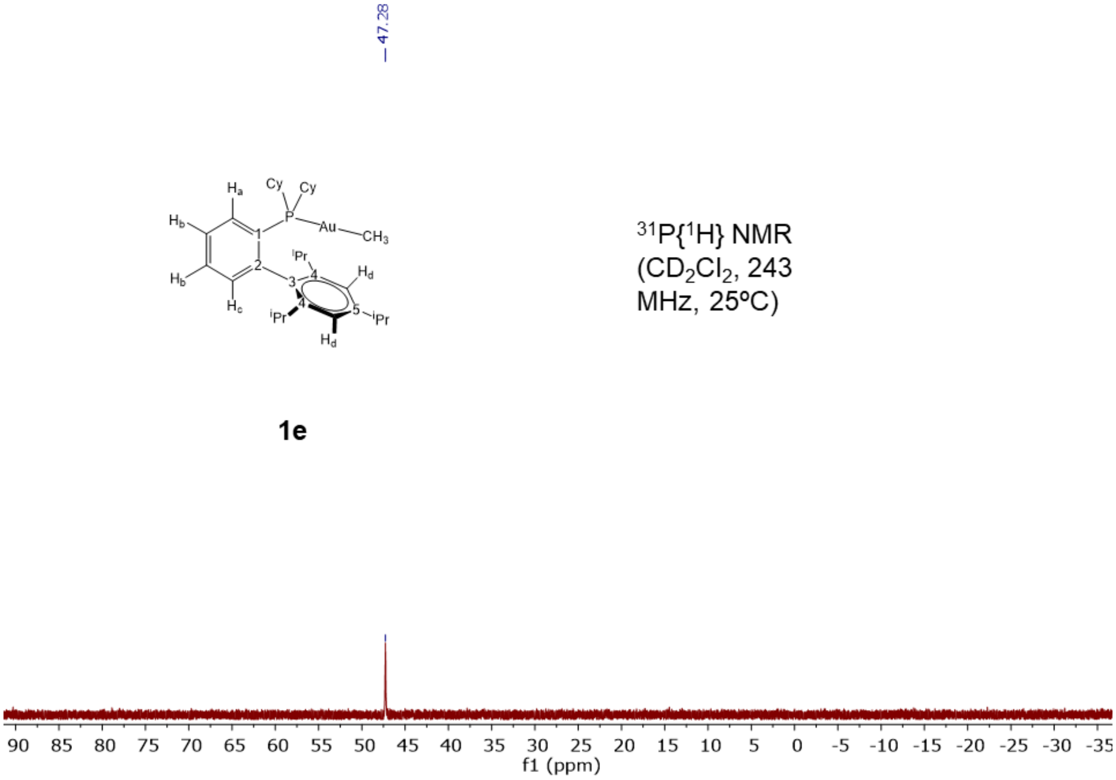

1e

$^{31}P\{^{1}H\}$ NMR (CD_2Cl_2, 243 MHz, 25ºC)

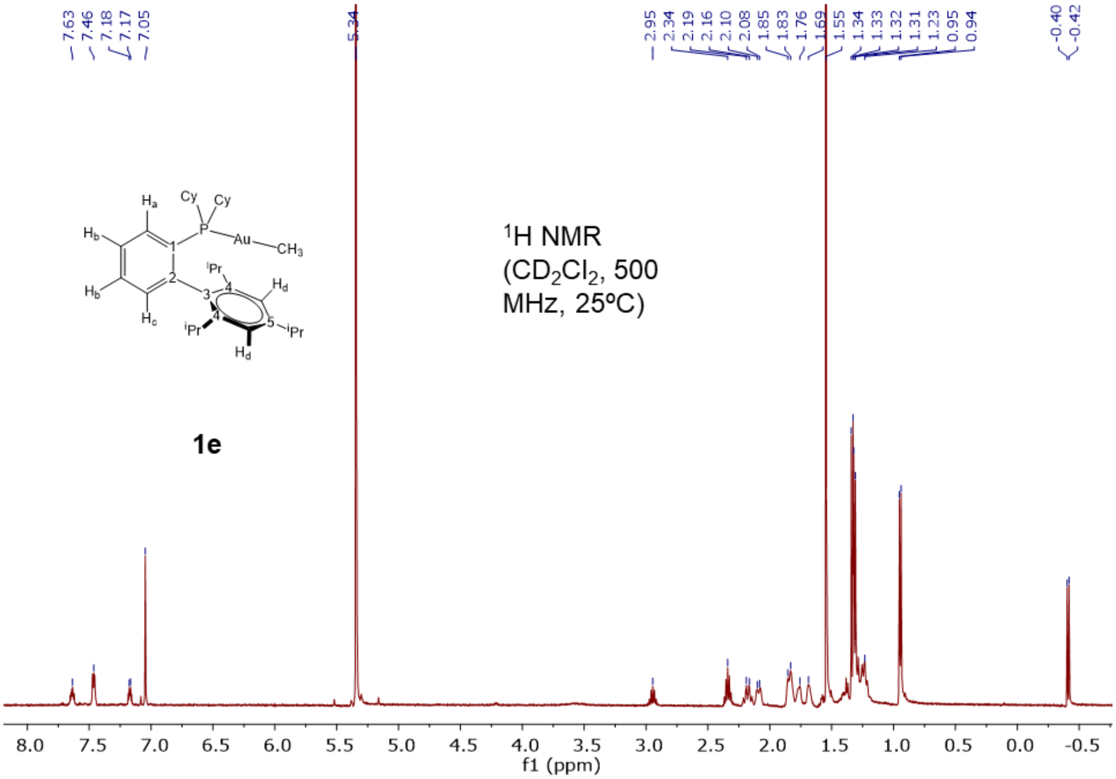

1e

^{1}H NMR (CD_2Cl_2, 500 MHz, 25ºC)

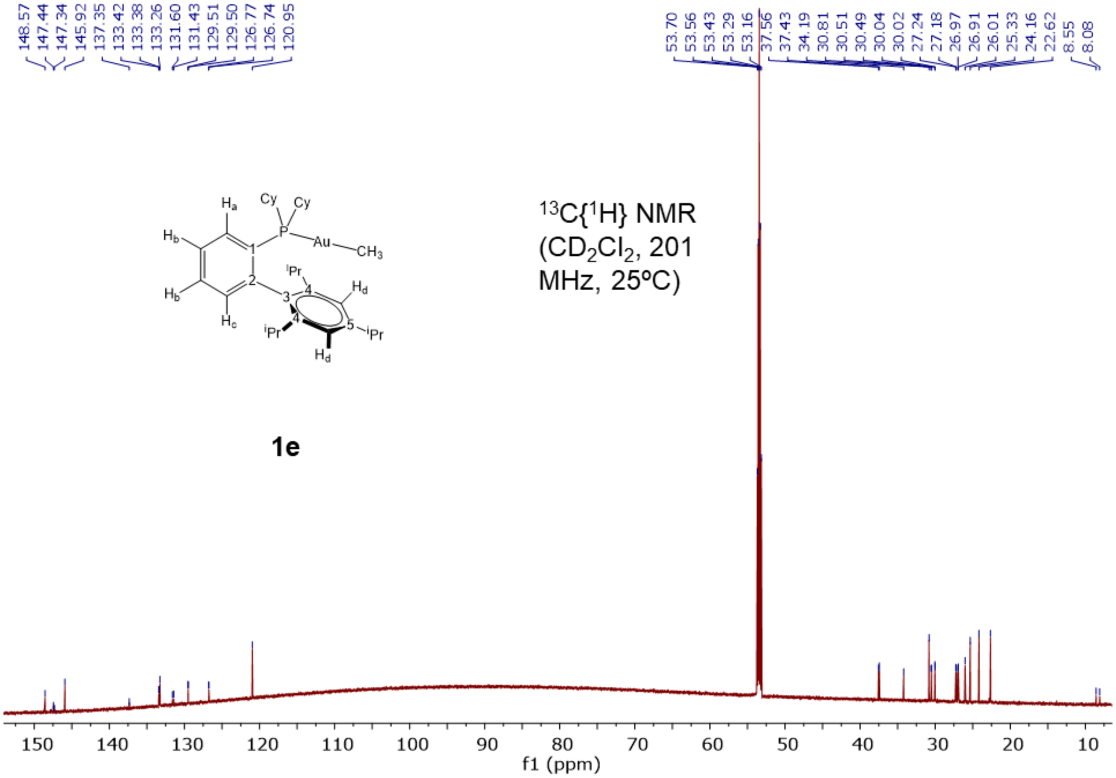

^{13}C{^{1}H} NMR (CD_2Cl_2, 201 MHz, 25ºC)

1e

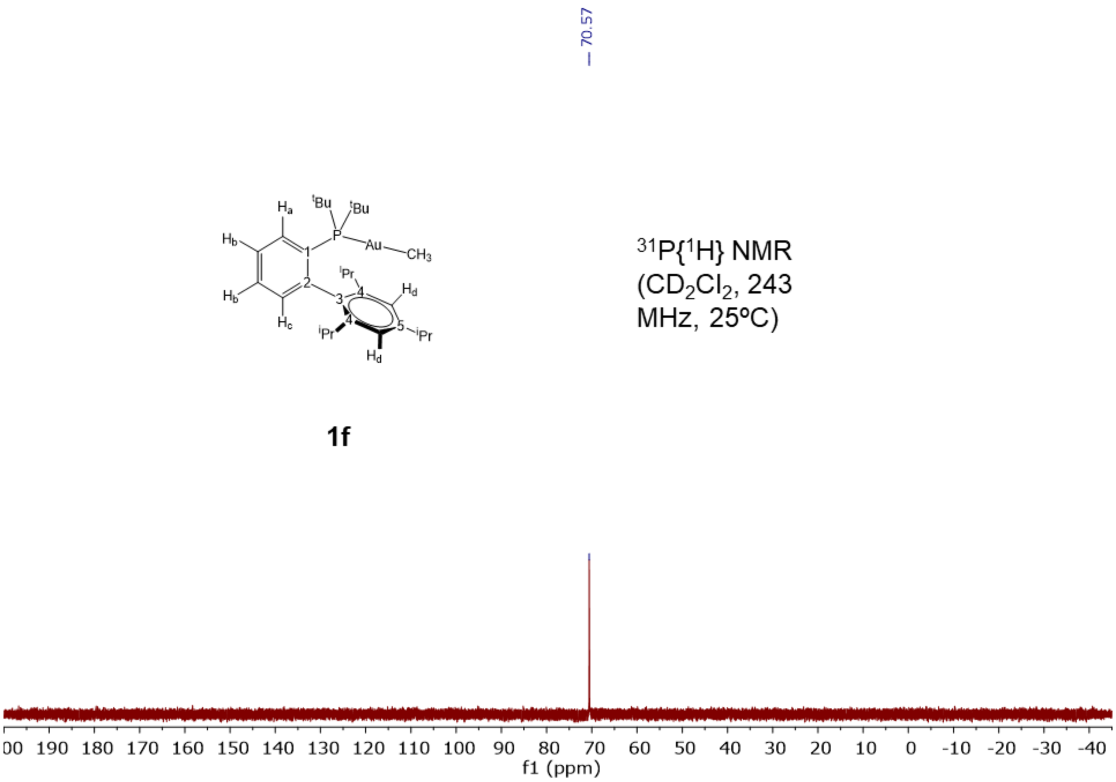

^{31}P{^{1}H} NMR (CD_2Cl_2, 243 MHz, 25ºC)

1f

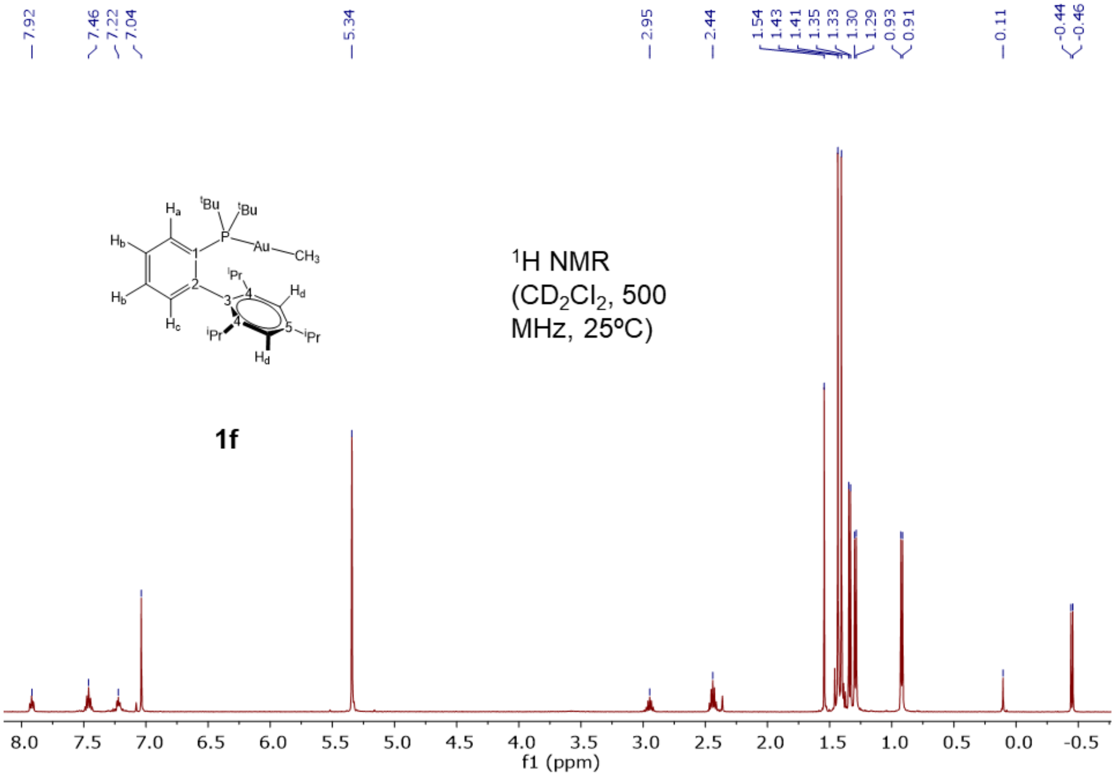

^{1}H NMR (CD_2Cl_2, 500 MHz, 25ºC)

1f

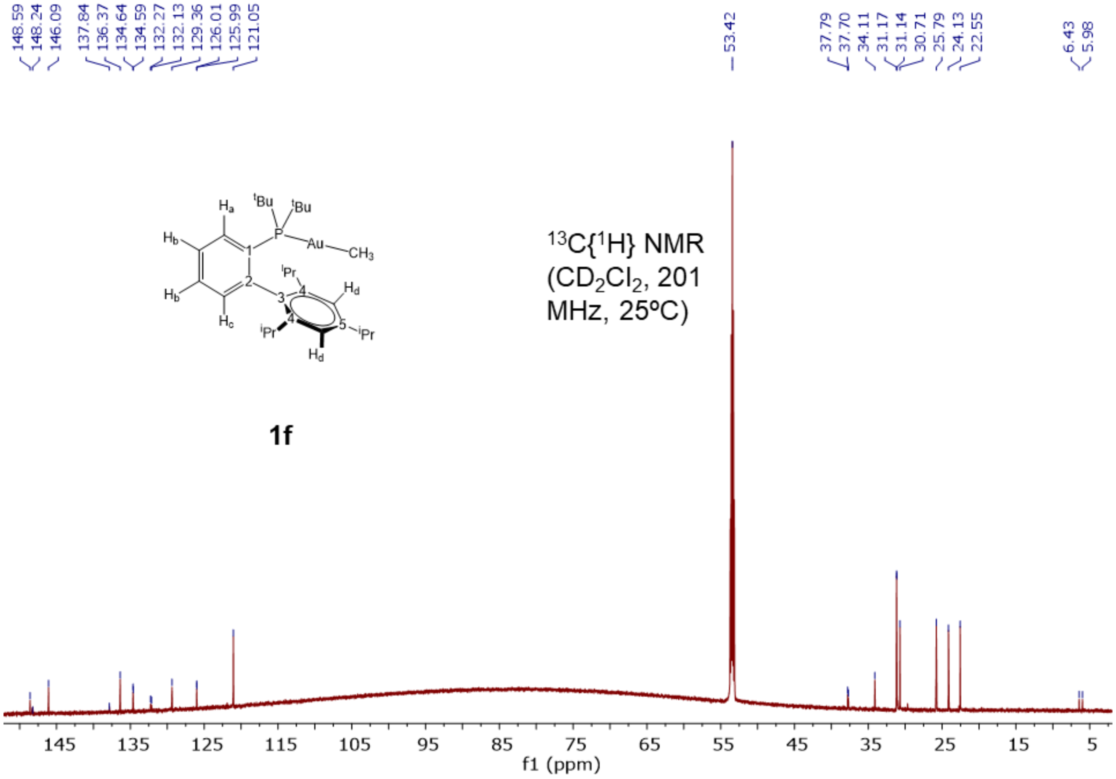

$^{13}C\{^1H\}$ NMR (CD_2Cl_2, 201 MHz, 25ºC)

1f

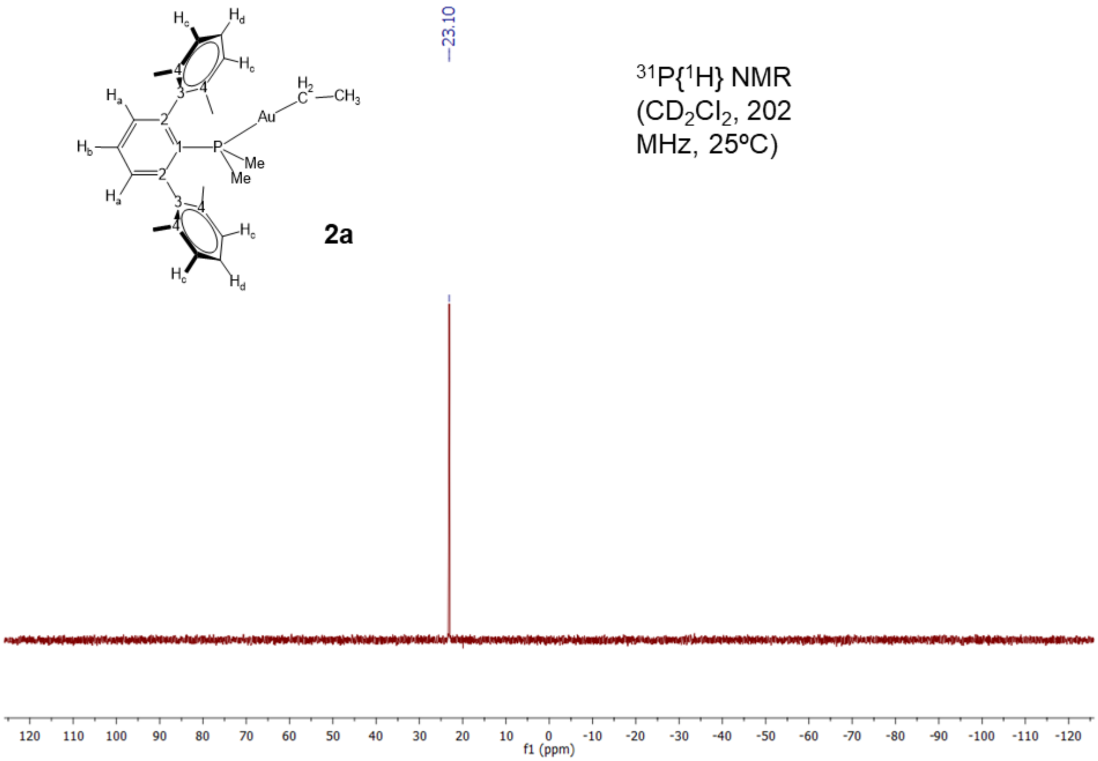

$^{31}P\{^1H\}$ NMR (CD_2Cl_2, 202 MHz, 25ºC)

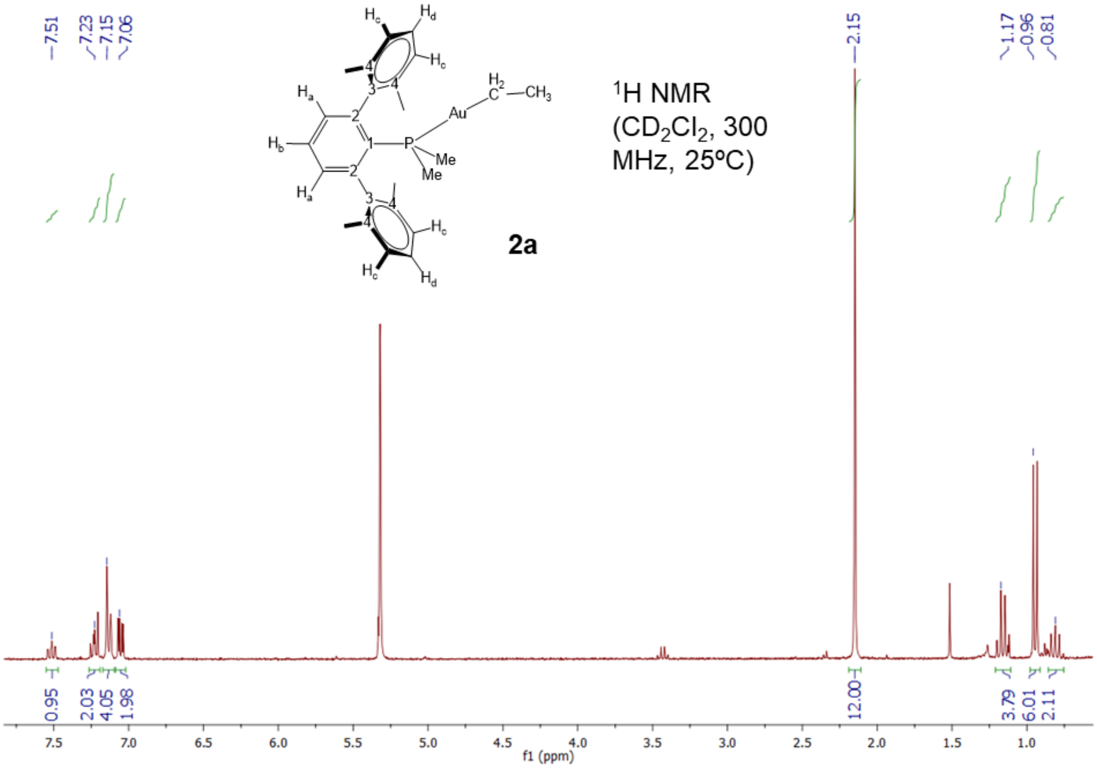

^1H NMR (CD_2Cl_2, 300 MHz, 25ºC)

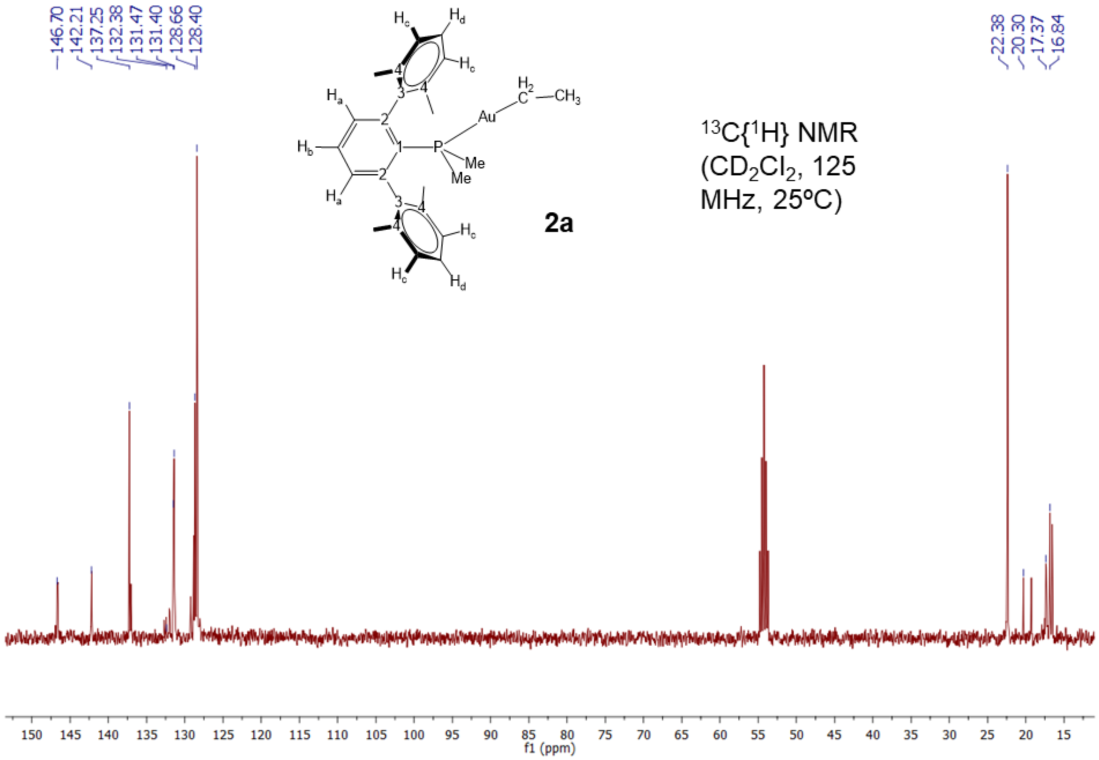

2a

$^{13}C\{^1H\}$ NMR (CD_2Cl_2, 125 MHz, 25ºC)

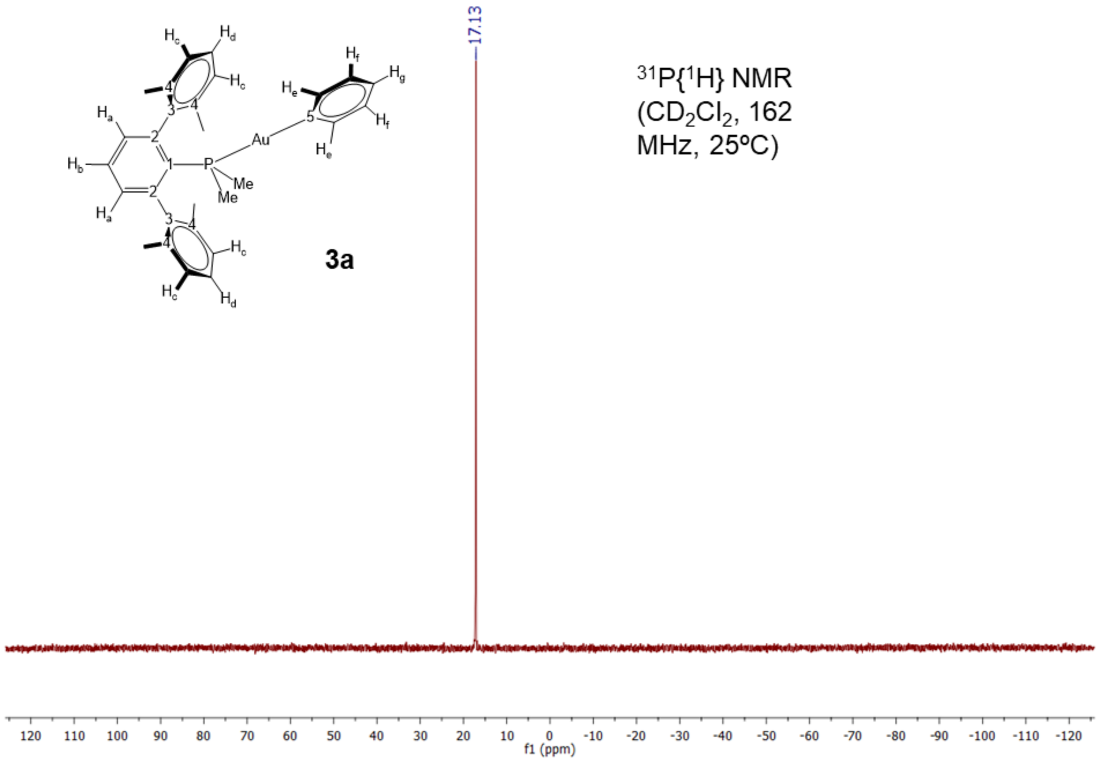

3a

$^{31}P\{^1H\}$ NMR (CD_2Cl_2, 162 MHz, 25ºC)

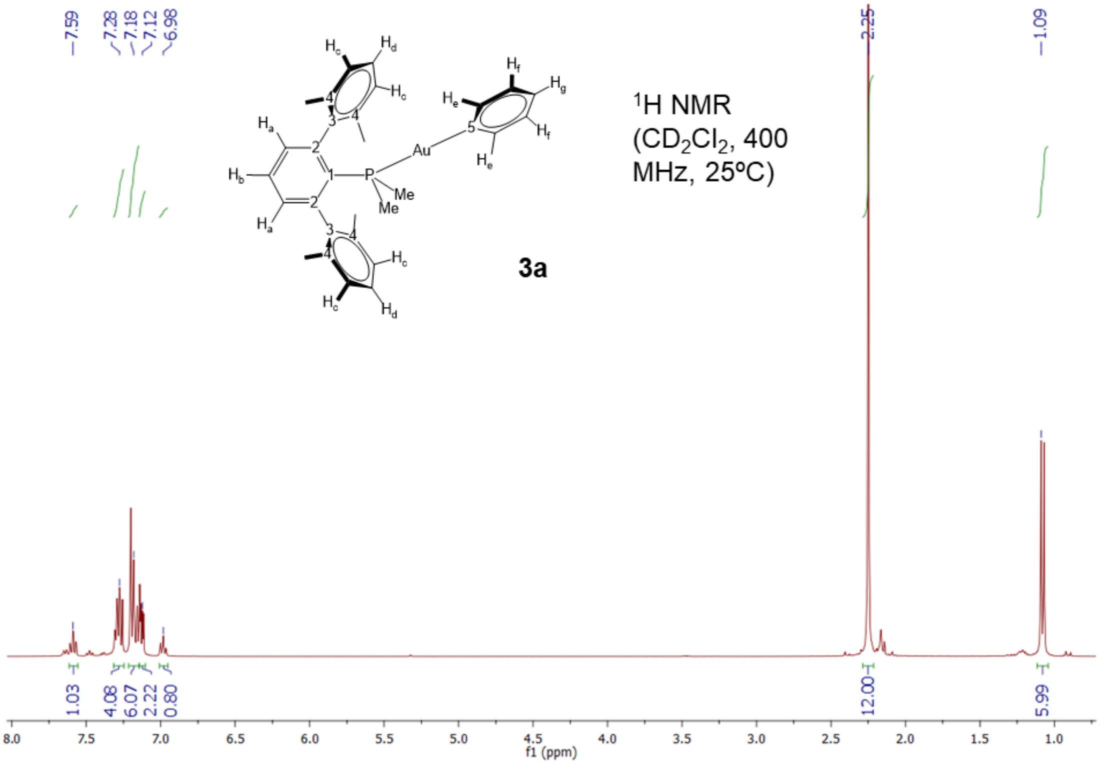

7.59
7.28
7.18
7.12
6.98
2.25
1.09
^{1}H NMR
(CD$_2$Cl$_2$, 400
MHz, 25ºC)
3a
1.03
4.08
6.07
2.22
0.80
12.00
5.99
8.0
7.5
7.0
6.5
6.0
5.5
5.0
4.5
4.0
3.5
3.0
2.5
2.0
1.5
1.0
f1 (ppm)

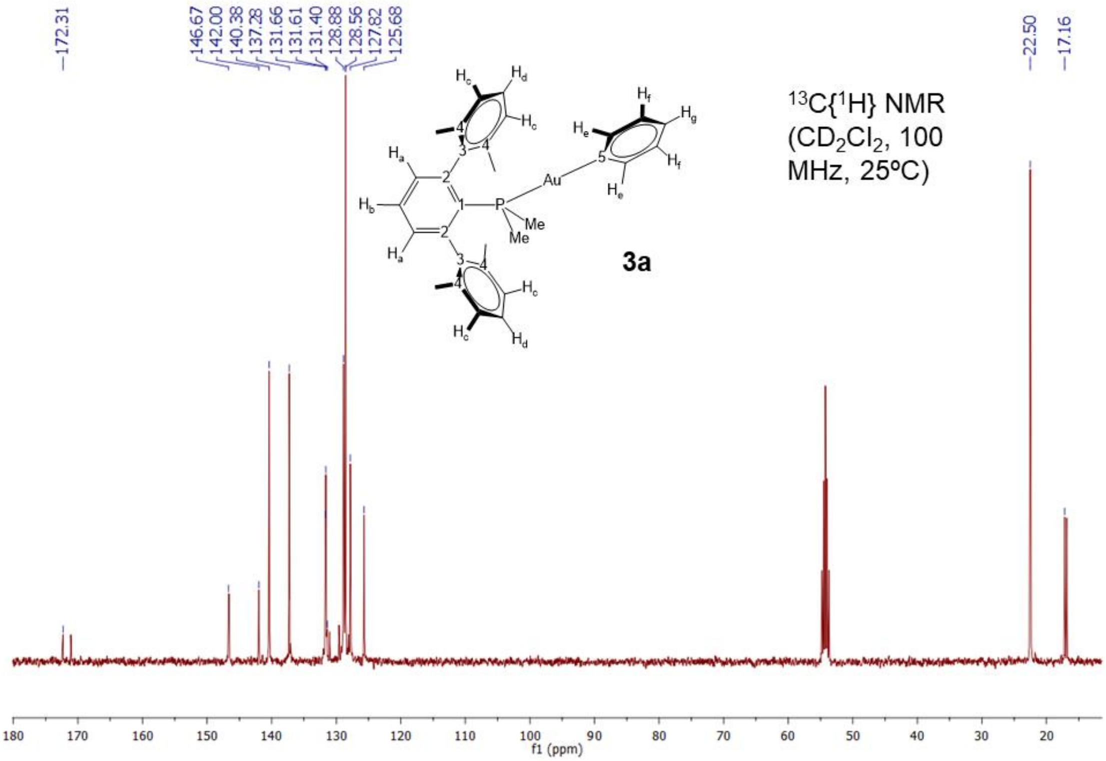

172.31
146.67
142.00
140.38
137.28
131.66
131.61
131.40
128.88
128.56
127.82
125.68
22.50
17.16
^{13}C{^{1}H} NMR
(CD$_2$Cl$_2$, 100
MHz, 25ºC)
3a
180
170
160
150
140
130
120
110
100
90
80
70
60
50
40
30
20
f1 (ppm)

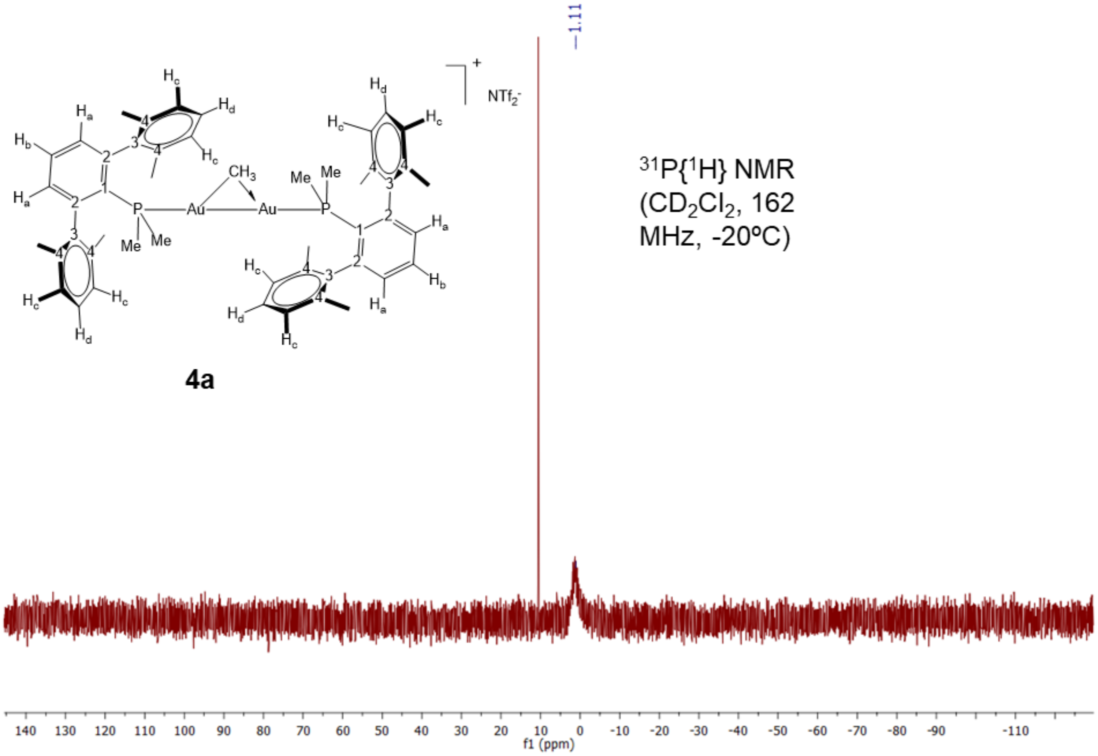
4a

$^{31}P\{^1H\}$ NMR (CD_2Cl_2, 162 MHz, -20ºC)

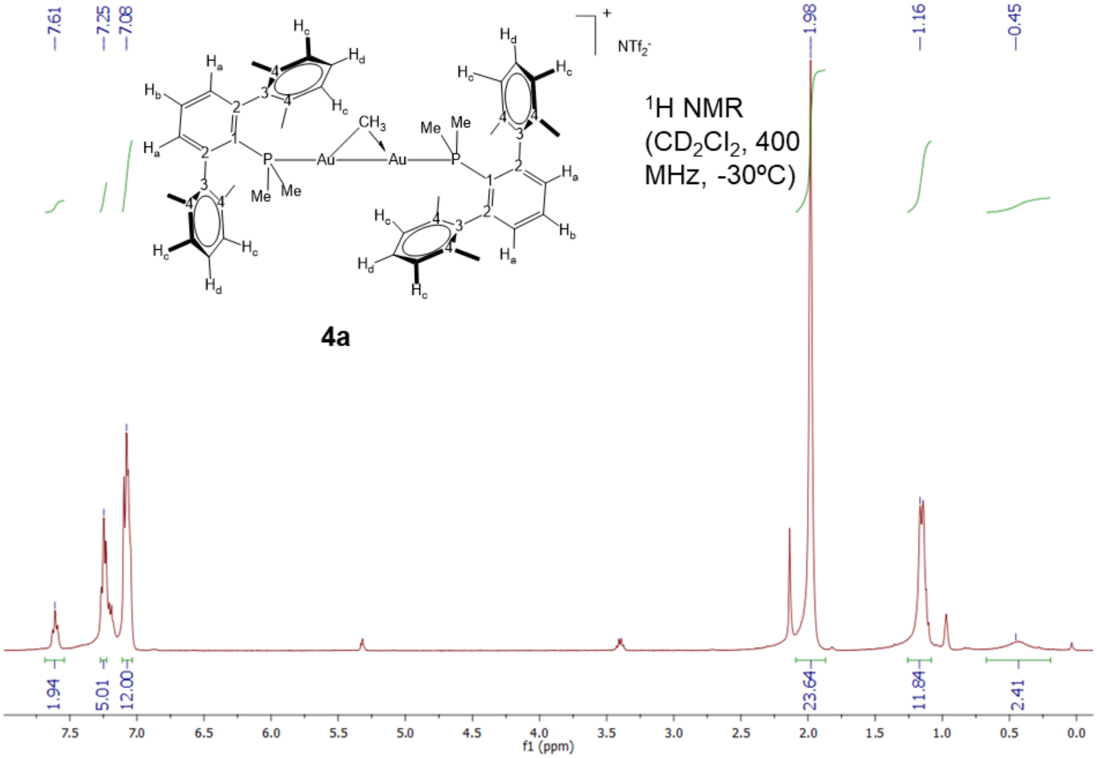
4a

^1H NMR (CD_2Cl_2, 400 MHz, -30ºC)

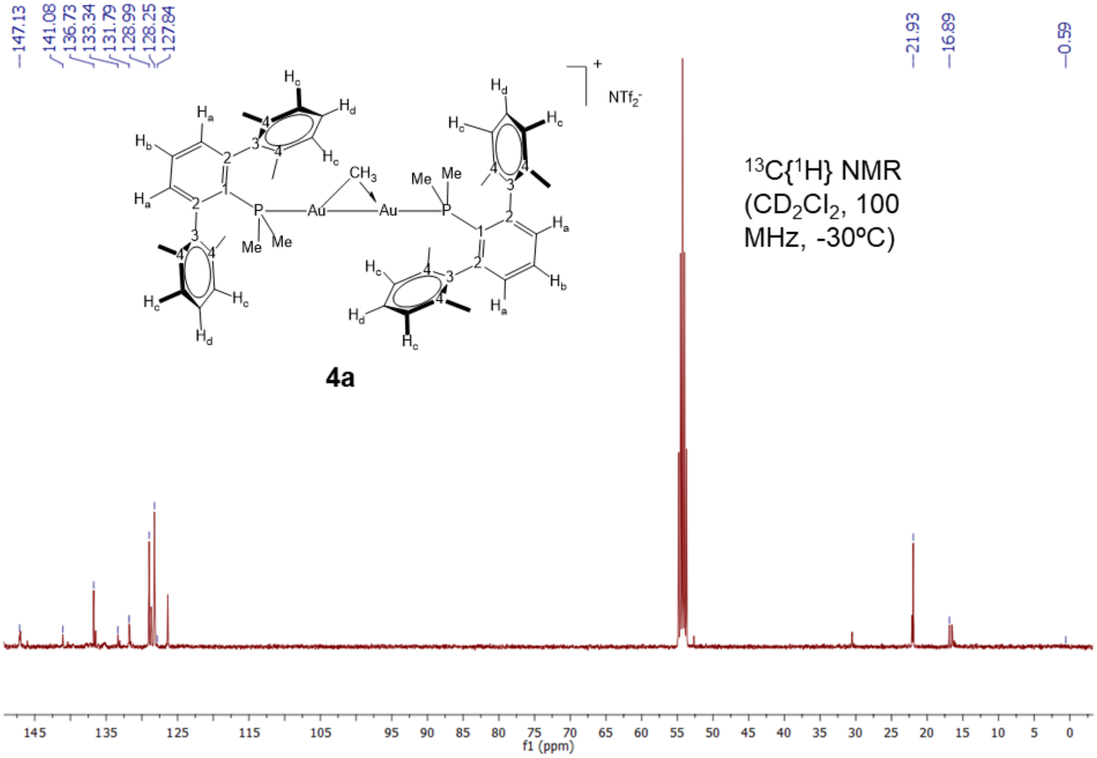

4a

$^{13}C\{^1H\}$ NMR (CD_2Cl_2, 100 MHz, -30ºC)

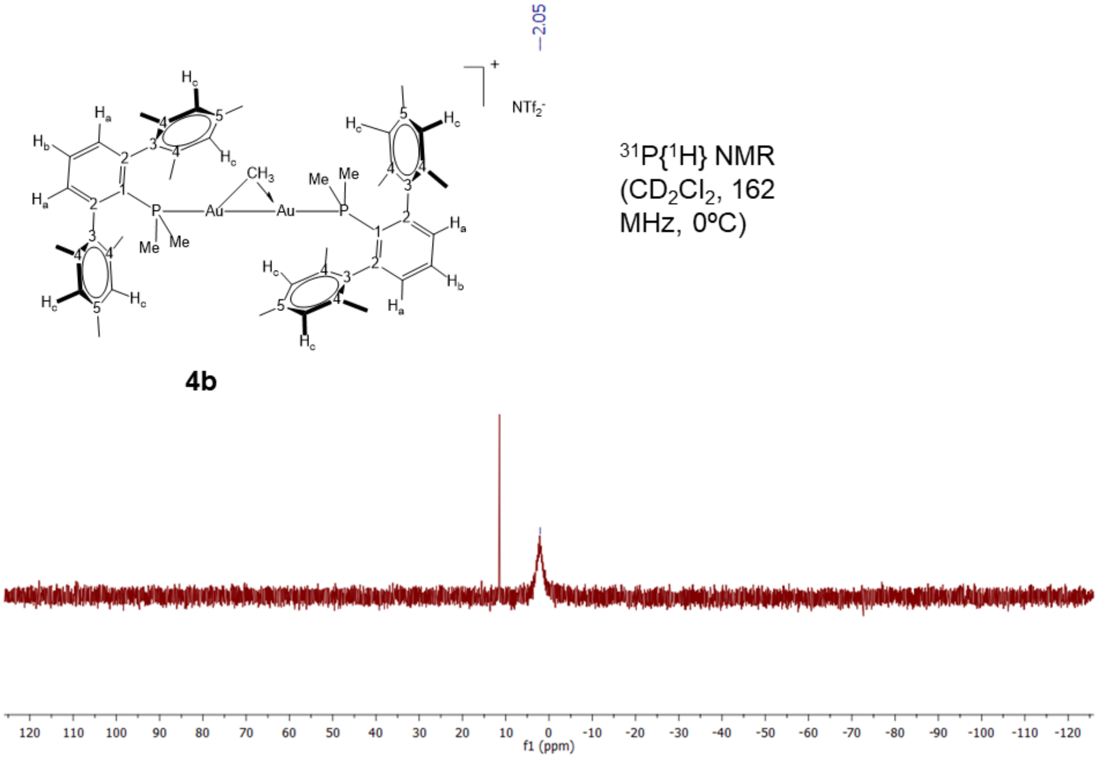

4b

$^{31}P\{^1H\}$ NMR (CD_2Cl_2, 162 MHz, 0ºC)

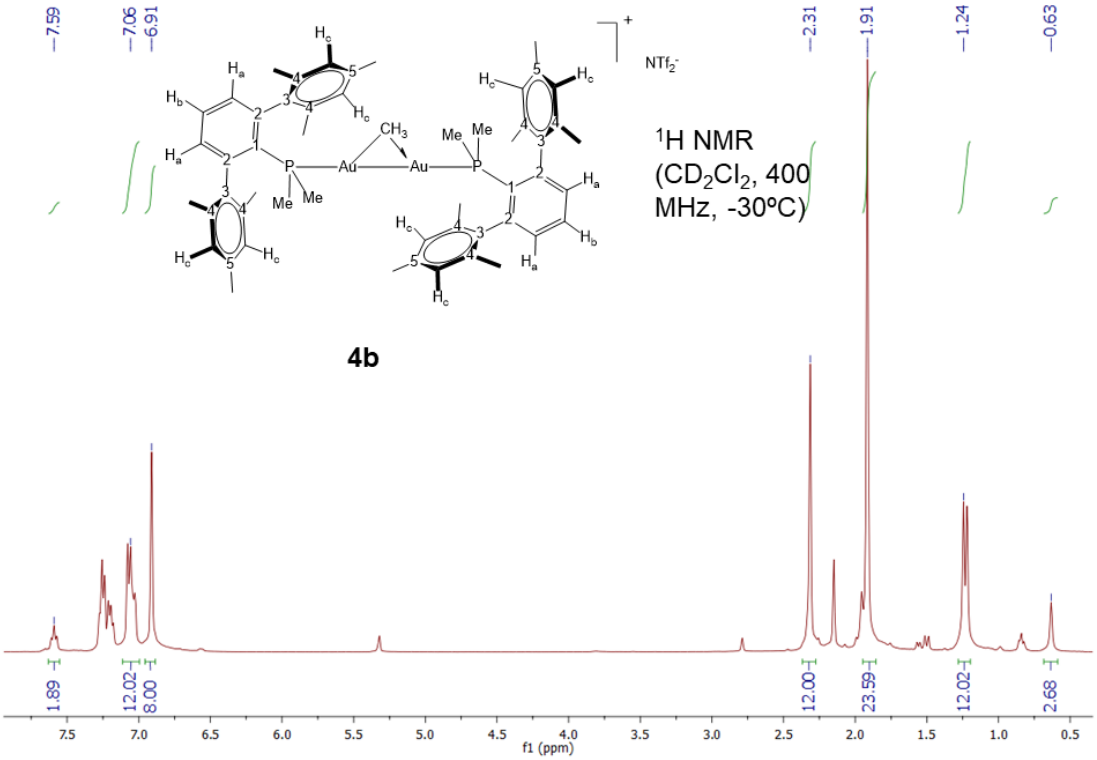
7.59
7.06
6.91
2.31
1.91
1.24
0.63
NTf2-
+
Ha
Hb
Hc
CH3
Me
P
Au
1
2
3
4
5
^{1}H NMR (CD$_2$Cl$_2$, 400 MHz, -30ºC)
1.89
12.02
8.00
12.00
23.59
12.02
2.68
7.5
7.0
6.5
6.0
5.5
5.0
4.5
4.0
3.5
3.0
2.5
2.0
1.5
1.0
0.5
f1 (ppm)

4b

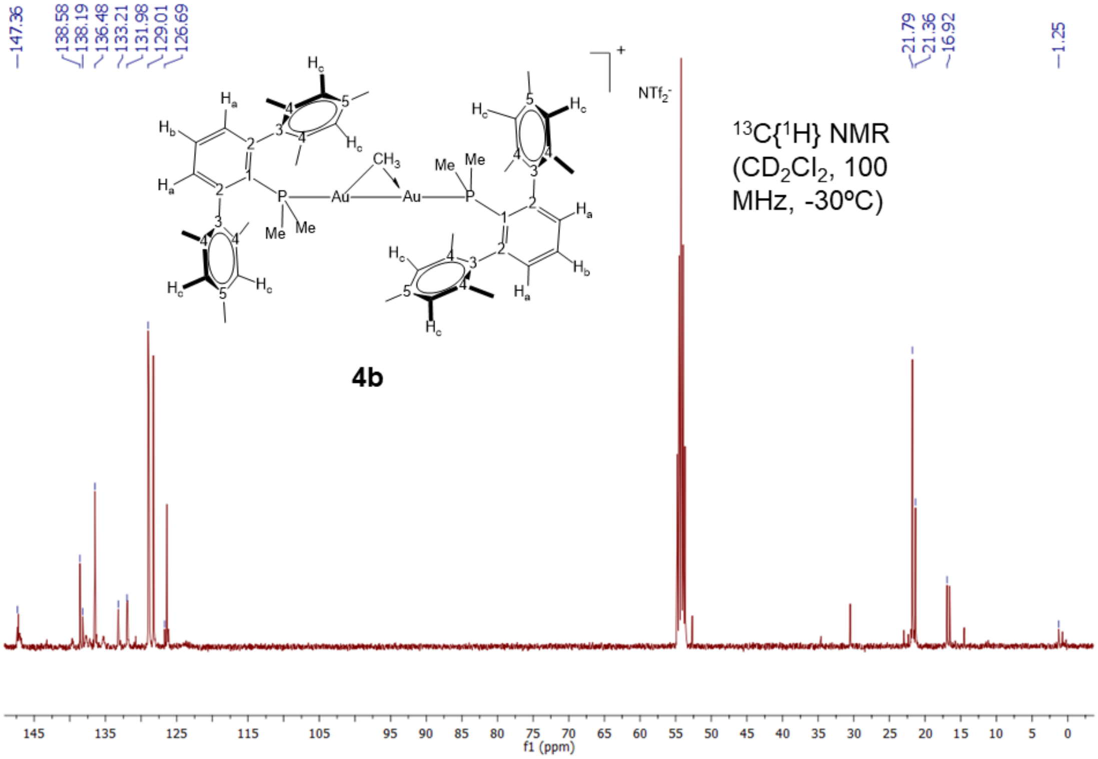
147.36
138.58
138.19
136.48
133.21
131.98
129.01
126.69
21.79
21.36
16.92
-1.25
NTf2-
+
Ha
Hb
Hc
CH3
Me
P
Au
1
2
3
4
5
^{13}C{^{1}H} NMR (CD$_2$Cl$_2$, 100 MHz, -30ºC)
145
135
125
115
105
95
90
85
80
75
70
65
60
55
50
45
40
35
30
25
20
15
10
5
0
f1 (ppm)

4b

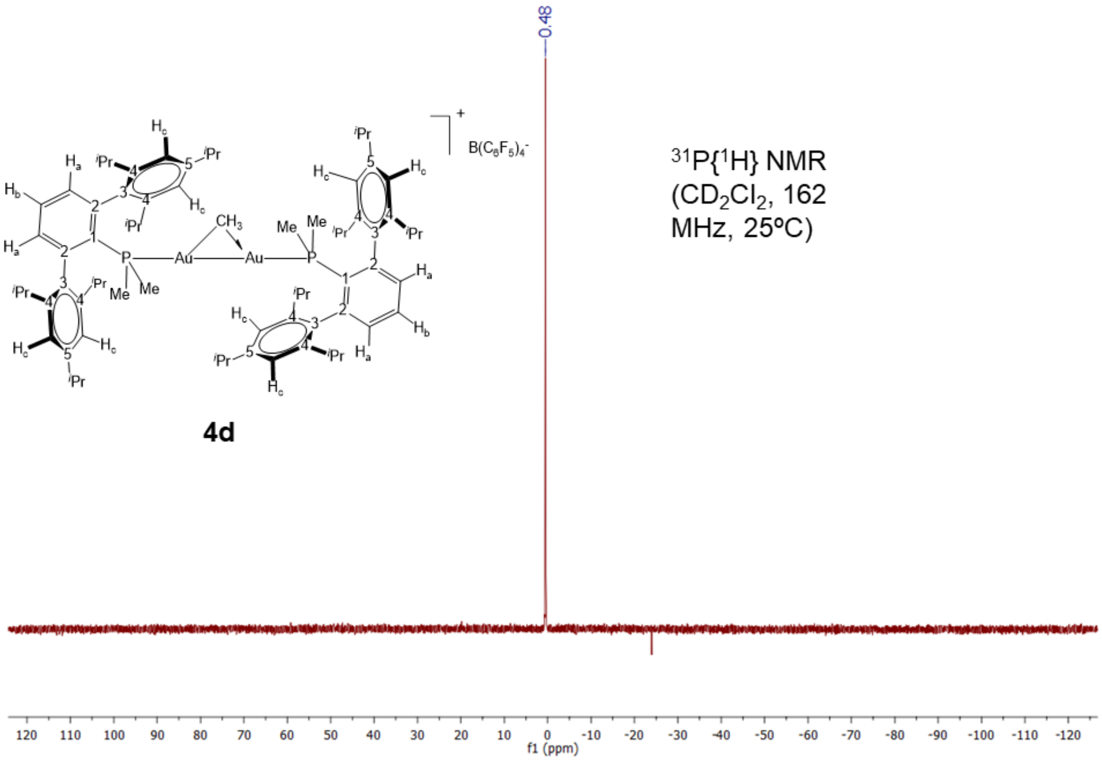

4d
B(C6F5)4-
31P{1H} NMR
(CD2Cl2, 162
MHz, 25ºC)
0.48
120 110 100 90 80 70 60 50 40 30 20 10 0 -10 -20 -30 -40 -50 -60 -70 -80 -90 -100 -110 -120
f1 (ppm)

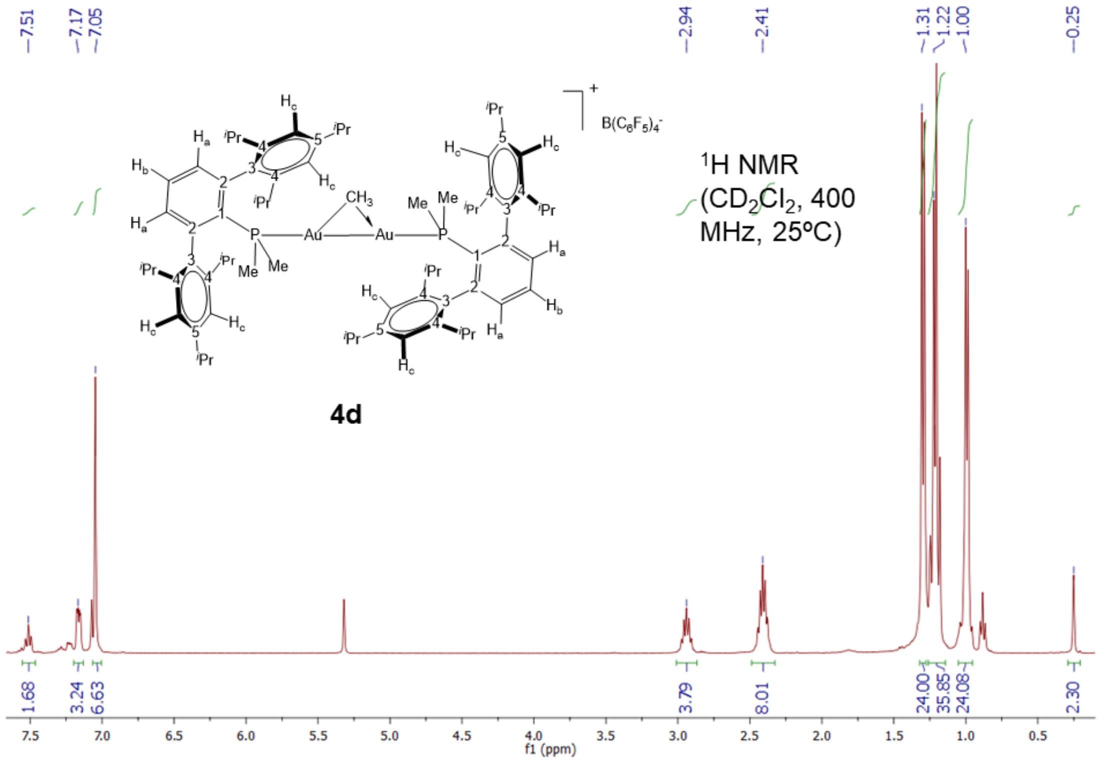

4d
B(C6F5)4-
1H NMR
(CD2Cl2, 400
MHz, 25ºC)
7.51
7.17
7.05
2.94
2.41
1.31
1.22
1.00
0.25
1.68
3.24
6.63
3.79
8.01
24.00
35.85
24.08
2.30
7.5 7.0 6.5 6.0 5.5 5.0 4.5 4.0 3.5 3.0 2.5 2.0 1.5 1.0 0.5
f1 (ppm)

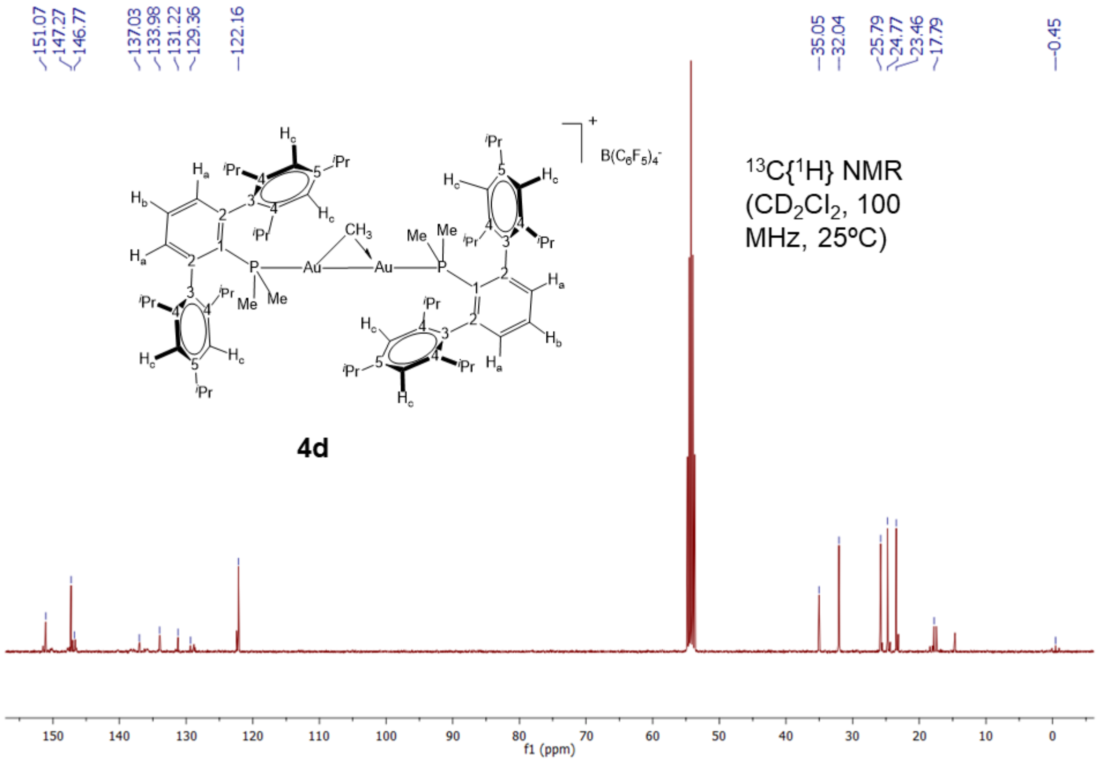

4d

$^{13}C\{^1H\}$ NMR (CD_2Cl_2, 100 MHz, 25ºC)

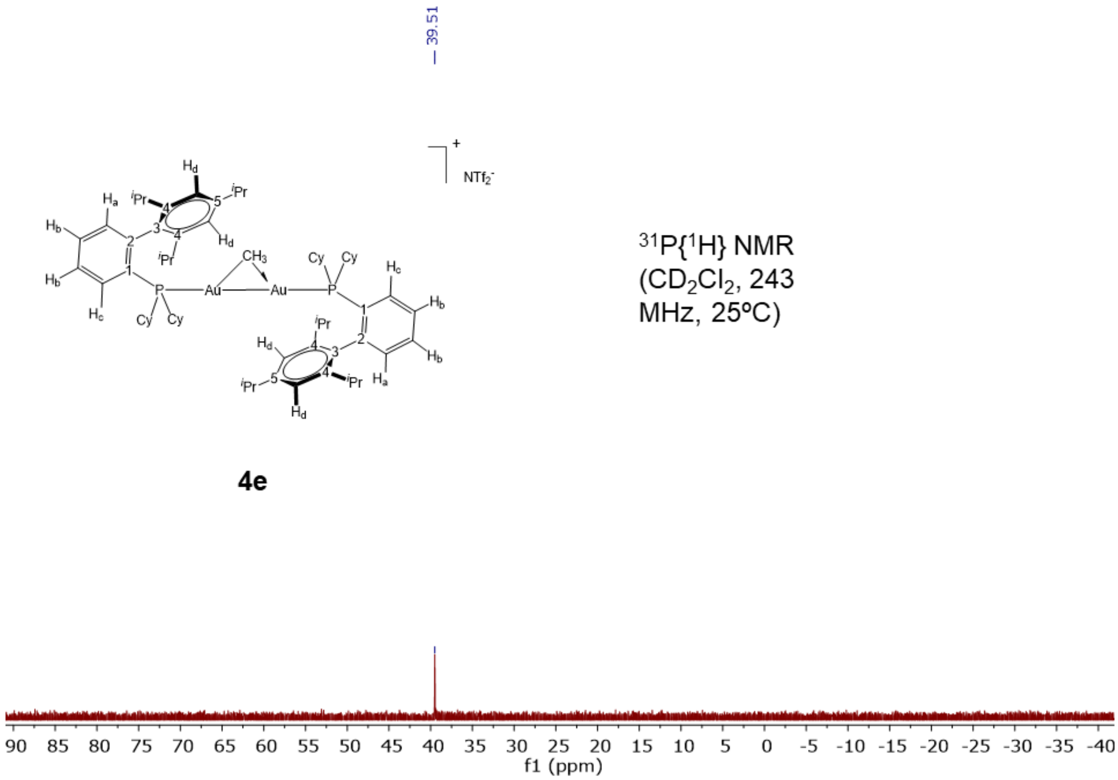

4e

$^{31}P\{^1H\}$ NMR (CD_2Cl_2, 243 MHz, 25ºC)

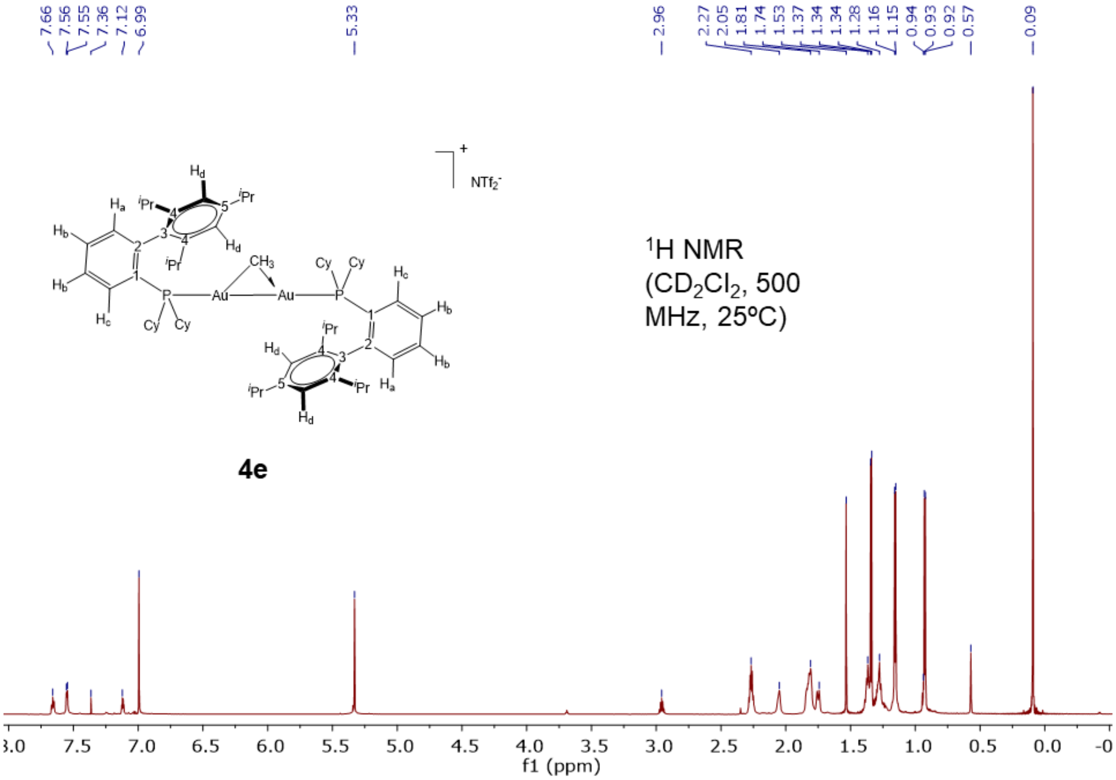

7.66
7.56
7.55
7.36
7.12
6.99
5.33
2.96
2.27
2.05
1.81
1.74
1.53
1.37
1.34
1.34
1.28
1.16
1.15
0.94
0.93
0.92
0.57
0.09
NTf2-
4e
^{1}H NMR
(CD$_2$Cl$_2$, 500
MHz, 25ºC)
f1 (ppm)

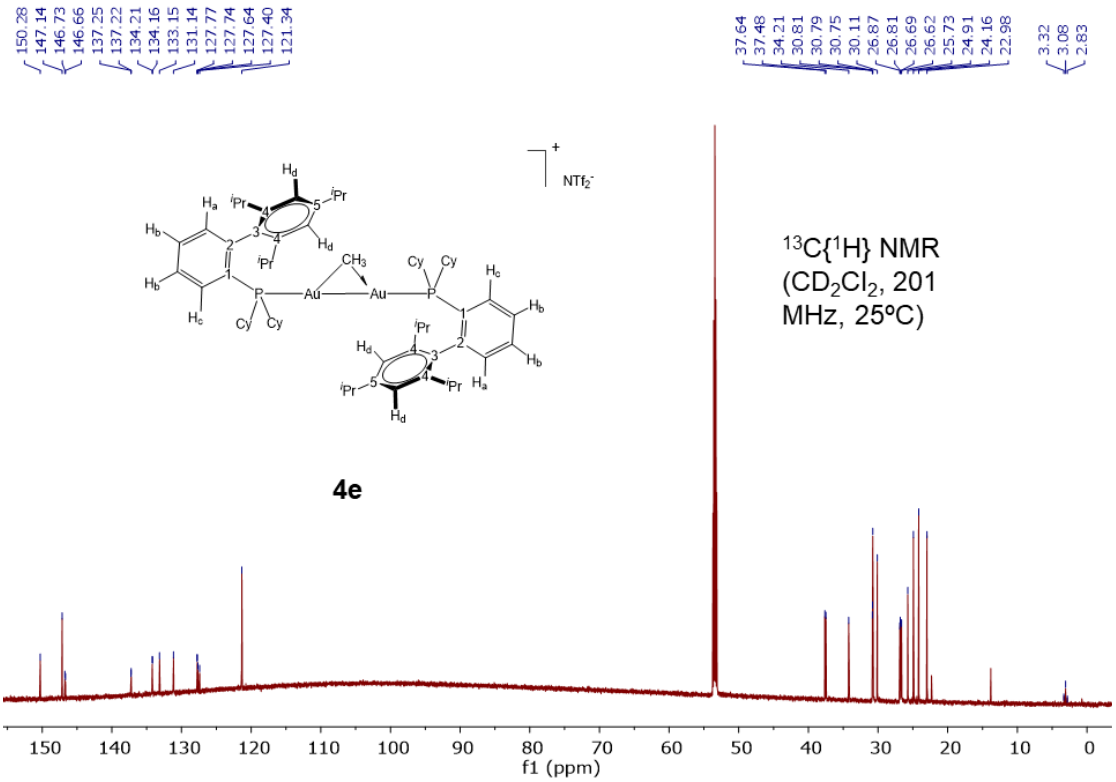

150.28
147.14
146.73
146.66
137.25
137.22
134.21
134.16
133.15
131.14
127.77
127.74
127.64
127.40
121.34
37.64
37.48
34.21
30.81
30.79
30.75
30.11
26.87
26.81
26.69
26.62
25.73
24.91
24.16
22.98
3.32
3.08
2.83
NTf2-
4e
^{13}C{^{1}H} NMR
(CD$_2$Cl$_2$, 201
MHz, 25ºC)
f1 (ppm)

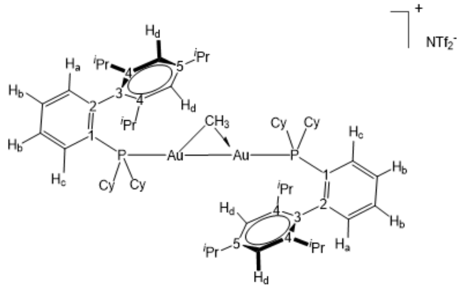

4e

^{19}F{^{1}H} NMR
(CD_2Cl_2, 565
MHz, 25 °C)

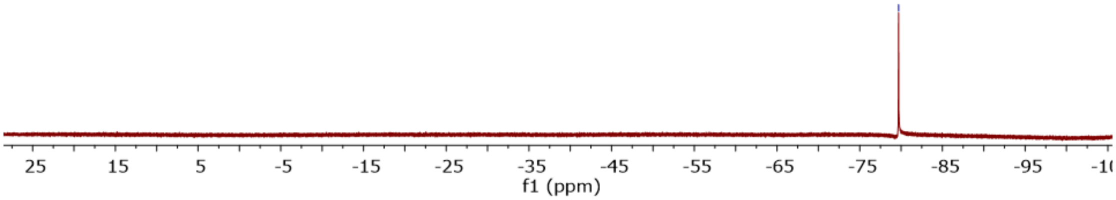

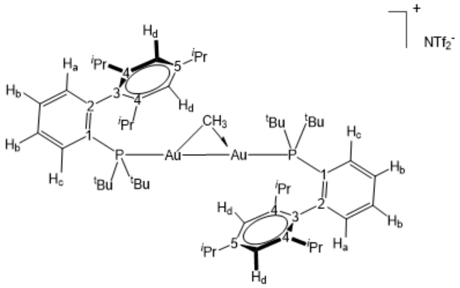

4f

^{31}P{^{1}H} NMR
(CD_2Cl_2, 243
MHz, 25ºC)

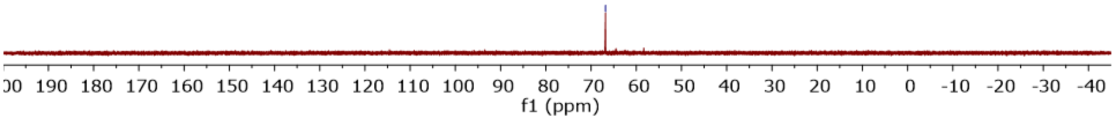

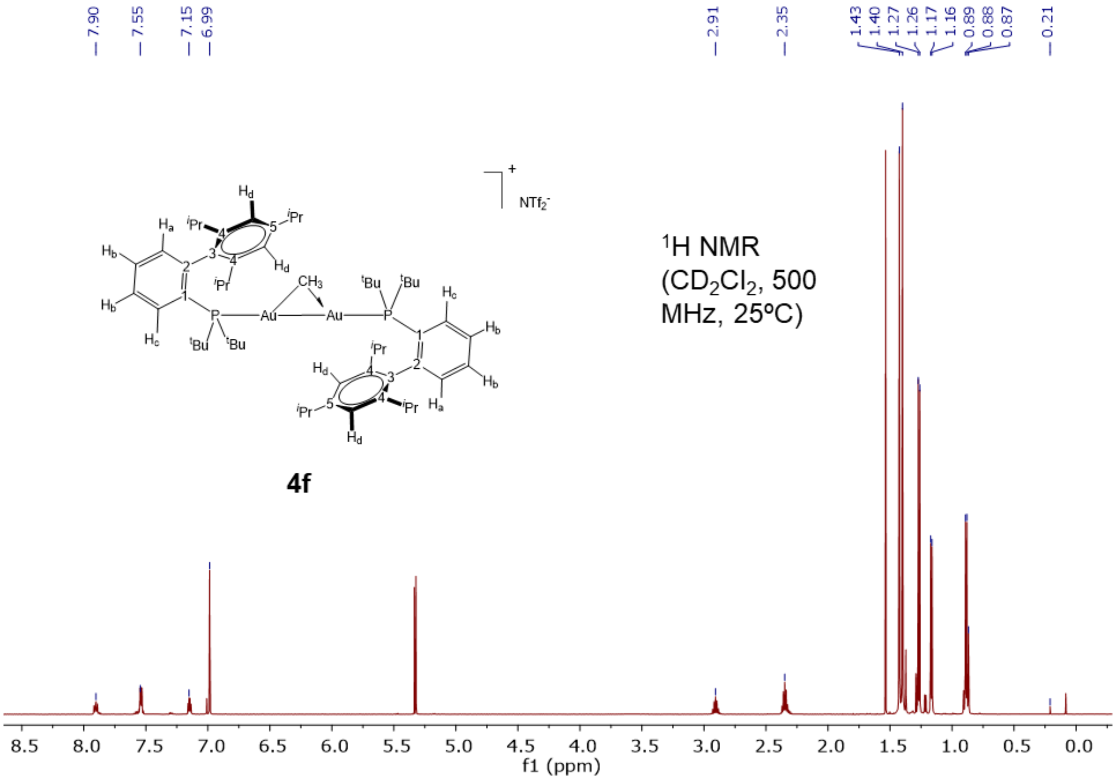
7.90
7.55
7.15
6.99
2.91
2.35
1.43
1.40
1.27
1.26
1.17
1.16
0.89
0.88
0.87
0.21
^{1}H NMR
(CD_2Cl_2, 500
MHz, 25ºC)
4f
NTf_2^-
8.5
8.0
7.5
7.0
6.5
6.0
5.5
5.0
4.5
4.0
3.5
3.0
2.5
2.0
1.5
1.0
0.5
0.0
f1 (ppm)

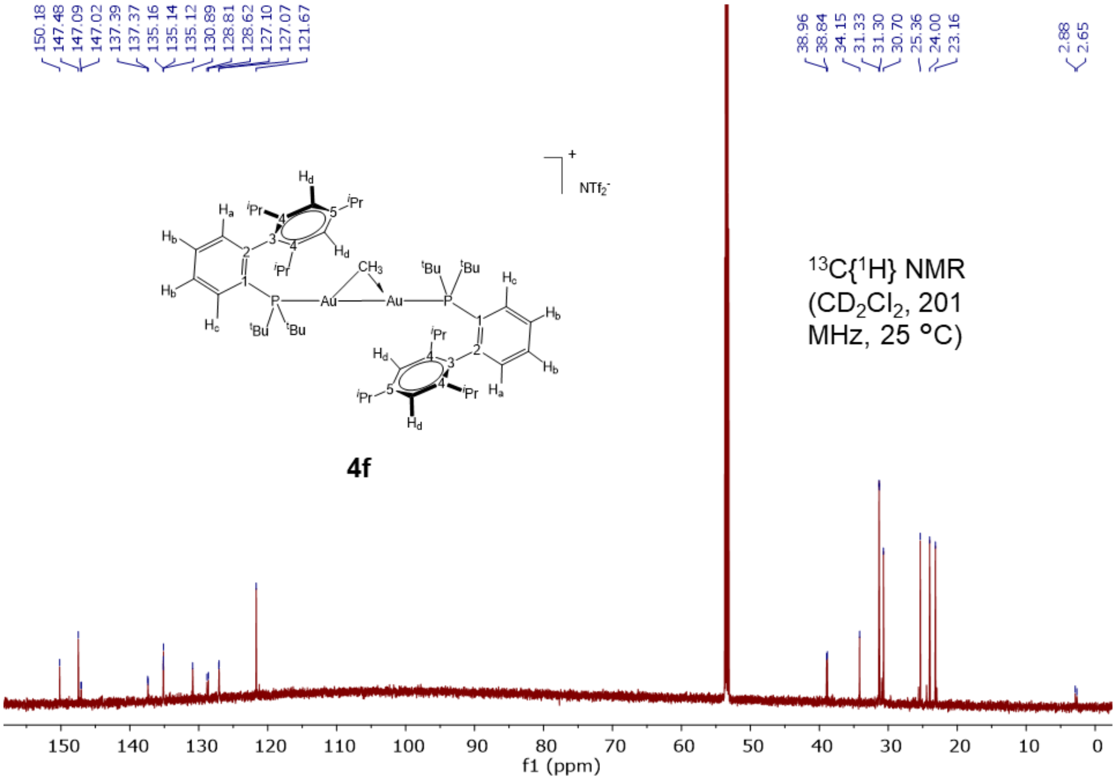
150.18
147.48
147.09
147.02
137.39
137.37
135.16
135.14
135.12
130.89
128.81
128.62
127.10
127.07
121.67
38.96
38.84
34.15
31.33
31.30
30.70
25.36
24.00
23.16
2.88
2.65
^{13}C{^{1}H} NMR
(CD_2Cl_2, 201
MHz, 25 °C)
4f
NTf_2^-
150
140
130
120
110
100
90
80
70
60
50
40
30
20
10
0
f1 (ppm)

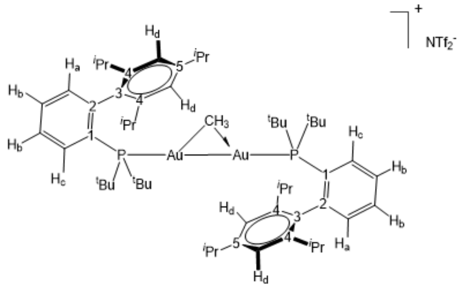

4f

$^{19}F\{^{1}H\}$ NMR (CD_2Cl_2, 565 MHz, 25 °C)

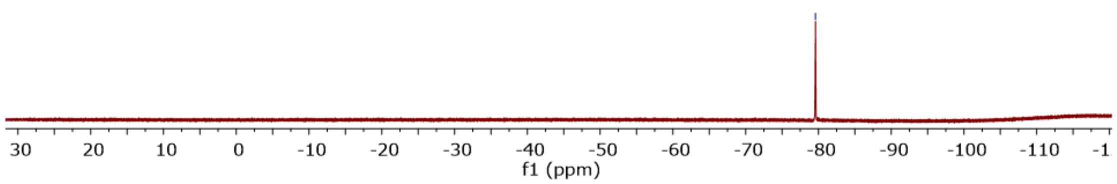

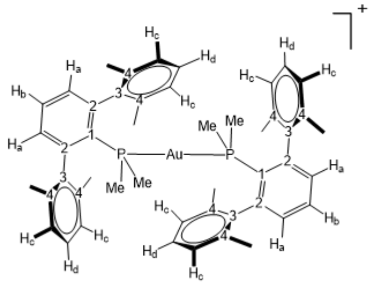

5a

$^{31}P\{^{1}H\}$ NMR (CD_2Cl_2, 162 MHz, 25ºC)

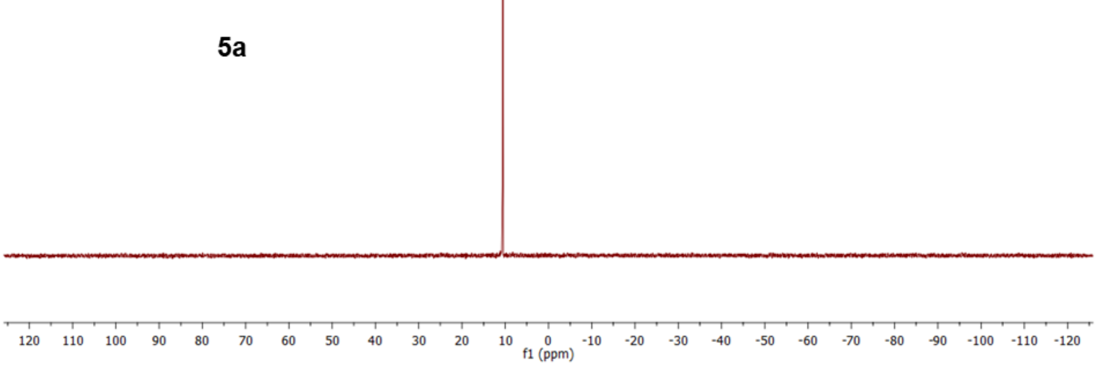

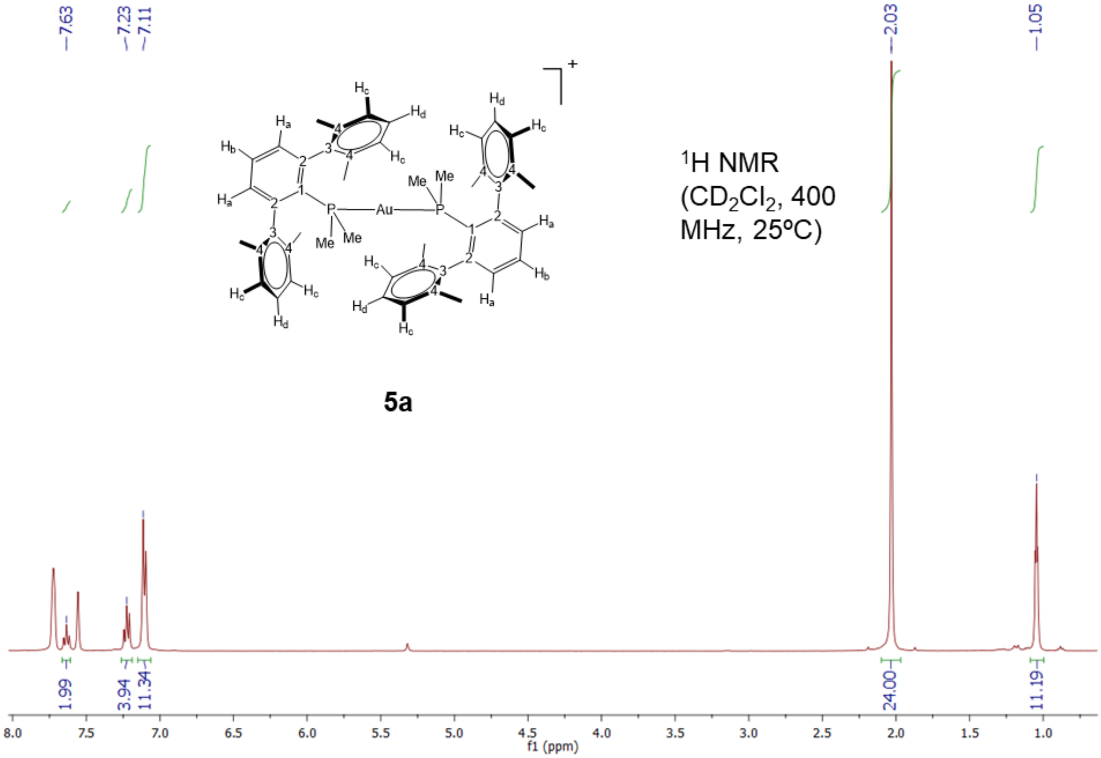

7.63
7.23
7.11
2.03
1.05
^{1}H NMR (CD$_2$Cl$_2$, 400 MHz, 25ºC)
1.99
3.94
11.34
24.00
11.19
8.0
7.5
7.0
6.5
6.0
5.5
5.0
4.5
4.0
3.5
3.0
2.5
2.0
1.5
1.0
f1 (ppm)

5a

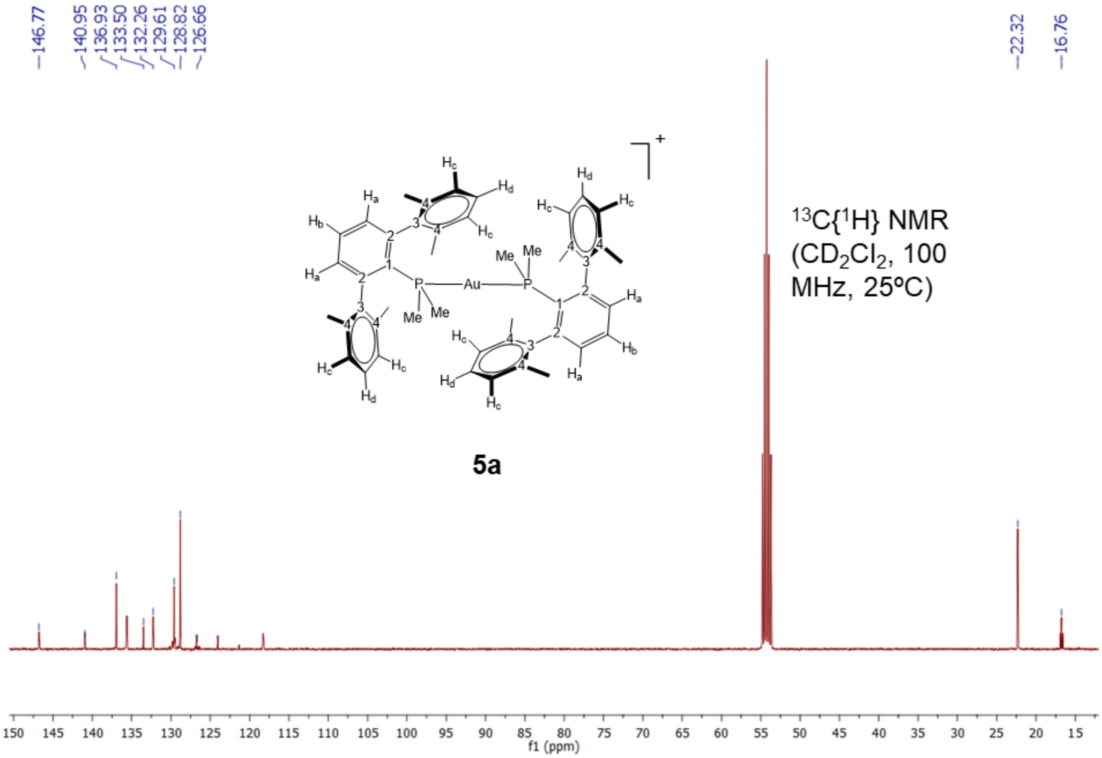

146.77
140.95
136.93
133.50
132.26
129.61
128.82
126.66
22.32
16.76
^{13}C{^{1}H} NMR (CD$_2$Cl$_2$, 100 MHz, 25ºC)
150
145
140
135
130
125
120
115
110
105
100
95
90
85
80
75
70
65
60
55
50
45
40
35
30
25
20
15
f1 (ppm)

5a

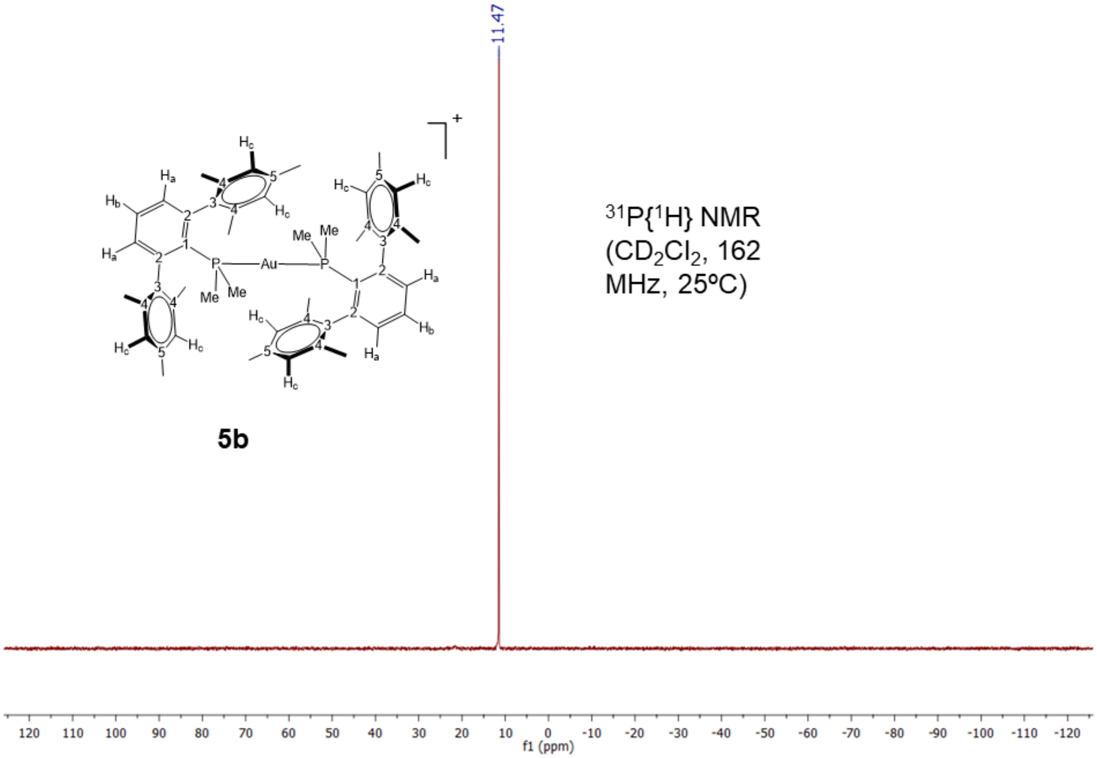

5b

$^{31}P\{^1H\}$ NMR (CD_2Cl_2, 162 MHz, 25ºC)

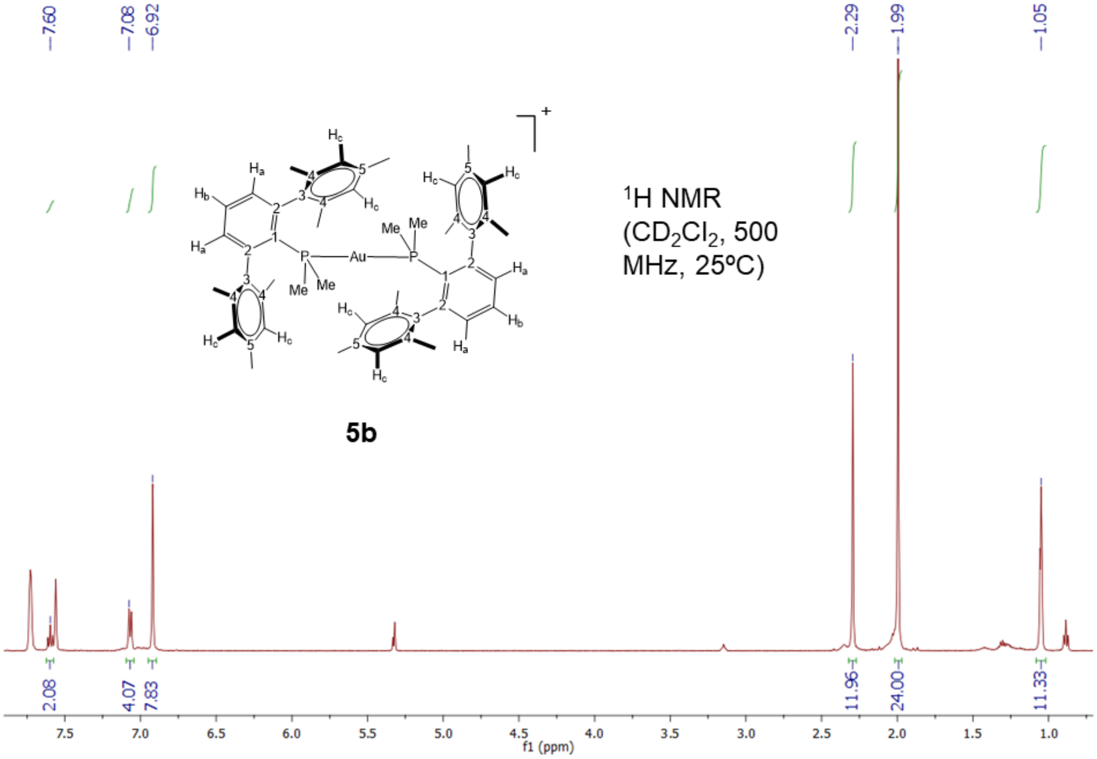

5b

^1H NMR (CD_2Cl_2, 500 MHz, 25ºC)

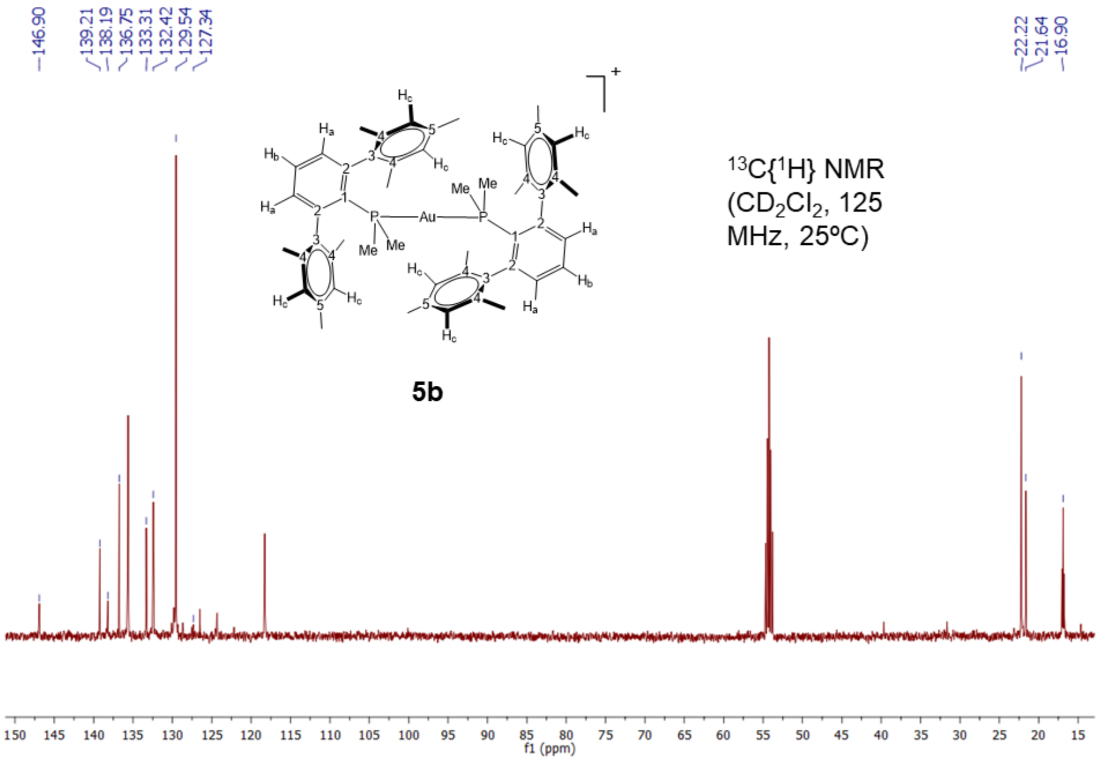

146.90
139.21
138.19
136.75
133.31
132.42
129.54
127.34
22.22
21.64
16.90
$^{13}C\{^1H\}$ NMR
(CD_2Cl_2, 125
MHz, 25ºC)
Ha
Hb
Hc
P
Au
Me
1
2
3
4
5
+
150 145 140 135 130 125 120 115 110 105 100 95 90 85 80 75 70 65 60 55 50 45 40 35 30 25 20 15
f1 (ppm)

5b

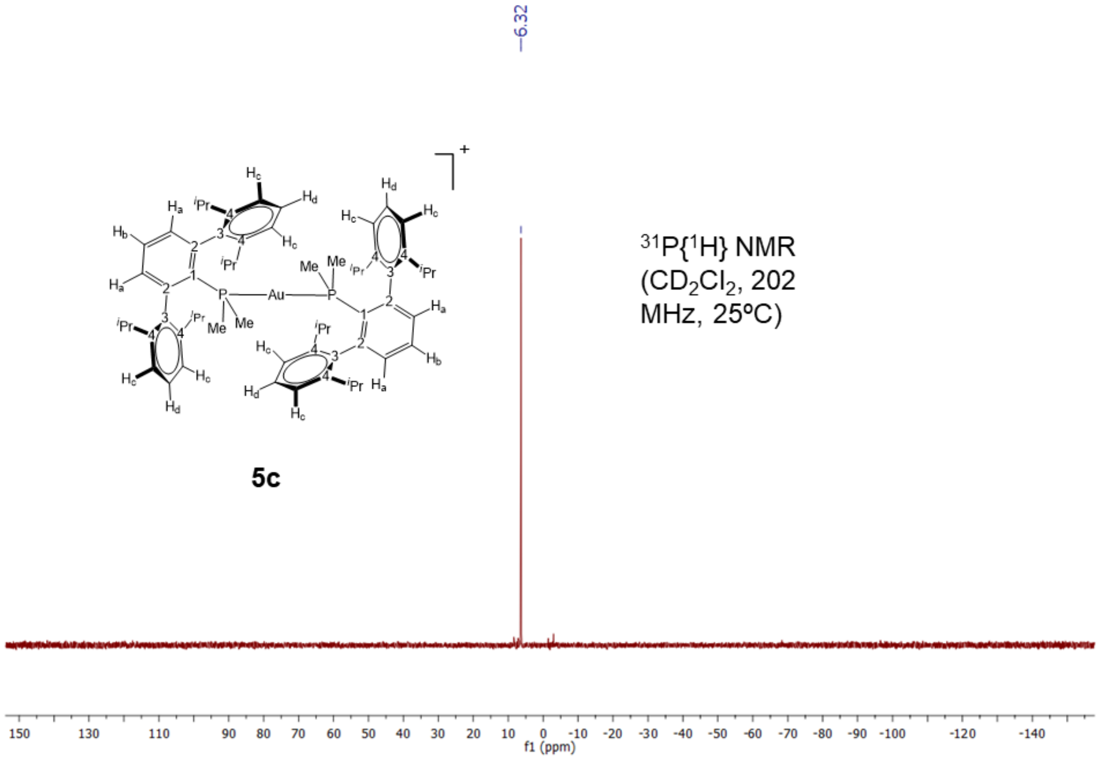

-6.32
$^{31}P\{^1H\}$ NMR
(CD_2Cl_2, 202
MHz, 25ºC)
Ha
Hb
Hc
Hd
^{i}Pr
P
Au
Me
1
2
3
4
+
150 130 110 90 80 70 60 50 40 30 20 10 0 -10 -20 -30 -40 -50 -60 -70 -80 -90 -100 -120 -140
f1 (ppm)

5c

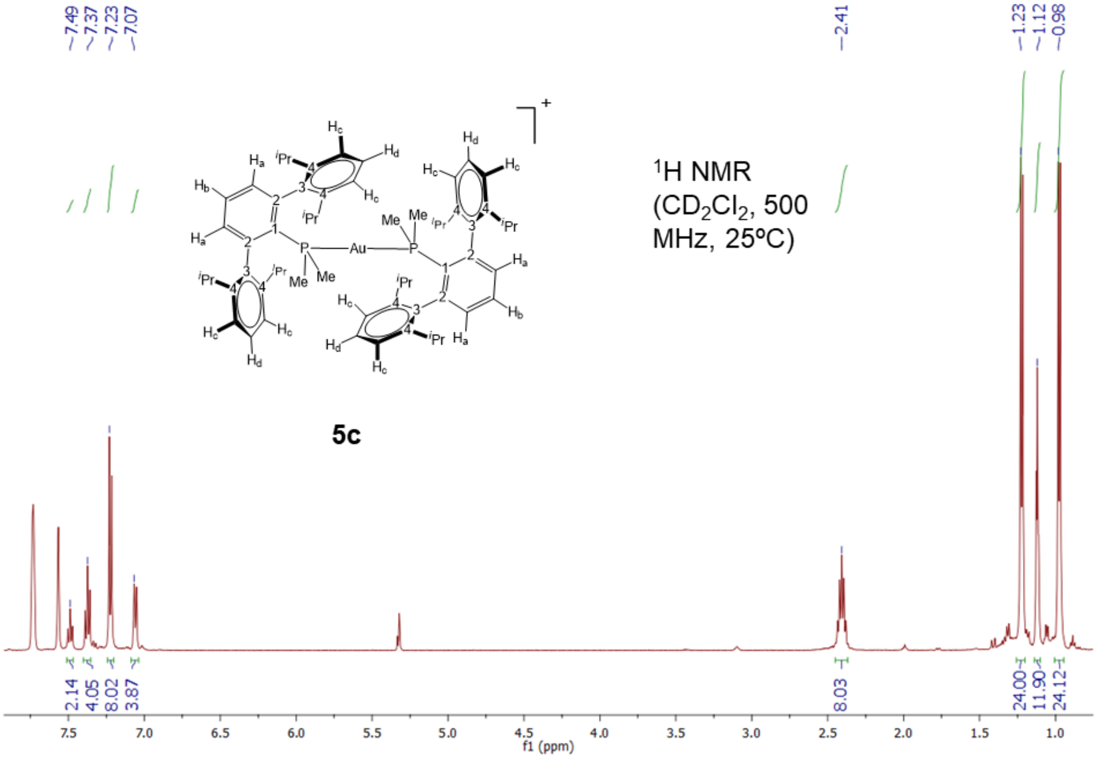
7.49
7.37
7.23
7.07
2.41
1.23
1.12
0.98
^{1}H NMR
(CD_2Cl_2, 500 MHz, 25ºC)
5c
2.14
4.05
8.02
3.87
8.03
24.00
11.90
24.12
7.5
7.0
6.5
6.0
5.5
5.0
4.5
4.0
3.5
3.0
2.5
2.0
1.5
1.0
f1 (ppm)

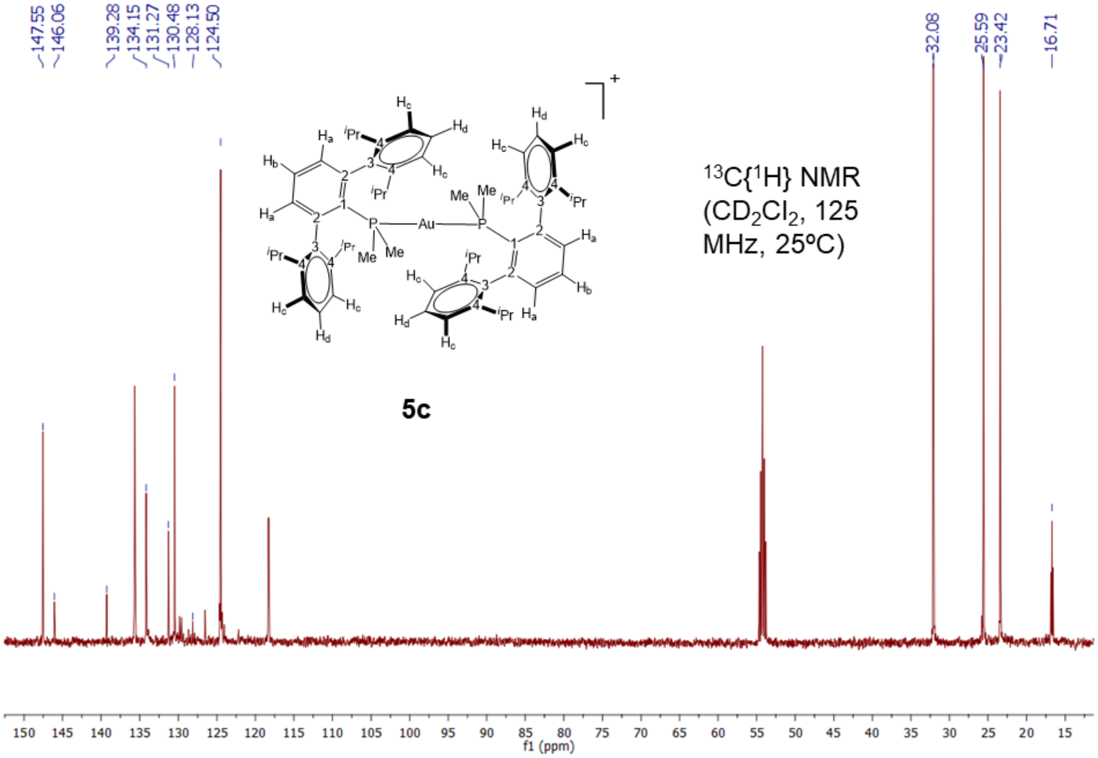
147.55
146.06
139.28
134.15
131.27
130.48
128.13
124.50
32.08
25.59
23.42
16.71
$^{13}C\{^1H\}$ NMR
(CD_2Cl_2, 125 MHz, 25ºC)
5c
150
145
140
135
130
125
120
115
110
105
100
95
90
85
80
75
70
65
60
55
50
45
40
35
30
25
20
15
f1 (ppm)

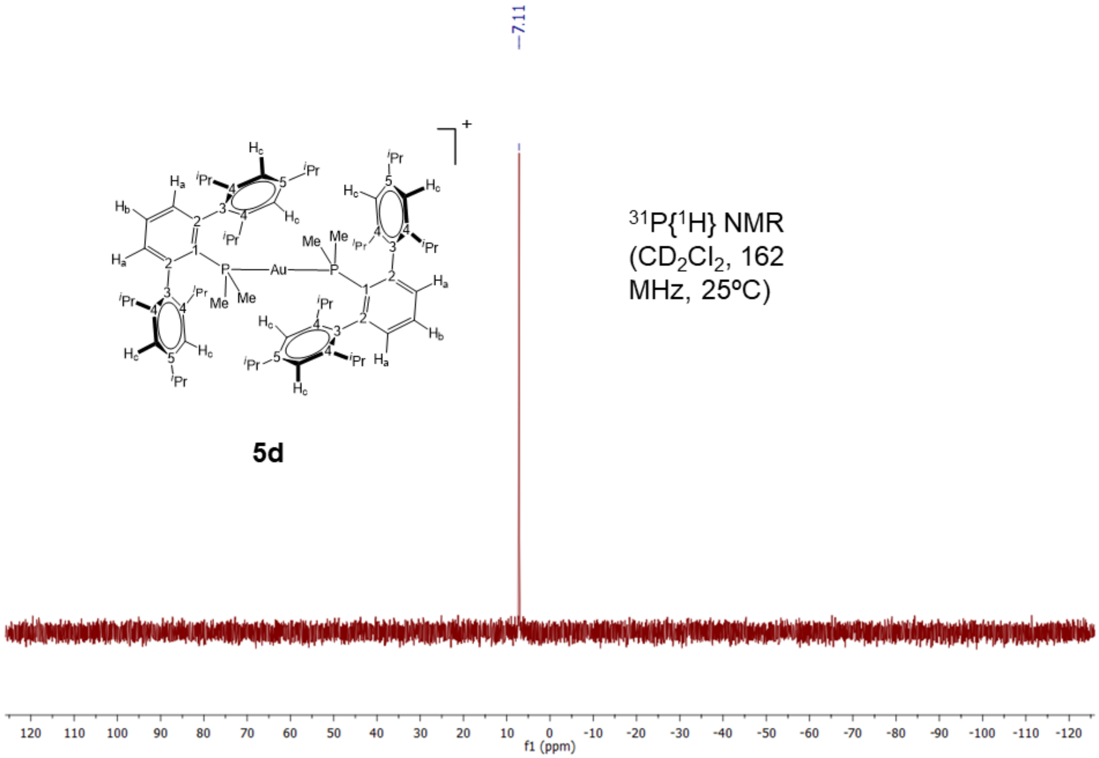
—7.11
31P{1H} NMR
(CD2Cl2, 162
MHz, 25ºC)
5d
120 110 100 90 80 70 60 50 40 30 20 10 0 -10 -20 -30 -40 -50 -60 -70 -80 -90 -100 -110 -120
f1 (ppm)

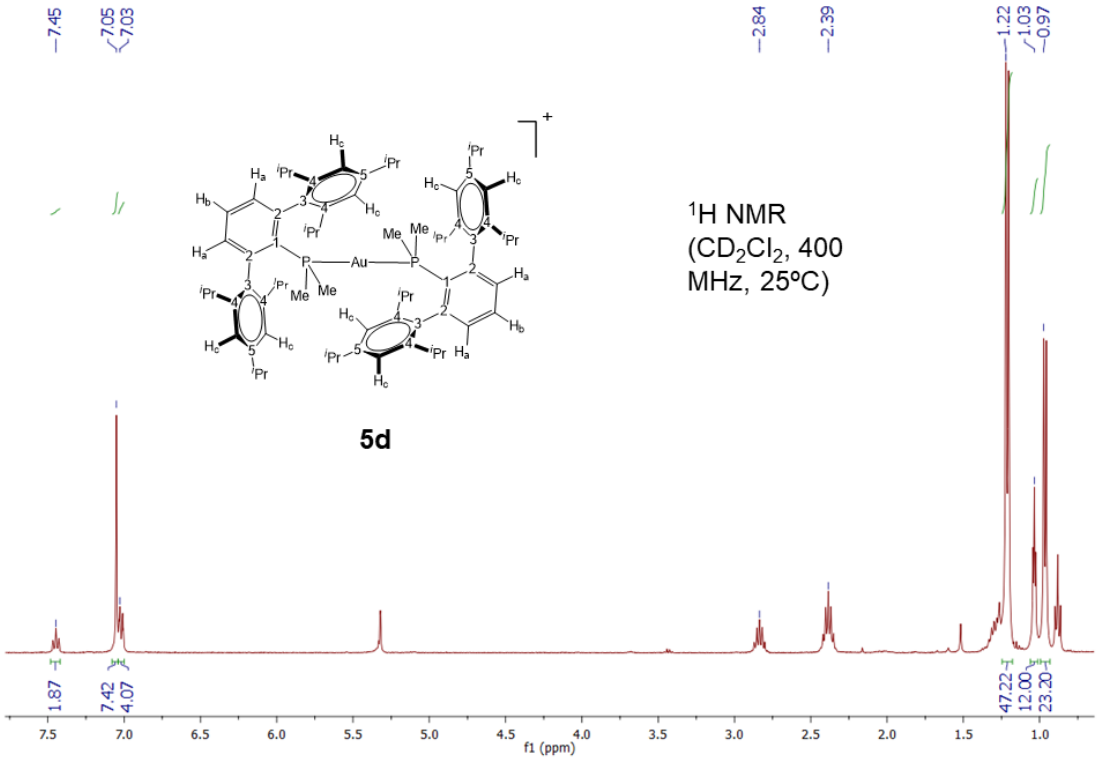
—7.45
7.05
7.03
—2.84
—2.39
1.22
1.03
0.97
1H NMR
(CD2Cl2, 400
MHz, 25ºC)
5d
1.87
7.42
4.07
47.22
12.00
23.20
7.5 7.0 6.5 6.0 5.5 5.0 4.5 4.0 3.5 3.0 2.5 2.0 1.5 1.0
f1 (ppm)

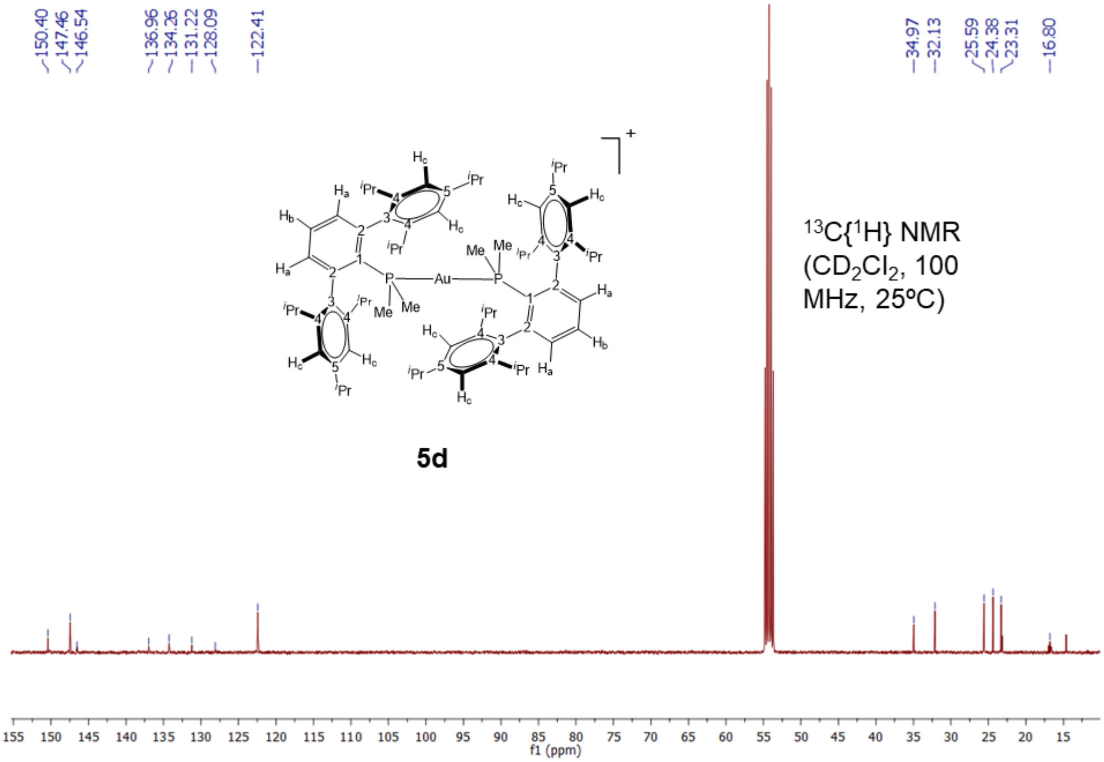

5d

$^{13}C\{^1H\}$ NMR (CD_2Cl_2, 100 MHz, 25ºC)

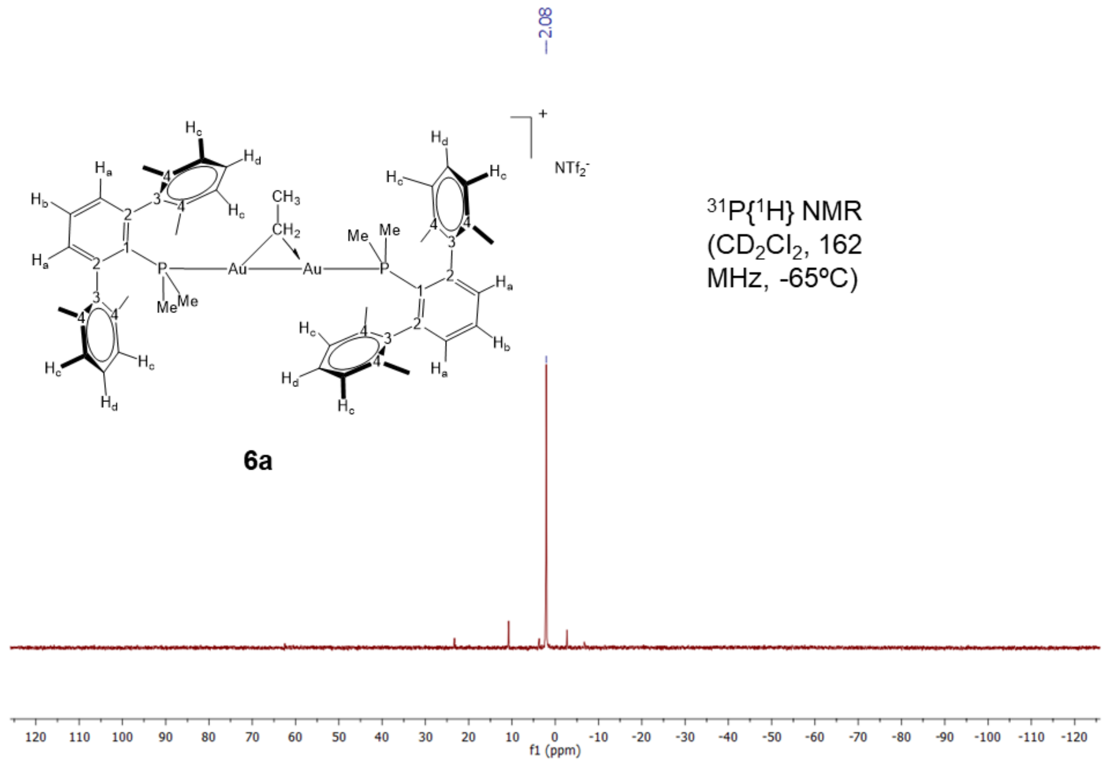

6a

$^{31}P\{^1H\}$ NMR (CD_2Cl_2, 162 MHz, -65ºC)

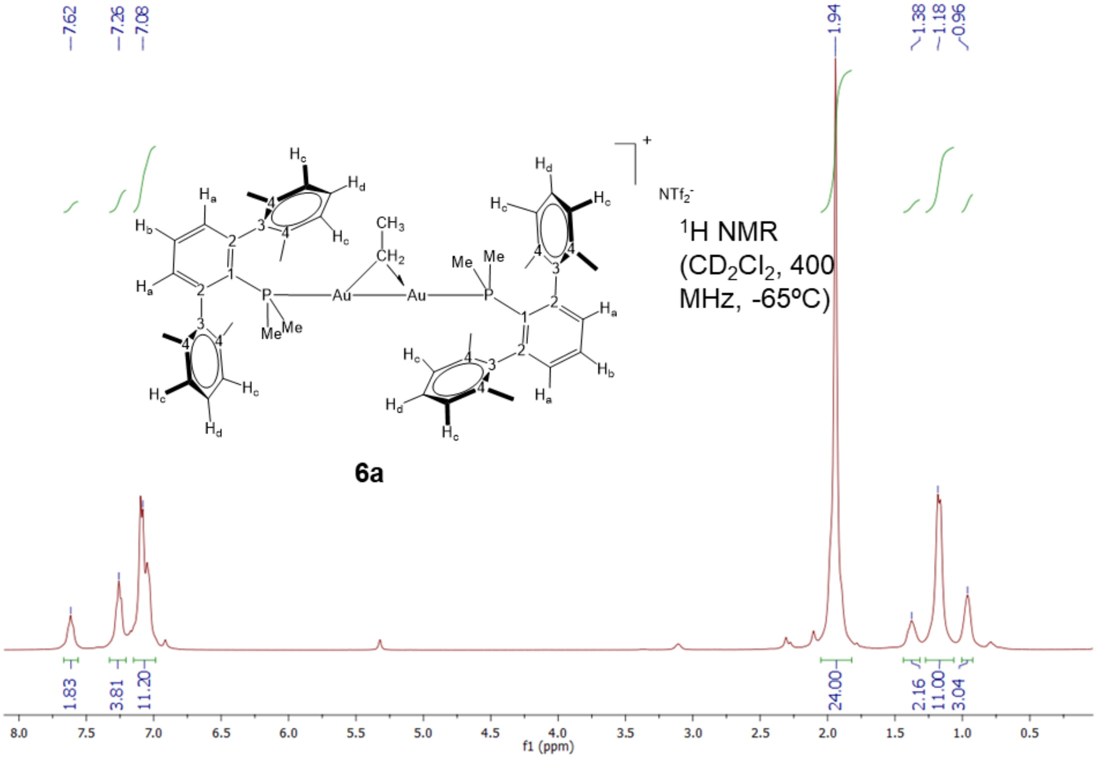
7.62
7.26
7.08
1.94
1.38
1.18
0.96
NTf$_2^-$
^{1}H NMR
(CD$_2$Cl$_2$, 400 MHz, -65ºC)
6a
1.83
3.81
11.20
24.00
2.16
11.00
3.04
8.0 7.5 7.0 6.5 6.0 5.5 5.0 4.5 4.0 3.5 3.0 2.5 2.0 1.5 1.0 0.5
f1 (ppm)

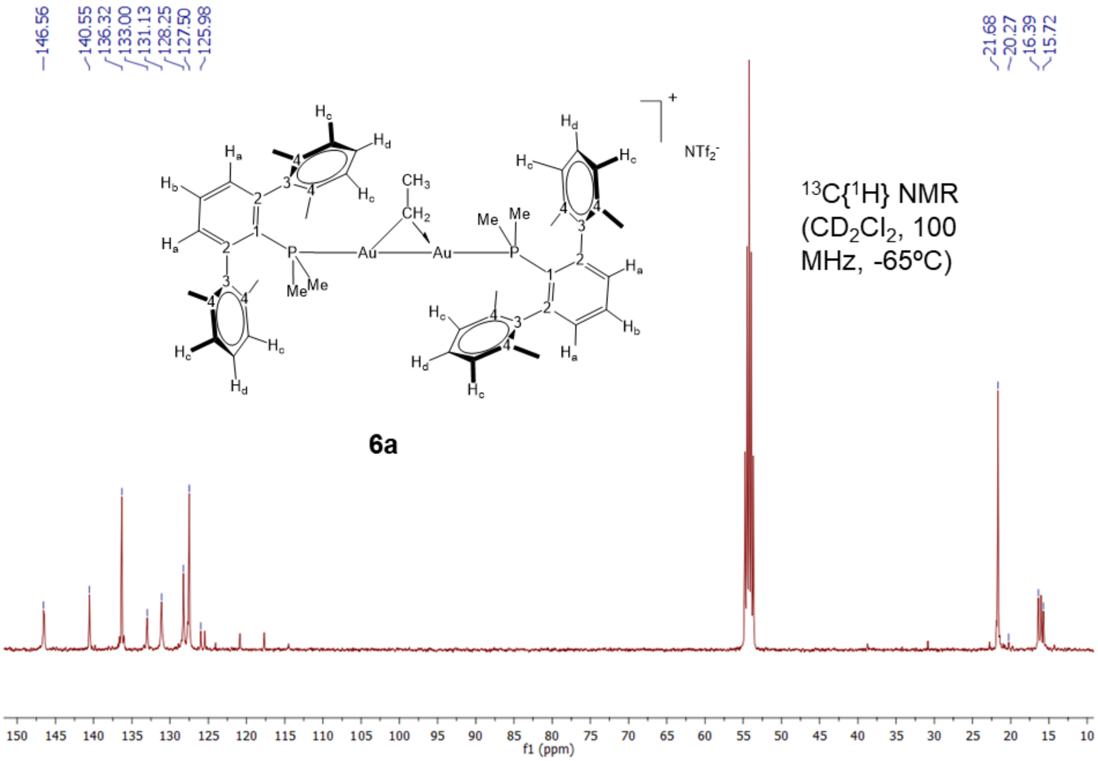
146.56
140.55
136.32
133.00
131.13
128.25
127.50
125.98
21.68
20.27
16.39
15.72
NTf$_2^-$
^{13}C{^{1}H} NMR
(CD$_2$Cl$_2$, 100 MHz, -65ºC)
6a
150 145 140 135 130 125 120 115 110 105 100 95 90 85 80 75 70 65 60 55 50 45 40 35 30 25 20 15 10
f1 (ppm)

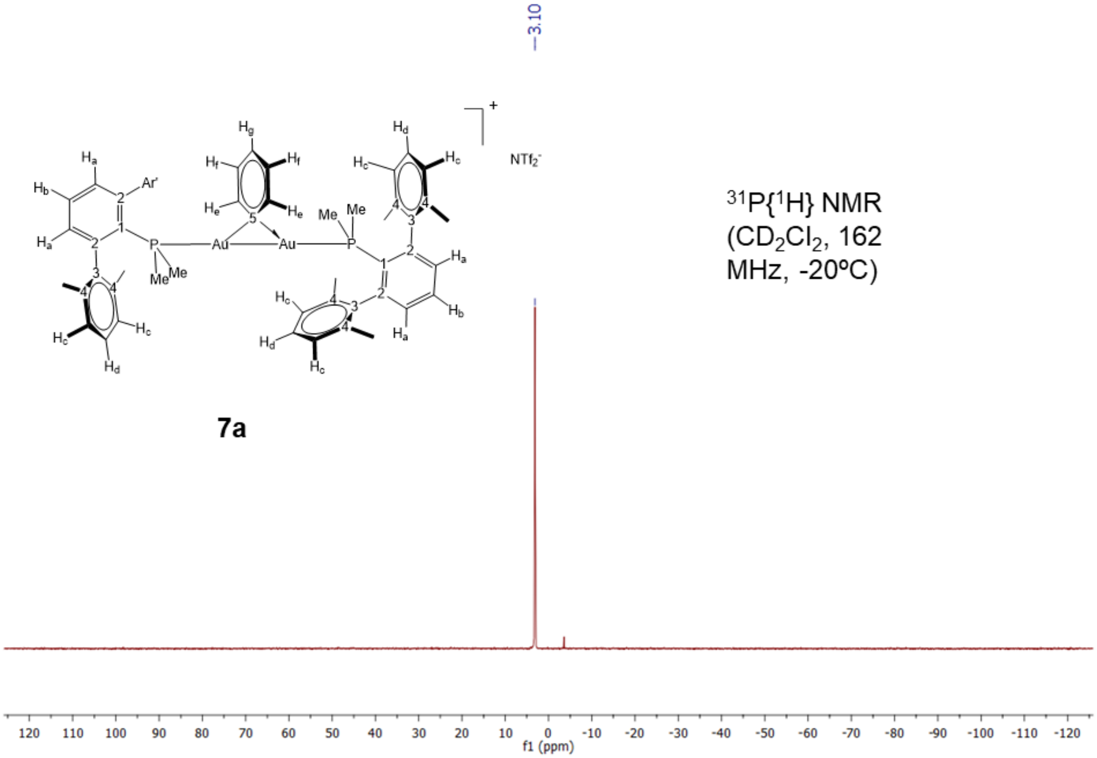

7a

$^{31}P\{^1H\}$ NMR (CD_2Cl_2, 162 MHz, -20ºC)

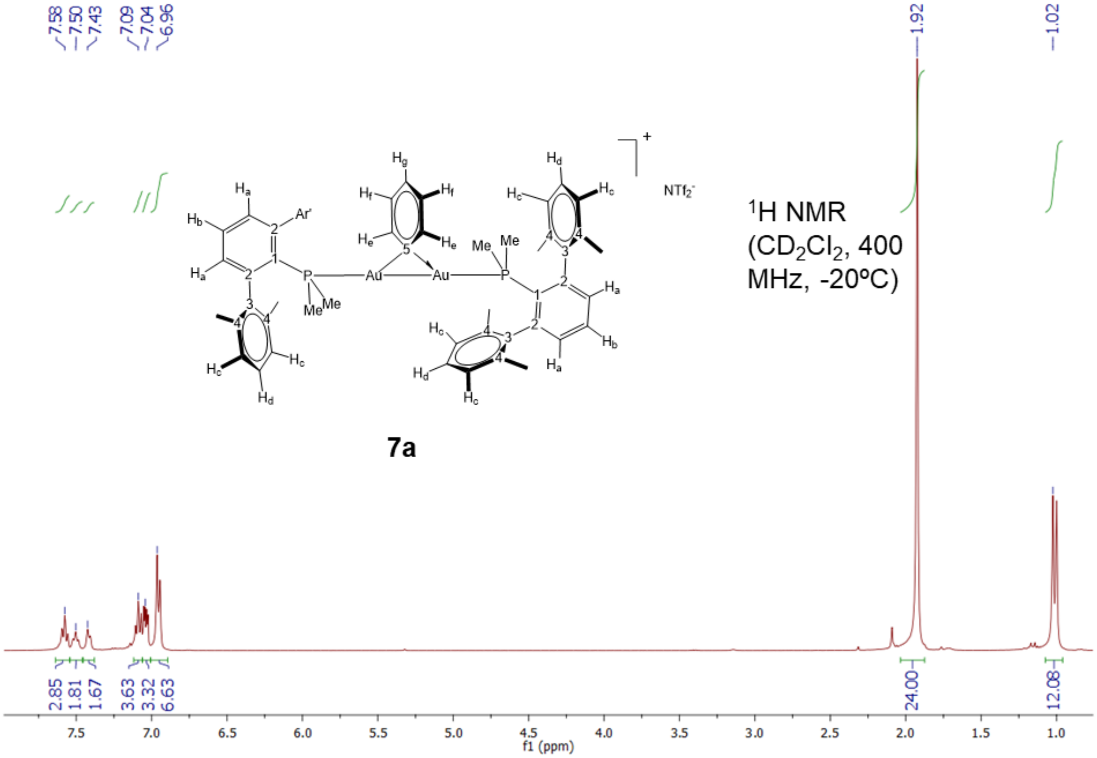

7a

^1H NMR (CD_2Cl_2, 400 MHz, -20ºC)

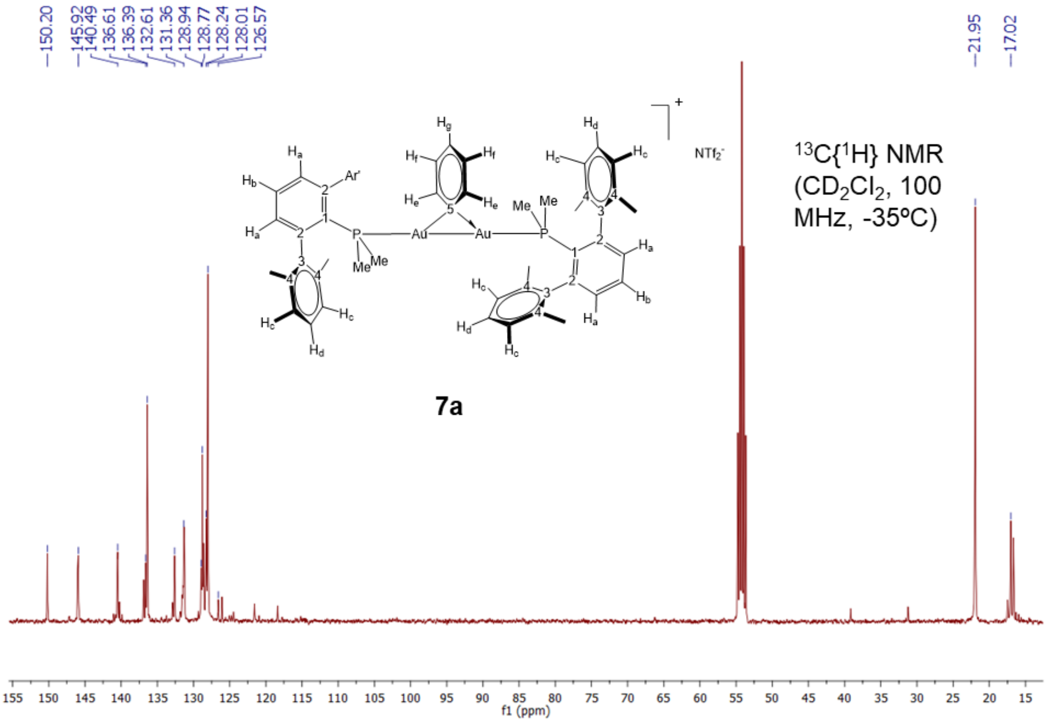

2.5 References

1. A. S. K. Hashmi, *Angewandte Chemie International Edition*, 2010, **49**, 5232-5241.
2. G. Henrion, T. E. J. Chavas, X. Le Goff and F. Gagosz, *Angewandte Chemie International Edition*, 2013, **52**, 6277-6282.
3. X. Zeng, M. Soleilhavoup and G. Bertrand, *Org. Lett.*, 2009, **11**, 3166-3169.
4. V. Lavallo, G. D. Frey, B. Donnadieu, M. Soleilhavoup and G. Bertrand, *Angewandte Chemie International Edition*, 2008, **47**, 5224-5228.
5. S. Gaillard, J. Bosson, R. S. Ramón, P. Nun, A. M. Z. Slawin and S. P. Nolan, *Chem. Eur. J.*, 2010, **16**, 13729-13740.
6. M. Joost, A. Amgoune and D. Bourissou, *Angewandte Chemie International Edition*, 2015, **54**, 15022-15045.

7. J. Wang, S. Lv, H. Chen, M. Shi and J. Zhang, *Dalton Trans.*, 2016, **45**, 17091-17094.
8. P. H.-Y. Cheong, P. Morganelli, M. R. Luzung, K. N. Houk and F. D. Toste, *J. Am. Chem. Soc.*, 2008, **130**, 4517-4526.
9. D. Weber, M. A. Tarselli and M. R. Gagné, *Angewandte Chemie International Edition*, 2009, **48**, 5733-5736.
10. M. D. Levin and F. D. Toste, *Angewandte Chemie International Edition*, 2014, **53**, 6211-6215.
11. W. J. Wolf, M. S. Winston and F. D. Toste, *Nature Chemistry*, 2014, **6**, 159-164.
12. S. Komiya and J. K. Kochi, *J. Am. Chem. Soc.*, 1976, **98**, 7599-7607.
13. W. Rao, M. J. Koh, D. Li, H. Hirao and P. W. H. Chan, *J. Am. Chem. Soc.*, 2013, **135**, 7926-7932.
14. A. Grirrane, H. Garcia, A. Corma and E. Álvarez, *Chem. Eur. J.*, 2013, **19**, 12239-12244.
15. B. G. Hashiguchi, S. M. Bischof, M. M. Konnick and R. A. Periana, *Acc. Chem. Res.*, 2012, **45**, 885-898.
16. C. J. Jones, D. Taube, V. R. Ziatdinov, R. A. Periana, R. J. Nielsen, J. Oxgaard and W. A. Goddard Iii, *Angew. Chem. Int. Ed.*, 2004, **43**, 4626-4629.
17. P. Lu, T. C. Boorman, A. M. Z. Slawin and I. Larrosa, *J. Am. Chem. Soc.*, 2010, **132**, 5580-5581.
18. T. C. Boorman and I. Larrosa, *Chem. Soc. Rev.*, 2011, **40**, 1910-1925.
19. U. Zavyalova, M. Holena, R. Schlögl and M. Baerns, *ChemCatChem*, 2011, **3**, 1935-1947.

20. B. L. Farrell, V. O. Igenegbai and S. Linic, *ACS Catal.*, 2016, **6**, 4340-4346.

21. A. M. Paul and B. E. Bent, *J. Catal.*, 1994, **147**, 264-271.

22. S. Komiya, T. A. Albright, R. Hoffmann and J. K. Kochi, *Journal of the American Chemical Society*, 1976, **98**, 7255-7265.

23. P. Lawrence Kuch and R. Stuart Tobias, *Journal of Organometallic Chemistry*, 1976, **122**, 429-446.

24. J. K. Kochi, *Accounts of Chemical Research*, 1974, **7**, 351-360.

25. A. Tamaki and J. K. Kochi, *Journal of Organometallic Chemistry*, 1973, **61**, 441-450.

26. H. Xu, J. B. Diccianni, J. Katigbak, C. Hu, Y. Zhang and T. Diao, *J. Am. Chem. Soc.*, 2016, **138**, 4779-4786.

27. L. A. Goj, E. D. Blue, S. A. Delp, T. B. Gunnoe, T. R. Cundari and J. L. Petersen, *Organometallics*, 2006, **25**, 4097-4104.

28. M. Lail, T. B. Gunnoe, K. A. Barakat and T. R. Cundari, *Organometallics*, 2005, **24**, 1301-1305.

29. M. T. Johnson, J. Marthinus Janse van Rensburg, M. Axelsson, M. S. G. Ahlquist and O. F. Wendt, *Chemical Science*, 2011, **2**, 2373-2377.

30. M. Kumar, J. Jasinski, G. B. Hammond and B. Xu, *Chem. Eur. J.*, 2014, **20**, 3113-3119.

31. K. L. Vikse, A. Zavras, T. H. Thomas, A. Ariafard, G. N. Khairallah, A. J. Canty, B. F. Yates and R. A. J. O’Hair, *Organometallics*, 2015, **34**, 3255-3263.

32. G. Seidel, C. W. Lehmann and A. Fürstner, *Angewandte Chemie International Edition*, 2010, **49**, 8466-8470.

33. A. Gómez-Suárez, *Angew. Chem.*, 2013, **125**, 972-976.
34. M. F. Espada, J. Campos, J. López-Serrano, M. L. Poveda and E. Carmona, *Angew. Chem. Int. Ed.*, 2015, **54**, 15379-15384.
35. P. Pérez-Galán, N. Delpont, E. Herrero-Gómez, F. Maseras and A. M. Echavarren, *Chem. Eur. J.*, 2010, **16**, 5324-5332.
36. Q.-L. Ni, X.-F. Jiang, T.-H. Huang, X.-J. Wang, L.-C. Gui and K.-G. Yang, *Organometallics*, 2012, **31**, 2343-2348.
37. I. Caracelli, J. Zukerman-Schpector and E. R. T. Tiekink, *Gold Bulletin*, 2013, **46**, 81-89.
38. G. Zuccarello, M. Zanini and A. M. Echavarren, *Isr. J. Chem.*, 2020, **60**, 360-372.
39. M. Marín, J. J. Moreno, C. Navarro-Gilabert, E. Álvarez, C. Maya, R. Peloso, M. C. Nicasio and E. Carmona, *Chem. - Eur. J.*, 2019, **25**, 260-272.
40. G. Li, C. Liu, Y. Lei and R. Jin, *Chem. Commun.*, 2012, **48**, 12005-12007.
41. G. Li, H. Abroshan, C. Liu, S. Zhuo, Z. Li, Y. Xie, H. J. Kim, N. L. Rosi and R. Jin, *ACS Nano*, 2016, **10**, 7998-8005.
42. B. Vilhanová, J. Václavík, L. Artiglia, M. Ranocchiari, A. Togni and J. A. van Bokhoven, *ACS Catal.*, 2017, **7**, 3414-3418.
43. M. Cher, *J. Phys. Chem.*, 1964, **68**, 1316-1321.
44. H. Schmidbaur and A. Schier, *Chem. Soc. Rev.*, 2008, **37**, 1931-1951.
45. H. Schmidbaur and A. Schier, *Chem. Soc. Rev.*, 2012, **41**, 370-412.
46. D. Weber, T. D. Jones, L. L. Adduci and M. R. Gagné, *Angew. Chem. Int. Ed.*, 2012, **51**, 2452-2456.
47. J. Campos, *J. Am. Chem. Soc.*, 2017, **139**, 2944-2947.

48. N. Hidalgo, J. J. Moreno, M. Pérez-Jiménez, C. Maya, J. López-Serrano and J. Campos, *Chem. - Eur. J.*, 2020, **26**, 5982-5993.
49. J. Schulz, E. Shcherbachenko and J. Roithová, *Organometallics*, 2015, **34**, 3979-3987.
50. L. Jin, D. R. Tolentino, M. Melaimi and G. Bertrand, *Sci. Adv.*, 2015, **1**, e1500304.
51. P. Buchwalter, J. Rosé and P. Braunstein, *Chem. Rev.*, 2015, **115**, 28-126.
52. C. M. Farley and C. Uyeda, *Trends Chem.*, 2019, **1**, 497-509.
53. L. Ortega-Moreno, M. Fernández-Espada, J. J. Moreno, C. Navarro-Gilabert, J. Campos, S. Conejero, J. López-Serrano, C. Maya, R. Peloso and E. Carmona, *Polyhedron*, 2016, **116**, 170-181.
54. R. Uson, A. Laguna, M. Laguna, D. A. Briggs, H. H. Murray and J. P. Fackler Jr, 1989.
55. A. S. K. Hashmi, M. Rudolph, J. Huck, W. Frey, J. W. Bats and M. Hamzić, *Angew. Chem. Int. Ed.*, 2009, **48**, 5848-5852.
56. N. Mézailles, L. Ricard and F. Gagosz, *Organic Letters*, 2005, **7**, 4133-4136.
57. T.-L. Ho, M. Fieser and L. Fieser, 2011, DOI: 10.1002/9780471264194.fos11741.
58. A. M. Mueting, B. D. Alexander, P. D. Boyle, A. L. Casalnuovo, L. N. Ito, B. J. Johnson, L. H. Pignolet, M. Leeaphon, K. E. Meyer, R. A. Walton, D. M. Heinekey and T. G. P. Harper, 1992, DOI: 10.1002/9780470132609.ch63.
59. C. Nieto-Oberhuber, S. López and A. M. Echavarren, *J. Am. Chem. Soc.*, 2005, **127**, 6178-6179.
60. Y. Wang, K. Ji, S. Lan and L. Zhang, *Angew. Chem. Int. Ed.*, 2012, **51**, 1915-1918.

61. F. Sánchez-Cantalejo, J. D. Priest and P. W. Davies, *Chem. - Eur. J.*, 2018, **24**, 17215-17219.

62. A. Zhdanko, M. Ströbele and M. E. Maier, *Chem. - Eur. J.*, 2012, **18**, 14732-14744.

63. C. Fehr, M. Vuagnoux, A. Buzas, J. Arpagaus and H. Sommer, *Chem. - Eur. J.*, 2011, **17**, 6214-6220.

64. M. G. Alférez, J. J. Moreno, N. Hidalgo and J. Campos, *Angew. Chem. Int. Ed.*, 2020, **n/a**.

65. Z.-Y. Han, R. Guo, P.-S. Wang, D.-F. Chen, H. Xiao and L.-Z. Gong, *Tetrahedron Letters*, 2011, **52**, 5963-5967.

66. C. Nieto-Oberhuber, S. López and A. M. Echavarren, *J. Am. Chem. Soc.*, 2005, **127**, 6178-6179.

[67]. G. M. Sheldrick, *Acta Cryst.* A., 2015, **71**, 3-8.

[68]. Bruker (2012). *Saint; SADABS; APEX3*. Bruker AXS Inc., Madison, WI, U.S.A.

[6]9. O. V. Dolomanov, L. J. Bourhis, R. J. Gildea, J. A. K. Howard, H. Puschmann, *J. Appl. Cryst.* 2009, **42**, 339-341.

70. Gaussian 09, Revision E.01, M. J. Frisch, G. W. Trucks, H. B. Schlegel, G. E. Scuseria, M. A. Robb, J. R. Cheeseman, G. Scalmani, V. Barone, B. Mennucci, G. A. Petersson, H. Nakatsuji, M. Caricato, X. Li, H. P. Hratchian, A. F. Izmaylov, J. Bloino, G. Zheng, J. L. Sonnenberg, M. Hada, M. Ehara, K. Toyota, R. Fukuda, J. Hasegawa, M. Ishida, T. Nakajima, Y. Honda, O. Kitao, H. Nakai, T. Vreven, J. A. Montgomery, Jr., J. E. Peralta, F. Ogliaro, M. Bearpark, J. J. Heyd, E. Brothers, K. N. Kudin, V. N. Staroverov, T. Keith, R. Kobayashi, J. Normand, K. Raghavachari, A. Rendell, J. C. Burant, S. S. Iyengar, J. Tomasi, M. Cossi, N.

Rega, J. M. Millam, M. Klene, J. E. Knox, J. B. Cross, V. Bakken, C. Adamo, J. Jaramillo, R. Gomperts, R. E. Stratmann, O. Yazyev, A. J. Austin, R. Cammi, C. Pomelli, J. W. Ochterski, R. L. Martin, K. Morokuma, V. G. Zakrzewski, G. A. Voth, P. Salvador, J. J. Dannenberg, S. Dapprich, A. D. Daniels, O. Farkas, J. B. Foresman, J. V. Ortiz, J. Cioslowski, and D. J. Fox, Gaussian, Inc., Wallingford CT, 2013.

71. J.-D. Chai, M. Head-Gordon, *Phys. Chem. Chem. Phys*., 2008, **10**, 6615.

72. a) W. J. Hehre, R. Ditchfield, J. A. Pople, *J. Phys. Chem.,* 1972, **56**, 2257; b) P. C. Hariharan, J. A. Pople, *Theor. Chim. Acta.,* 1973, **28**, 213; c) M. M. Francl, W. J. Pietro, W. J. Hehre, J. S. Binkley, M. S. Gordon, D. J. Defrees, J. A. Pople, *J. Chem. Phys.,* 1982, **77**, 3654.

73. D. Andrae, U. Haeussermann, M. Dolg, H. Stoll, H. Preuss, *Theor. Chim. Acta.,* 1990, **77**, 123.

74. A. V. Marenich, C. J. Cramer, D. G. Truhlar, *J. Phys. Chem. B*., 2009, **113**, 6378.

75. R. F. Ribeiro, A. V. Marenich, C. J. Cramer, D. G. Truhlar, *J. Phys. Chem. B.,* 2011, **115**, 14556.

76. I. Funes-Ardoiz, R. S. Paton, 2016 Goodvibes: Goodvibes 2.0.2 https://doi.org/10.5281/zenodo.595246

3 Oxidative Alkenylation of Arenes Using Supported Rh Materials and [Rh(μ-OAc)(η^2-C_2H_4)$_2$]$_2$: Evidence that Active Catalysts are Formed by Rh Leaching to form a Soluble Catalyst

3.1 Introduction to alkenyl arenes synthesis

Alkyl and alkenyl arenes are used as precursors for a range of high-value chemicals, including detergent precursors, plastics, elastomers and pharmaceuticals.[1-5] For example, linear alkylbenzenes, which are primarily 2-aryl alkanes, serve as chemical precursors for alkylbenzene sulfonates – an active component in detergents.[6] Styrene is used for polystyrene plastics and synthetic rubber manufacturing.[7] The current industrial production of alkylbenzenes uses Friedel-Crafts and zeolite acid-based technologies.[8] Two general technologies for styrene production, including the ethylbenzene/styrene monomer process (EB/SM) and the propylene oxide/styrene monomer process (PO/SM), have been commercialized (Scheme 3.1).[3, 9-11] Although the EB/SM and PO/SM processes have been commercialized in various downstream refinery plants, these industrial processes have some disadvantages, including: 1) multi-step processes; for example, EB/SM processes include benzene alkylation, multiple distillations, transalkylation, and ethylbenzene dehydrogenation, while the PO/SM process involves benzene alkylation, oxidation, oxygen atom transfer to form propylene oxide and 1-phenylethanol, and dehydration; 2) energy-intensive operations such as trans-alkylation and distillations and endothermic dehydrogenation; and 3) an inability to produce anti-Markovnikov products (i.e., 1-aryl alkenes or alkanes).[12] Thus, there is increased interest in developing new catalytic processes for direct arene alkenylation at a low operating temperature that offers anti-Markovnikov selectivity.[13-15]

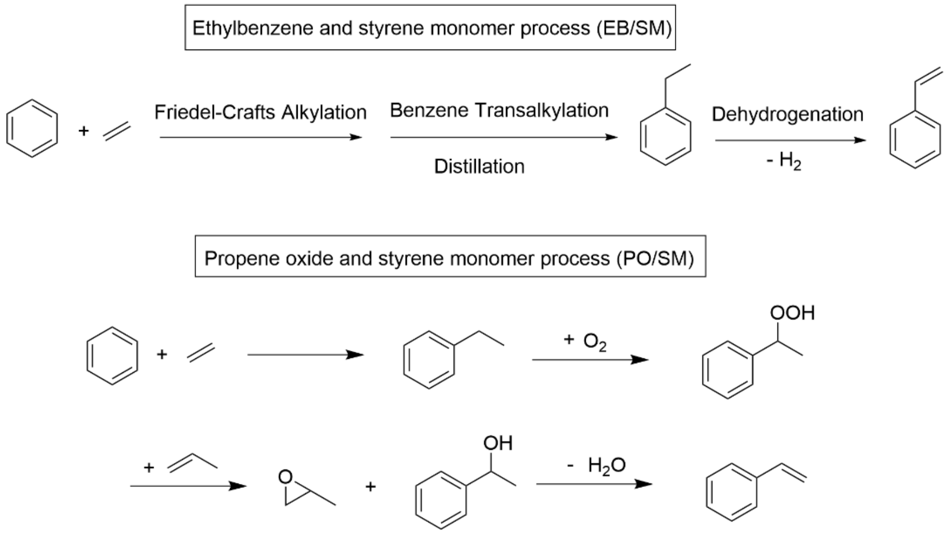

Scheme 3.1. Industrial processes for styrene monomer production: EB/SM process (top) and PO/SM process (bottom).

Transition metal-catalyzed arene alkenylation (*i.e.*, oxidative olefin hydroarylation) that functions by a pathway involving transition metal-mediated arene C–H activation and olefin insertion offers possible advantages over traditional acid-catalyzed arene alkylation (Scheme 3.2).[14, 16-20] The potential advantages of transition metal-mediated catalysis include: a) direct arene alkenylation (rather than alkylation) via catalytic processes that involve β-hydride elimination after the olefin insertion step, b) selective production of 1-aryl alkane/alkene by circumventing carbocationic intermediates that lead to Markovnikov selectivity, c) conversion of electron-deficient arenes, d) new regioselectivity for alkenylation or alkylation of substituted arenes, and e) inhibition of polyalkylation since alkylated or alkenylated products can be less reactive than starting arenes.[14] Molecular catalysts involving Ni, Ir, Ru, Pt, Pd and Rh have been studied for catalytic C–H alkylation or alkenylation of arenes with olefins.[15, 16, 21-35]

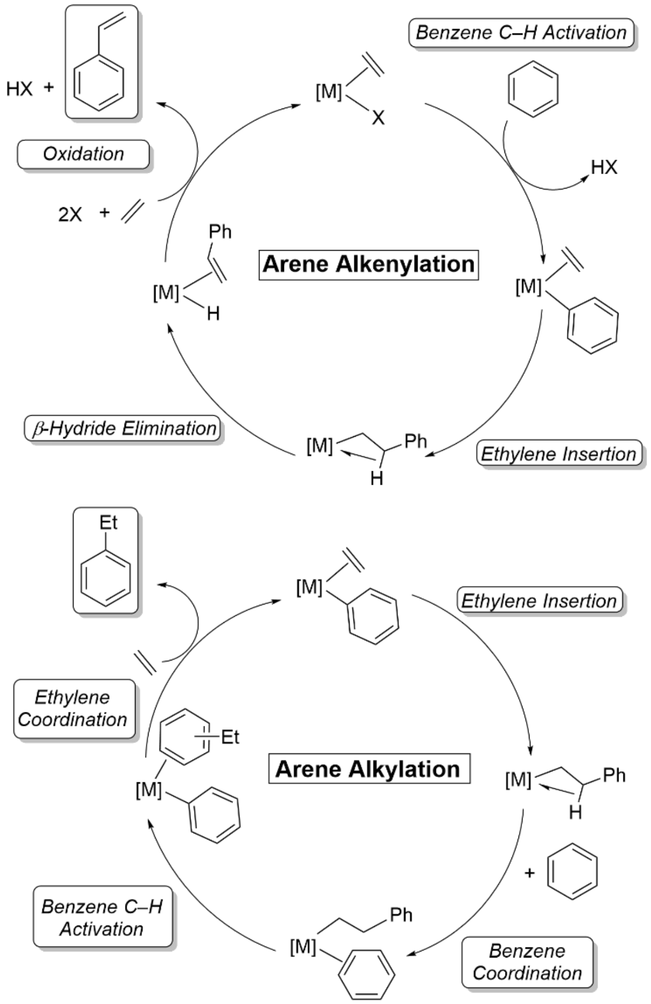

Scheme 3.2. Generic catalytic cycles for transition metal-catalyzed arene alkenylation and alkylation.[14]

Recently, we reported Rh-catalyzed arene alkenylation to directly synthesize styrene and 1-aryl alkenes at 150 °C.[13, 14, 36-41] Based on the mechanistic studies, our initial proposed catalytic cycle involves: a) Rh-carboxylate group assisted arene C–H activation (Scheme 3.3), b) olefin coordination and insertion into a Rh–aryl bond, c) β-hydride elimination from the resulting Rh–alkyl intermediate(s), and d) alkenyl arene dissociation and oxidation of Rh–H intermediate with CuX_2 (X = carboxylate) to regenerate the starting catalyst. Under some conditions using $[Rh(\mu\text{-}OAc)(\eta^2\text{-}C_2H_4)_2]_2/Cu(OAc)_2$ catalysts, we observed an induction period during styrene synthesis at 150 °C.[13, 36, 37]

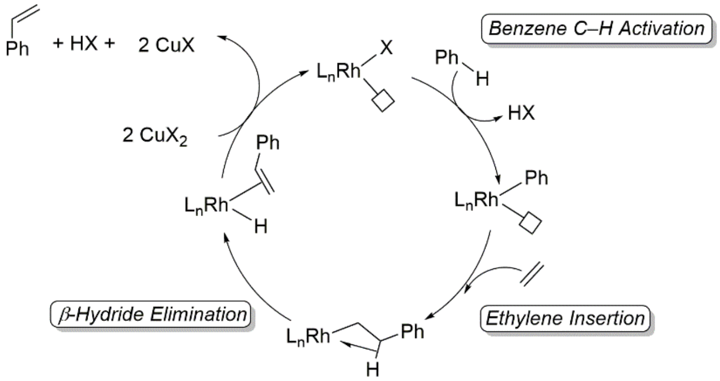

Scheme 3.3. General proposed reaction mechanism for Rh-mediated arene alkenylation using benzene and ethylene substrates.

In various Pd-catalyzed C–C coupling reactions, dissolution and re-adsorption of supported Pd pre-catalysts have been reported.[42-49] For example, the Davis, Kohler and Jones groups used Pd catalysts supported on silica (Pd/SiO_2), zeolite (Pd/NaY), titania (Pd/TiO_2), and aluminum oxide (Pd/Al_2O_3) for Heck coupling reactions and found that dissolution of palladium is correlated with reaction rate.[42, 46, 49] The solid Pd catalyst functions as a reservoir for molecular Pd species in solution (Scheme 3.4A). The agglomeration and redeposition of dissolved Pd species can occur in the presence of supports such as SiO_2, Al_2O_3, and TiO_2, which forms Pd(0)/MO_x catalyst precursors (Scheme 3.4B).[46, 48-50] In the presence of phosphine ligands, it was proposed that aryl halides likely oxidizes Pd(0) to form molecular L_nPd^{II}(Ar)(X) (X = Br or Cl; L = phosphine), which participates in a Pd(II)/Pd(0) catalytic cycle (Scheme 3.4C).[48, 49]

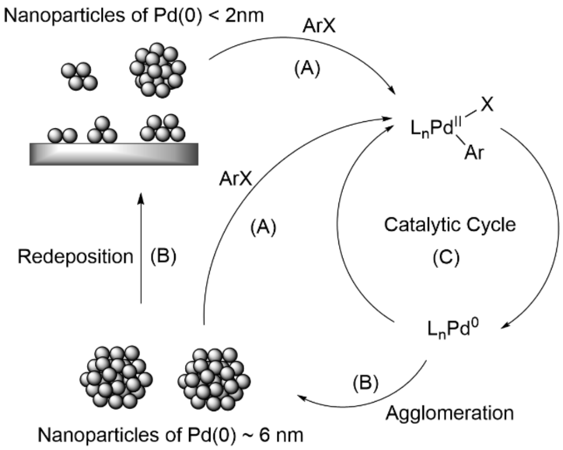

Scheme 3.4. General leaching/dissolution process (oxidation of Pd) to liberate soluble, catalytically active molecular palladium species (A), agglomeration and redeposition of Pd(0) (B), and catalytic cycle (C).

As part of our efforts to delineate the dynamics between heterogeneous Rh and soluble Rh species in the oxidative alkenylation of arenes, we prepared supported Rh nanoparticles on silica (SiO_2) and nitrogen-doped carbon (NC) and studied their reactivity as catalyst precursors. Also, in this chapter, the apparent induction period observed in the $[Rh(\mu\text{-}OAc)(\eta^2\text{-}C_2H_4)_2]_2/Cu(OAc)_2$ catalytic system is interrogated using X-ray photoelectron spectroscopy (XPS) and transmission electron microscopy (TEM) spectroscopies. Herein, we report on the use of supported Rh as a catalyst precursor for the synthesis of styrene and other alkenyl arenes with evidence that catalytic activity is a result of leaching of soluble Rh from the supported materials. Further, when commercial $Cu(OAc)_2$ is used with the molecular Rh catalyst precursor $[Rh(\mu\text{-}OAc)(\eta^2\text{-}C_2H_4)_2]_2$, we propose that observed induction periods are likely due to the rapid decomposition of the soluble Rh catalyst precursor to form insoluble Rh(s) followed by formation of the active catalyst through dissolution of Rh(s).

3.2 Results and Discussion

3.2.1 Synthesis of supported Rh materials. We prepared Rh nanoparticles supported on silica (Rh/SiO_2) using a modified ion-exchange method.[51, 52] The weight loading of Rh was measured by inductively coupled plasma optical emission spectrometry (ICP-OES) analysis to be 3.6 wt%. Further characterization of Rh/SiO_2 was performed using transmission electron microscopy (TEM), dihydrogen chemisorption, and X-ray photoelectron spectroscopy (XPS). Dihydrogen chemisorption of the synthesized Rh/SiO_2 indicated a metal dispersion of ~0.7 (H/Rh ratio), and the average metal particle size measured by TEM was found to be 2.2(5) nm (Figure 3.1, Table 3.1). The presence of metallic Rh(0) was confirmed with XPS, which showed a binding energy at 307.3 eV (Figure 3.2).[37, 53, 54]

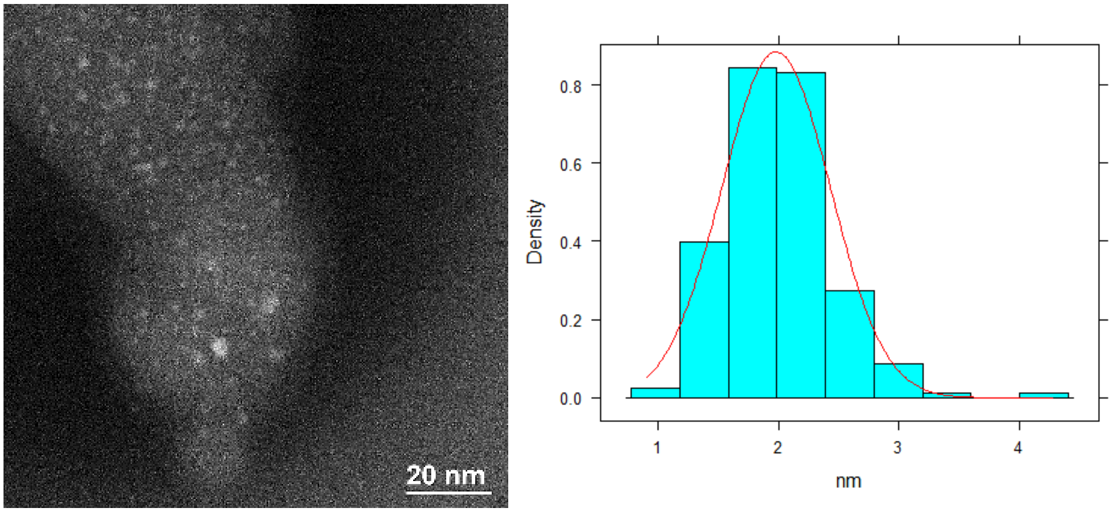

Figure 3.1. HAADF-STEM image of synthesized Rh/SiO_2 (left) and the particle size distribution (right).

Table 3.1. Characterization of Rh/SiO_2 material.

Catalyst	Particle Size		Weight Loading	Oxidation State
	Surface-weighted avg. diameter ^{a} (nm)	$1/(H/Rh)^{b}$ (nm)	ICP-OES	XPS
Rh/SiO_2	2.2 (5)	1.4	3.6 wt%	Rh(0), 307.3 eV (Rh $3d_{5/2}$)

[a] Result calculated from $\Sigma d^3/\Sigma d^2$ where diameter(d) is measured using STEM images.
[b] Result estimated from hydrogen chemisorption.

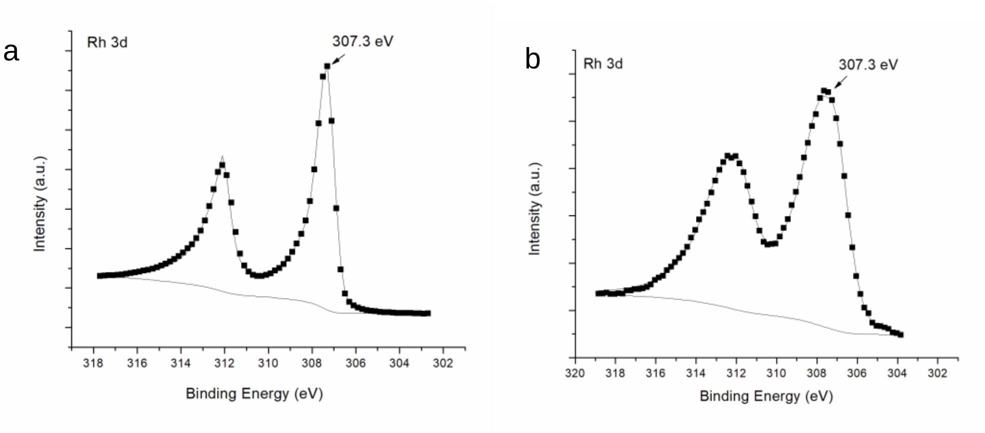

Figure 3.2. XPS spectra (Rh 3d region) of (a) Rh metal foil and (b) Rh/SiO_2 nanoparticles.

Nitrogen-doped carbon (NC) has been used as a support for single-atom catalysts with transition metals such as Co,[55-57] Mn,[54] Ni,[54] Fe,[54] Rh,[58] and Pd.[59] Supported Rh on nitrogen-doped carbons (Rh/NC-HCl and Rh/NC-IWI) were prepared using a modified high-temperature thermal treatment as discussed in detail in the experimental section.[56] The catalyst labeled as Rh/NC-HCl was treated with aqueous HCl (in an attempt to remove metal particles) followed by a thermal treatment with H_2. The Rh/NC-IWI material was prepared using an incipient wetness impregnation (IWI) method (a capillary impregnation or dry impregnation method is commonly used for the synthesis of heterogeneous catalysts. Basically, the mental-containning precusor solution is added to a catalyst support containing the same pore volume as the volume of the solutions that was added) for deposition of the Rh precursor $Rh(NO_3)_3$. According to ICP-OES analysis, the Rh loading was approximately 1 wt% for Rh/NC-HCl materials and 1.5 wt% for Rh/NC-IWI catalysts. The Rh detected by ICP-OEP analysis is associated with only the fraction of metal that could be removed from the sample for analysis. TEM characterization of the Rh/NC-HCl material showed Rh nanoparticles (Figure 3.3). The recovered Rh/NC-HCl material after microwave digestion showed that some Rh could not be removed from the NC support, which suggests that some of the Rh nanoparticles are likely embedded inside the NC matrix (Figure 3.4).

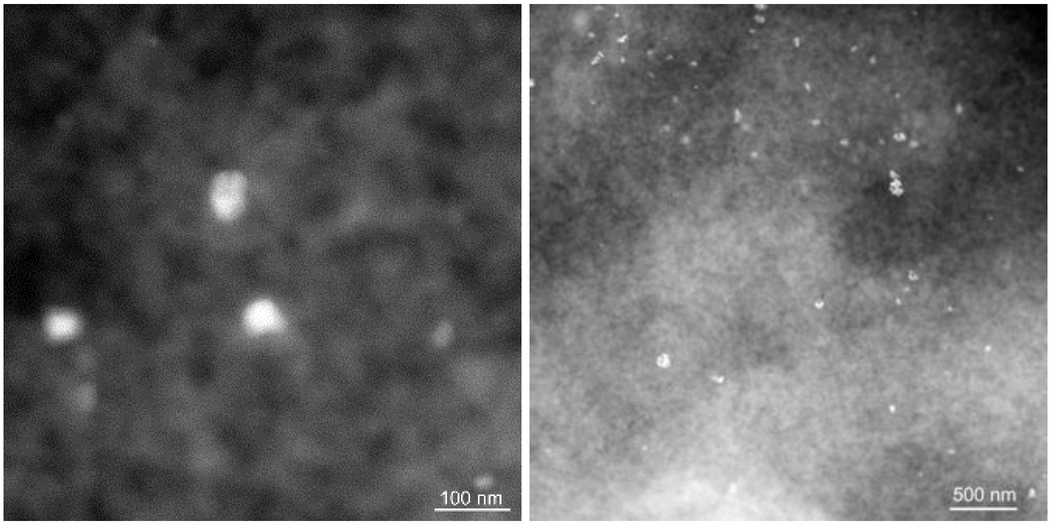

Figure 3.3. High-Angle Annular Dark Field-Scanning Transmission Electron Microscopy (HAADF-STEM) images of the synthesized Rh/NC-HCl material.

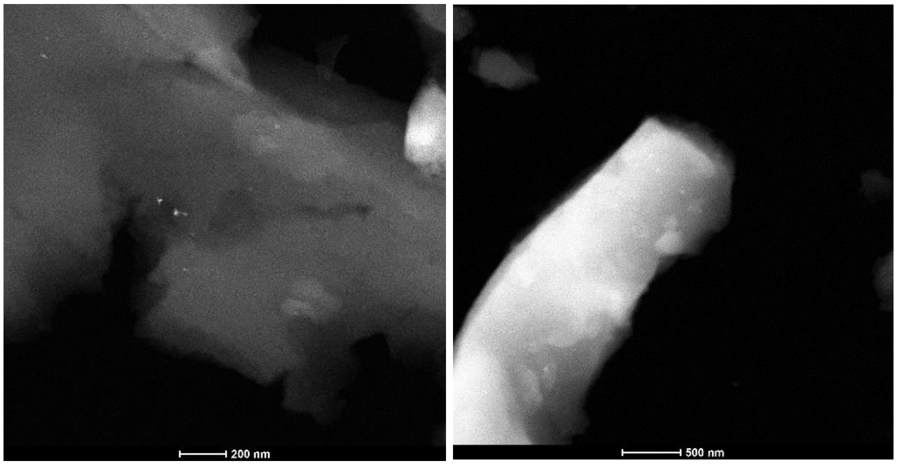

Figure 3.4. HAADF-STEM images of recovered Rh/NC-HCl catalysts after microwave digestion.

For the Rh/NC-HCl sample, XPS analysis of N1s core level shows a broad envelop associated with multiple N species in the carbon matrix. Assuming only two types of sites for simplicity, quantitative analysis reveals about a 2:1 ratio of pyridinic sites (binding energy of ~398.3 eV) and graphitic sites (binding energy of ~400.8 eV; Figure 3.5).[56] TEM analysis of Rh/NC-IWI showed that the size of synthesized Rh nanoparticles was ~20 nm (Figure 3.6).

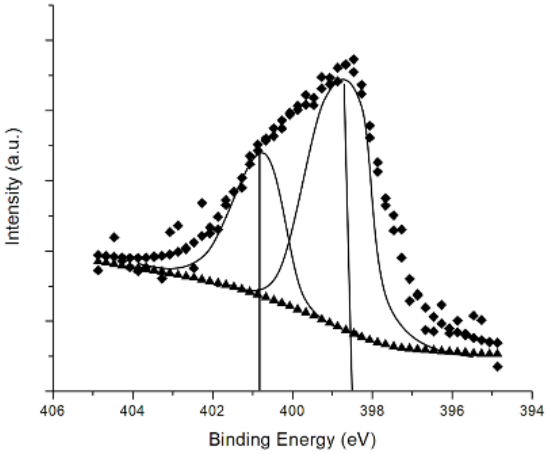

Figure 3.5. XPS characterization of N1s from Rh/NC-HCl shows two types of sites: 1) pyridinic sites at binding energy ~398.3 eV and 2) graphitic sites with binding energy ~400.8 eV.

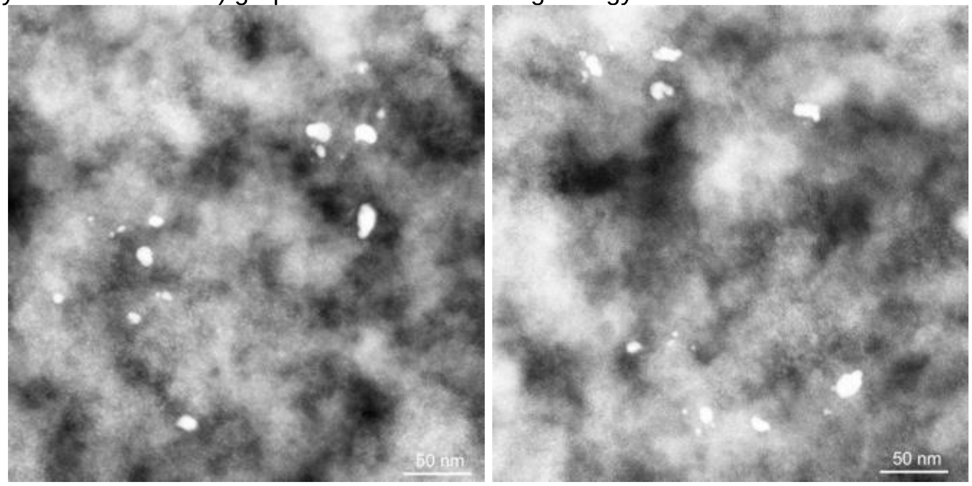

Figure 3.6. HAADF-STEM images of the synthesized Rh/NC-IWI catalyst.

3.2.2 Catalytic Arene Alkenylation using Rh/SiO$_2$ as Catalyst Precursor. We began our studies of catalysis using supported Rh materials with the conversion of benzene and ethylene to styrene using conditions that are similar to our previously reported catalysis using molecular Rh catalyst precursors.[13, 14, 36-38] Unless otherwise noted, all reaction tests were performed in triplicate with results reported together with standard deviations. Heating mixtures of Rh/SiO$_2$, benzene, ethylene and Cu(OPiv)$_2$ (OPiv = trimethylacetate) to 150 °C results in the production of styrene (note: assuming 2 equivalents of CuX$_2$ (X = carboxylate) are consumed per equivalent of styrene, the maximum turnovers (TOs) with y equivalents of CuX$_2$ as limiting reagent is y/2).[13] As these experiments were performed under anaerobic conditions, Cu(I) should not be reoxidized to Cu(II) *in situ*. Thus, Cu(II) is the limiting reagent. Monitoring the styrene production after 26 hours reveals ~60(3)% yield based on the starting amount of Cu(II) (Figure 3.7).

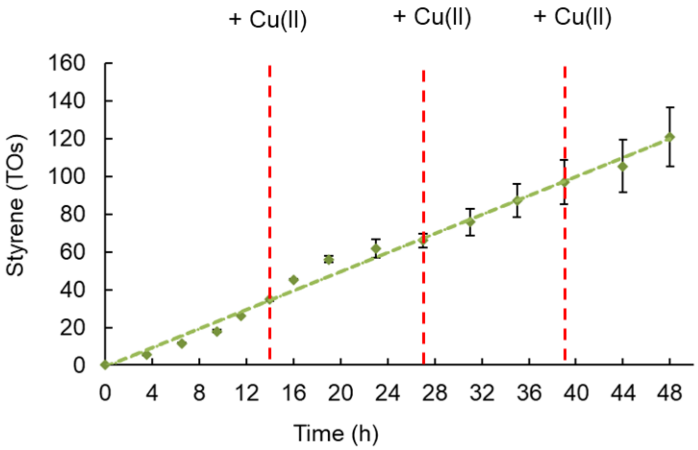

Figure 3.7. Styrene turnover (TOs) versus time plot using Rh/SiO$_2$ and Cu(OPiv)$_2$ (120 eq., relative to surface Rh atoms). An additional 120 eq. Cu(OPiv)$_2$ was added at 14 h, 26 h and 38 h. Catalytic conditions: 5.3 mg of Rh/SiO$_2$ (0.00112 mmol surface Rh atoms), 10 mL benzene, 36 mg Cu(OPiv)$_2$, 20 eq. hexamethylbenzene as the internal standard, 40 psig ethylene at 150 °C.

The number of surface Rh atoms of the Rh/SiO$_2$ material was determined from H$_2$ chemisorption, which indicated ~70% of Rh atoms in the metal particles were located on the surface (Table 3.1). If the surface Rh atoms are considered to be active for catalysis, then an estimated turnover frequency (TOF) calculation can be made from the observed rate of styrene production normalized by surface Rh atoms in the reactor, which gives an apparent TOF of 5.0(3) x 10^{-4} s^{-1}. It is important to emphasize that this is not an actual TOF as it assumes that all surface Rh atoms are active for catalysis. We use this apparent TOF to compare (see next) to the apparent TOF using soluble and molecular Rh. Thus,under the same reaction conditions using the molecular Rh(I) precursor $[Rh(\mu\text{-}OAc)(\eta^2\text{-}C_2H_4)_2]_2$, the styrene production rate after 0.5 hour, which corresponds to 70(2)% conversion of Cu(II) (Figure 3.8), gives an apparent TOF (~1.8(3) x 10^{-2}) that is approximately 36 times greater than Rh/SiO_2 catalyst precursor. The difference in apparent TOFs is consistent with either slower catalysis using Rh/SiO_2 (compared to soluble and molecular Rh catalysis) or leaching of a small amount of Rh from the Rh/SiO_2 to give soluble catalyst that is comparable in activity to $[Rh(\mu\text{-}OAc)(\eta^2\text{-}C_2H_4)_2]_2$.

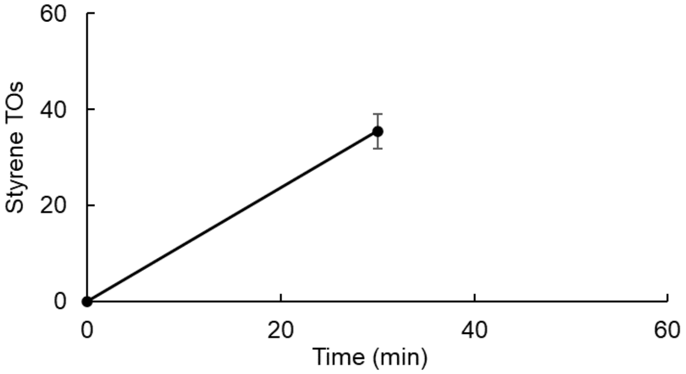

Figure 3.8. Styrene turnovers (TOs) after 0.5 h using $[Rh(\mu\text{-}OAc)(\eta^2\text{-}C_2H_4)_2]_2$ (0.00112 mmol) as catalyst precursor. Reaction conditions: 10 mL benzene, 120 eq. $Cu(OPiv)_2$ (relative to Rh atoms), 20 eq. hexamethylbenzene as the internal standard, 40 psig ethylene and 150 °C.

Next, we performed standard experiments to probe Rh leaching using ICP-OES measurement and the Maitlis' filtration test.[49, 60, 61] During the styrene synthesis mediated by Rh/SiO_2 (conditions listed above), a Maitlis filtration using a 200 µm filter at room temperature was performed after 12 h of reaction, which corresponded to 50(3)% conversion (based on Cu(II) as limited reagent) of the reaction (Figure 3.9). We then tested the filtrate for catalytic activity. Under the same conditions used to test Rh/SiO_2, we observed only a small amount of styrene (Figure 3.9, red plot). The minimal catalytic activity of the filtrate is consistent with ICP-OES measurement of the filtrate (after Maitlis filtration) indicating that only approximately 1 mol % of the original amount of Rh from Rh/SiO_2 leached into the filtrate. The polymer poly(vinylpyridine) (PVPy) has been used as a Pd(II) trap to confirm the leaching of Pd(II) from Pd catalyst on silica support.[42, 62-64] We performed similar trapping experiment to probe the possible leaching from catalysis using Rh/SiO_2. The addition of 500 equivalents of PVPy to the catalytic reaction using Rh/SiO_2 prevented the formation of styrene (Figure 3.9, blue plot), which is consistent with the hypothesis that the observed reactivity from Rh/SiO_2 might be from the leached and soluble Rh species. If it is assumed that catalytic styrene production using fresh Rh/SiO_2 is due to leached Rh, using the calculated apparent TOFs (~$1.8(3) \times 10^{-2}$ for $[Rh(\mu\text{-}OAc)(\eta^2\text{-}C_2H_4)_2]_2$ versus $5.0(3) \times 10^{-4}$ s^{-1} for Rh/SiO_2), we can estimate that approximately 3 mol % of the Rh from Rh/SiO_2 is solubilized. Given that this is an approximation, complicated by the dynamic nature of leaching, potential readsorption/trapping by the filter and standard deviations for TOF determinations, this estimate fits well with the 1% leaching determined by ICP-OES.

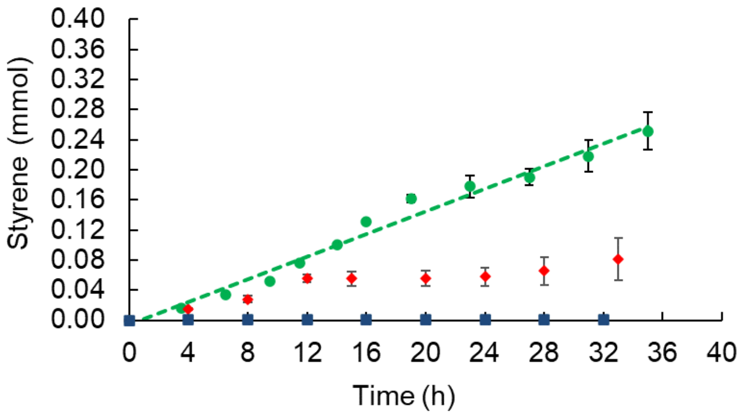

Figure 3.9. Catalytic performance using Rh/SiO_2 for styrene synthesis without filtration (green), with addition of 500 eq. of poly(vinylpyridine (relative to surface Rh atoms) at time of zero for catalysis using Rh/SiO_2 (blue), and using the filtrate (solution) collected from a Maitlis filtration test at 12 h (red). Catalytic conditions: 5.3 mg Rh/SiO_2 material (0.00112 mmol), 15.5 mg poly(vinylpyridine), 10 mL benzene, 72 mg Cu(OPiv)$_2$ (240 eq. relative to Rh), 20 eq. hexamethylbenzene as the internal standard, 40 psig ethylene at 150 °C.

Using an α-olefin such as propylene for the arene alkenylation can result in multiple products depending on the regioselectivity of olefin insertion and selectivity of β-hydride elimination (Scheme 3.5). Using propylene and benzene conversion as a probe reaction, thee "linear" products (or anti-Markovnikov products) and one "branched product" (Markovnikov product) are observed (Scheme 3.5). For benzene and propylene, we compared the regioselectivity using Rh/SiO_2 as catalyst precursor to catalysis using the molecular precursor $[Rh(\mu\text{-}OAc)(\eta^2\text{-}C_2H_4)_2]_2$. Using Cu(OPiv)$_2$ as an oxidant, the L/B ratio (i.e., the ratio of anti-Markovnikov to Markovnikov products) for Rh/SiO_2 mediated benzene and propylene was 10(2):1 (through the chapter, results are from a minimum of three independent experiments with standard deviations given in parenthesis), which is statistically similar to L/B selectivity (14(2):1) using $[Rh(\mu\text{-}OAc)(\eta^2\text{-}C_2H_4)_2]_2$ as catalyst precursor under the identical conditions (Table 3.2). When Cu(OHex)$_2$ was used an oxidant, statistically identical L/B selectivity was observed with 8.0(2):1 for Rh/SiO_2 and 7.4 (1):1 for $[Rh(\mu\text{-}OAc)(\eta^2\text{-}C_2H_4)_2]_2$ (Table 3.3). These results are consistent with the same active catalyst from the molecular catalyst precursor Rh(μ-OAc)(η^2-C_2H_4)$_2$]$_2$ and Rh/SiO_2.

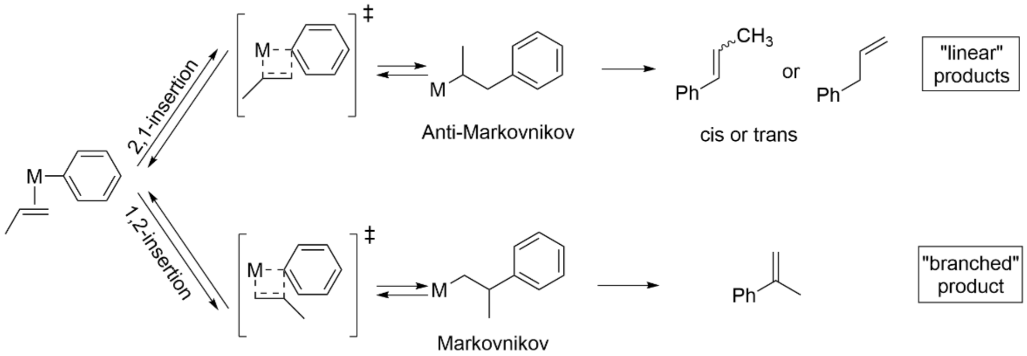

Scheme 3.5. Linear/branched product selectivity is dictated by the olefin insertion step and, in some circumstances, the relative rates of subsequent reactions (*i.e.*, Curtin−Hammett conditions).[14]

Table 3.2. Comparison of anti-Markovnikov to Markovnikov (*i.e.*, linear to branched or L/B) selectivity for the conversion of benzene and propylene using Rh/SiO_2 and the molecular Rh complex [Rh(μ-OAc)(η^2-C_2H_4)$_2$]$_2$ as catalyst precursor. Catalytic conditions: 5.3 mg Rh/SiO_2 material (0.00112 mmol) or eq. amount of molecular catalysts [Rh(μ-OAc)(η^2-C_2H_4)$_2$]$_2$, 10 mL benzene, 72 mg Cu(OPiv)$_2$ (240 eq. relative to Rh atom), 100 eq. HOPiv, 20 eq. hexamethylbenzene as the internal standard, 35 psig propylene and 150 °C. The L/B selectivity is determined when copper(II) is consumed.

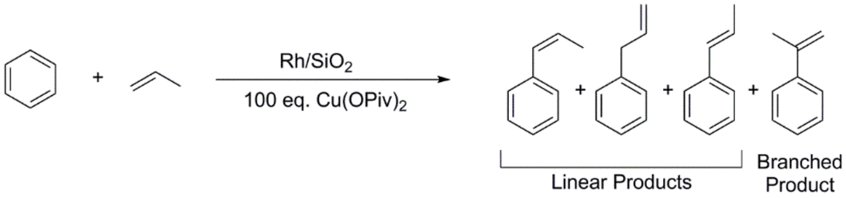

Catalyst Precursor	L/B selectivity
Rh/SiO_2	10(2)
[Rh(μ-OAc)(η^2-C_2H_4)$_2$]$_2$	14(2)

Table 3.3. Comparison of anti-Markovnikov to Markovnikov (i.e., linear to branched or L/B) selectivity for the conversion of benzene and propylene suing Rh/SiO_2 and the molecular Rh complex [Rh(μ-OAc)(η^2-C_2H_4)$_2$]$_2$ as catalyst precursor using Cu(OHex)$_2$. Catalytic conditions: 10 mL benzene, 35 psig propylene , Rh/SiO_2 (5.3 mg, 0.00112 mmol surface Rh atoms) or eq. amount of molecular catalysts [Rh(μ-OAc)(η^2-C_2H_4)$_2$]$_2$, 153 mg Cu(OHex)$_2$, (400 eq. relative to Rh), hexamethylbenzene (0.0224 mmol, 20 eq. relative to Rh) as the internal standard and 150 °C. The L/B selectivity is determined at when copper(II) is consumed.

Catalyst Precursor	L/B selectivity

Rh/SiO_2	8.0(2)
$[Rh(\mu\text{-}OAc)(\eta^2\text{-}C_2H_4)_2]_2$	7.4(1)

Since CuX and HX (X = carboxylate) can be air-recycled to form CuX_2 and H_2O, the Rh-catalyzed arene alkenylation has the potential to use catalytic amounts of Cu(II).[39] We have examined the reactivity of the Rh/SiO_2 catalyst precursor for aerobic styrene synthesis (1 atm air) and compared its aerobic catalytic performance in the presence and absence of $Cu(OPiv)_2$ (Figure 3.10). Heating Rh/SiO_2 in a mixture of benzene, 40 psig ethylene, 1 atm air, 100 eq. $Cu(OPiv)_2$ and 1000 eq. HOPiv at 150 °C, the supported catalyst precursor Rh/SiO_2 exhibited catalytic activity for styrene production. Compared with catalysis using *stoichiometric* Cu(II) oxidants, a 185(10) TO of styrene production was achieved at 100 h when 1 atm air was added (Figure 3.10, black plot). In the absence of Cu(II) salt using air as the sole oxidant, only 35(5) TOs of styrene were be achieved after 104 h (Figure 3.10, red plot).

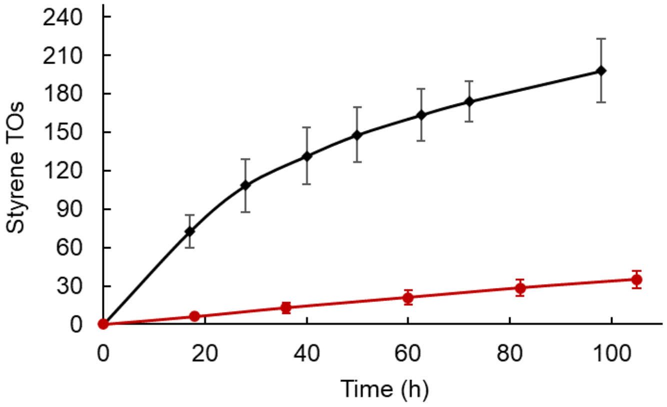

Figure 3.10. Rh/SiO_2 mediated aerobic catalysis for styrene production in the presence of $Cu(OPiv)_2$ (black) and in the absence of $Cu(OPiv)_2$ (red). (Aerobic conditions: 10 mL benzene, 40 psig ethylene, Rh/SiO_2 (5.3mg, 0.00112 mmol surface Rh atoms), 72 mg $Cu(OPiv)_2$ ((240 eq. relative to Rh, black) or no $Cu(OPiv)_2$ (red), hexamethylbenzene (20 eq.) as the internal standard, 1 atm air, 1000 eq. HOPiv (relative to Rh) and 150 °C).

3.2.3 Impact of Carboxylate and Induction Period. Using Rh/SiO_2 as catalyst precursor, catalysis with Cu(OHex)$_2$ is approximately 3 times more rapid than using Cu(OPiv)$_2$. For example, using Cu(OHex)$_2$ as an oxidant, we found that Rh/SiO_2 mediated styrene synthesis gave an overall yield approximately 70(4)% {based on stoichiometric and limiting Cu(II)} after 8 h (Figure 3.11). Under similar conditions using Cu(OPiv)$_2$, Rh/SiO_2 catalysts gave a 65(3)% yield after 26 h (Figure 3.7). For the molecular precursor [Rh(μ-OAc)(η^2-C_2H_4)$_2$]$_2$, the apparent TOF using Cu(OHex)$_2$ and Cu(OPiv)$_2$ oxidants are more similar, at $3.0(2) \times 10^{-2}$ s^{-1} and $1.5(2) \times 10^{-2}$ s^{-1}, respectively, than when using Rh/SiO_2. Moreover, during the Rh/SiO_2 and Cu(OHex)$_2$ mediated styrene production, a filtration test was conducted after 3 h of reaction. ICP-OES analysis of the filtrate from the reaction mixture confirmed that approximately 34% of Rh (compared with overall Rh amount on the silica support) leached from the silica support into solution. These results indicate that substantially more Rh leaches from Rh/SiO_2 when Cu(OHex)$_2$ is used as the oxidant (34%) compared to the use of Cu(OPiv)$_2$ (~1% leaching of Rh). The enhanced leaching of Rh with Cu(OHex)$_2$ likely explains the increased rate of styrene production using Cu(OHex)$_2$ and Rh/SiO_2 versus Cu(OPiv)$_2$ when using Rh/SiO_2 as the catalyst precursor. Thus, the extent of Rh leaching appears to be dependent on the identity of the carboxylate ligand, which could be due to the difference in basicity or a steric effect. Regardless, these results demonstrate that the oxidant {i.e., Cu(II)} and pro-ligand (carboxylate) are important for the Rh leaching process.

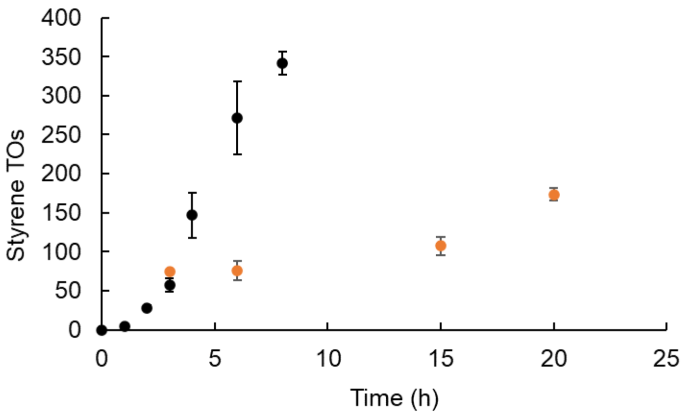

Figure 3.11. Catalytic performance (turnovers versus time plots) of styrene synthesis using fresh Rh/SiO_2 without isolation (black) and using recovered Rh/SiO_2 solid (centrifuge/separation methods used; orange). Reaction conditions: 10 mL benzene, 40 psig ethylene, Rh/SiO_2 (5.3 mg, 0.00112 mmol surface Rh atoms), 400 eq. $Cu(OHex)_2$ (relative to surface Rh atoms), 20 eq. hexamethylbenzene (3.7 mg) as the internal standard (relative to surface Rh atoms) at 150 °C. Catalyst isolation and separation were conducted at 3 h and fresh benzene, $Cu(OHex)_2$, and ethylene were recharged.

When commercial $Cu(OAc)_2$ is used as the oxidant for styrene synthesis using the molecular precursor $[Rh(\mu\text{-}OAc)(\eta^2\text{-}C_2H_4)_2]_2$, a variable induction period of 4h with an apparent TOF of 2.8(2) x 10^{-3} s^{-1} was observed (Figure 3.12). We sought to use XPS and TEM analysis to characterize the transformation of $[Rh(\mu\text{-}OAc)(\eta^2\text{-}C_2H_4)_2]_2$ during the induction period. To evaluate the binding energy of Rh(0), we obtained the photoemission spectrum of Rh metal foil and silica-supported Rh nanoparticles. As shown in Figure 3.2, the $3d_{3/2}$ binding energy Rh(0) was measured to be 307.3 eV. We then examined the black precipitate formed during the thermal decomposition of $[Rh(\mu\text{-}OAc)(\eta^2\text{-}C_2H_4)_2]_2$ in benzene in the absence of $Cu(OAc)_2$. As expected, the Rh $3d_{3/2}$ binding energy of the Rh species in the precipitate is 307.3 eV (Figure 3.13), which is the same as observed for the Rh foil. Thus, we conclude that $[Rh(\mu\text{-}OAc)(\eta^2\text{-}C_2H_4)_2]_2$ decomposes to Rh(0) species upon heating in benzene in the absence of Cu(II) or another oxidant, which is consistent with results from TEM studies that confirm the presence of Rh(0) nanoparticles.

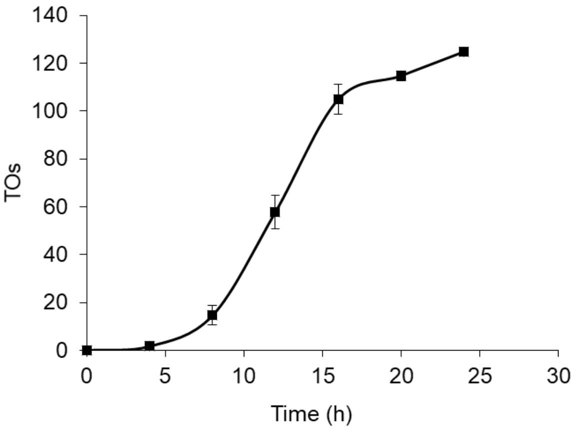

Figure 3.12. Plot of TOs versus time for styrene production catalyzed by [Rh(μ-OAc)(η^2-C_2H_4)$_2$]$_2$ with an induction period of approximately 4 h observed. Reaction conditions: 0.001 mol % of Rh (relative to benzene), 240 equiv. of $Cu(OAc)_2$ (relative to Rh),10 mL C_6H_6, 40 psig C_2H_4, 150 °C. Each data point is the average of three separate experiments. Error bars represent the standard deviations based on a minimum of three independent experiments.

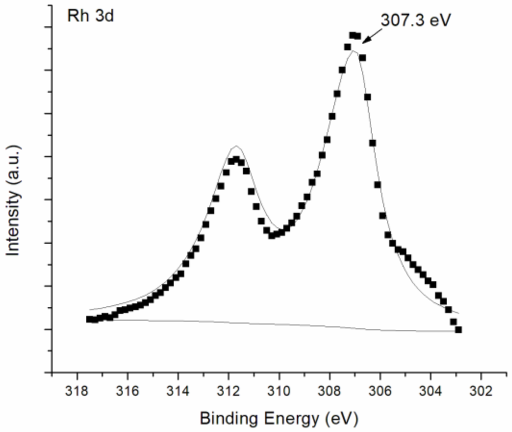

Figure 3.13. XPS spectrum (region Rh 3d) of insoluble Rh species formed during the thermal decomposition of [Rh(μ-OAc)(η^2-C_2H_4)$_2$]$_2$ (0.001 mol % Rh relative to benzene) at 150 °C under 40 psig of ethylene in benzene in the absence of $Cu(OAc)_2$. All manipulations were performed under inert atmosphere. The sample was sealed in a vacuum transfer vessel in the glovebox prior to XPS analysis.

Subsequently, we examined the recovered Rh species after 1 h (during the induction period) and 12 h (after the induction period) in the catalysis with ethylene and [Rh(μ-OAc)(η^2-C_2H_4)$_2$]$_2$ using 240 equiv. of untreated $Cu(OAc)_2$ (Figure 3.14a and 3.14b). For comparison, the XPS data of Rh species recovered after 1 h of the catalytic reaction using activated $Cu(OAc)_2$ (activated means preheating the copper salt in benzene 150 °C for 8h) are presented in Figure 3.14c. In all three cases, the corresponding reaction mixture was treated under vacuum to remove the benzene and recover the solid. All three samples of the recovered Rh species showed a Rh $3d_{3/2}$ binding energy in the range of 308.9-309.2 eV, which is higher than that of Rh(0). These results suggest that the insoluble Rh species formed under catalytic conditions is in a higher oxidation state than Rh(0).

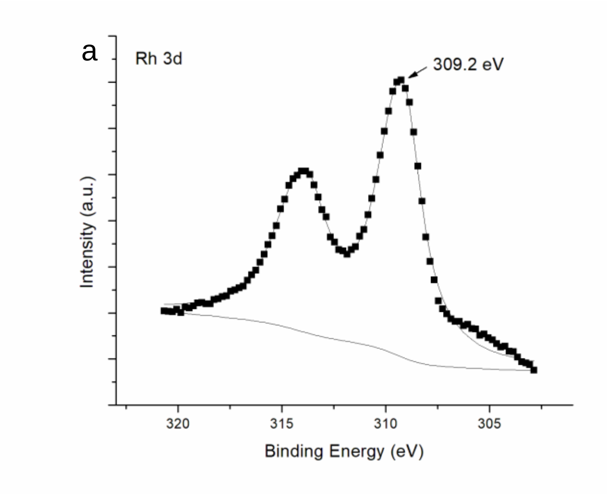

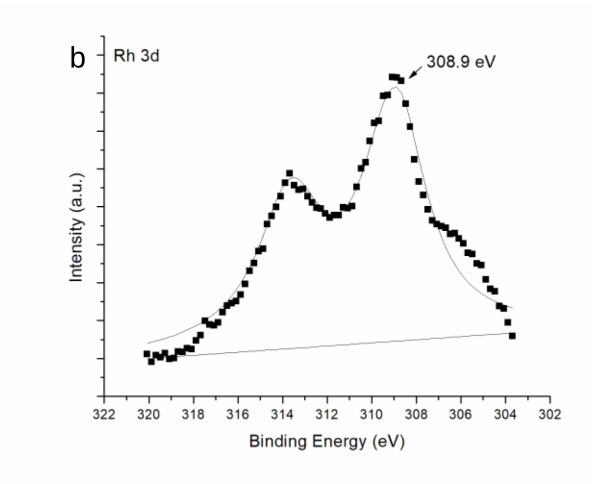

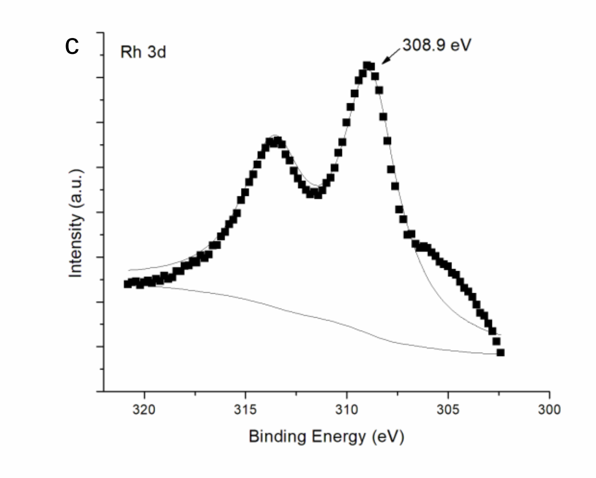

Figure 3.14. XPS spectra (region Rh 3d) of recovered Rh species formed (a and b) after 1 h and 12 h of catalysis, respectively, with 40 psig ethylene and $[Rh(\mu\text{-}OAc)(\eta^2\text{-}C_2H_4)_2]_2$ (0.001 mol % Rh relative to benzene) using **untreated** $Cu(OAc)_2$ (240 equiv. relative to Rh); (c) after 1 h in the catalysis with 40 psig ethylene and $[Rh(\mu\text{-}OAc)(\eta^2\text{-}C_2H_4)_2]_2$ (0.001 mol % Rh relative to benzene) using **activated** $Cu(OAc)_2$ (240 equiv. relative to Rh). The samples were prepared by removing solvent *in vacuo* in the glovebox. The samples were sealed in a vacuum transfer vessel in the glovebox prior to XPS analysis.

In a control experiment, $[Rh(\mu\text{-}OAc)(\eta^2\text{-}C_2H_4)_2]_2$ was heated together with 50 mg of mesoporous silica in benzene at 150 °C for 1 h in an attempt to capture the reduced Rh species on the silica support. The non-volatile materials after this thermolysis reaction were analyzed by XPS and TEM-EDS. A $3d_{3/2}$ peak at 307.0 eV was observed by XPS (Figure 3.15), similar to metallic Rh. Indeed, TEM/EDS and lattice constant analysis confirmed that Rh(0) nanoparticles were captured by silica (Figure 3.16). Characterization results from our control experiment using synthesized Rh/SiO_2 catalyst verified that our sample recovery method and air-free handling techniques were sufficient to observe Rh(0) nanoparticles if they were formed during the catalytic reaction.

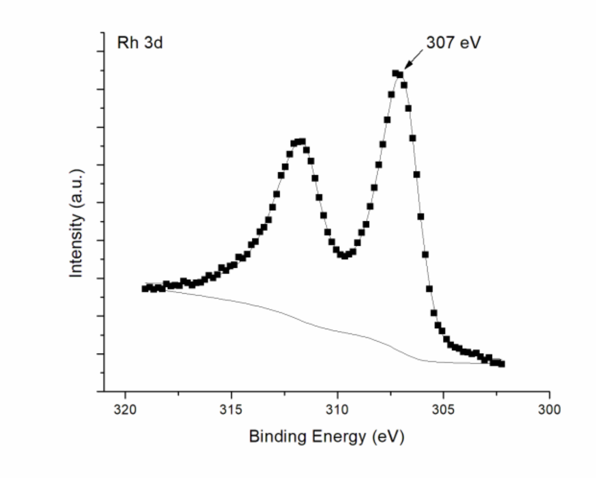

Figure 3.15. XPS spectrum (region Rh 3d) of recovered Rh species from the thermal decomposition of $[Rh(\mu\text{-}OAc)(\eta^2\text{-}C_2H_4)_2]_2$ (0.001 mol % Rh relative to benzene) in benzene after 1 h in the presence of silica. The sample was prepared by solvent removal *in vacuo* in the glovebox. The sample was sealed in a vacuum transfer vessel in the glovebox prior to XPS analysis.

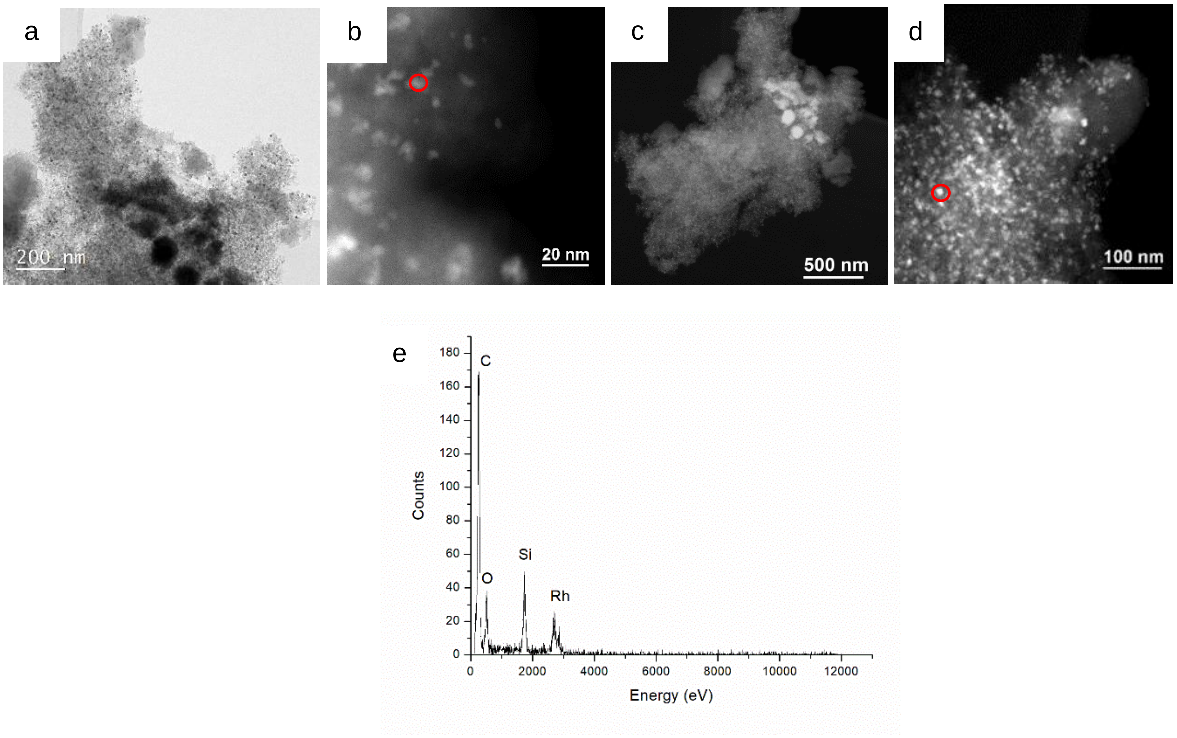

Figure 3.16. TEM/STEM images and EDS analysis of recovered Rh species from the thermal decomposition of $[Rh(\mu\text{-}OAc)(\eta^2\text{-}C_2H_4)_2]_2$ (0.001 mol % Rh relative to benzene) in benzene after 1 h in the presence of silica. (a) bright field TEM images of SiO_2 captured Rh species; (b-d) dark-field STEM images of silica captured Rh species; (e) EDS analysis of selected particle 1 (red circle) in d.

We also characterized the recovered Rh species formed after 1 h of catalysis using untreated $Cu(OAc)_2$ by scanning transmission electron microscopy (STEM). The STEM-

EDS analysis of non-volatile materials collected after the reaction indicated the presence of rhodium species present in the small bright spots in Figure 3.17. Although Rh nanoparticles formed during the thermal decomposition of $[Rh(\mu\text{-}OAc)(\eta^2\text{-}C_2H_4)_2]_2$ in benzene in the absence of $Cu(OAc)_2$ (see above), the nature of the Rh species in Figure 3.17 is ambiguous. Figure 3.18 shows compositional mapping in the vicinity of the features associated with Rh, confirming that Rh is present in a separate phase from the Cu component.

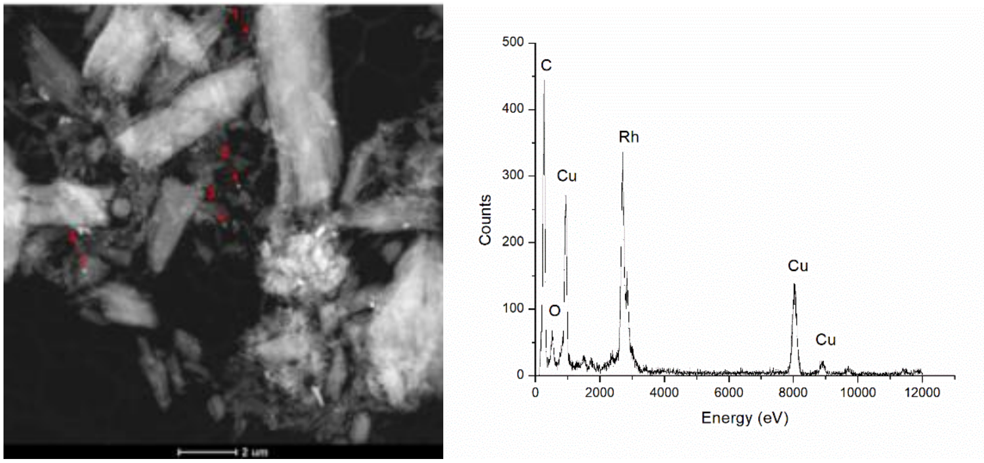

Figure 3.17. A STEM image of recovered Rh species formed after 1 h of catalysis with 40 psig ethylene and $[Rh(\mu\text{-}OAc)(\eta^2\text{-}C_2H_4)_2]_2$ (0.001 mol % Rh relative to benzene) using untreated $Cu(OAc)_2$ (240 equiv. relative to Rh)(left) and EDS analysis of selected single particle 1 on the left STEM image (right)

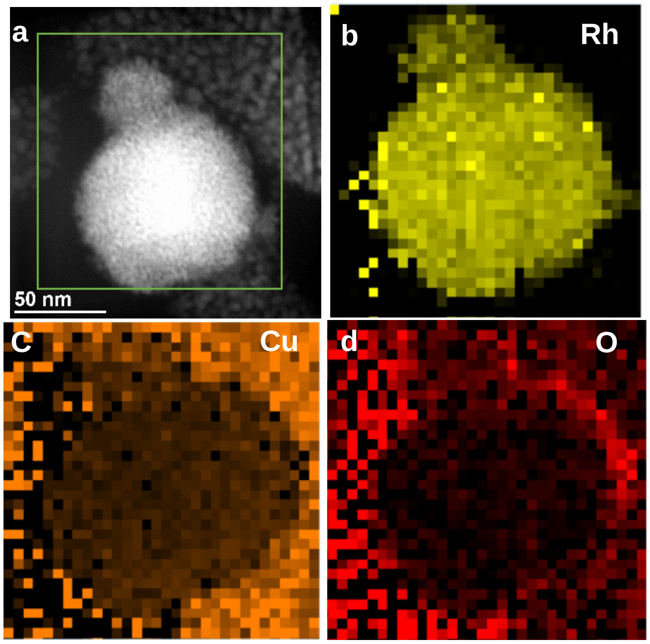

Figure 3.18. STEM-EDS maps of recovered Rh species formed after 1 h in the catalysis with 40 psig ethylene and [Rh(μ-OAc)(η^2-C_2H_4)$_2$]$_2$ (0.001 mol % Rh relative to benzene) using untreated Cu(OAc)$_2$ (240 equiv. relative to Rh). (a) overall dark-field STEM image; (b) EDS map of Rh; (c) EDS maps of Cu; (d) EDS maps of O. Rh, Cu and O are shown yellow, orange and red, respectively.

We also sought to characterize the black precipitate formed during the thermolysis of [Rh(μ-OAc)(η^2-C_2H_4)$_2$]$_2$ in the absence of Cu(OAc)$_2$ by TEM. A 10 mL benzene solution of [Rh(μ-OAc)(η^2-C_2H_4)$_2$]$_2$ under 40 psig of ethylene was heated to 150 °C for 1 hour. The resulting mixture was decanted after centrifuging to isolate the insoluble black solid. Lattice parameter analysis, TEM-EDS measurement and selected area diffraction were used to characterize the black solid (Figure 3.19). These data confirm Rh nanoparticles are formed during the thermal decomposition. Rh(111) and Rh(200) planes are observed in the lattice constant analysis. The lattice parameters for Rh(111), Rh(200) and Rh(220) are found to be 0.22 nm, 0.19 nm and 0.13 nm, respectively. Also, broad beam TEM-EDS measurement is consistent with the formation of Rh nanoparticles. In selected area diffraction measurement of the particles, three common planes of Rh nanoparticles, Rh(111), Rh(200) and Rh(220) were found. According to the results of kinetic studies and TEM analysis, one possible route for the decomposition of [Rh(μ-OAc)(η^2-C_2H_4)$_2$]$_2$ involves initial dissociation of ethylene. The resulting Rh(I) species can be reduced by ethylene to form acetic acid and Rh(0) particles. The similar rates of decomposition in different arene solvents suggests that the solvent is not likely the reducing agent. Therefore, when commercial Cu(OAc)$_2$ is used as the oxidant, we propose that the induction period is likely due to the rapid decomposition of the soluble Rh catalyst precursor to form insoluble Rh(s) followed by formation of the active catalyst through dissolution of Rh from the inactive Rh(0) species (Scheme 3.6).

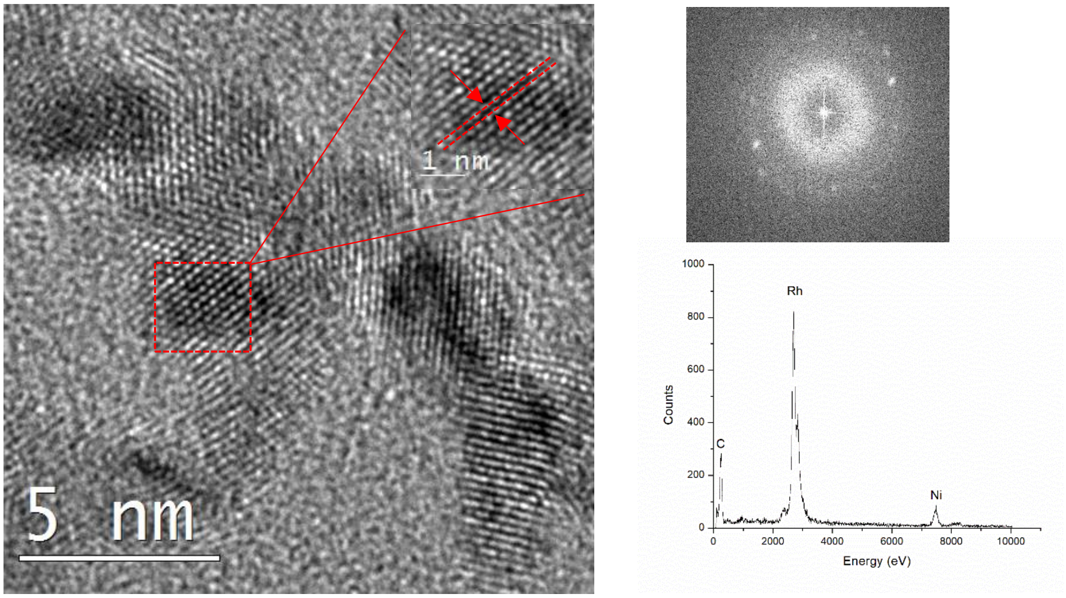

Figure 3.19. TEM lattice analysis (left), TEM-EDS measurement (top right) and selected area diffraction analysis (bottom right) of Rh species from thermal decomposition of $[Rh(\mu\text{-}OAc)(\eta^2\text{-}C_2H_4)_2]_2$ at 150 °C under 40 psig of ethylene in benzene in the absence of $Cu(OAc)_2$.

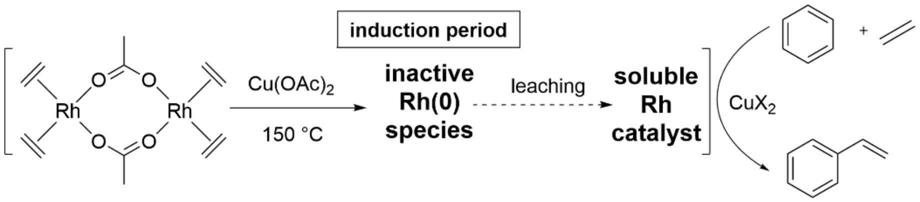

Scheme 3.6. The proposed induction period pathway for Rh(I) medicated styrene synthesis using $Cu(OAc)_2$ as the oxidant (X = carboxylate groups).[37]

3.2.4 Recycling of Rh/SiO₂. We tested the catalytic activity of recycled Rh/SiO_2 (recovered catalysts from styrene synthesis reaction after 3 h of reaction; Figure 3.11). Using Rh/SiO_2 isolated from an initial catalytic reaction, we probed the conversion of benzene, ethylene and $Cu(OHex)_2$ to styrene at 150 °C. Figure 3.12 shows comparative reaction profiles using freshly made Rh/SiO_2 and the recovered Rh/SiO_2 material. A reaction using the recovered Rh/SiO_2 shows a longer induction period and a slower overall rate of styrene production. In contrast, using the filtrate after 3h of reaction (Figure 3.20) shows comparable catalysis to the catalytic reaction using fresh Rh/SiO_2. Again, the results are consistent with the active catalyst being formed by leaching of Rh into solution.

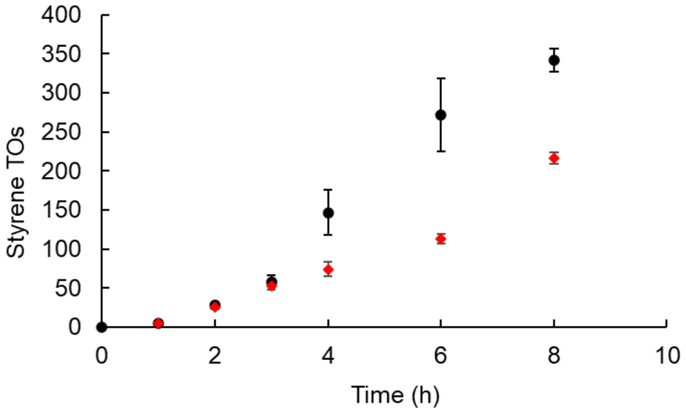

Figure 3.20. Catalytic performance (turnovers versus time plots) for styrene synthesis using fresh Rh/SiO_2 without isolation (black) and using the recovered filtrate after centrifuge/separation test (red). Reaction conditions: 10 mL benzene, 40 psig ethylene, 3.6 wt% Rh/SiO_2 (5.3 mg, 0.00112 mmol surface Rh atoms), 400 eq. $Cu(OHex)_2$ (relative to surface Rh atoms), 20 eq. hexamethylbenzene as the internal standard and 150 °C. Catalyst separation and isolation were conducted at 3 h. Then, to the filtrate, 400 eq. of Cu(II) oxidant, and ethylene were recharged. The catalysis using the filtrate solution is shown in red with the starting time at 3 h.

Compared with an induction period of ~1 h when new Rh/SiO_2 is used for the styrene synthesis, the recovered Rh/SiO_2 material showed a longer introduction period of ~12 h (Figure 3.11, note: the start time point for the recycled catalytic reaction is at 3h in Figure 3.11). Although approximately 66% of the overall Rh species in the Rh/SiO_2 catalyst did not leach into the solution during the catalysis at 3 h (based on ICP-OES analysis, see above), the reactivity of recovered Rh/SiO_2 catalysts is substantially reduced. One explanation for the long induction period observed with the recovered Rh/SiO_2 material is oxidation of Rh during the isolation of Rh/SiO_2 (transfer step in and out of the glove box) following the initial catalytic reaction, which could inhibit leaching and/or catalysis. Thus, we probed dihydrogen reduction of the recovered Rh/SiO_2 material at 150 °C prior to attempted catalysis.[65, 66] The dihydrogen-treated, recovered Rh/SiO_2 exhibited similar reactivity compared with the recovered and untreated Rh/SiO_2 (Figure 3.21), which suggests that dioxygen does not deactivate the recovered Rh/SiO_2 catalysts.

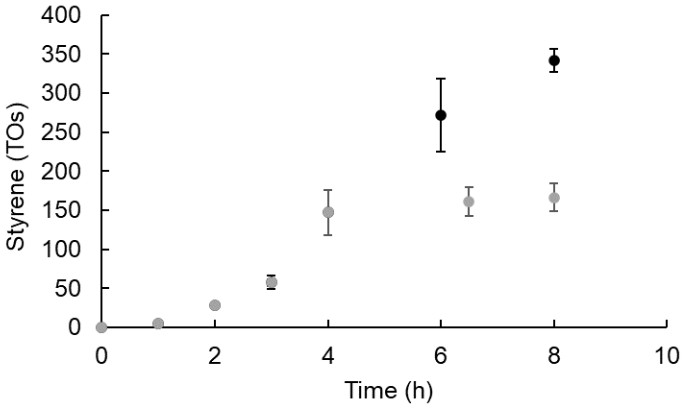

Figure 3.21. Catalytic performance (turnover versus time plot) of styrene synthesis using fresh Rh/SiO_2 without isolation (black), and using recovered Rh/SiO_2 at 4h (dihydrogen pretreatment at 150 °C was conducted before the catalytic recycle) (grey). Reaction conditions: 10 mL benzene, 40 psig ethylene, 3.6 wt% Rh/SiO_2 (5.3 mg, 0.00112 mmol surface Rh atoms), 400 eq. $Cu(OHex)_2$, 20 eq. hexamethylbenzene as the internal standard and 150 °C. Catalyst isolation and separation were conducted at 4 h and fresh benzene, copper oxidants, and ethylene were recharged.

We hypothesize that the Cu(II) salts might influence the catalysis in two roles beyond serving as the oxidant for the arene alkenylation: 1) Cu(II) likely oxidizes Rh(0) to form soluble catalyst, and 2) reduced Cu might be deposited on the Rh/SiO_2 material as the reaction proceeds, which could inhibit continued leaching of Rh into solution. TEM and XPS characterization of recovered Rh/SiO_2 material after 3 h of reaction were used to analyze for possible copper deposition. Indeed, energy-filtered TEM mapping of copper on recovered Rh/SiO_2 (red and blue box regions in Figure 3.22) showed Cu deposition (bright spots within the blue box) on the recovered solid (Figure 3.22). Moreover, XPS analysis of recovered Rh/SiO_2 confirmed Cu deposition with a binding energy of approximately 933 eV, which was attributed to Cu(I)/Cu(0) species (Figure 3.23).[67-69]

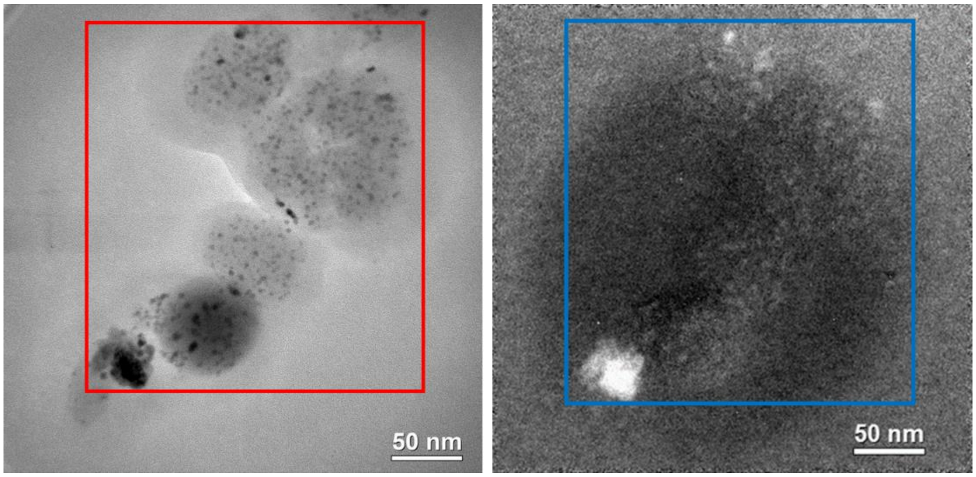

Figure 3.22. TEM images of Rh/SiO$_2$ (left) recovered after 3 h of catalysis (Rh/SiO$_2$, Cu(OHex)$_2$, ethylene, benzene, 150 °C) and energy-filtered TEM map of copper at the recovered Rh/SiO$_2$ (right). Red box and blue box are the regions that energy-filtered TEM map of copper was examined with the bright spots on the right indicating copper.

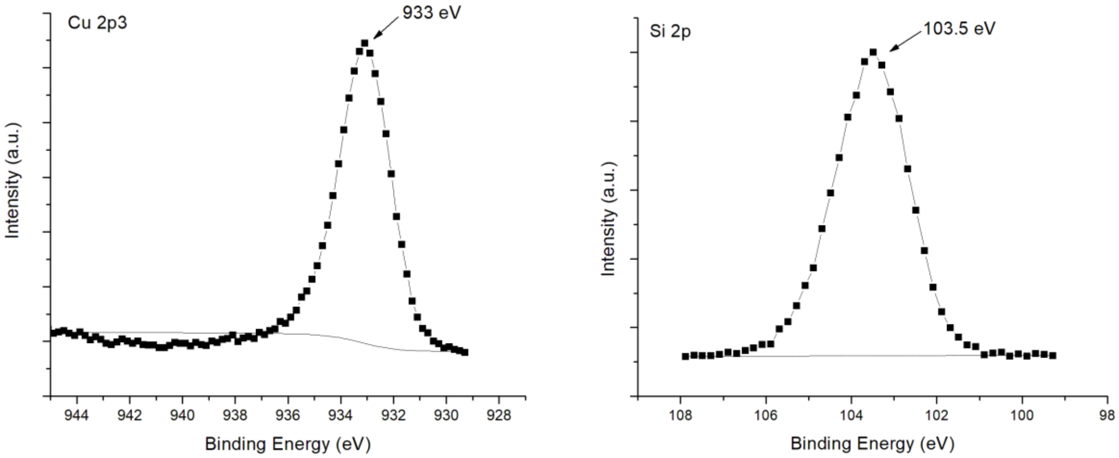

Figure 3.23. XPS spectra of Cu 2p3 (left) and Si 2p (right) from the recovered Rh/SiO$_2$ catalysts at 3h during styrene synthesis. Catalytic conditions: Rh/SiO$_2$ (5.3 mg, 0.00112 mmol surface Rh atoms), 400 eq. Cu(OHex)$_2$, 20 eq. hexamethylbenzene as the internal standard, 40 psig ethylene, and 150 °C.

When Rh/SiO$_2$ is pretreated in a benzene solution with 400 eq. Cu(OHex)$_2$ at 150 °C for 3 h, and 40 psig ethylene is charged afterwards, the catalytic performance of the Cu(II) pretreated Rh/SiO$_2$ (Cu(II)-pretreated Rh/SiO$_2$) showed about one-third of the activity compared to catalysis using fresh Rh/SiO$_2$ (Figure 3.24, blue). Separately, we treated Rh/SiO$_2$ with 2 bar dihydrogen and 200 eq. of Cu(OHex)$_2$ salt (relative to the amount of surface Rh) at 150 °C for 3 h assuming that reduced Cu(s) would be formed. Using this

H_2/Cu-Rh/SiO_2 material for styrene synthesis, the rate of styrene formation is dramatically reduced compared with using fresh Rh/SiO_2 (Figure 3.24, yellow). These results are consistent with the hypothesis that Cu deposition might inhibit Rh leaching from the Rh/SiO_2 material. Moreover, when a pretreatment of Rh/SiO_2 with 40 psig ethylene and benzene was carried out at 150 °C for 3 h before the addition of 400 eq. Cu(OHex)$_2$ salts (relative to the number of surface Rh atoms), catalytic reactivity was reduced substantially (Figure 3.24, orange). This result indicated that ethylene and/or benzene might also deactivate the Rh/SiO_2 catalyst.

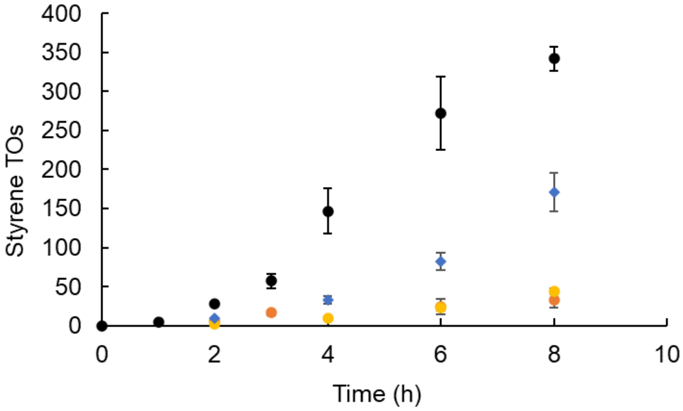

Figure 3.24. Catalytic performance (turnovers versus time plot) of styrene synthesis using fresh Rh/SiO_2 (black), and Cu(II)-pretreated Rh/SiO_2 (blue), H_2/Cu-Rh/SiO_2 (yellow) and ethylene-benzene treated Rh/SiO_2 (orange). Reaction conditions: 10 mL benzene, 40 psig ethylene, 3.6 wt% Rh/SiO_2 (5.3 mg, 0.00112 mmol surface Rh atoms), 400 eq. Cu(OHex)$_2$ (relative to surface Rh atoms), 20 eq. hexamethylbenzene as the internal standard (relative to surface Rh atoms) and 150 °C. Catalyst isolation and separation are conducted at 3 h and fresh benzene, copper oxidants, and ethylene are recharged.

3.2.5 Catalytic Arene Alkenylation using Rh/NC catalysts. In our effort to compare the impact of the solid support on arene alkenylation using Rh nanomaterials as catalyst precursors, we prepared Rh materials supported on nitrogen-doped carbon (NC). The NC support has been demonstrated to stabilize supported transition metal catalysts.[56, 59, 70-72] The synthesis and characterization of Rh-NC material have been discussed above.

Using 1 wt% Rh/NC-HCl as the catalyst precursor with $Cu(OHex)_2$ as the oxidant for the conversion of benzene and ethylene (40 psig) to styrene at 150 °C, a short induction period of ~4 h was observed (Figure 3.25). After 28 h, a 35(3)% yield (relative to Cu(II) oxidant) was achieved. In the absence of the Rh, the NC support showed no catalytic reactivity for styrene production even after 38 h (Figure 3.26).

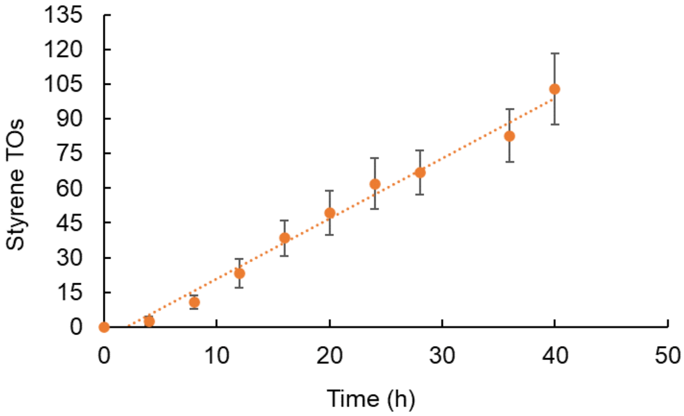

Figure 3.25. Turnovers versus time plot using 1 wt% Rh/NC-HCl mediated styrene synthesis. Conditions: 10 mL benzene, 40 psig ethylene, 1 wt% Rh/NC-HCl (13 mg, 0.00112 mmol surface Rh atoms), 400 eq. $Cu(OHex)_2$ 2 (relative to Rh measured through ICP-OES), and 20 eq. hexamethylbenzene (0.0224 mmol) as the internal standard at 150 °C.

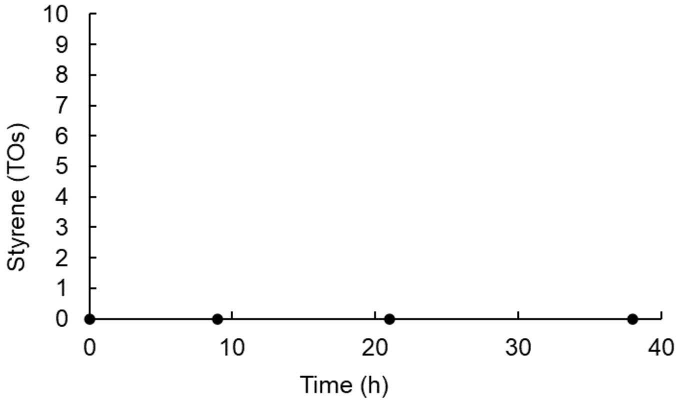

Figure 3.26. Styrene turnover numbers versus time plot when NC-HCl support, without Rh, was used to mediate styrene synthesis. Conditions: 10 mL benzene, 40 psig ethylene, NC-HCl support (13 mg), 153 mg $Cu(OHex)_2$, hexamethylbenzene (0.0224 mmol) as the internal standard and 150 °C.

As described above for catalysis using Rh/SiO_2, we performed centrifuge and decanting experiments, which involved the isolation of solid Rh/NC-HCl material after 28 h and 72 h of reaction. We then probed catalysis with the recovered Rh/NC-HCl material for styrene production (Figure 3.27). After specific time points, these experiments involved centrifuging reaction solutions and decanting to separate insoluble materials from soluble filtrate species. Then, the recovered solid material was recharged with Cu(II), benzene and ethylene, heated to 150 °C and styrene production quantified. In a representative experiment, we recovered and recycled insoluble Rh/NC-HCl twice (Figure 3.27). Catalytic cycles 2 and 3 show comparable styrene production rates to the initial run. Compared with the ~4 h induction period when fresh Rh/NC-HCl is used, a slightly longer induction period (~8 h) was observed for both cycles 2 and 3 (Figure 3.27). In contrast to observations with Rh/SiO$_2$ (see above), the soluble materials in the filtrate from cycle 1 were not active for the styrene production (Figure 3.28). Compared with overall Rh loading at beginning of the catalysis, ICP-OES measurement of the recovered Rh/NC-HCl catalysts at 116 h (cycle 3) and the soluble filtrate Rh species/solution (116 h) showed approximately 47% of the starting Rh loading and 0.4% of Rh in the solution (*i.e.*, the filtrate), respectively.

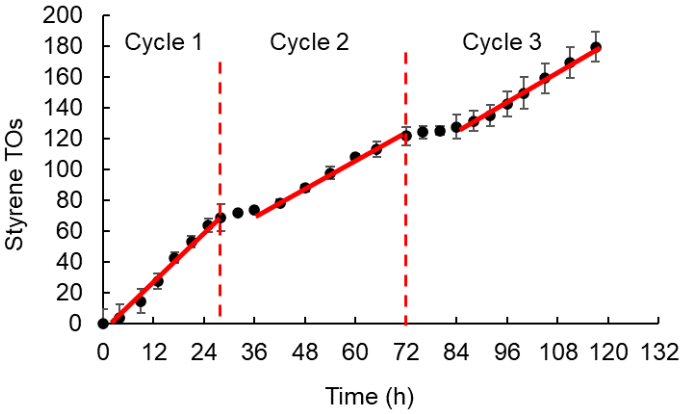

Figure 3.27. Catalytic turnovers versus time plots using Rh/NC-HCl as catalyst precursor for styrene synthesis: cycle 1 (0 - 28 h), cycle 2 (32 h - 68 h), and cycle 3 (84 h to 116 h). Reaction conditions: 10 mL benzene, 40 psig ethylene, 1 wt% Rh/NC-HCl (39 mg, 0.00336 mmol Rh), 400 Deq. Cu(OHex)$_2$ (relative to Rh measured through ICP-OES), and 20 eq. hexamethylbenzene as an internal standard at 150 °C.

Insoluble solid material was separated and recycled between each cycle with fresh benzene, Cu(II) oxidant, ethylene, and internal standard recharged.

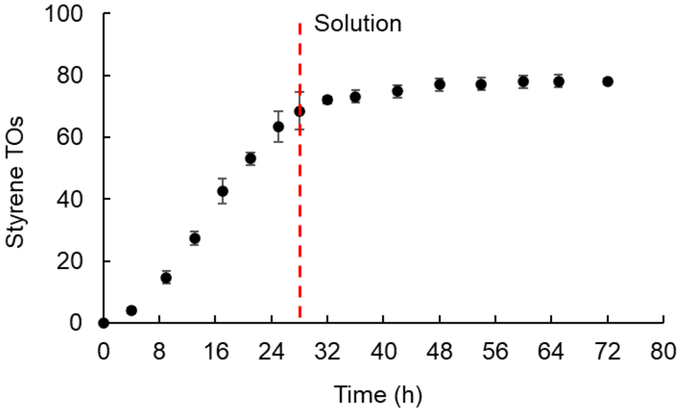

Figure 3.28. Reactivity performance of filtrate solution after 28 h using Rh/NC-HCl precursor mediated styrene synthesis. Reaction conditions: 10 mL benzene, 40 psig ethylene, 1 wt% Rh/NC-HCl (39 mg, 0.00336 mmol Rh), 400 eq. $Cu(OHex)_2$, 20 eq. hexamethylbenzene as the internal standard and 150 °C. Catalyst isolation and separation was conducted at 28 h and fresh benzene, copper oxidants, and ethylene were recharged.

Similar to 1 wt% Rh/NC-HCl catalysts, 1.5 wt% Rh/NC-IWI was synthesized and characterized as described above. Large Rh nanoparticles (~20 nm) were observed on the Rh/NC-IWI material. We tested Rh/NC-IWI as catalyst precursor at conditions similar to those used to test Rh/NC-HCl (see above). The Rh/NC-IWI precursor showed no discernable induction period (Figure 3.29). Compared with Rh/NC-HCl, catalysis normalized by Rh atom (measured by ICP-OES) sing Rh/NC-IWI was much faster, which gives a 87(3)% yield (relative to Cu(II) oxidant) of styrene at 2 h (Figure 3.29) versus a 53(7)% yield(relative to Cu(II) oxidant) of styrene at 40 h (Figure 3.25).

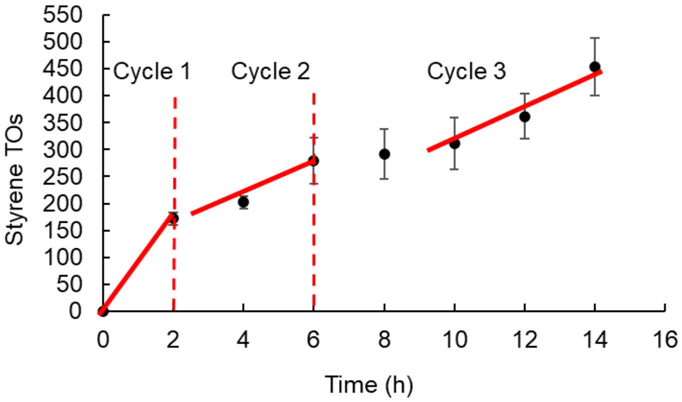

Figure 3.29. Catalytic turnovers versus time plots using Rh/NC-IWI precursor mediated styrene synthesis: cycle 1 (0 – 2 h), cycle 2 (2 h – 6 h), and cycle 3 (6 h to 14 h). Reaction conditions: 10 mL benzene, 40 psig ethylene, 1 wt% Rh/NC-IWI (13 mg, 0.00112 mmol surface Rh atoms), 400 eq. $Cu(OHex)_2$ (relative to Rh measured through ICP-OES), 20 eq. hexamethylbenzene as the internal standard (relative to Rh loading) at 150 °C. Insoluble solid material was separated and recycled between each cycle with fresh benzene, Cu(II) oxidant, ethylene, and internal standard recharged.

In contrast to Rh/SiO_2 material, the insoluble solid materials using Rh/NC precursors could be recycled without substantial loss in activity or increased induction periods. The differences between Rh/SiO_2 and Rh/NC materials could possibly be explained by 1) the Rh/NC materials are active heterogeneous catalysts or, 2) for Rh/NC-HCl and Rh/NC-IWI mediated styrene production, leaching of soluble Rh into the solution under catalytic conditions is reversible and re-adsorption occurs prior to filtration. To further compare Rh/NC materials with soluble and molecular Rh catalysis, we compared regioselectivities for arene alkenylation using the α-olefins propylene and 1-pentene to quantify Markovnikov vs. anti-Markovnikov selectivity (Schemes 3.5 and 3.7). We assumed that if the Rh/NC material is a heterogeneous catalyst that different Markovnikov vs. anti-Markovnikov selectivity would be observed. Herein, we refer to anti-Markovnikov products as linear and Markovnikov products as branched (Schemes 3.5 and 3.7). The use of toluene provides an opportunity to determine *ortho/meta/para* selectivity (Schemes 3.7 and 3.8).

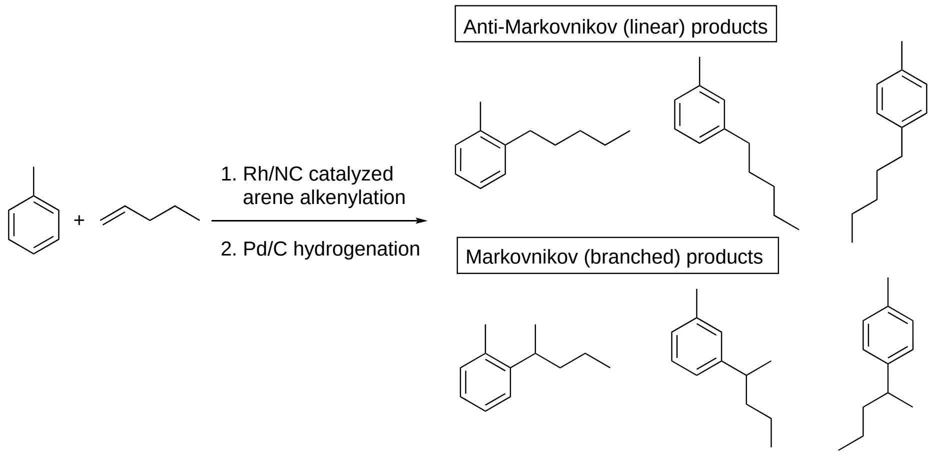

Scheme 3.7. Rh/NC mediated linear/branched product selectivity for coupling reactions between toluene and 1-pentene with possible ortho, meta, and para selectivity. The alkyl arenes are formed after hydrogenation of the initial alkenyl arene products.

Under identical catalytic conditions, the L/B selectivities induced from Rh/SiO$_2$, Rh/NC-HCl and [Rh(μ-OAc)(η^2-C$_2$H$_4$)$_2$]$_2$ for both benzene and propylene coupling and toluene and 1-pentene were examined (Scheme 3.8). The L/B selectivities for benzene and propylene coupling are statistically identical for Rh/SiO$_2$, Rh/NC-HCl and the molecular Rh complex [Rh(μ-OAc)(η^2-C$_2$H$_4$)$_2$]$_2$ (Table 3.4). For the benzene and propylene, the L/B selectivity observed for Rh/NC-HCl is 7.5(2), while Rh/SiO$_2$ and molecular complex [Rh(μ-OAc)(η^2-C$_2$H$_4$)$_2$]$_2$ gives 8.0(2) and 7.4(1), respectively. Likewise, arene alkenylation using toluene and 1-pentene for Rh/NC-HCl, Rh/SiO$_2$ and [(C$_2$H$_4$)$_2$Rh(μ-OAc)]$_2$ catalysts gave statically identical L/B selectivities, 8.2(9):1, 10.4(2):1, and 9.9(6):1, respectively. Also, the meta/para ratio for Rh/NC-HCl, Rh/SiO$_2$ and [Rh(μ-OAc)(η^2-C$_2$H$_4$)$_2$]$_2$ catalysts is statistically identical at 1.7(1):1, 1.8(1):1, and 1.7(1):1, respectively (Table 3.5).

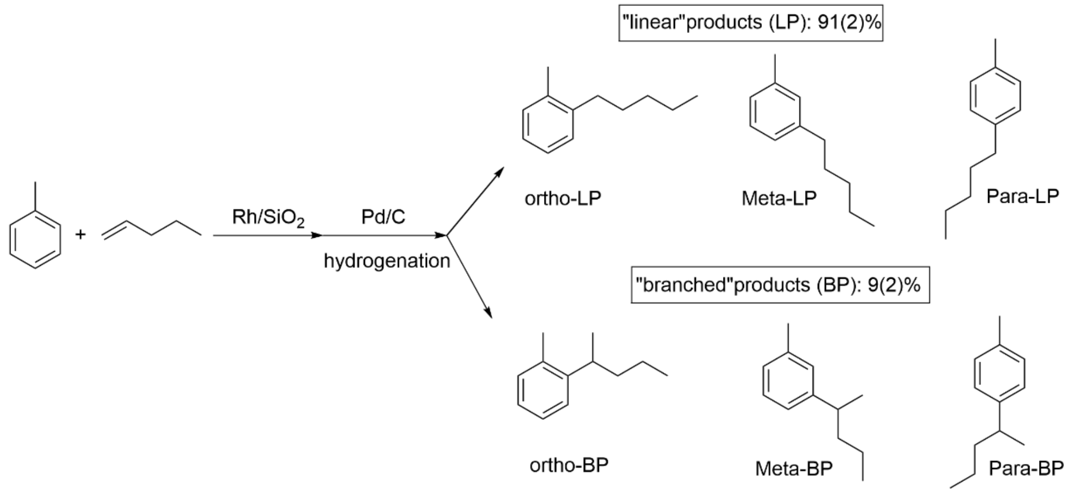
+
Rh/SiO$_2$
Pd/C
hydrogenation
"linear"products (LP): 91(2)%
ortho-LP
Meta-LP
Para-LP
"branched"products (BP): 9(2)%
ortho-BP
Meta-BP
Para-BP

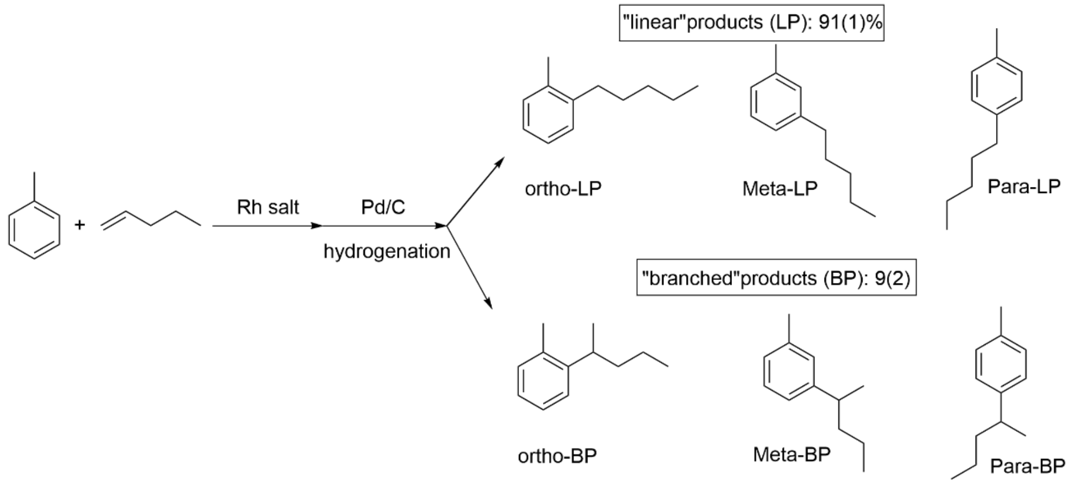
+
Rh salt
Pd/C
hydrogenation
"linear"products (LP): 91(1)%
ortho-LP
Meta-LP
Para-LP
"branched"products (BP): 9(2)
ortho-BP
Meta-BP
Para-BP

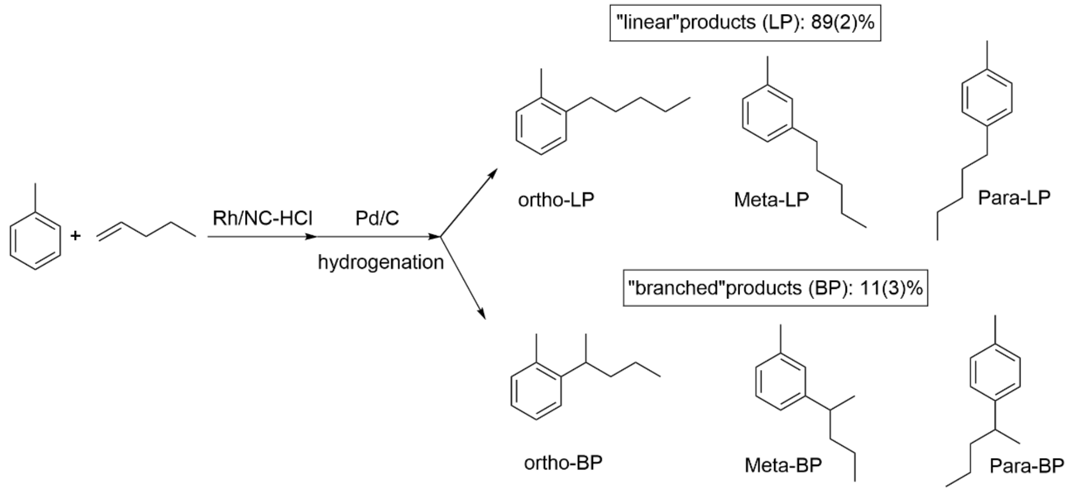
+
Rh/NC-HCl
Pd/C
hydrogenation
"linear"products (LP): 89(2)%
ortho-LP
Meta-LP
Para-LP
"branched"products (BP): 11(3)%
ortho-BP
Meta-BP
Para-BP

Scheme 3.8. L/B selectivity using Rh/SiO_2 precursor, Rh salt ([Rh(μ-OAc)(η^2-C_2H_4)$_2$]$_2$) and Rh/NC-HCl for toluene and 1-pentene coupling reaction at 150 °C. Catalytic conditions: Rh/SiO_2 (5.3 mg, 0.00112 mmol surface Rh atoms) or [Rh(μ-OAc)(η^2-C_2H_4)$_2$]$_2$ (0.00112 mmol surface Rh atoms) or Rh/NC-HCl (13 mg, 0.00112 mmol surface Rh atoms), 400 eq. Cu(OHex)$_2$, 20 eq. hexamethylbenzene as the internal standard, 1000 eq. 1-pentene, and 150 °C. For the pentyl-products quantification, synthesized products are hydrogenated with 10 wt% Pd/C (10 mg) catalyst at 100 psig H_2 at room temperature overnight. L/B selectivity is determined at end of the reaction when copper is fully consumed.

Table 3.4. L/B selectivity comparison of Rh/NC-HCl, Rh/SiO_2 and Rh(I) salt [Rh(μ-OAc)(η^2-C_2H_4)$_2$]$_2$ mediated propylene and 1-pentene arene alkenylation.

Catalysts	L/B selectivity for benzene and propylene	L/B selectivity for toluene and 1-pentene
Rh/NC-HCl	7.5(2)	8.2(9)
Rh/SiO_2	8.0(2)	10.4(2)
[Rh(μ-OAc)(η^2-C_2H_4)$_2$]$_2$	7.4(1)	9.9(6)

Catalytic conditions: 10 mL benzene or toluene, 25 psig propylene , or 1000 eq. 1-pentene, 1 wt% Rh/NC-HCl (13 mg, 0.00112 mmol surface Rh atoms) or equivalent Rh/SiO_2 (5.3 mg, 0.00112 mmol surface Rh atoms) or [Rh(μ-OAc)(η^2-C_2H_4)$_2$]$_2$ (0.00112 mmol), 400 eq. Cu(OHex)$_2$ (relative to Rh), 20 eq. hexamethylbenzene as the internal standard (relative to Rh) and 150 °C. For the pentyl-products quantification, synthesized products are hydrogenated with 10 wt% Pd/C (10 mg) catalyst at 100 psig H_2 at room temperature overnight.

Table 3.5. *Meta/para* ratio comparison of Rh/NC-HCl, Rh/SiO_2 and the molecular complex [Rh(μ-OAc)(η^2-C_2H_4)$_2$]$_2$ mediated toluene and 1-pentene arene alkenylation.

Catalysts	*meta/para* ratio for toluene and 1-pentene
Rh/NC-HCl	1.7(1)
Rh/SiO_2	1.8(2)
[Rh(μ-OAc)(η^2-C_2H_4)$_2$]$_2$	1.7(1)

Catalytic conditions: 10 mL toluene, 1000 eq. 1-pentene , 1 wt% Rh/NC-HCl (13 mg, 0.00112 mmol surface Rh atoms) or equivalent Rh/SiO_2 (5.3 mg, 0.00112 mmol surface Rh atoms) or [Rh(μ-OAc)(η^2-C_2H_4)$_2$]$_2$ (0.00112 mmol), 400 eq. Cu(OHex)$_2$ (relative to Rh), 20 eq. hexamethylbenzene as the internal standard (relative to Rh) and 150 °C. For the pentyl-products quantification, synthesized products are hydrogenated with 10 wt% Pd/C (10 mg) catalyst at 100 psig H_2 at room temperature overnight. L/B selectivity is determined at end of the reaction when copper is fully consumed.

3.2.6 Summary and Conclusions

Supported Rh nanoparticles on silica (3.6 wt% Rh/SiO_2) and nitrogen-doped carbon (1 wt% Rh/NC-HCl and 1.5 wt% Rh/NC-IWI) were synthesized and characterized by TEM, XPS, and ICP-OES. For styrene formation, the catalytic performances of supported Rh nanoparticles were tested and compared. In this work, we have demonstrated the leaching of 34% of the Rh/SiO_2 catalyst during styrene synthesis is likely due to the oxidation of reduced Rh upon reaction with Cu(II) salt. The leached and soluble Rh is likely the active catalyst for arene alkenylation. Although our studies indicate that the leaching of Rh forms the soluble and active catalyst, the nitrogen-doped carbon supports facilitate catalyst recycling. Compared with Rh/SiO_2 catalyst, nitrogen-doped carbon supported Rh catalysts underwent a possible dissolution and re-adsorption process.

When $Cu(OAc)_2$ oxidants were used for styrene synthesis, the observed induction period from molecular $[Rh(\mu\text{-}OAc)(\eta^2\text{-}C_2H_4)_2]_2$ is likely due to the Rh decomposition to insoluble Rh species followed by dissolution to active and soluble Rh catalyst. In our mechanistic study, we found that in the absence of $Cu(OAc)_2$ oxidants, $[Rh(\mu\text{-}OAc)(\eta^2\text{-}C_2H_4)_2]_2$ undergoes thermal decomposition to form Rh(0) species as evidenced by ^1H NMR spectroscopy, TEM/EDS and XPS analysis.[37] ICP-OES analysis and reactivity comparison experiments indicate that the generation of catalytically inactive and insoluble Rh from $[Rh(\mu\text{-}OAc)(\eta^2\text{-}C_2H_4)_2]_2$ occurs in the early stage of catalysis when commercial $Cu(OAc)_2$ is used as the oxidant. But, TEM analysis of the insoluble Rh species showed no evidence of the existence of Rh nanoparticle species, and XPS studies indicate that the formed insoluble Rh species are in a higher oxidation state than Rh(0). Yet, when $Cu(OAc)_2$ is omitted or when silica is added, evidence for the formation of Rh nanoparticles has been obtained. We hypothesize that the untreated $Cu(OAc)_2$ serves to capture the reduced Rh, as either single atom or small clusters (which cannot be observed with current data), and this results in the insoluble Rh in a higher oxidation state than Rh(0). With continued heating, the $Cu(OAc)_2$ trapped Rh can leach back into solution to catalyze arene alkenylation.

3.3 Experimental Section

3.3.1 General Methods. All **r**eactions were performed under inert conditions employing standard Schlenk techniques or in a dinitrogen-filled glovebox unless specified otherwise. Glovebox purity was maintained by periodic dinitrogen purges and was monitored by a dioxygen analyzer (O_2 concentration was < 15 ppm for all reactions). Tetrahydrofuran (THF) was dried over potassium benzophenone ketyl under dinitrogen. Benzene was dried by passage through columns of activated alumina. Pentane was dried over sodium benzophenone ketyl. Benzene-d_6 was used as received and stored under a dinitrogen atmosphere over 4 Å molecular sieves. ^1H NMR spectra were acquired on a Varian Mercury 600 MHz spectrometer. All ^1H and ^{13}C spectra are referenced against residual proton signals (^1H NMR) of deuterated solvents. GC/FID was performed using a Shimadzu GC-2014 system with a 30 m x 90.25 mm HP5 column with 0.25 μm film thickness.

For sampling reaction mixture in heated Fisher-Porter reactors, the reactors were allowed to cool to room temperature, sampled under dinitrogen, recharged with olefin, and reheated. Aliquots of the reaction mixture (< 100 μL) were analyzed by GC/FID using relative peak areas versus the internal standard (hexamethylbenzene). Styrene, allyl benzene, α-methyl styrene, trans-β-methyl styrene, and cis-β-methyl styrene production were quantified using linear regression analysis of gas chromatograms of standard samples of the authentic product. A plot of peak area ratios versus molar ratios gave a regression line using hexamethylbenzene (HMB) as the internal standard. For the GC/FID instrument, the slope and correlation coefficient of the regression lines were 1.67 and 0.99 (styrene), 0.87 and 0.99 (trans-stilbene), 1.40 and 0.99 (allylbenzene), 1.23 and 0.99 (α-methyl styrene), 1.47 and 0.99 (cis-β-methyl styrene), 1.38 and 0.99 (trans-β-methyl styrene), respectively.[37] The turnover (TO) is defined as the product (i.e., styrene or linear alkenyl arenes) per catalyst site at any given time. Ethylene and propylene were purchased in gas cylinders from GTS-Welco and used as received. Copper(II) 2-ethylhexanoate was purchased from Sigma-Aldrich and used as received. Copper (II) pivalate and $[Rh(\eta^2\text{-}C_2H_4)_2(\mu\text{-OAc})]_2$ was prepared according to literature procedures.[73,72] All other reagents were purchased from commercial sources and used as received. Before each catalysis, the supported Rh catalysts were treated with 2 bar of dihydrogen at 150°C for 1h. Caution: Mixtures of hydrocarbons and oxidants are potentially explosive. In these experiments, we took precautions to ensure safe mixtures and use pressure relief valves.

3.3.2 Rh/SiO_2 synthesis. Silica-supported Rh nanoparticle catalysts (Rh/SiO_2) were prepared via an ion exchange method[51, 52] of the Rh precursor using Davisil 636 silica (Sigma-Aldrich) as support. $RhCl_3$ $3H_2O$ precursor (0.250 g, 99%, Sigma-Aldrich) was dissolved in a solution of aqueous ammonia (5.5 mL ammonium hydroxide (14.8 M, 28%-30% of NH_3 in water), ACS plus, Fisher Scientific, in 282 mL distilled deionized water). The $RhCl_3$ solution was added dropwise over 10 min to 4.75 g of acid-washed Davisil 636 silica in 114 mL of distilled deionized water at 70 °C. The mixture was stirred for 60 min at 70 °C, and then cooled to room temperature. The mixture was washed with water and vacuum dried overnight. After calcination in flowing air (medical grade, GTS-Welco) at 400 °C for 2 h, the sample was reduced in flowing dihydrogen (99.999%, GTS-Welco) at 250 °C for 2 h. After reduction, the system was evacuated and cooled to 30 °C for analysis. At 30 °C, the stoichiometric ratio of H to surface Rh is assumed to be 1:1. Using dihydrogen chemisorption on a Micromeritics ASAP 2020 adsorption system,[52] the number of available metal sites was determined by extrapolating the linear portion of the isotherm to zero pressure with the assumption of no dihydrogen uptake on the support.

3.3.3 Rh/NC synthesis. Rhodium supported on nitrogen-doped carbon (Rh/NC-HCl) was prepared similar to a method reported previously.[56, 58, 74] In particular, Carbon Black Pearls 2000 from Cabot Corporation was used as the carbon support. All of the other chemicals were purchased from Sigma-Aldrich Corporation. An aqueous solution of $Rh(NO_3)_2 \cdot 6H_2O$ was mixed with an ethanol solution of 1,10-phenanthroline (Rh:phenanthroline = 1:2) for 20 min at 80 °C. The mixture was added dropwise to a vigorously stirred slurry of carbon black in a 0.1 M NaOH aqueous solution at 80 °C for two hours. The slurry was then cooled, filtered, and thoroughly washed with DI water. The complex was then impregnated with an acetone solution of 80 wt% dicyandiamide relative to the complex, with vigorous stirring followed by drying at 70 °C overnight. The solid was then thermally treated at 700 °C for two hours under ultrahigh-purity N_2 flow (100 mL min^{-1}) with a ramp rate of 10 °C min^{-1}. A vigorously stirred, room-temperature, 1 M HCl solution was then used to remove any formed Rh nanoparticles from the surface. After the acid treatment, the solid was thoroughly washed with DI water and dried overnight at 120 °C. Before use, the sample was heated at 10 °C min^{-1} to 450 °C in ultrahigh purity H_2 (100 mL min^{-1}) and held at that temperature for 2 h. This catalyst has been labeled as Rh/NC-HCl. A metal-free nitrogen carbon catalyst (NC) was synthesized using an acetone solution of 0.4 g dicyandiamide impregnated into 0.5 g of carbon black using the same initial thermal treatment as the metal catalyst.

Additionally, a 1.5 wt% Rh/NC-IWI catalyst was synthesized using the NC support. A solution of 5 wt% Rh metal from an aqueous $Rh(NO_3)_2 \cdot 6H_2O$ solution was impregnated onto the NC and subsequentially dried overnight at 120 °C. The solid was then heated to 450 °C with a ramp rate of 10 °C min^{-1} in ultrahigh-purity H_2 flow (100 mL min^{-1}) and held at that temperature for 2 h.

3.3.4 Transmission electron microscopy (TEM). Samples analyzed by transmission electron microscopy (TEM) were prepared by dispersing the powders in cyclohexane or hexanes (99.5%, anhydrous, Sigma-Aldrich) and sonicating for 1 minute before mounting on Au-supported holey carbon grids. The catalyst samples were imaged using an FEI Titan 80–300 operating at 300 kV. The Rh/SiO_2 sample was also characterized by an EDAX energy dispersive spectrometer (EDS) system in the scanning mode of TEM for single-nanoparticle composition analyses and elemental mapping. Lattice spacings were determined from selected-area electron diffraction and Fourier transforms of high-resolution TEM images.

3.3.5 X-ray photoelectron spectroscopy (XPS). The XPS was performed using a Phi VersaProbe III with a monochromatic Al Kα X-ray source (1486.7 eV) and a hemispherical analyzer; instrument base pressure was ~10^{-7} Pa. Due to the air-sensitivity of Rh catalysts, a PHI vacuum transfer vessel (Model 04-111) was used to protect the sample from exposure to the ambient atmosphere during the transfer from the glovebox to the XPS analysis chamber. Thus, the entire procedure was performed without exposing the catalyst to air or moisture. An X-ray beam of 100 μm was utilized and was rastered over 1.4 mm to reduce the X-ray flux on the target. The electron-energy analyzer was operated with a pass energy of 55 eV for high-resolution scans with a 50 ms per step dwell time. Dual-charge compensation, using a low-energy flood gun with a bias of 1 eV and a low-energy Ar^+ beam, was utilized during data acquisition. The Si $2p_{3/2}$ peak for SiO_2 (103.5 eV) and C1s (284.6 eV) peak were used as a binding energy reference for the spectra.

3.3.6 ICP-OES measurement. Quantitative elemental analyses for the supported Rh catalysts are carried out with inductively coupled plasma optical emission spectrometry (ICP-OES) on a PerkinElmer Avio-200 ICP spectrometer, and a microwave digestion method was developed based on a modified literature method.[58] In a typical ICP sample preparation procedure, a certain amount of Rh sample (i.e. 10 mg Rh/SiO_2 or 13 mg of Rh/NC) and aqua regia (6 mL) are added in a quartz vessel. With the assistance of microwaves, the solution was heated at 180 °C for 7 min with a ramp rate of about 10 °C/min. After cooling, the solution was transferred into a 10 mL tube. A fraction of the above solution (0.2 mL) was diluted in a 10 mL volumetric flask by the addition of 0.2 wt% HNO_3 solution. The concentration of Rh in the diluted solution was analyzed by ICP-OES. To certify the accuracy of this method, the digestion was compared to a reference sample analyzed by Galbraith Laboratories (2323 Sycamore Drive, Knoxville, TN 37921). The analytic results we measured are consistent with the results reported from Galbraith Laboratories.

3.3.7 Catalytic alkenylation of benzene with ethylene and propylene using Cu(X)$_2$ {(X = OPiv (trimethylacetate) or OHex (2-ethyl hexanoate)}. Representative catalytic reactions are described here. A stock solution containing $[Rh(\mu\text{-}OAc)(\eta^2\text{-}C_2H_4)_2]_2$ (0.011 mmol, 0.001 mol % of Rh relative to benzene) or equivalent amount solid Rh catalysts: Rh/SiO$_2$, Rh/NC-HCl or Rh/NC-IWI, hexamethylbenzene (0.046 g, 0.23 mmol), and benzene (10 mL) was prepared in a volumetric flask. Fisher-Porter reactors were charged with 10 mL solution of benzene and copper salt (400 equiv. relative to per Rh, 4.4 mmol). The vessels were sealed, pressurized with ethylene (40 psig) or propylene (25 psig), and subsequently stirred and heated to 150 °C. For the catalysis with ethylene, the reactions were sampled every 2 or 4 h. For the catalysis with propylene, the reactions were sampled when the solution turned yellowish brown and Cu oxidant is consumed.

3.3.8 Catalytic alkenylation of toluene with 1-pentene using Cu(OHex)$_2$ (OHex (2-ethyl hexanoate)**.** A stock solution containing $[Rh(\mu\text{-}OAc)(\eta^2\text{-}C_2H_4)_2]_2$ (0.011 mmol, 0.001 mol % of Rh relative to benzene) or equivalent amount solid Rh catalysts: Rh/SiO$_2$, Rh/NC-HCl or Rh/NC-IWI, hexamethylbenzene (0.046 g, 0.23 mmol), and benzene (10 mL) was prepared in a volumetric flask. Fisher-Porter reactors were charged with 10 mL solution of toluene, 1000 equivalent 1-pentene (relative to Rh), copper salt (400 equiv. relative to per Rh, 4.4 mmol). The vessels were sealed and pressurized with nitrogen (50 psig), and subsequently stirred and heated to 150 °C. For the catalysis evaluation of supported Rh catalysts, the reactions were sampled every 4 h.

3.3.9 Catalytic alkenylation of benzene with ethylene using Cu(OAc)$_2$ (untreated Cu(OAc)$_2$ or dried Cu(OAc)$_2$). Representative catalytic reactions are described here. A stock solution containing an diimine rhodium complex or $[Rh(\mu\text{-}OAc)(\eta^2\text{-}C_2H_4)_2]_2$ (0.011

mmol, 0.001 mol % of Rh relative to benzene), hexamethylbenzene (0.073 g, 0.46 mmol), and benzene (200 mL) was prepared in a volumetric flask. Fisher-Porter reactors were charged with stock solution (10 mL) and copper acetate (240 equiv. relative to per Rh, 0.049 g, 0.27 mmol). The vessels were sealed, pressurized with ethylene (40 psig), and subsequently stirred and heated to 150 °C. For the catalysis with ethylene, the reactions were sampled every 4 h until 24 h.

3.4 References

1. de Almeida, J. L. G.; Dufaux, M.; Taarit, Y. B.; Naccache, C. Linear alkylbenzene. *J. Am. Oil Chem. Soc.* **1994,** *71*, 675-694.

2. Kocal, J. A.; Vora, B. V.; Imai, T. Production of linear alkylbenzenes. *Appl. Catal., A* **2001,** *221*, 295-301.

3. Perego, C.; Ingallina, P. Recent advances in the industrial alkylation of aromatics: new catalysts and new processes. *Catal. Today* **2002,** *73*, 3-22.

4. Galadima, A.; Muraza, O. Role of zeolite catalysts for benzene removal from gasoline via alkylation: A review. *Microporous Mesoporous Mater.* **2015,** *213*, 169-180.

5. Röper, M.; Gehrer, E.; Narbeshuber, T.; Siegel, W.

6. Perego, C.; Pollesel, P., Chapter 2 - Advances in Aromatics Processing Using Zeolite Catalysts. In *Advances in Nanoporous Materials*, Ernst, S., Ed. Elsevier: 2010; Vol. 1, pp 97-149.

7. Chandrasekaran, V. C., CHAPTER 6 - Rubbers, Chemicals and Compounding for ‘O’ Rings and Seals. In *Rubber Seals for Fluid and Hydraulic Systems*, Chandrasekaran, V. C., Ed. William Andrew Publishing: Oxford, 2010; pp 57-69.

8. Buijink, J. K. F.; Lange, J.-P.; Bos, A. N. R.; Horton, A. D.; Niele, F. G. M., Chapter 13 - Propylene Epoxidation via Shell's SMPO Process: 30 Years of Research and Operation. In *Mechanisms in Homogeneous and Heterogeneous Epoxidation Catalysis*, Oyama, S. T., Ed. Elsevier: Amsterdam, 2008; pp 355-371.

9. Perego, C.; Ingallina, P. Combining alkylation and transalkylation for alkylaromatic production. *Green Chem.* **2004,** *6*, 274-279.

10. Gerzeliev, I. M.; Khadzhiev, S. N.; Sakharova, I. E. Ethylbenzene synthesis and benzene transalkylation with diethylbenzenes on zeolite catalysts. *Pet. Chem.* **2011,** *51*, 39-48.

11. Lee, E. H. Iron Oxide Catalysts for Dehydrogenation of Ethylbenzene in the Presence of Steam. *Catal. Rev.* **1974,** *8*, 285-305.

12. Caro, J.; Noack, M., Chapter 1 - Zeolite Membranes – Status and Prospective. In *Advances in Nanoporous Materials*, Ernst, S., Ed. Elsevier: 2010; Vol. 1, pp 1-96.

13. Vaughan, B. A.; Webster-Gardiner, M. S.; Cundari, T. R.; Gunnoe, T. B. A rhodium catalyst for single-step styrene production from benzene and ethylene. *Science* **2015,** *348*, 421.

14. Zhu, W.; Gunnoe, T. B. Advances in Rhodium-Catalyzed Oxidative Arene Alkenylation. *Acc. Chem. Res.* **2020,** *53*, 920-936.

15. Saper, N. I.; Ohgi, A.; Small, D. W.; Semba, K.; Nakao, Y.; Hartwig, J. F. Nickel-catalysed anti-Markovnikov hydroarylation of unactivated alkenes with unactivated arenes facilitated by non-covalent interactions. *Nat. Chem.* **2020,** *12*, 276-283.

16. Foley, N. A.; Lee, J. P.; Ke, Z.; Gunnoe, T. B.; Cundari, T. R. Ru(II) Catalysts Supported by Hydridotris(pyrazolyl)borate for the Hydroarylation of Olefins: Reaction

Scope, Mechanistic Studies, and Guides for the Development of Improved Catalysts. *Acc. Chem. Res.* **2009,** *42*, 585-597.

17. Andreatta, J. R.; McKeown, B. A.; Gunnoe, T. B. Transition metal catalyzed hydroarylation of olefins using unactivated substrates: Recent developments and challenges. *J. Organomet. Chem.* **2011,** *696*, 305-315.

18. Ritleng, V.; Sirlin, C.; Pfeffer, M. Ru-, Rh-, and Pd-Catalyzed C−C Bond Formation Involving C−H Activation and Addition on Unsaturated Substrates: Reactions and Mechanistic Aspects. *Chem. Rev.* **2002,** *102*, 1731-1770.

19. Ackermann, L. Carboxylate-Assisted Transition-Metal-Catalyzed C−H Bond Functionalizations: Mechanism and Scope. *Chem. Rev.* **2011,** *111*, 1315-1345.

20. Gandeepan, P.; Müller, T.; Zell, D.; Cera, G.; Warratz, S.; Ackermann, L. 3d Transition Metals for C–H Activation. *Chem. Rev.* **2019,** *119*, 2192-2452.

21. Luedtke, A. T.; Goldberg, K. I. Intermolecular Hydroarylation of Unactivated Olefins Catalyzed by Homogeneous Platinum Complexes. *Angew. Chem. Int. Ed.* **2008,** *47*, 7694-7696.

22. Suslick, B. A.; Liberman-Martin, A. L.; Wambach, T. C.; Tilley, T. D. Olefin Hydroarylation Catalyzed by (pyridyl-indolate)Pt(II) Complexes: Catalytic Efficiencies and Mechanistic Aspects. *ACS Catal.* **2017,** *7*, 4313-4322.

23. McKeown, B. A.; Gonzalez, H. E.; Gunnoe, T. B.; Cundari, T. R.; Sabat, M. PtII-Catalyzed Ethylene Hydrophenylation: Influence of Dipyridyl Chelate Ring Size on Catalyst Activity and Longevity. *ACS Catal.* **2013,** *3*, 1165-1171.

24. Fujiwara, Y.; Moritani, I.; Danno, S.; Asano, R.; Teranishi, S. Aromatic substitution of olefins. VI. Arylation of olefins with palladium(II) acetate. *J. Am. Chem. Soc.* **1969,** *91*, 7166-7169.

25. McKeown, B. A.; Prince, B. M.; Ramiro, Z.; Gunnoe, T. B.; Cundari, T. R. PtII-Catalyzed Hydrophenylation of α-Olefins: Variation of Linear/Branched Products as a Function of Ligand Donor Ability. *ACS Catal.* **2014,** *4*, 1607-1615.

26. Clement, M. L.; Grice, K. A.; Luedtke, A. T.; Kaminsky, W.; Goldberg, K. I. Platinum(II) Olefin Hydroarylation Catalysts: Tuning Selectivity for the anti-Markovnikov Product. *Chem. - Eur. J.* **2014,** *20*, 17287-17291.

27. Rej, S.; Chatani, N. Rhodium(I)-Catalyzed C8-Alkylation of 1-Naphthylamide Derivatives with Alkenes through a Bidentate Picolinamide Chelation System. *ACS Catal.* **2018,** *8*, 6699-6706.

28. Zell, D.; Bursch, M.; Müller, V.; Grimme, S.; Ackermann, L. Full Selectivity Control in Cobalt(III)-Catalyzed C−H Alkylations by Switching of the C−H Activation Mechanism. *Angew. Chem. Int. Ed.* **2017,** *56*, 10378-10382.

29. Jia, X.; Gary, J. B.; Gu, S.; Cundari, T. R.; Gunnoe, T. B. Oxidative Hydrophenylation of Ethylene Using a Cationic Ru(II) Catalyst: Styrene Production with Ethylene as the Oxidant. *Isr. J. Chem.* **2017,** *57*, 1037-1046.

30. Joslin, E. E.; McMullin, C. L.; Gunnoe, T. B.; Cundari, T. R.; Sabat, M.; Myers, W. H. Catalytic Hydroarylation of Ethylene Using TpRu(L)(NCMe)Ph (L = 2,6,7-Trioxa-1-phosphabicyclo[2,2,1]heptane): Comparison to TpRu(L′)(NCMe)Ph Systems (L′ = CO, PMe3, P(pyr)3, or P(OCH2)3CEt). *Organometallics* **2012,** *31*, 6851-6860.

31. Burgess, S. A.; Joslin, E. E.; Gunnoe, T. B.; Cundari, T. R.; Sabat, M.; Myers, W. H. Hydrophenylation of ethylene using a cationic Ru(ii) catalyst: comparison to a neutral Ru(ii) catalyst. *Chem. Sci.* **2014,** *5*, 4355-4366.

32. Matsumoto, T.; Taube, D. J.; Periana, R. A.; Taube, H.; Yoshida, H. Anti-Markovnikov Olefin Arylation Catalyzed by an Iridium Complex. *J. Am. Chem. Soc.* **2000,** *122*, 7414-7415.

33. Bhalla, G.; Liu, X. Y.; Oxgaard, J.; Goddard, W. A.; Periana, R. A. Synthesis, Structure, and Reactivity of O-Donor Ir(III) Complexes: C−H Activation Studies with Benzene. *J. Am. Chem. Soc.* **2005,** *127*, 11372-11389.

34. Bhalla, G.; Bischof, S. M.; Ganesh, S. K.; Liu, X. Y.; Jones, C. J.; Borzenko, A.; Tenn, I. I. I. W. J.; Ess, D. H.; Hashiguchi, B. G.; Lokare, K. S.; Leung, C. H.; Oxgaard, J.; Goddard, I. I. I. W. A.; Periana, R. A. Mechanism of efficient anti-Markovnikov olefin hydroarylation catalyzed by homogeneous Ir(iii) complexes. *Green Chem.* **2011,** *13*, 69-81.

35. Sevov, C. S.; Hartwig, J. F. Iridium-Catalyzed Oxidative Olefination of Furans with Unactivated Alkenes. *J. Am. Chem. Soc.* **2014,** *136*, 10625-10631.

36. Vaughan, B. A.; Khani, S. K.; Gary, J. B.; Kammert, J. D.; Webster-Gardiner, M. S.; McKeown, B. A.; Davis, R. J.; Cundari, T. R.; Gunnoe, T. B. Mechanistic Studies of Single-Step Styrene Production Using a Rhodium(I) Catalyst. *J. Am. Chem. Soc.* **2017,** *139*, 1485-1498.

37. Zhu, W.; Luo, Z.; Chen, J.; Liu, C.; Yang, L.; Dickie, D. A.; Liu, N.; Zhang, S.; Davis, R. J.; Gunnoe, T. B. Mechanistic Studies of Single-Step Styrene Production

Catalyzed by Rh Complexes with Diimine Ligands: An Evaluation of the Role of Ligands and Induction Period. *ACS Catal.* **2019,** *9*, 7457-7475.

38. Webster-Gardiner, M. S.; Chen, J.; Vaughan, B. A.; McKeown, B. A.; Schinski, W.; Gunnoe, T. B. Catalytic Synthesis of "Super" Linear Alkenyl Arenes Using an Easily Prepared Rh(I) Catalyst. *J. Am. Chem. Soc.* **2017,** *139*, 5474-5480.

39. Chen, J.; Nielsen, R. J.; Goddard, W. A.; McKeown, B. A.; Dickie, D. A.; Gunnoe, T. B. Catalytic Synthesis of Superlinear Alkenyl Arenes Using a Rh(I) Catalyst Supported by a "Capping Arene" Ligand: Access to Aerobic Catalysis. *J. Am. Chem. Soc.* **2018,** *140*, 17007-17018.

40. Liebov, N. S.; Zhu, W.; Chen, J.; Webster-Gardiner, M. S.; Schinski, W. L.; Gunnoe, T. B. Rhodium-Catalyzed Alkenylation of Toluene Using 1-Pentene: Regioselectivity To Generate Precursors for Bicyclic Compounds. *Organometallics* **2019,** *38*, 3860-3870.

41. Jia, X.; Frye, L. I.; Zhu, W.; Gu, S.; Gunnoe, T. B. Synthesis of Stilbenes by Rhodium-Catalyzed Aerobic Alkenylation of Arenes via C–H Activation. *J. Am. Chem. Soc.* **2020**.

42. Ji, Y.; Jain, S.; Davis, R. J. Investigation of Pd Leaching from Supported Pd Catalysts during the Heck Reaction. *J. Phys. Chem. B* **2005,** *109*, 17232-17238.

43. Davies, I. W.; Matty, L.; Hughes, D. L.; Reider, P. J. Are Heterogeneous Catalysts Precursors to Homogeneous Catalysts? *J. Am. Chem. Soc.* **2001,** *123*, 10139-10140.

44. Zalesskiy, S. S.; Ananikov, V. P. Pd2(dba)3 as a Precursor of Soluble Metal Complexes and Nanoparticles: Determination of Palladium Active Species for Catalysis and Synthesis. *Organometallics* **2012,** *31*, 2302-2309.

45. Reay, A. J.; Fairlamb, I. J. S. Catalytic C–H bond functionalisation chemistry: the case for quasi-heterogeneous catalysis. *Chem. Commun.* **2015,** *51*, 16289-16307.

46. Pröckl, S. S.; Kleist, W.; Gruber, M. A.; Köhler, K. In Situ Generation of Highly Active Dissolved Palladium Species from Solid Catalysts—A Concept for the Activation of Aryl Chlorides in the Heck Reaction. *Angew. Chem. Int. Ed.* **2004,** *43*, 1881-1882.

47. Röhlich, C.; Köhler, K. Macrocyclic Palladium(II) Complexes in C□C Coupling Reactions: Efficient Catalysis by Controlled Temporary Release of Active Species. *Adv. Synth. Catal.* **2010,** *352*, 2263-2274.

48. Gnad, C.; Abram, A.; Urstöger, A.; Weigl, F.; Schuster, M.; Köhler, K. Leaching Mechanism of Different Palladium Surface Species in Heck Reactions of Aryl Bromides and Chlorides. *ACS Catal.* **2020**, 6030-6041.

49. Phan, N. T. S.; Van Der Sluys, M.; Jones, C. W. On the Nature of the Active Species in Palladium Catalyzed Mizoroki–Heck and Suzuki–Miyaura Couplings – Homogeneous or Heterogeneous Catalysis, A Critical Review. *Adv. Synth. Catal.* **2006,** *348*, 609-679.

50. Del Zotto, A.; Zuccaccia, D. Metallic palladium, PdO, and palladium supported on metal oxides for the Suzuki–Miyaura cross-coupling reaction: a unified view of the process of formation of the catalytically active species in solution. *Catal. Sci. Technol.* **2017,** *7*, 3934-3951.

51. Lam, Y. L.; Boudart, M. Preparation of small Au-Pd particles on silica. *J. Catal.* **1977,** *50*, 530-540.

52. Kaylor, N.; Xie, J.; Kim, Y.-S.; Pham, H. N.; Datye, A. K.; Lee, Y.-K.; Davis, R. J. Vapor phase deoxygenation of heptanoic acid over silica-supported palladium and palladium-tin catalysts. *J. Catal.* **2016,** *344*, 202-212.

53. Paál, Z.; Teschner, D.; Rodriguez, N. M.; Baker, R. T. K.; Tóth, L.; Wild, U.; Schlögl, R. Rh/GNF catalysts: Characterization and catalytic performance in methylcyclopentane reactions. *Catal. Today* **2005,** *102-103*, 254-258.

54. Alsalahi, W.; Tylus, W.; Trzeciak, A. M. Green Synthesis of Rhodium Nanoparticles that are Catalytically Active in Benzene Hydrogenation and 1-Hexene Hydroformylation. *ChemCatChem* **2018,** *10*, 2051-2058.

55. Zhang, M.; Wang, Y.-G.; Chen, W.; Dong, J.; Zheng, L.; Luo, J.; Wan, J.; Tian, S.; Cheong, W.-C.; Wang, D.; Li, Y. Metal (Hydr)oxides@Polymer Core–Shell Strategy to Metal Single-Atom Materials. *J. Am. Chem. Soc.* **2017,** *139*, 10976-10979.

56. Xie, J.; Kammert, J. D.; Kaylor, N.; Zheng, J. W.; Choi, E.; Pham, H. N.; Sang, X.; Stavitski, E.; Attenkofer, K.; Unocic, R. R.; Datye, A. K.; Davis, R. J. Atomically Dispersed Co and Cu on N-Doped Carbon for Reactions Involving C–H Activation. *ACS Catal.* **2018,** *8*, 3875-3884.

57. Huang, K.; Fu, H.; Shi, W.; Wang, H.; Cao, Y.; Yang, G.; Peng, F.; Wang, Q.; Liu, Z.; Zhang, B.; Yu, H. Competitive adsorption on single-atom catalysts: Mechanistic insights into the aerobic oxidation of alcohols over CoNC. *J. Catal.* **2019,** *377*, 283-292.

58. Xiong, Y.; Dong, J.; Huang, Z.-Q.; Xin, P.; Chen, W.; Wang, Y.; Li, Z.; Jin, Z.; Xing, W.; Zhuang, Z.; Ye, J.; Wei, X.; Cao, R.; Gu, L.; Sun, S.; Zhuang, L.; Chen, X.; Yang, H.; Chen, C.; Peng, Q.; Chang, C.-R.; Wang, D.; Li, Y. Single-atom Rh/N-doped carbon electrocatalyst for formic acid oxidation. *Nat. Nanotechnol.* **2020,** *15*, 390-397.

59. Vorobyeva, E.; Fako, E.; Chen, Z.; Collins, S. M.; Johnstone, D.; Midgley, P. A.; Hauert, R.; Safonova, O. V.; Vilé, G.; López, N.; Mitchell, S.; Pérez-Ramírez, J. Atom-by-Atom Resolution of Structure–Function Relations over Low-Nuclearity Metal Catalysts. *Angew. Chem. Int. Ed.* **2019,** *58*, 8724-8729.

60. Widegren, J. A.; Finke, R. G. A review of the problem of distinguishing true homogeneous catalysis from soluble or other metal-particle heterogeneous catalysis under reducing conditions. *J. Mol. Catal. A: Chem.* **2003,** *198*, 317-341.

61. Crabtree, R. H. Resolving Heterogeneity Problems and Impurity Artifacts in Operationally Homogeneous Transition Metal Catalysts. *Chem. Rev.* **2012,** *112*, 1536-1554.

62. Hartley, F. R. Palladium and Platinum. *Coord. Chem. Rev.* **1981,** *35*, 143-209.

63. Yu, K.; Sommer, W.; Weck, M.; Jones, C. W. Silica and polymer-tethered Pd–SCS-pincer complexes: evidence for precatalyst decomposition to form soluble catalytic species in Mizoroki–Heck chemistry. *J. Catal.* **2004,** *226*, 101-110.

64. Weck, M.; Jones, C. W. Mizoroki−Heck Coupling Using Immobilized Molecular Precatalysts: Leaching Active Species from Pd Pincers, Entrapped Pd Salts, and Pd NHC Complexes. *Inorg. Chem.* **2007,** *46*, 1865-1875.

65. Liu, J.; Tao, R.; Guo, Z.; Regalbuto, J. R.; Marshall, C. L.; Klie, R. F.; Miller, J. T.; Meyer, R. J. Selective Adsorption of Manganese onto Rhodium for Optimized Mn/Rh/SiO2 Alcohol Synthesis Catalysts. *ChemCatChem* **2013,** *5*, 3665-3672.

66. Liu, Y.; Göeltl, F.; Ro, I.; Ball, M. R.; Sener, C.; Aragão, I. B.; Zanchet, D.; Huber, G. W.; Mavrikakis, M.; Dumesic, J. A. Synthesis Gas Conversion over Rh-Based Catalysts Promoted by Fe and Mn. *ACS Catal.* **2017,** *7*, 4550-4563.

67. Biesinger, M. C.; Lau, L. W. M.; Gerson, A. R.; Smart, R. S. C. Resolving surface chemical states in XPS analysis of first row transition metals, oxides and hydroxides: Sc, Ti, V, Cu and Zn. *Appl. Surf. Sci.* **2010,** *257*, 887-898.

68. Swadźba-Kwaśny, M.; Chancelier, L.; Ng, S.; Manyar, H. G.; Hardacre, C.; Nockemann, P. Facile in situ synthesis of nanofluids based on ionic liquids and copper oxide clusters and nanoparticles. *Dalton Transactions* **2012,** *41*, 219-227.

69. Devaraj, M.; Saravanan, R.; Deivasigamani, R.; Gupta, V. K.; Gracia, F.; Jayadevan, S. Fabrication of novel shape Cu and Cu/Cu2O nanoparticles modified electrode for the determination of dopamine and paracetamol. *J. Mol. Liq.* **2016,** *221*, 930-941.

70. Deng, D.; Chen, X.; Yu, L.; Wu, X.; Liu, Q.; Liu, Y.; Yang, H.; Tian, H.; Hu, Y.; Du, P.; Si, R.; Wang, J.; Cui, X.; Li, H.; Xiao, J.; Xu, T.; Deng, J.; Yang, F.; Duchesne, P. N.; Zhang, P.; Zhou, J.; Sun, L.; Li, J.; Pan, X.; Bao, X. A single iron site confined in a graphene matrix for the catalytic oxidation of benzene at room temperature. *Sci. Adv.* **2015,** *1*, e1500462.

71. Chen, Z.; Vorobyeva, E.; Mitchell, S.; Fako, E.; López, N.; Collins, S. M.; Leary, R. K.; Midgley, P. A.; Hauert, R.; Pérez-Ramírez, J. Single-atom heterogeneous catalysts based on distinct carbon nitride scaffolds. *Natl. Sci. Rev.* **2018,** *5*, 642-652.

72. Gilliland, S. E.; Tengco, J. M. M.; Yang, Y.; Regalbuto, J. R.; Castano, C. E.; Gupton, B. F. Electrostatic adsorption-microwave synthesis of palladium nanoparticles on graphene for improved cross-coupling activity. *Appl. Catal., A* **2018,** *550*, 168-175.

73. Xie, L.-H.; Suh, M. P. Flexible Metal–Organic Framework with Hydrophobic Pores. *Chem. - Eur. J.* **2011,** *17*, 13653-13656.

74. Liu, Q.; Li, Y.; Zheng, L.; Shang, J.; Liu, X.; Yu, R.; Shui, J. Sequential Synthesis and Active-Site Coordination Principle of Precious Metal Single-Atom Catalysts for Oxygen Reduction Reaction and PEM Fuel Cells. *Adv. Energy Mater.* **2020,** *10*, 2000689.

4 Development of Co-catalytic Processes for Hydrocarbon Oxidation: A Proof-of-Concept Study of Nanoparticle Catalyzed Hydrogenolysis of (^{t}bpy)Pt(OPh)Cl

4.1 Introduction

Current industrial utilization of methane is an indirect process (syngas process) involving steam reforming reactions and Fischer-Tropsch synthesis.[1, 2] The syngas process is operated at high pressures and temperatures (40 atm and >800 °C) and is energy-intensive, which results significant capital investment for new plants.[1, 2] The development of a catalytic route for a direct and low-temperature conversion of methane to methanol (MTM)[3] that achieves high selectivity and conversion is attractive due to the potential advantages it could offer compared to syngas routes to methanol.[4]

A common strategy in the development of MTM catalysis is the use of a homogeneous catalyst that is capable of activating the methane C−H bond and releasing a functionalized or protected product, as MeX (X = OH, halide, $OOCCF_3$, OSO_3H, etc.), which can be hydrolyzed to methanol.[5, 6] This strategy has afforded some success, perhaps the most promising of which employs a (bpm)$PtCl_2$ (bpm = 2,2’-bipyrimidine) catalyst in concentrated H_2SO_4, which acts as both the solvent and the oxidant for the process.[5] While this system affords > 70% yield (based on methane) with greater than 90% selectivity, the process is not commercially viable due to dramatically reduced reactivity when the H_2SO_4 concentration is lowered below 96%.[7] Heterogeneous catalysts have also been employed for selective, low-temperature MTM catalysis.[8-10] In this area, copper-based zeolite catalysts have shown the promise due to their ability to catalytically oxidize methane to methanol using molecular oxygen directly as the oxidant at temperatures from 210-225 °C.[8] However, these zeolite-based catalysts offer their own set of challenges, including 1) the nature of catalytic sites is debated (could be di-copper[9,11] or tri-copper sites[10]) and 2) catalysis can only be carried out at very low oxygen concentrations (25 ppm) to avoid over-oxidation to CO and CO_2.[8]

One possible route to achieve direct MTM processes is the development of transition metal catalysts that can couple methane C−H activation and subsequently lead to oxy-functionalization via oxygen atom insertion to form C−O bonds. While both the C−H activation[12-15] and C−O bond formation[16-18] steps have been demonstrated, catalysts that that can perform both key steps are rare. For example, methyltrioxorhenium(VII) is known to mediate C–O bond formation by oxy-insertion into the Re–Me bond (C–O bond formation).[16-18] However, (MeO)ReO_3 is not capable of performing methane C−H activation (Scheme 4.1).

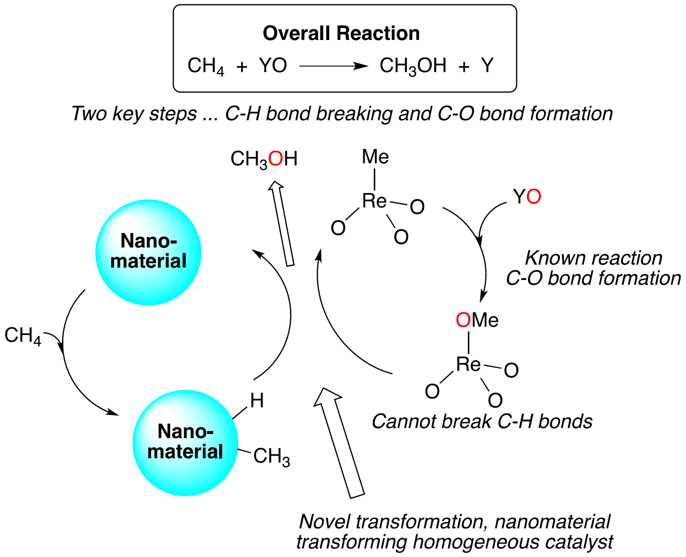

Scheme 4.1. The new concept of co-catalytic catalysis that combines a soluble molecular catalyst ($MeReO_3$) with a heterogeneous catalyst (blue, nanomaterial) for the conversion of methane to methanol.

Given the inherent challenges associated with both homogeneous and heterogeneous MTM catalysis, we have considered a co-catalytic strategy in which 1) the homogeneous catalyst mediates C−O bond formation via oxy-insertion into a metal-hydrocarbyl bond,[16-18] 2) a heterogeneous catalyst mediates alkane C−H activation[19, 20] and then transfers an alkyl group to a tunable homogeneous catalyst, and 3) the heterogeneous catalyst mediates the release of functionalized alcohol product via stepwise or concerted proton/hydrocarbyl transfer (Scheme 4.1). This process would use catalysts that are known to perform the two key steps of hydrocarbon partial oxidation (C−H bond breaking and C–O bond formation) in separate processes. This strategy is distinct from previous efforts where a single catalyst is required to perform all steps of hydrocarbon partial oxidation.[5-10]

Of particular interest is the interaction of nanomaterials with the homogeneous transition metal complexes, in particular M−OR groups of molecular complexes. For initial studies, we used dihydrogen as a more reactive model substrate than methane[19] and a mechanistic study of the catalytic addition of dihydrogen across M−OR bonds[21, 22](*i.e.*, hydrogenolysis) to produce alcohol will be carried out (equation 1).

$$\mathrm{L_nM\text{-}OR} + \mathrm{H_2} \xrightarrow{\text{Nanocatalyst}} \mathrm{HOR} + \mathrm{L_nM\text{-}H} \qquad (1)$$

The primary aims of this study are 1) to determine the relative efficacy of various nanomaterials for the catalytic hydrogenolysis of M−OR bonds, 2) understand the mechanism of the net hydrogenolysis reaction, especially the interfacial interaction between nanomaterial and homogenous organometallic complexes, and 3) understand the differences between hydrogenolysis of M–OR bonds versus C=C or C=O bonds. We will focused on silica-supported Pd, Rh, and Pt nanoparticles catalyzed hydrogenolysis of (^{t}bpy)Pt(OPh)Cl to form phenol (Scheme 4.2).

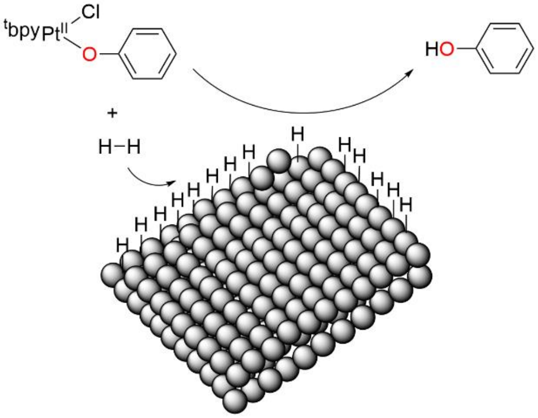

Scheme 4.2. A model reaction of nanomaterial-catalyzed hydrogenolysis of (^{t}bpy)Pt(OPh)Cl.

4.2 Results and Discussion

The addition of dihydrogen across the M−OR bonds of the molecular complexes including (Py)(CH_3O)ReO_3 (Py = pyridine) and (^{t}bpy)Pt(OPh)Cl (**1**) (^{t}bpy= 4,4'-di-tert-butyl-2,2'-bipyridine) have been studied in this project (Scheme 4.3).

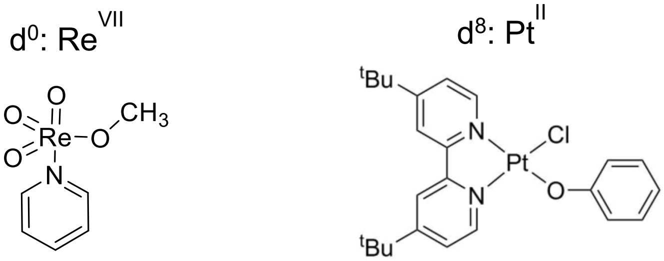

Scheme 4.3. Examples of M−OR substrates synthesized to study the addition of dihydrogen across the M−OR bond.

Initial efforts focused on the isolation of the (CH_3O)ReO_3 complex and a study of its reactivity with dihydrogen. The synthesis of (CH_3O)ReO_3 is challenging due to its thermal instability and sensitivity to moisture.[23] Periana and co-workers reported characterization data for this species when synthesized *in situ* (NMR yield = 40%) and observed the methoxide signal in the ^{1}H NMR (δ = 4.48 ppm in THF-d_8),[16, 18] but $(CH_3O)ReO_3$ was not isolated. To improve the yield and isolate the $CH_3O{-}Re$ species, we added excess CF_3CH_2OH during the synthesis, which afforded ~70% yield of a $(CH_3O)Re$ complex (δ = 4.49 ppm) by ^{1}H NMR spectroscopy (Figure 4.1). However, integration of additional resonances in the ^{1}H NMR spectrum indicated that a pyridine ligand (9.0, 8.5, and 8.1 ppm) was also coordinated to the $(CH_3O)ReO_3$ complex (Figure 4.1). Initial attempts to react the isolated $(CH_3O)ReO_3(Py)$ material with proton sources (H_2O, CH_3COOH, H_2, etc.) did not result in the release of methanol, which could indicate that the crude product did not contain a Re–OMe bond, or that the coordinated pyridine shut down the reactivity of the methoxide ligand. Based on these observations, it was determined that $(CH_3O)ReO_3$ was not a suitable target for the mechanistic study of nanoparticle-mediated hydrogenolysis reaction.

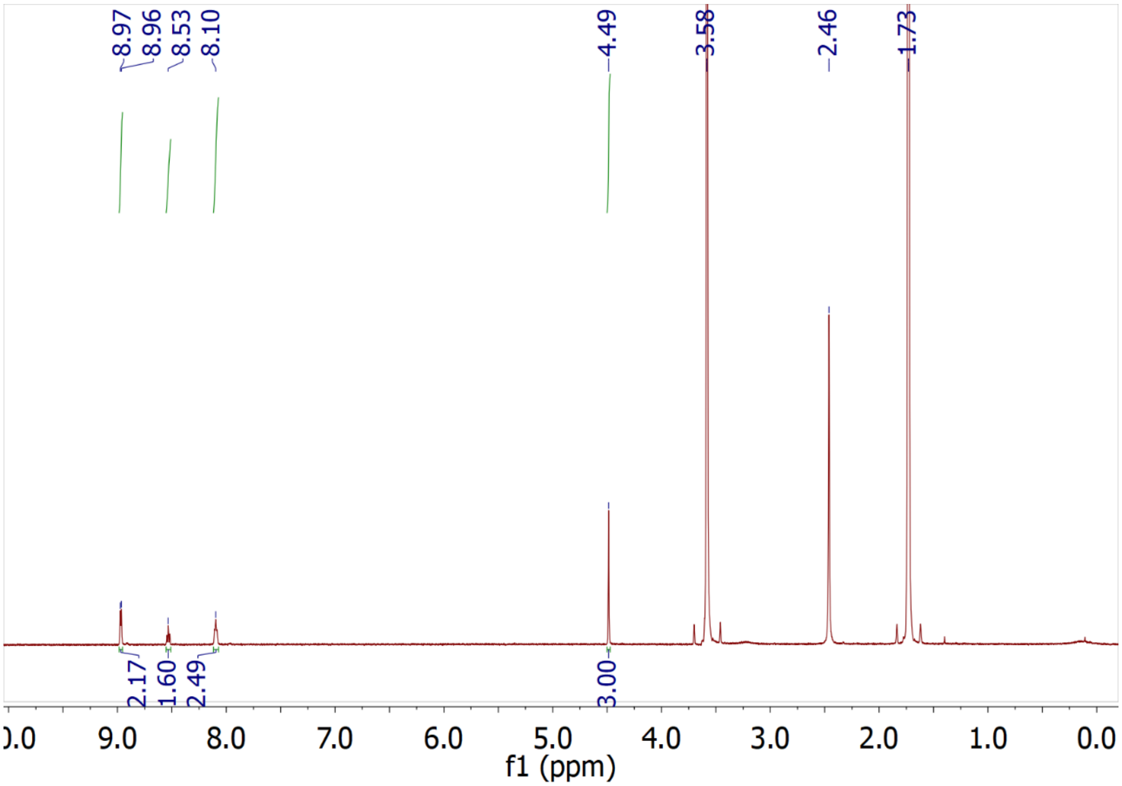

Figure 4.1. ^{1}H NMR spectrum of isolated $(CH_3O)ReO_3(Py)$ in THF-d_8.

The hydrogenolysis reaction of M–OR complexes result in the formation of metal hydrides in addition to the M–OHR (or free HOR) products,[22, 24] but, early and mid-transition metal hydrides (Zr^{IV}, Ru^{II,} and Fe^{II}) have been shown to react with alcohols to form corresponding transition metal alkoxide or aryloxide products.[24-26] Hence, instead of synthesizing early and mid-transition M–OR complexes, Pt alkoxide or aryloxide complexes were targeted (Scheme 4.3). The (^{t}bpy)Pt(OCH$_3$)Cl complex was selected as an initial target. However, multiple attempts to synthesize and isolate the precursor, (^{t}bpy)Pt(OCH$_3$)$_2$, were unsuccessful. This is likely a result of β-H elimination from the (^{t}bpy)Pt(OCH$_3$)$_2$ complex, which Bercaw and co-workers reported was facile.[27] Given this, (^{t}bpy)Pt(OPh)Cl (**1**) was selected due to its lack of β−hydrogens. Complex **1** was synthesized with 70% isolated yield and characterized by ^{1}H, ^{13}C NMR spectroscopy and elemental analysis. A single crystal of **1** was also structurally characterized using single crystal X-ray diffracdtion (Figure 4.2 and Table 4.1). The bond distance of Pt–O in complex **1** is 1.988(10) Å, which is similar to Pt–O bond distances of (^{t}bpy)Pt(OPh)$_2$ (2.001(4) Å and 2.014(4) Å).[28]

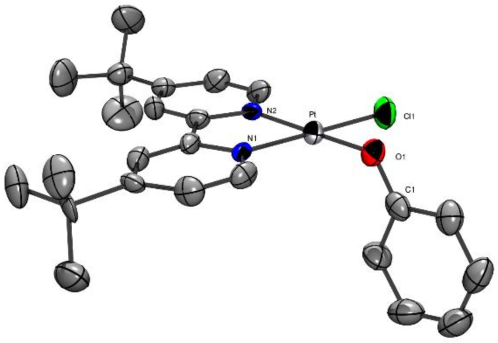

Figure 4.2. ORTEP of (^{t}bpy)Pt(OPh)Cl at the 30% probability level. Hydrogen atoms have been omitted for clarity. Selected bond lengths [Å] and angles [°]: Pt-O(1) = 1.988(10); Pt-Cl(1) =2.291(3), C(1)-O(1)-Pt= 124.3(9).

In collaboration with the Davis Group (UVA Chemical Engineering), uniform noble metal catalysts on silica support (Pd/SiO_2,[29] Rh/SiO_2 and Pt/SiO_2) were synthesized and characterized. Both 5.0 wt% Pd/SiO_2 and 1.0 wt% Pt/SiO_2 catalysts were used for this study.[29, 30] The 3.6 wt% Rh/SiO_2 catalyst was previously discussed in detail in Chapter 3. A typical HAADF−STEM image of Pd/SiO_2 is shown in Figure 4.3. From the particle size distribution analysis, the Pd nanocatalysts are ~1.1(4) nm in diameter, and they are well dispersed on the silica support. From the H_2 chemical absorption analysis, the dispersion of Pd atoms is ~80%, which corresponds to 80% of Pd atoms occupying the surface of the 1.1(4) nm Pd nanoparticles. For the subsequent analyses, all of the surface Pd atoms are assumed to be the catalytically active sites. The same characterization techniques and catalytic assumptions were used for Rh and Pt nanoparticles dispersed on silica supports.

Table 4.1 Crystal data and structure refinement for (^{t}bpy)Pt(OPh)Cl.

Empirical formula	C27 H35 Cl N2 O2 Pt	
Formula weight	650.11	
Temperature	296(2) K	
Wavelength	0.71073 Å	
Crystal system	Monoclinic	
Space group	$P2_1/n$	
Unit cell dimensions	a = 13.128(2) Å	
	b = 12.130(2) Å	β= 110.202(3)°.
	c = 18.167(3) Å	
Volume	2714.8(6) $Å^3$	
Z	4	
Density (calculated)	1.591 mg/m^3	
Absorption coefficient	5.292 mm^{-1}	
F(000)	1288	
Crystal size	0.260 x 0.240 x 0.220 mm^3	

Theta range for data collection	3.530 to 27.716°.
Index ranges	-17<=h<=17, -15<=k<=15, -23<=l<=23
Reflections collected	36206
Independent reflections	6223 [R(int) = 0.1006]
Completeness to theta = 25.242°	98.7 %
Absorption correction	Empirical
Refinement method	Full-matrix least-squares on F^2
Data / restraints / parameters	6223 / 0 / 306
Goodness-of-fit on F^2	1.191
Final R indices [I>2sigma(I)]	R1 = 0.0784, wR2 = 0.1469
R indices (all data)	R1 = 0.1474, wR2 = 0.1741
Largest diff. peak and hole	1.603 and -0.948 e.Å^{-3}

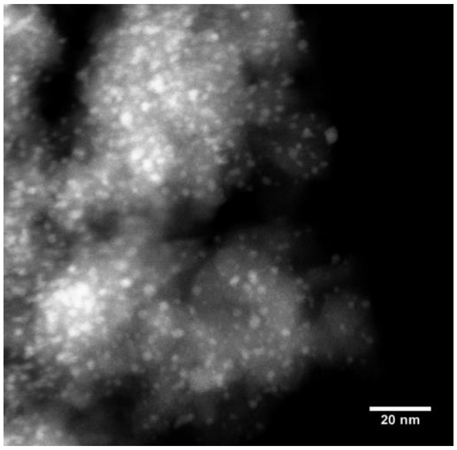

Figure 4.3. A HAADF-STEM image of synthesized SiO_2 supported Pd nanoparticles (Pd/SiO_2).

The reaction of complex **1** with H_2 in the presence of Pd/SiO_2 catalysts resulted in the net hydrogenolysis of Pt–OPh to produce phenol, (^{t}bpy)PtCl_2, free ^{t}bpy, and Pt(s), (Scheme 4.4). In a typical kinetic measurement (Figure 4.4), the disappearance of the resonance at 6.3 ppm in the ^{1}H NMR spectrum, which is assigned to (^{t}bpy)Pt(OPh)Cl, was monitored. New peaks due to PhOH (6.6, 7.1 and 8.1 ppm), free ^{t}bpy (7.3, 8.5, and 8.6 ppm), and (^{t}bpy)PtCl_2 (7.6, 8.2 and 9.4 ppm) evolved simultaneously. Through quantification of ^{1}H NMR spectra, a typical concentration profile of H_2 (purple), PhOH (red), and (^{t}bpy)Pt(OPh)Cl (blue) was obtained (Figure 4.5). The control reaction of **1** with H_2 in the absence of the heterogeneous catalyst produced phenol at a greatly reduced rate (<10% conversion in 8 h compared to almost 80% conversion in 6 h when Pd nanoparticles were present). Therefore, the heterogeneous Pd catalyst accelerated the hydrogenolysis reaction resulting in the release of PhOH as the product.

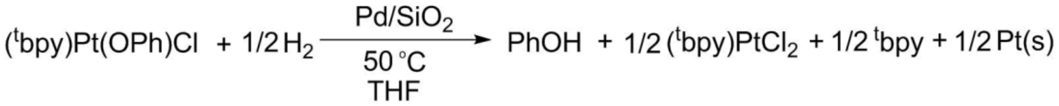

$$(^t\text{bpy})\text{Pt(OPh)Cl} + 1/2\,H_2 \xrightarrow[\text{50 °C, THF}]{\text{Pd/SiO}_2} \text{PhOH} + 1/2\,(^t\text{bpy})\text{PtCl}_2 + 1/2\,^t\text{bpy} + 1/2\,\text{Pt(s)}$$

Scheme 4.4. Pd/SiO_2 catalyzed hydrogenolysis of (^{t}bpy)Pt(OPh)Cl complex(**1**) for phenol production (^{t}bpy = 4,4'-di-tert-butyl-2,2'-bipyridine).

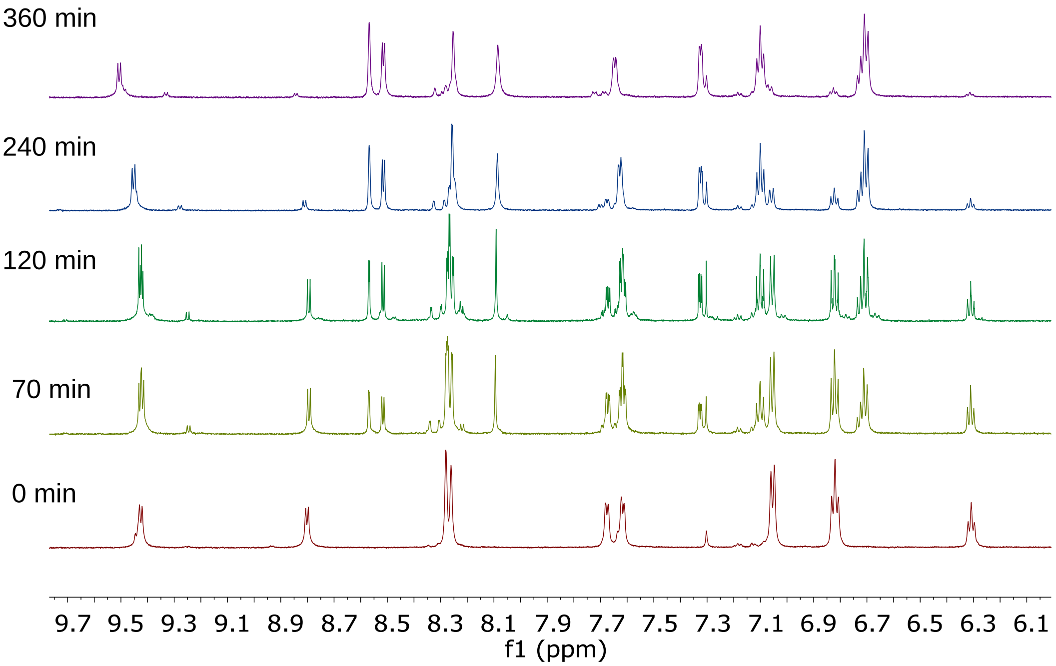

Figure 4.4. ^{1}H NMR spectra of soluble protonation products in THF-d_8 for a typical Pd/SiO_2 mediated hydrogenolysis of (^{t}bpy)PtCl(OPh). Reaction conditions:(^{t}bpy)Pt(OPh)Cl: 13.2 mmol/L, 20 psi H_2 (~7-11 mmol/L in solution), Pd/SiO_2 (5 wt%, 1.23 x 10^{-6} mol Pd_{surf}), T= 50 °C, THF-d_8, internal standard hexamethyldisilane: 2.33 mmol/L.

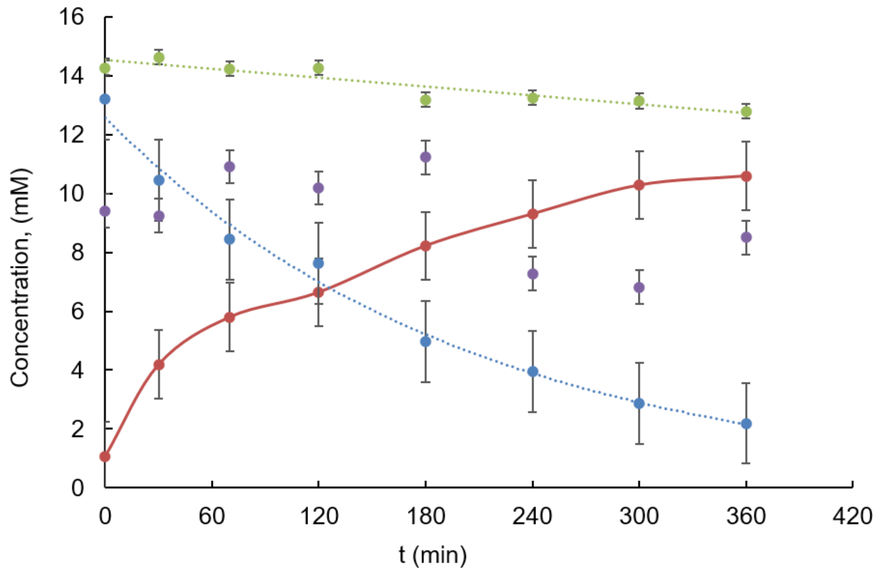

Figure 4.5. Concentration profiles of reactants and products from Pd/SiO_2 catalyzed hydrogenolysis of (^{t}bpy)Pt(OPh)Cl: sum of [HOPh] and [(^{t}bpy)Pt(OPh)Cl] (green), [H_2] (purple), [PhOH] (red), and [(^{t}bpy)Pt(OPh)Cl] (blue). Reaction conditions: (^{t}bpy)Pt(OPh)Cl: 13.2 mmol/L, 20 psi H_2 (~7-11 mmol/L in solution), Pd/SiO_2 (5 wt%, 1.23 x 10^{-6} mol Pd_{surf}), T= 50 °C, THF-d_8, internal standard hexamethyldisilane: 2.33 mmol/L.

In Figure 4.5, the disappearance of **1** and production of PhOH were both monitored by ^{1}H NMR spectroscopy. A first-order dependence on **1** was observed for the Pd nanoparticle promoted hydrogenolysis (Figure 4.6), which is different from previously reported hydrogenolysis of the Pt–NHPh bond of (^{t}bpy)Pt(NHPh)(CH_3), which exhibited a zero-order dependence on (^{t}bpy)Pt(NHPh)(CH_3).[16]

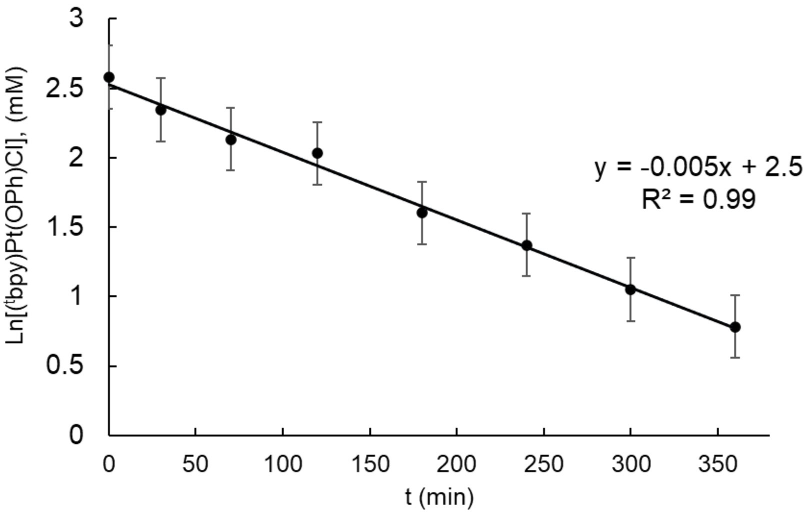

Figure 4.6. First order dependence on (^{t}bpy)Pt(OPh)Cl complex. Reaction conditions: (^{t}bpy)Pt(OPh)Cl: 13.2 mmol/L, 20 psi H_2 (~7-11 mmol/L in solution), Pd/SiO_2 (5 wt%, 1.23 x 10^{-6} mol Pd_{surf}), T= 50 °C, THF-*d*$_8$, internal standard hexamethyldisilane: 2.33 mmol/L.

The rate for the hydrogenolysis of (^{t}bpy)Pt(OPh)Cl was found to be proportional to the number of active sites on Pd nanoparticles. The catalytic rate from observed k_{obs} increased by about 5 times by increasing Pd nanoparticle loading from 0.15 moles to 0.8 moles (relative to 1 mole of complex **1**) (Figure 4.7). This linear dependence on the amount of Pd nanoparticle indicated the surface Pd catalysts were responsible for accelerated hydrogenolysis rate of complex **1** to release PhOH.

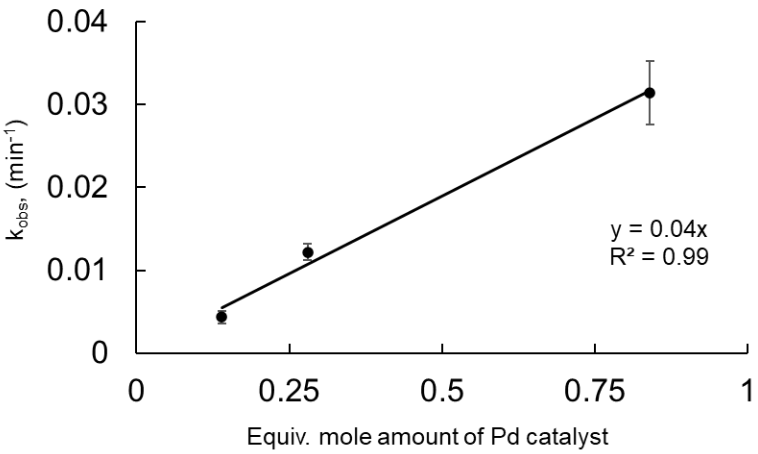

Figure 4.7. k_{obs} plot versus various amounts of Pd nanoparticles loading. Reaction conditions: (^{t}bpy)Pt(OPh)Cl: 13.2 mmol/L; 20 psi H_2 : ~7−11 mmol/L in solution; Pd/SiO_2 (5 wt%, 3.44 x 10^{-7} mol, 3.44 x 10^{-7} mol, and 1.23 x 10^{-6} mol Pd_{surf}); T= 50 °C, THF−d_8; hexamethyldisilane: 2.33 mmol/L. The k_{obs} values are the result of at least three independent experiments with standard deviations indicated.

During catalysis using the Pd supported materials, elemental Pt was deposited on the Pd surface after reaction as observed using the TEM−EDS mapping of Pt, Pd, and Si (Figure 4.8). From the TEM-EDS analysis of selected regions of recovered Pd/SiO_2 (isolated from 1h of catalysis), about 16 percent of atomic Pt was deposited on the Pd surface (Figure 4.8). Inductively coupled plasma optical emission spectroscopy (ICP−OES) measurements have further confirmed and quantified the formation of Pt on Pd nanoparticles (about 10 percent atomic Pt on Pd nanoparticles). Particle size analysis of the Pd nanoparticles following reaction with **1** revealed that the nanoparticles had sintered from 1.1(4) to about 2.0(5) nm in diameter (Figure 4.9) during catalysis.

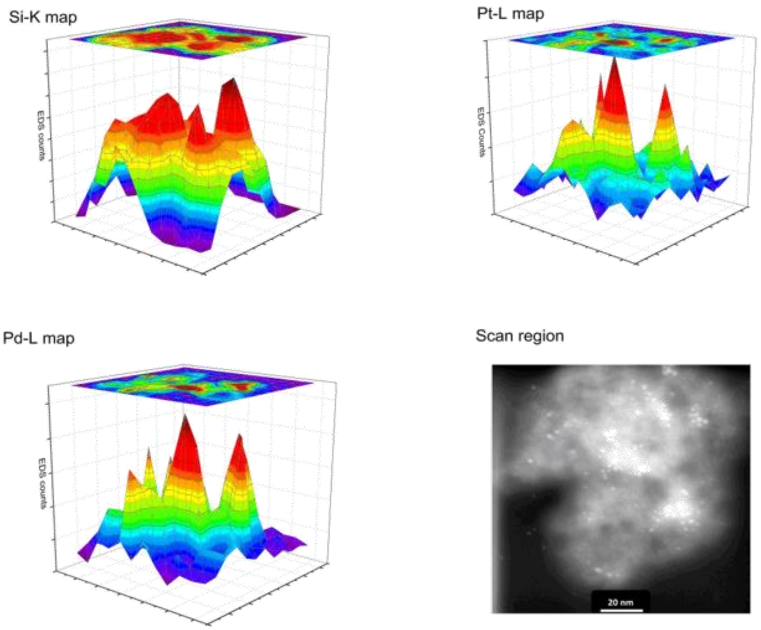

Figure 4.8. TEM-EDS mapping of selective areas of supported Pd nanoparticles after 1 h of reaction. Reaction conditions: (^{t}bpy)Pt(OPh)Cl: 13.2 mmol/L, 20 psi H_2 (~7-11 mmol/L in solution), Pd/SiO_2 (5 wt%, 1.23 x 10^{-6} mol Pd_{surf}), T= 50 °C, THF-d_8, internal standard hexamethyldisilane: 2.33 mmol/L.

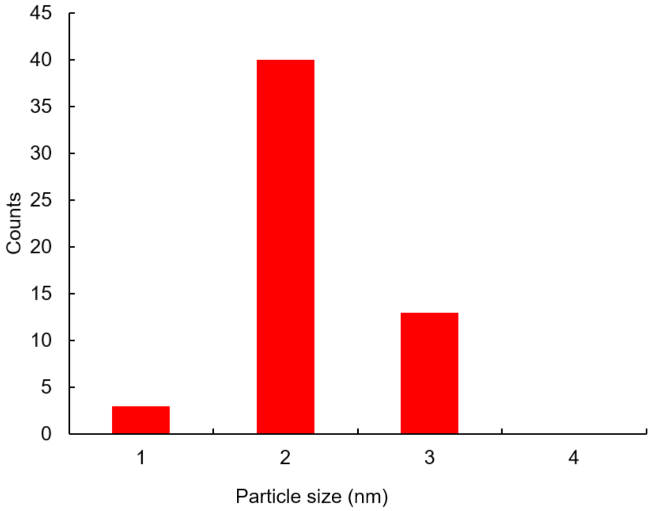

Figure 4.9. The particle size distribution of recovered Pd catalysts (measured through TEM analysis).

The 3.6 wt% Rh/SiO_2 and 1.0 wt% Pt/SiO_2 nanomaterials of similar size (2.2(5) nm) to their Pd congeners were tested to compare their activity for hydrogenolysis of the Pt–OPh bond of complex **1**. Table 4.2 shows a comparison of apparent TOFs for Pd, Rh, and Pt nanoparticles (based on estimated surface atoms). With similar amounts of catalyst loadings, the rate of hydrogenolysis of **1** follows the trend: Pd > Rh > Pt. Relative to Pt, the Pd nanoparticles gave an apparent TOF that was 5.2 times faster than Pt catalyst. The Rh/SiO_2 material gave an apparent TOF value was 1.4 times larger than the apparent TOF using Pt/SiO_2 nanomaterials. This trend is consistent with previously reported results for the liquid phase cyclohexene hydrogenation with noble metal nanocatalysts.[31]

In addition, attempts have been made to test the efficacy of Pd/SiO_2, Rh/SiO_2, and Pt/SiO_2 catalyzed hydrogenation of butanone C=O bonds. For Pd and Rh catalyzed hydrogenation reaction of C=O, a rapid H/D exchange occurred between the butanone molecule and H_2/D_2O intermediates, which complicated the quantification of the hydrogenation rate using ^{1}H NMR spectroscopy. Therefore, the hydrogenation rates mediated by Pd/SiO_2 and Rh/SiO_2 were not able to be quantified. The Pt promoted hydrogenation of C=O in butanone was reported to be 3.6×10^{-3} s^{-1},[32] which is two orders of magnitude faster than the Pt catalyzed hydrogenolysis rate of the Pt−OPh bond of complex **1**.

Table 4.2. TOFs for nanoparticles promoted C=C hydrogenation, C=O hydrogenation, and Pt−OPh hydrogenolysis.

TOFs for	Pd, s^{-1}	Rh, s^{-1}	Pt, s^{-1}
C=C[31]	1.32 −1.72	1.16 − 1.36	0.55−0.66
C=O[32]	N.A.	N.A.	3.6×10^{-3}
Pt−OPh[a]	$2.5(6)\times10^{-4}$	$6.9(4)\times10^{-5}$	$4.9(4)\times10^{-5}$

[a] TOF = (mole of complex **1** reacted)/(mole of surface atoms)/t(s). Reaction conditions: 10 mM complex **1** in 0.5 mL THF−*d*$_8$, ~1.23×10^{-6} mol surface Pd, Pt and Rh atoms, 20 psig hydrogen, 50 °C and 2mM hexamethyldisilane as an internal standard. N.A. = not available (due to a rapid H/D exchange between D_2O/H_2 and butanone).

Surprisingly, although Pt is deposited on the Pd nanoparticles, the observed rates of reaction still appeared to have a first-order dependence on complex **1**. Given that Pt nanoparticles were not as active as Pd nanoparticles for the hydrogenolysis of **1**(*vide supra*), deposition of Pt onto the Pd nanoparticles can potentially poison active Pd sites. Therefore, the rate would be expected to decrease throughout the reaction. Because neither the rate nor the order with respect to **1** changed, it is possible that deposited Pt results in the formation of Pd-Pt bimetallic nanoparticles[33] that are reactive. Alternatively, the rate of Pd catalyzed hydrogenolysis of Pt−OPh bonds is about an order of magnitude faster than Pt promoted hydrogenolysis rate and the loss of 10-15% of active sites on the Pd/SiO_2 might not affect the overall catalytic rate. Another possibility is that in the presence of H_2, Pd atoms migrate to the surface of the nanoparticles despite the deposition of Pt atoms.[33] It is difficult to elucidate the operative pathway for phenol formation in these co-catalytic processes because no technique allows the observation of the interaction between a homogeneous complex and a heterogeneous material. The analysis is made additionally complicated by the short-lived nature of intermediates produced in these reactions. Indeed, no intermediates have been observed in the ^1H NMR experiments.

Two possible mechanisms for M–OR bond hydrogenolysis are shown in Schemes 4.5 and 4.6. In pathway 1, H_2 is activated heterolytically[14, 16, 17, 34] and transferred across the Pt–OPh bond as H^+/H^-[35] in an Eley−Rideal type mechanism without the direct interaction of the Pt complex with the nanoparticle surface (Scheme 4.5). In contrast, pathway 2 involves the initial cleavage of both the H−H and Pt−OPh bonds to generate surface-bound phenoxide and surface-bound hydrogen. Efforts to elucidate the reaction pathway included ex situ detection via spectroscopy (*e.g.*, Raman spectroscopy) of absorbed *OPh and other fragments on the nanoparticle surface that would emerge if the Pt−OPh bond is cleaved during catalysis. Raman Spectrum of Pd nanoparticles after reaction with **1** suggested that a "Pt–OPh" species might be formed on the nanoparticle surface (Figure 4.10). This hypothesis was supported by the observation of a Pt−O vibration[36] (~573 cm^{-1}), a C−O bending absorption (~505 cm^{-1}), and a C−O stretch (~1240 cm^{-1}) in the Raman spectrum. Further evidence for the potential formation of surface bound "Pt–OPh" can be observed when the recovered Pd nanoparticles from reaction with **1** were treated with 20 psi H_2 at 50 °C for 2 h, resulting in the release of free ^{t}bpy as observed by ^{1}H NMR spectroscopy. Using Raman and ^{1}H NMR spectroscopies, we hypothesize that the formation of (^{t}bpy)Pt(OPh) species or intermediates might occur during the catalysis.

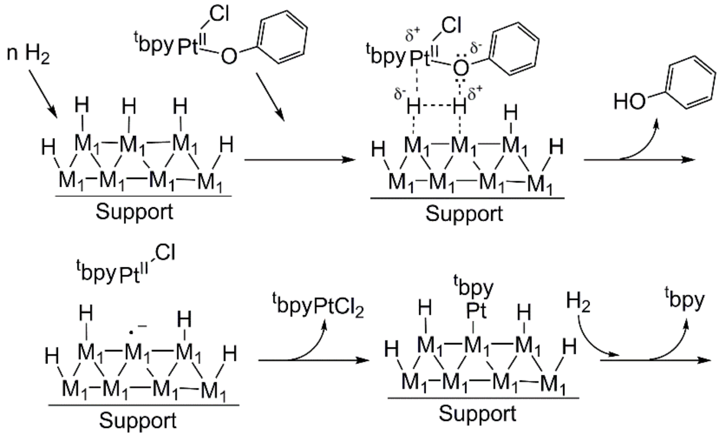

Pathway 1. Partial Polarization of H_2
Eley-Rideal Mechanism

Scheme 4.5. Proposed Eley-Rideal type mechanism: polarization of H_2 for hydrogenolysis of Pt–OPh bond to release PhOH.

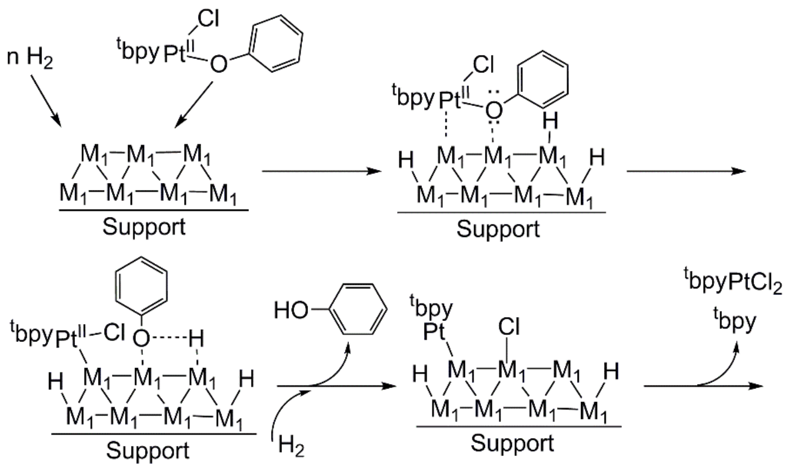

Pathway 2. H_2 Activation and Pt-OPh Cleavage
Langmuir-Hinshelwood Mechanism

Scheme 4.6. Proposed Langmuir-Hinshelwood type mechanism: H_2 activation and Pt-OPh cleavage to release PhOH.

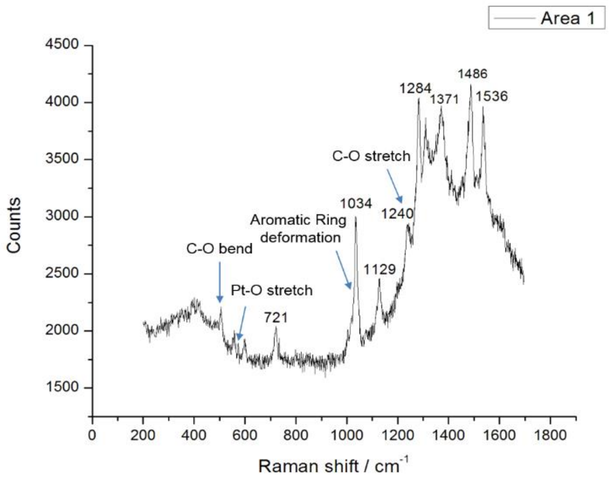

Figure 4.10. Raman spectrum of recovered Pd catalysts after hydrogenolysis of complex 1 for 1h. Reaction conditions: (^{t}bpy)Pt(OPh)Cl: 13.2 mmol/L, 20 psi H_2 (~7-11 mmol/L in solution), Pd/SiO_2 (5 wt%, 1.23 x 10^{-6} mol Pd_{surf}), T= 50 °C, THF-d_8, internal standard hexamethyldisilane: 2.33 mmol/L.

Based on the mechanistic study through ^{1}H NMR and Raman spectroscopies, the overall reaction for Pt–OPh hydrogenolysis can be possibly divided into four steps (Scheme 4.7). First, H_2 is adsorbed on the nanocatalyst surface and it is activated and polarized. When (^{t}bpy)Pt(OPh)Cl reacts, the polarization of the Pd–H bond results in the delivery of a proton to Pt–OPh, which releases PhOH. The reducing equivalent remaining on the catalytic material reduces the $[(^{t}bpy)PtCl]^{+}$ fragment to $(^{t}bpy)PtCl$, which undergoes disproportionation to release $(^{t}bpy)PtCl_2$, free ^{t}bpy, and Pt(s). Another possibility is it might form a $(^{t}bpy)Pt(H)Cl$ intermediate after releasing PhOH. The $(^{t}bpy)Pt(H)Cl$ intermediate might not be stable and could undergo reductive elimination of HCl and $(^{t}bpy)Pt$. HCl can easily react with another $(^{t}bpy)Pt(OPh)Cl$ molecule, forming $(^{t}bpy)PtCl_2$ and PhOH.

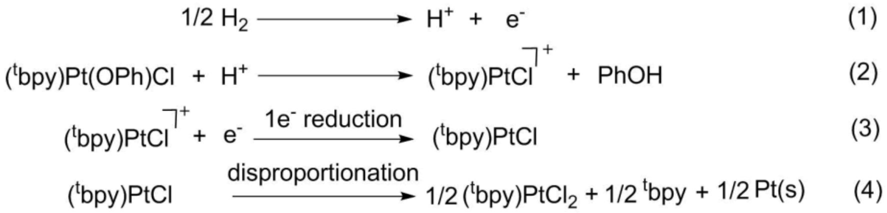

$$\frac{1}{2}H_2 \longrightarrow H^+ + e^- \quad (1)$$

$$(^{t}bpy)Pt(OPh)Cl + H^+ \longrightarrow [(^{t}bpy)PtCl]^+ + PhOH \quad (2)$$

$$[(^{t}bpy)PtCl]^+ + e^- \xrightarrow{1e^-\ \text{reduction}} (^{t}bpy)PtCl \quad (3)$$

$$(^{t}bpy)PtCl \xrightarrow{\text{disproportionation}} 1/2\,(^{t}bpy)PtCl_2 + 1/2\,^{t}bpy + 1/2\,Pt(s) \quad (4)$$

Scheme 4.7. Proposed individual steps for the Eley-Rideal type mechanism.

4.3 Conclusions

Using $(^{t}bpy)Pt(OPh)Cl$ (**1**) as a probe molecule, it has been demonstrated that nanocatalysts promote hydrogenolysis of Pt–OPh bonds to release PhOH. Using ^{1}H NMR spectroscopy, a first-order dependence on Pd/SiO_2 and $(^{t}bpy)Pt(OPh)Cl$ complex has been confirmed. For the noble metal mediated hydrogenolysis of $(^{t}bpy)Pt(OPh)Cl$ complex and C=C bonds, they follow the same trend: Pd > Rh > Pt. From TEM-EDS mapping and ICP-OES measurement of recovered Pd catalysts, 10-15% Pt deposition on Pd/SiO_2 surface was confirmed and quantified. However, the kinetic rate does not change with the deposited of Pt atom or Pt complex on the Pd surface. Both the Eley-Rideal type of mechanism and Langmuir-Hinshelwood type mechanism have been proposed as an explanation of the reaction pathway.

4.4 Experimental Methods

4.4.1 General Methods

The glovebox purity was maintained by periodic nitrogen purges and was monitored by an oxygen analyzer (O_2 <15 ppm for all reactions). THF-d_8 was distilled over sodium/benzophenone and was stored over 4Å molecular sieves. ^{1}H NMR and ^{13}C NMR spectra were acquired using a 600 MHz (^{1}H NMR) and 800 MHz (^{13}C NMR) and referenced to THF-d_8 using residual proton signals or the ^{13}C resonance of the deuterated acetone solvent. Medium-walled high-pressure glass NMR tubes with a PV-ANV Teflon valve (maximum pressure rating 150 psi) were purchased from Wilmad-Lab glass and used for all 20 psi H_2 experiments. Tubes were charged with H_2 using a stainless steel gas pressure line (maximum pressure rating 3000 psi) connected directly to the gas cylinder. (^{t}bpy)$PtCl_2$ and (^{t}bpy)$Pt(OPh)_2$ were synthesized based on literature procedure.[1] Noble metal on silica catalysts were prepared by the ion exchange method.[2] In general, the cation solution of the metal precursor was stirred in a silica gel solution. The surface protons of silica gel exchanged with metal cations forming a precursor, which was subsequently reduced in hydrogen.

4.4.2 Synthesis of (^{t}bpy)Pt(OPh)Cl (1). HCl (138 µl of 1M HCl in ether) was added to 90 mg (0.138 mmol) of (^{t}bpy)$Pt(OPh)_2$ in an acetone (5 mL) and THF (30 mL) reaction mixture in a dry ice bath. The reaction mixture was cooled for half an hour and then was warmed up slowly to room temperature. Once HCl was added, the color of the solution changed from orange to yellow. For the workup, the reaction mixture was condensed to about 1 mL, and excess hexane was added to precipitate a yellow product. The precipitate was washed extensively (~20 mL each time) with hexane and ether (10 mL each time). Pure (^{t}bpy)Pt(OPh)Cl was obtained in ~70% yield. ^{1}H NMR (600 MHz, acetone-*d*$_6$, ppm), δ= 7.14 (d, $^3J_{HH}$ = 9 Hz, 2H, *o*-OPh), 6.92(t, $^3J_{HH}$ = 9 Hz, 2H, *m*-OPh), 6.40(t, $^3J_{HH}$ = 7 Hz, 1H, *p*-OPh), 9.50(d, 1H, 6 Hz, ^{t}bpy), 8.85(d, $^3J_{HH}$ = 6 Hz, 1H, ^{t}bpy), 7.83(dd, $^3J_{HH}$ = 6 Hz, $^4J_{HH}$ =2Hz, 1H, ^{t}bpy), 7.81(dd, $^3J_{HH}$ = 6 Hz, $^4J_{HH}$ =2Hz, 1H, ^{t}bpy), 8.57(d, $^4J_{HH}$ =2Hz, 1H, ^{t}bpy), 8.55(d, $^4J_{HH}$ =2Hz, 1H, ^{t}bpy), 1.47(s, 9H,^{t}Bu), 1.44(s, 9H,^{t}Bu). ^{13}C {^{1}HNMR (200 MHz, acetone-*d*$_6$, ppm), δ= 29.4, (C(***C***H$_3$)$_3$), 29.4, (C(***C***H$_3$)$_3$),35.8 (***C***(CH$_3$)$_3$), 35.9 (***C***(CH$_3$)$_3$), 164.3 (^{t}bpy, p-***C***), 168.6 (^{t}bpy, p-***C***), 124.3 (^{t}bpy, m-***C***), 124.2 (^{t}bpy, m-***C***), 150.1 (^{t}bpy, m-***C***), 120.9 (^{t}bpy, m-***C***), 121(^{t}bpy, m-***C***), 146.6 (^{t}bpy, o-***C***), 156.5 (^{t}bpy, o-***C***), 157.5 (^{t}bpy, o-***C***), 164.4 (phenoxide, O-***C***), 119.4 (phenoxide, o-***C***), 127.9 (phenoxide, m-***C***), 114.3 (phenoxide, p-***C***). **Anal. Calcd.** for $C_{24}H_{29}PtN_2ClO$: C, 46.69; H, 4.94; N, 4.73 **Found**: C, 48.72; H, 4.92; N, 4.76. The ^{1}H NMR and ^{13}C NMR spectra are shown below. Single crystals suitable for X-ray diffraction analysis were obtained from a mixture of acetone solution layered with pentane at -1 °C.

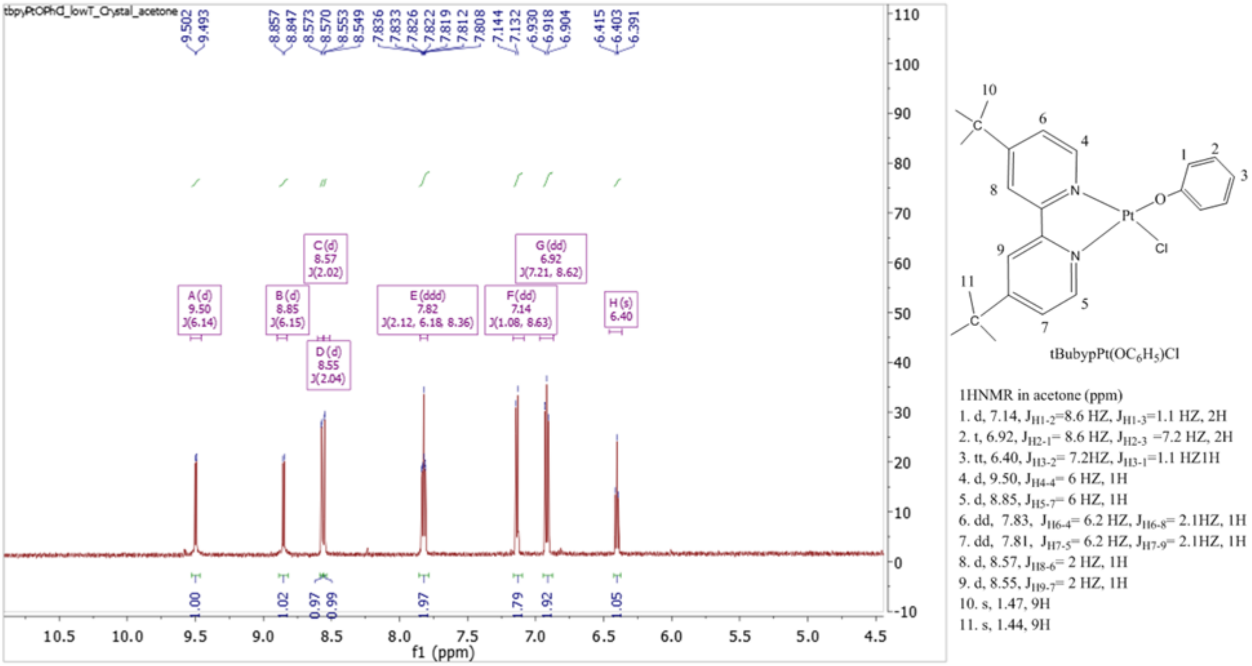

1HNMR in acetone (ppm)
1. d, 7.14, $J_{H1\text{-}2}$=8.6 HZ, $J_{H1\text{-}3}$=1.1 HZ, 2H
2. t, 6.92, $J_{H2\text{-}1}$= 8.6 HZ, $J_{H2\text{-}3}$ =7.2 HZ, 2H
3. tt, 6.40, $J_{H3\text{-}2}$= 7.2HZ, $J_{H3\text{-}1}$=1.1 HZ1H
4. d, 9.50, $J_{H4\text{-}4}$= 6 HZ, 1H
5. d, 8.85, $J_{H5\text{-}7}$= 6 HZ, 1H
6. dd, 7.83, $J_{H6\text{-}4}$= 6.2 HZ, $J_{H6\text{-}8}$= 2.1HZ, 1H
7. dd, 7.81, $J_{H7\text{-}5}$= 6.2 HZ, $J_{H7\text{-}9}$= 2.1HZ, 1H
8. d, 8.57, $J_{H8\text{-}6}$= 2 HZ, 1H
9. d, 8.55, $J_{H9\text{-}7}$= 2 HZ, 1H
10. s, 1.47, 9H
11. s, 1.44, 9H

Figure 4.11. Aromatic part of ^{1}H NMR spectrum of (^{t}bpy)Pt(OPh)Cl in acetone-d_6.

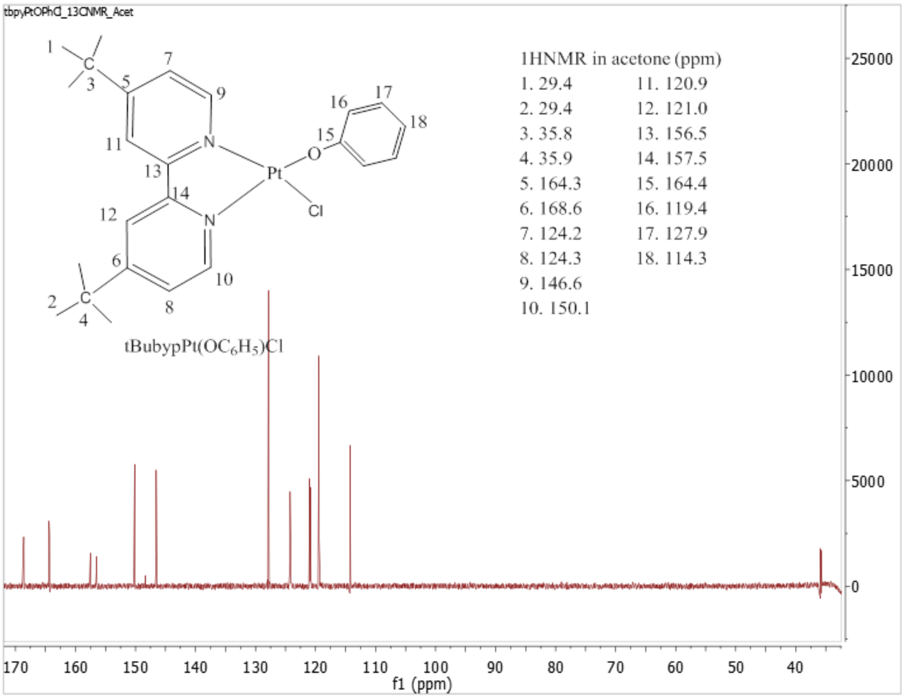

1HNMR in acetone (ppm)
1. 29.4
2. 29.4
3. 35.8
4. 35.9
5. 164.3
6. 168.6
7. 124.2
8. 124.3
9. 146.6
10. 150.1
11. 120.9
12. 121.0
13. 156.5
14. 157.5
15. 164.4
16. 119.4
17. 127.9
18. 114.3

Figure 4.12. ^{13}C NMR spectrum of (^{t}bpy)Pt(OPh)Cl in acetone-d_6.

4.4.3 Synthesis of silica-supported noble metal catalysts. 3.6 wt% silica-supported Rh nanoparticle catalysts (Rh/SiO_2) were prepared via an ion exchange method[29, 37] of the Rh precursor using Davisil 636 silica (Sigma-Aldrich) as support. $RhCl_3•3H_2O$ precursor (0.250 g, 99%, Sigma-Aldrich) was dissolved in a solution of aqueous ammonia (14.8 M, 28%-30% of NH_3 in water, ACS plus, Fisher Scientific,), which was prepared by dissolving 5.5 mL ammonium hydroxide in 282 mL distilled deionized water. The $RhCl_3$ solution was added dropwise over 10 min to 4.75 g of acid-washed Davisil 636 silica in 114 mL of distilled deionized water at 70 °C. The mixture was stirred for 60 min at 70 °C and then cooled to room temperature. The mixture was washed with water and vacuum dried overnight. After calcination in flowing air (medical grade, GTS-Welco) at 400 °C for 2 h, the sample was reduced in flowing dihydrogen (99.999%, GTS-Welco) at 250 °C for 2 h. After reduction, the system was evacuated and cooled to 30 °C for analysis. At 30 °C, the stoichiometric ratio of H to surface Rh is assumed to be 1:1. Using dihydrogen chemisorption on a Micromeritics ASAP 2020 adsorption system,[29] the number of available metal sites was determined by extrapolating the linear portion of the isotherm to zero pressure with the assumption of no dihydrogen uptake on the support. Similarly, 5 wt% Pd/SiO_2 and 1 wt% Pt/SiO_2 were synthesized, characterized, and reported in the literature. [29, 30]

4.4.4 Kinetic measurements. The reaction of (^{t}bpy)Pt(OPh)Cl with H_2 in the presence of nanoparticles (Pd, Rh, and Pt) was monitored in ^{1}H NMR spectroscopy (with a 10 s relaxation delay). Note: to ensure reproducibility, each kinetic experiment was performed in triplicate. A representative procedure is given below. A medium-walled glass high-pressure NMR tube with a Teflon valve was charged with 0.5 mL of THF-d_8,

(^{t}bpy)Pt(OPh)Cl (0.006 mmol, 0.012 M), 3 mg Pd on SiO_2 (5% wt. Pd loading, 1.23 x 10^{-6} mol Pd_{surf}), and hexamethyldisilane (0.002 M, as internal standard). An initial ^1H NMR spectrum was acquired. Then, the tube was charged with H_2 (~ 20 psi). The reaction mixture was monitored by ^1H NMR spectroscopy every hour until about 90% conversion to free PhOH, (^{t}bpy)$PtCl_2$ and ^{t}bpy were observed. The rate of the reaction was determined by monitoring the disappearance of ^{t}bpyPt(OPh)Cl using 6.31 ppm for reference.

4.5 References

1. Chinchen, G. C.; Denny, P. J.; Jennings, J. R.; Spencer, M. S.; Waugh, K. C. Synthesis of Methanol: Part 1. Catalysts and Kinetics. *Applied Catalysis* **1988,** *36*, 1-65.
2. de Klerk, A. Fischer–Tropsch Process. In Kirk-Othmer Encyclopedia of Chemical Technology, (Ed.). **2013**.
3. Latimer, A. A.; Kakekhani, A.; Kulkarni, A. R.; Nørskov, J. K. Direct Methane to Methanol: The Selectivity–Conversion Limit and Design Strategies. *ACS Catal.* **2018,** *8*, 6894-6907.
4. Munz, D.; Strassner, T. Alkane C–H Functionalization and Oxidation with Molecular Oxygen. *Inorg. Chem.* **2015,** *54*, 5043-5052.
5. Periana, R. A.; Taube, D. J.; Gamble, S.; Taube, H.; Satoh, T.; Fujii, H. Platinum Catalysts for the High-Yield Oxidation of Methane to a Methanol Derivative. *Science* **1998,** *280*, 560.

6. Muehlhofer, M.; Strassner, T.; Herrmann, W. A. New Catalyst Systems for the Catalytic Conversion of Methane into Methanol. *Angew. Chem. Int. Ed.* **2002,** *41*, 1745-1747.

7. Conley, B. L.; Tenn, W. J.; Young, K. J. H.; Ganesh, S. K.; Meier, S. K.; Ziatdinov, V. R.; Mironov, O.; Oxgaard, J.; Gonzales, J.; Goddard, W. A.; Periana, R. A. Design and study of homogeneous catalysts for the selective, low temperature oxidation of hydrocarbons. *J. Mol. Catal. A: Chem.* **2006,** *251*, 8-23.

8. Narsimhan, K.; Iyoki, K.; Dinh, K.; Román-Leshkov, Y. Catalytic Oxidation of Methane into Methanol over Copper-Exchanged Zeolites with Oxygen at Low Temperature. *ACS Cent. Sci.* **2016,** *2*, 424-429.

9. Groothaert, M. H.; Smeets, P. J.; Sels, B. F.; Jacobs, P. A.; Schoonheydt, R. A. Selective Oxidation of Methane by the Bis(μ-oxo)dicopper Core Stabilized on ZSM-5 and Mordenite Zeolites. *J. Am. Chem. Soc.* **2005,** *127*, 1394-1395.

10. Grundner, S.; Markovits, M. A. C.; Li, G.; Tromp, M.; Pidko, E. A.; Hensen, E. J. M.; Jentys, A.; Sanchez-Sanchez, M.; Lercher, J. A. Single-site trinuclear copper oxygen clusters in mordenite for selective conversion of methane to methanol. *Nat. Commun.* **2015,** *6*, 7546.

11. Brezicki, G.; Kammert, J. D.; Gunnoe, T. B.; Paolucci, C.; Davis, R. J. Insights into the Speciation of Cu in the Cu-H-Mordenite Catalyst for the Oxidation of Methane to Methanol. *ACS Catal.* **2019,** *9*, 5308-5319.

12. Bercaw, J. E.; Hazari, N.; Labinger, J. A. Activation of a C−H Bond in Indene by [(COD)Rh(μ2-OH)]2. *Organometallics* **2009,** *28*, 5489-5492.

13. Tenn, W. J.; Young, K. J. H.; Bhalla, G.; Oxgaard, J.; Goddard, W. A.; Periana, R. A. CH Activation with an O-Donor Iridium−Methoxo Complex. *J. Am. Chem. Soc.* **2005,** *127*, 14172-14173.

14. Kloek, S. M.; Heinekey, D. M.; Goldberg, K. I. C□H Bond Activation by Rhodium(I) Hydroxide and Phenoxide Complexes. *Angew. Chem. Int. Ed.* **2007,** *46*, 4736-4738.

15. Feng, Y.; Lail, M.; Barakat, K. A.; Cundari, T. R.; Gunnoe, T. B.; Petersen, J. L. Evidence for the Net Addition of Arene C−H Bonds across a Ru(II)−Hydroxide Bond. *J. Am. Chem. Soc.* **2005,** *127*, 14174-14175.

16. Conley, B. L.; Ganesh, S. K.; Gonzales, J. M.; Tenn, W. J.; Young, K. J. H.; Oxgaard, J.; Goddard, W. A.; Periana, R. A. Facile Functionalization of a Metal Carbon Bond by O-Atom Transfer. *J. Am. Chem. Soc.* **2006,** *128*, 9018-9019.

17. Pouy, M. J.; Milczek, E. M.; Figg, T. M.; Otten, B. M.; Prince, B. M.; Gunnoe, T. B.; Cundari, T. R.; Groves, J. T. Flavin-Catalyzed Insertion of Oxygen into Rhenium–Methyl Bonds. *J. Am. Chem. Soc.* **2012,** *134*, 12920-12923.

18. Gonzales, J. M.; Distasio, R.; Periana, R. A.; Goddard, W. A.; Oxgaard, J. Methylrhenium Trioxide Revisited: Mechanisms for Nonredox Oxygen Insertion in an M−CH3 Bond. *J. Am. Chem. Soc.* **2007,** *129*, 15794-15804.

19. Webb, J. R.; Pierpont, A. W.; Munro-Leighton, C.; Gunnoe, T. B.; Cundari, T. R.; Boyle, P. D. Net Hydrogenation of Pt−NHPh Bond Is Catalyzed by Elemental Pt. *J. Am. Chem. Soc.* **2010,** *132*, 4520-4521.

20. Lohr, T. L.; Piers, W. E.; Parvez, M. Arene C–H bond activation across Pt(ii)–OH bonds: catalyzed vs. uncatalyzed pathways. *Chem. Sci.* **2013,** *4*, 770-775.

21. Fulmer, G. R.; Muller, R. P.; Kemp, R. A.; Goldberg, K. I. Hydrogenolysis of Palladium(II) Hydroxide and Methoxide Pincer Complexes. *J. Am. Chem. Soc.* **2009,** *131*, 1346-1347.

22. Fulmer, G. R.; Herndon, A. N.; Kaminsky, W.; Kemp, R. A.; Goldberg, K. I. Hydrogenolysis of Palladium(II) Hydroxide, Phenoxide, and Alkoxide Complexes. *J. Am. Chem. Soc.* **2011,** *133*, 17713-17726.

23. Edwards, P.; Wilkinson, G. Trioxorhenium(VII) alkoxides, di-isopropylamides, carboxylates and related compounds. *Journal of the Chemical Society, Dalton Transactions* **1984**, 2695-2702.

24. Perrotin, P.; El-Zoghbi, I.; Oguadinma, P. O.; Schaper, F. Replacing Chloride by Alkoxide: Cp2Zr(H)OR, Searching for Alternatives to Schwartz's Reagent. *Organometallics* **2009,** *28*, 4912-4922.

25. Belkova, N. V.; Revin, P. O.; Epstein, L. M.; Vorontsov, E. V.; Bakhmutov, V. I.; Shubina, E. S.; Collange, E.; Poli, R. Kinetics and Mechanism of the Proton Transfer to Cp*Fe(dppe)H: Absence of a Direct Protonation at the Metal Site. *J. Am. Chem. Soc.* **2003,** *125*, 11106-11115.

26. Belkova, N. V.; Dub, P. A.; Baya, M.; Houghton, J. Kinetics and thermodynamics of proton transfer to Cp∗Ru(dppe)H: Via dihydrogen bonding and (η2-H2)-complex to the dihydride. *Inorganica Chimica Acta* **2007,** *360*, 149-162.

27. Bryndza, H. E.; Calabrese, J. C.; Marsi, M.; Roe, D. C.; Tam, W.; Bercaw, J. E. .beta.-Hydride elimination from methoxo vs. ethyl ligands: thermolysis of (DPPE)Pt(OCH3)2, (DPPE)Pt(CH2CH3)(OCH3) and (DPPE)Pt(CH2CH3)2. *J. Am. Chem. Soc.* **1986,** *108*, 4805-4813.

28. Webb, J. R.; Munro-Leighton, C.; Pierpont, A. W.; Gurkin, J. T.; Gunnoe, T. B.; Cundari, T. R.; Sabat, M.; Petersen, J. L.; Boyle, P. D. Pt(II) and Pt(IV) Amido, Aryloxide, and Hydrocarbyl Complexes: Synthesis, Characterization, and Reaction with Dihydrogen and Substrates that Possess C−H Bonds. *Inorg. Chem.* **2011,** *50*, 4195-4211.

29. Kaylor, N.; Xie, J.; Kim, Y.-S.; Pham, H. N.; Datye, A. K.; Lee, Y.-K.; Davis, R. J. Vapor phase deoxygenation of heptanoic acid over silica-supported palladium and palladium-tin catalysts. *J. Catal.* **2016,** *344*, 202-212.

30. Xie, J.; Huang, B.; Yin, K.; Pham, H. N.; Unocic, R. R.; Datye, A. K.; Davis, R. J. Influence of Dioxygen on the Promotional Effect of Bi during Pt-Catalyzed Oxidation of 1,6-Hexanediol. *ACS Catal.* **2016,** *6*, 4206-4217.

31. Boudart, M.; Sajkowski, D. J. Catalytic hydrogenation of cyclohexene: liquid-phase reaction on rhodium. *Faraday Discussions* **1991,** *92*, 57-67.

32. Falcone, D. D.; Hack, J. H.; Davis, R. J. Aqueous-Phase Hydrogenation of Saturated and Unsaturated Ketones and Aldehydes over Supported Platinum–Rhenium Catalysts. *ChemCatChem* **2016,** *8*, 1074-1083.

33. Tao, F.; Grass, M. E.; Zhang, Y.; Butcher, D. R.; Renzas, J. R.; Liu, Z.; Chung, J. Y.; Mun, B. S.; Salmeron, M.; Somorjai, G. A. Reaction-Driven Restructuring of Rh-Pd and Pt-Pd Core-Shell Nanoparticles. *Science* **2008,** *322*, 932.

34. Chen, G.; Xu, C.; Huang, X.; Ye, J.; Gu, L.; Li, G.; Tang, Z.; Wu, B.; Yang, H.; Zhao, Z.; Zhou, Z.; Fu, G.; Zheng, N. Interfacial electronic effects control the reaction selectivity of platinum catalysts. *Nature Materials* **2016,** *15*, 564-569.

35. Findlater, M.; Bernskoetter, W. H.; Brookhart, M. Proton-Catalyzed Hydrogenation of a d8 Ir(I) Complex Yields a trans Ir(III) Dihydride. *J. Am. Chem. Soc.* **2010,** *132*, 4534-4535.

36. Wang, Y.-Y.; Chen, D.-J.; Tong, Y. J. Mechanistic Insight into Sulfide-Enhanced Oxygen Reduction Reaction Activity and Stability of Commercial Pt Black: An in Situ Raman Spectroscopic Study. *ACS Catal.* **2016,** *6*, 5000-5004.

37. Lam, Y. L.; Boudart, M. Preparation of small Au-Pd particles on silica. *J. Catal.* **1977,** *50*, 530-540.

5 Summary and Future Directions

5.1 Summary of Au-mediated reductive coupling reactions

As discussed in Chapter 2, Au-mediated C-C coupling processes have emerged as strategies for organic synthesis. Despite reports on the synthetic applicability of Au catalysts, mechanistic questions remain. Previous studies have placed formal Au(I)/Au(III) redox couples at the center of several Au mediated C–C coupling reactions. In Chapter 2, we demonstrated that phosphine ligated Au(I) complexes could mediate homo- and hetero- C−C coupling reactions from -40 °C to 90 °C, and Au(I) cations play a critical role for the C–C coupling reactions. We have demonstrated that gem-digold methyl complexes of the type $[Au_2(\mu\text{-}CH_3)(PR_2Ar')_2][NTf_2]$ promotehomocoupling of the bridging methyl fragments to produce ethane at a higher rate than parent neutral species $Au(CH_3)(PR_2Ar')$. We have determined that this approach permits the heterocoupling of the bridging methyl group with ethyl and phenyl fragments. The stability of compounds of the type $[Au_2(\mu\text{-}CH_3)(PR_2Ar')_2][NTf_2]$ towards reductive homocoupling is dependent on the steric bulk of the phosphine ligand. The compound based on PPh_3 readily liberates ethane at -40 ºC, and those bearing terphenyl phosphines (PMe_2Ar') exhibit enhanced stability, which is further increased by the use of the more hindered XPhos and tBuXPhos, the latter being unable to mediate C–C coupling even at 90 °C. Our kinetic studies revealed a second-order dependence on gem-digold methyl complexes of the type $[Au_2(\mu\text{-}CH_3)(PR_2Ar')_2][NTf_2]$ for ethane evolution, whereas a distinctive change towards a first-order dependence was ascertained in the presence of excess BPh_3. Based on our experimental studies combined with DFT computational methods, we proposed a mechanism that involves rapid dissociation of a molecule of $[Au_2(\mu\text{-}CH_3)(PMe_2Ar')_2][NTf_2]$

towards Au(PMe$_2$Ar')(NTf$_2$) and Au(CH$_3$)(PMe$_2$Ar'). While Au(PMe$_2$Ar')(NTf$_2$) mediates phosphine dissociation from a second molecule of [Au$_2$(μ-CH$_3$)(PMe$_2$Ar')$_2$][NTf$_2$] by a trimetallic intermediate, Au(CH$_3$)(PMe$_2$Ar')reacts with the resulting highly reactive and masked 'AuMe' fragment to effect the C–C coupling event, most likely by a multinuclear gold species. These studies highlight the relevance of multimetallic mechanisms in mediating uncommon transformations while also boosting the rate at which the C–C coupling transformation occurs. Since Au-based nanoclusters and organometallic complexes have been proven to be active for methane C–H activation and functionalization, an Au-based catalytic system for the oxidative methane coupling reaction would be of great scientific interest to pursue next.

5.2 Summary of supported Rh mediated styrene and linear alkenyl arenes synthesis

In Chapter 3, supported Rh nanoparticles on silica (3.6 wt% Rh/SiO$_2$) and nitrogen-doped carbon (1 wt% Rh/NC-HCl and 1.5 wt% Rh/NC-IWI) were synthesized and characterized by transmission electron microscopy (TEM), X-ray photoelectron spectroscopy (XPS), and inductively coupled plasma optical emission spectrometry (ICP-OES). The catalytic performances for styrene formation using supported Rh nanoparticles and molecular Rh salt [Rh(μ-OAc)(η^2-C$_2$H$_4$)$_2$]$_2$ were tested and compared. In this project, we have demonstrated that leaching of 34% of the Rh species from the Rh/SiO$_2$ catalyst during styrene synthesis is likely due to the oxidation of reduced Rh upon reaction with Cu(II) salt. The leached and soluble Rh is likely the active catalyst for arene alkenylation. Although our studies indicate that the leaching of Rh forms the soluble and active catalyst, the nitrogen-doped carbon support facilitates catalyst recycling. Compared with the

Rh/SiO_2 catalyst, nitrogen-doped carbon supported Rh catalysts undergoes a possible dissolution and re-adsorption process.

When $Cu(OAc)_2$ oxidants and molecular Rh precursors $[Rh(\mu\text{-}OAc)(\eta^2\text{-}C_2H_4)_2]_2$ are used for the direct styrene synthesis, the observed induction period is likely due to the decomposition of molecular $[Rh(\mu\text{-}OAc)(\eta^2\text{-}C_2H_4)_2]_2$ to insoluble Rh species followed by dissolution to an active and soluble Rh catalyst. We found that in the absence of $Cu(OAc)_2$ oxidants, $[Rh(\mu\text{-}OAc)(\eta^2\text{-}C_2H_4)_2]_2$ undergoes thermal decomposition to form Rh(0) species as evidenced by ^1H NMR spectroscopy, TEM/EDS, and XPS analysis.[1] ICP-OES analysis and reactivity comparison experiments indicated that the generation of catalytically inactive and insoluble Rh from $[Rh(\mu\text{-}OAc)(\eta^2\text{-}C_2H_4)_2]_2$ occurred in the early stages of catalysis when commercial $Cu(OAc)_2$ is used as the oxidant. But, TEM analysis of the insoluble Rh species showed no evidence of the existence of Rh nanoparticle species, and XPS studies indicated that the formed insoluble Rh species is in a higher oxidation state than Rh(0). Yet, when $Cu(OAc)_2$ is omitted or silica is added, evidence for the formation of Rh nanoparticles has been obtained. We hypothesize that the untreated $Cu(OAc)_2$ serves to capture the reduced Rh, as either single atom or small clusters (which cannot be observed with the current data), and this results in the insoluble Rh in a higher oxidation state than Rh(0). With continued heating, the $Cu(OAc)_2$ trapped Rh can leach back into solution to catalyze arene alkenylation.

5.3 Summary of hydrogenolysis study

In Chapter 4, using hydrogenolysis of a (^{t}bpy)Pt(OPh)Cl complex as a model reaction, we have identified the relative reactivity rate of heterogeneous nanoparticle catalyzed H_2 activation and the hydrogenolysis reaction of (^{t}bpy)Pt(OPh)Cl follows the trend: Pd > Rh > Pt. Compared with the hydrogenolysis of a (^{t}bpy)Pt(OPh)Cl complex in the absence of nanocatalysts, silica-supported Pd, Rh, and Pt catalysts accelerate the hydrogenolysis rate of Pt–OPh bonds to release PhOH. Using ^{1}H NMR spectroscopy, a first-order dependence on Pd/SiO_2 and (^{t}bpy)Pt(OPh)Cl complex has been confirmed. Through TEM-EDS mapping and ICP-OES measurements of recovered Pd catalysts (after 1h of hydrogenolysis of (^{t}bpy)Pt(OPh)Cl, 10-15% Pt deposition on the Pd/SiO_2 surface was quantified. To demonstrate the proof-of-concept tandem catalysis strategy, incorporating C−H bond activation into co-catalytic processes of light alkane (*i.e.,* methane and ethane) functionalization needs to be further developed.

5.4 Future direction for oxidative arene alkenylation reactions

Many industrially-relevant chemical transformations occur between a solid catalyst and liquid reactants, and the spectroscopic techniques to identify working catalysts intermediates at the solid-liquid interface is limited. Various *in situ*/operando spectroscopic methods, such as infrared spectroscopy, Raman spectroscopy, X-ray absorption spectroscopy (XAS), and X-ray photoelectron spectroscopy (XPS), have been used to elucidate catalytic species.[2] Although significant advancement has been reported for various Rh mediated C–C coupling reactions, mechanistic details of the active Rh catalyst mediated arene alkylation and alkenylation are still under consideration. In various reported Rh(I) mediated oxidative arene alkenylations, the oxidation state and active Rh species under catalytic conditions remained unidentified. Furthermore, the catalytic cycle and the identity of the active catalysts are not fully defined.[1, 3-5]

Yu and coworkers demonstrated Rh(II)-catalyzed oxidative alkenylation of arenes with high selectivity towards monoalkenylated products at *meta/para* positions (Scheme 5.1).[11] The mechanistic details for Rh(II) catalyzed coupling reaction is undetermined.

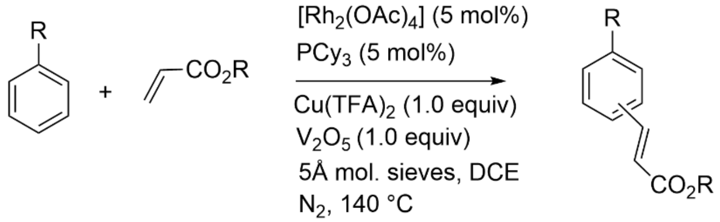

Scheme 5.1. Observed Rh(II)-catalyzed oxidative alkenylation of arenes, R = alkyl or electron-donating group or electron-withdrawing group, DCE=1,2-dichloroethane.[11]

As reported in various Pd(II) based coupling reaction studies, the dynamics of Pd(II) catalyst transformation and deactivation under catalytic conditions can be captured using an *in situ* XAS study.[12, 13] For example, an operando XAS reactor cell combined with a powder X-ray diffraction (PXRD) has been used to detect mechanistic features of a Pd@MOFs catalyzed Heck C–C coupling reaction.[14] Through operando PXRD and XAS measurements, it is proposed that the mononuclear Pd(II) complex is the dominant active catalysts at the beginning of the reaction, and it gradually transforms into Pd nanoclusters with 13-20 Pd atoms in a later catalytic cycle, which is further poisoned by the coordinated Cl^- ions. Therefore, an *in situ* XAS study of Rh catalyzed arene alkenylations with a focus on the catalyst's oxidation states, coordination environments, catalyst transformation and deactivation under catalytic conditions is scientifically significant and meaningful. A deep understanding of the active Rh catalysts will enable researchers to design more-efficient catalysts and tune reaction conditions to improve the longevity and performance of catalysts.

Although leaching of Rh from supported catalysts including Rh/SiO_2 and Rh/NC is inevitable (as discussed in detail in Chapter 3), using single-atom Rh catalysts such as Rh-NaY-zeolite could potentially provide a new strategy to heterogenize Rh catalysts. It has been demonstrated in the literature that supported Pd(II)/Cu(II)-NaY zeolite catalysts can catalyze Wacker oxidation of ethylene in a gas phase reaction and an efficient electron-transfer between Pd(II) and Cu(II) solid interface is possible. Therefore, it would be interesting to synthesize Rh-NaY zeolite catalysts (Rh(I) or Rh(III)/Cu(II)-NaY) and study their reactivity towards oxidative arenes alkenylation and alkenylation in both the solution-phase and gas phase. This thrust could potentially offer the following innovations: 1) take advantage of the shape selectivity of zeolite support, 2) replace carboxylate group ions with an anion in a zeolite (Z^-) to anchor molecular or single-atom Rh catalyst to a solid support, and 3) utilize redox chemistry and electron-transfer chemistry at the solid interface of Rh and Cu. In fact, our preliminary study, single-atom 1 wt% Rh-NaY-H_2 zeolite and 1 wt% Rh-NaY-air zeolite was synthesized[15, 16] and characterized by ICP-OES, carbon monoxide-diffuse reflectance infrared Fourier transform spectroscopy (CO-DRIFT) and XPS (Figure 5.1 and 5.2). The Rh-CO bonds at 2042 cm^{-1} and 2108 cm^{-1} were attributed to the symmetric and asymmetric CO stretching bands of a $Rh^I(CO)_2$ species in the Rh-NaY-Zeolite-H_2.[17-19] XPS characterizations of Rh-NaY-H_2 and Rh-Na-Y-air showed binding energy at 307.5 eV and 308.2 eV, respectively. The next step is to test their efficacy for oxidative alkenylation reactions. Instead of using zeolite support, an alternative strategy is to explore carbon supports such as carbon nitride,[20-22] graphene,[23] or graphene oxides,[24] which have been proven to be effective for Pd-catalyzed C–C coupling reactions.

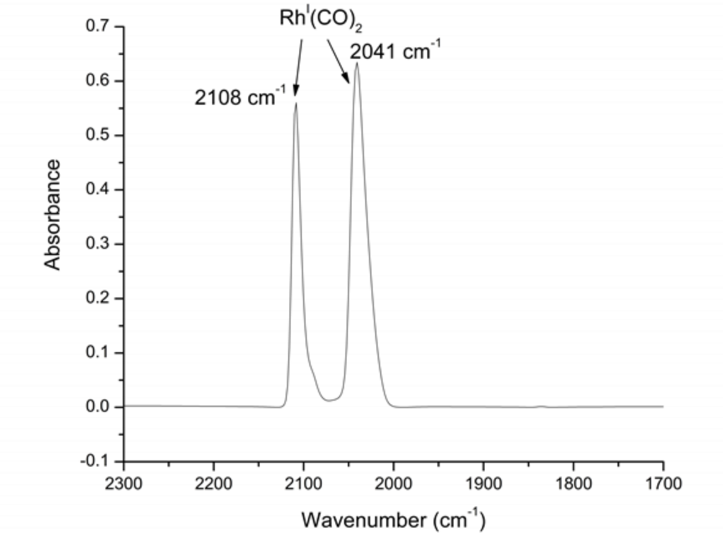

Figure 5.1. Room temperature CO-DRIFTs spectrum of synthesized Rh-NaY-H_2.

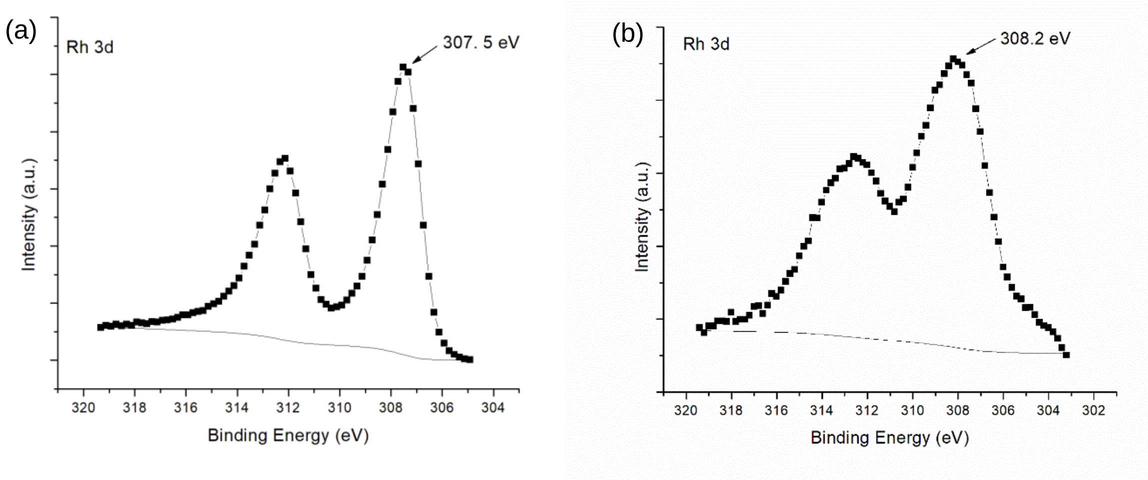

Figure 5.2. Rh 3d XPS peak of 1 wt% Rh-NaY-R-H_2 (a) and 1 wt% Rh-NaY-Air (b).

Furthermore, using Au-based catalysts for arene alkylation or alkenylation might be of great interest. Au(I) complexes are versatile for halogenation or homocoupling reactions of phenyl vinyl Au(I) compounds (Scheme 5.2). Designing a ligated gold organometallic catalyst precursor for oxidative arene alkylation or alkenylation might open a new door.

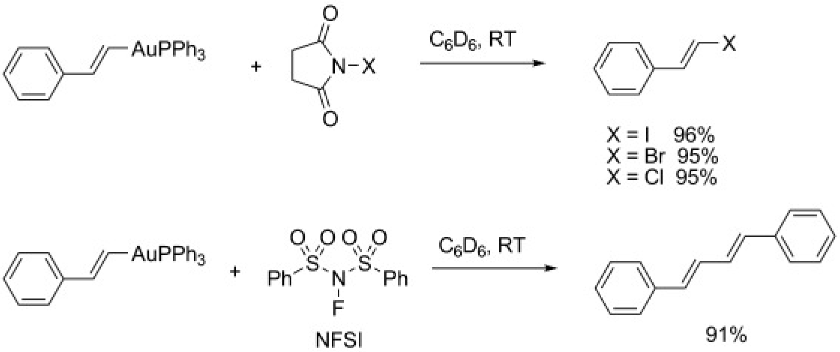

Scheme 5.2. Halogenation and homocoupling of organogold(I) complexes.[25]

Lastly, instead of targeting scientific advancement and innovation towards commodity chemicals synthesis (*e.g.*, styrene), pivoting Rh chemistry towards the synthesis of high-value and low-volume products including active pharmaceutic ingredients (API),[26-28] industrial chemicals[29, 30] (*i.e.,* lubricants and diesel fuels) or fine chemicals[31] is also attractive. As substantial waste is generated during API manufacturing, it is of great interest to develop cost-effective and sustainable routes for chemical and pharmaceutical syntheses. Compared with traditional acid-[32] or zeolite-based alkylation reactions, Rh catalyzed reactions have demonstrated new features for C–C coupling products that are complementary to the existing products. Since using a robotic platform combined with a predictive algorithm has proven to accelerate the innovation of organic compound synthesis and process development,[33, 34] it might be interesting to use machine learning-based algorithms to design Rh-catalyzed oxidative alkenylation reactions for certain pharmaceutical compounds.[35] One possible example is to explore and extend asymmetric catalysis using efficient Rh based catalysts for the synthesis of linear ortho-alkylation products.[36]

5.5 References

1. Zhu, W.; Luo, Z.; Chen, J.; Liu, C.; Yang, L.; Dickie, D. A.; Liu, N.; Zhang, S.; Davis, R. J.; Gunnoe, T. B. Mechanistic Studies of Single-Step Styrene Production Catalyzed by Rh Complexes with Diimine Ligands: An Evaluation of the Role of Ligands and Induction Period. *ACS Catal.* **2019,** *9*, 7457-7475.

2. Negahdar, L.; Parlett, C. M. A.; Isaacs, M. A.; Beale, A. M.; Wilson, K.; Lee, A. F. Shining light on the solid–liquid interface: in situ/operando monitoring of surface catalysis. *Catal. Sci. Technol.* **2020,** *10*, 5362-5385.

3. Vaughan, B. A.; Webster-Gardiner, M. S.; Cundari, T. R.; Gunnoe, T. B. A rhodium catalyst for single-step styrene production from benzene and ethylene. *Science* **2015,** *348*, 421.

4. Vaughan, B. A.; Khani, S. K.; Gary, J. B.; Kammert, J. D.; Webster-Gardiner, M. S.; McKeown, B. A.; Davis, R. J.; Cundari, T. R.; Gunnoe, T. B. Mechanistic Studies of Single-Step Styrene Production Using a Rhodium(I) Catalyst. *J. Am. Chem. Soc.* **2017,** *139*, 1485-1498.

5. Zhu, W.; Gunnoe, T. B. Advances in Rhodium-Catalyzed Oxidative Arene Alkenylation. *Acc. Chem. Res.* **2020,** *53*, 920-936.

6. Ghosh, K.; Mihara, G.; Nishii, Y.; Miura, M. Nondirected C-H Alkenylation of Arenes with Alkenes under Rhodium Catalysis. *Chem. Lett.* **2018,** *48*, 148-151.

7. Pham, M. V.; Cramer, N. Aromatic Homologation by Non-Chelate-Assisted RhIII-Catalyzed C□H Functionalization of Arenes with Alkynes. *Angew. Chem. Int. Ed.* **2014,** *53*, 3484-3487.

8. Matsumoto, T.; Periana, R. A.; Taube, D. J.; Yoshida, H. Direct Synthesis of Styrene by Rhodium-Catalyzed Oxidative Arylation of Ethylene with Benzene. *J. Catal.* **2002,** *206*, 272-280.

9. Guo, S.; Pan, R.; Guan, Z.; Li, P.; Cai, L.; Chen, S.; Lin, A.; Yao, H. Synthesis of Indole-Fused Polycyclics via Rhodium-Catalyzed Undirected C–H Activation/Alkene Insertion. *Organic Letters* **2019,** *21*, 6320-6324.

10. Sun, J.; Wang, K.; Wang, P.; Zheng, G.; Li, X. Rhodium(III)-Catalyzed Oxidative Allylic C–H Indolylation via Nucleophilic Cyclization. *Organic Letters* **2019,** *21*, 4662-4666.

11. Vora, H. U.; Silvestri, A. P.; Engelin, C. J.; Yu, J.-Q. Rhodium(II)-Catalyzed Nondirected Oxidative Alkenylation of Arenes: Arene Loading at One Equivalent. *Angew. Chem. Int. Ed.* **2014,** *53*, 2683-2686.

12. Ellis, P. J.; Fairlamb, I. J. S.; Hackett, S. F. J.; Wilson, K.; Lee, A. F. Evidence for the Surface-Catalyzed Suzuki–Miyaura Reaction over Palladium Nanoparticles: An Operando XAS Study. *Angew. Chem. Int. Ed.* **2010,** *49*, 1820-1824.

13. Reay, A. J.; Fairlamb, I. J. S. Catalytic C–H bond functionalisation chemistry: the case for quasi-heterogeneous catalysis. *Chem. Commun.* **2015,** *51*, 16289-16307.

14. Yuan, N.; Pascanu, V.; Huang, Z.; Valiente, A.; Heidenreich, N.; Leubner, S.; Inge, A. K.; Gaar, J.; Stock, N.; Persson, I.; Martín-Matute, B.; Zou, X. Probing the Evolution of Palladium Species in Pd@MOF Catalysts during the Heck Coupling Reaction: An Operando X-ray Absorption Spectroscopy Study. *J. Am. Chem. Soc.* **2018,** *140*, 8206-8217.

15. Shan, J.; Li, M.; Allard, L. F.; Lee, S.; Flytzani-Stephanopoulos, M. Mild oxidation of methane to methanol or acetic acid on supported isolated rhodium catalysts. *Nature* **2017,** *551*, 605-608.

16. Tang, Y.; Li, Y.; Fung, V.; Jiang, D.-e.; Huang, W.; Zhang, S.; Iwasawa, Y.; Sakata, T.; Nguyen, L.; Zhang, X.; Frenkel, A. I.; Tao, F. Single rhodium atoms anchored in micropores for efficient transformation of methane under mild conditions. *Nat. Commun.* **2018,** *9*, 1231.

17. Ogino, I.; Chen, C.-Y.; Gates, B. C. Zeolite-supported metal complexes of rhodium and of ruthenium: a general synthesis method influenced by molecular sieving effects. *Dalton Transactions* **2010,** *39*, 8423-8431.

18. Basile, F.; Bersani, I.; Del Gallo, P.; Fiorilli, S.; Fornasari, G.; Gary, D.; Mortera, R.; Onida, B.; Vaccari, A. In Situ IR Characterization of CO Interacting with Rh Nanoparticles Obtained by Calcination and Reduction of Hydrotalcite-Type Precursors. *International Journal of Spectroscopy* **2011,** *2011*, 458089.

19. Lepage, M.; Visser, T.; Soulimani, F.; Beale, A. M.; Iglesias-Juez, A.; van der Eerden, A. M. J.; Weckhuysen, B. M. Promotion Effects in the Oxidation of CO over Zeolite-Supported Rh Nanoparticles. *The Journal of Physical Chemistry C* **2008,** *112*, 9394-9404.

20. Chen, Z.; Vorobyeva, E.; Mitchell, S.; Fako, E.; López, N.; Collins, S. M.; Leary, R. K.; Midgley, P. A.; Hauert, R.; Pérez-Ramírez, J. Single-atom heterogeneous catalysts based on distinct carbon nitride scaffolds. *Natl. Sci. Rev.* **2018,** *5*, 642-652.

21. Vorobyeva, E.; Fako, E.; Chen, Z.; Collins, S. M.; Johnstone, D.; Midgley, P. A.; Hauert, R.; Safonova, O. V.; Vilé, G.; López, N.; Mitchell, S.; Pérez-Ramírez, J. Atom-

by-Atom Resolution of Structure–Function Relations over Low-Nuclearity Metal Catalysts. *Angew. Chem. Int. Ed.* **2019,** *58*, 8724-8729.

22. Xiong, Y.; Dong, J.; Huang, Z.-Q.; Xin, P.; Chen, W.; Wang, Y.; Li, Z.; Jin, Z.; Xing, W.; Zhuang, Z.; Ye, J.; Wei, X.; Cao, R.; Gu, L.; Sun, S.; Zhuang, L.; Chen, X.; Yang, H.; Chen, C.; Peng, Q.; Chang, C.-R.; Wang, D.; Li, Y. Single-atom Rh/N-doped carbon electrocatalyst for formic acid oxidation. *Nat. Nanotechnol.* **2020,** *15*, 390-397.

23. Yang, Y.; Reber, A. C.; Gilliland, S. E.; Castano, C. E.; Gupton, B. F.; Khanna, S. N. More than just a support: Graphene as a solid-state ligand for palladium-catalyzed cross-coupling reactions. *J. Catal.* **2018,** *360*, 20-26.

24. Gilliland, S. E.; Tengco, J. M. M.; Yang, Y.; Regalbuto, J. R.; Castano, C. E.; Gupton, B. F. Electrostatic adsorption-microwave synthesis of palladium nanoparticles on graphene for improved cross-coupling activity. *Appl. Catal., A* **2018,** *550*, 168-175.

25. Blakemore, D. C.; Castro, L.; Churcher, I.; Rees, D. C.; Thomas, A. W.; Wilson, D. M.; Wood, A. Organic synthesis provides opportunities to transform drug discovery. *Nat. Chem.* **2018,** *10*, 383-394.

26. Verghese, J.; Kong, C. J.; Rivalti, D.; Yu, E. C.; Krack, R.; Alcázar, J.; Manley, J. B.; McQuade, D. T.; Ahmad, S.; Belecki, K.; Gupton, B. F. Increasing global access to the high-volume HIV drug nevirapine through process intensification. *Green Chem.* **2017,** *19*, 2986-2991.

27. Paul, S. M.; Mytelka, D. S.; Dunwiddie, C. T.; Persinger, C. C.; Munos, B. H.; Lindborg, S. R.; Schacht, A. L. How to improve R&D productivity: the pharmaceutical industry's grand challenge. *Nature Reviews Drug Discovery* **2010,** *9*, 203-214.

28. Shinde, S. H.; Rode, C. V. Friedel–Crafts Alkylation over Zr-Mont Catalyst for the Production of Diesel Fuel Precursors. *ACS Omega* **2018,** *3*, 5491-5501.

29. Liu, S.; Josephson, T. R.; Athaley, A.; Chen, Q. P.; Norton, A.; Ierapetritou, M.; Siepmann, J. I.; Saha, B.; Vlachos, D. G. Renewable lubricants with tailored molecular architecture. *Sci. Adv.* **2019,** *5*, eaav5487.

30. Jia, X.; Frye, L. I.; Zhu, W.; Gu, S.; Gunnoe, T. B. Synthesis of Stilbenes by Rhodium-Catalyzed Aerobic Alkenylation of Arenes via C–H Activation. *J. Am. Chem. Soc.* **2020**.

31. Crafts, C. F. J. M. Organic chemistry. *Journal of the Chemical Society* **1877,** *32*, 725-791.

32. Coley, C. W.; Thomas, D. A.; Lummiss, J. A. M.; Jaworski, J. N.; Breen, C. P.; Schultz, V.; Hart, T.; Fishman, J. S.; Rogers, L.; Gao, H.; Hicklin, R. W.; Plehiers, P. P.; Byington, J.; Piotti, J. S.; Green, W. H.; Hart, A. J.; Jamison, T. F.; Jensen, K. F. A robotic platform for flow synthesis of organic compounds informed by AI planning. *Science* **2019,** *365*, eaax1566.

33. Kaiser, D.; Yang, J.; Wuitschik, G. Using Data Analysis To Evaluate and Compare Chemical Syntheses. *Organic Process Research & Development* **2018,** *22*, 1222-1235.

34. Newton, M. A.; Knorpp, A. J.; Sushkevich, V. L.; Palagin, D.; van Bokhoven, J. A. Active sites and mechanisms in the direct conversion of methane to methanol using Cu in zeolitic hosts: a critical examination. *Chem. Soc. Rev.* **2020,** *49*, 1449-1486.

35. Evano, G.; Theunissen, C. Beyond Friedel and Crafts: Directed Alkylation of C−H Bonds in Arenes. *Angew. Chem. Int. Ed.* **2019,** *58*, 7202-7236.